UNIVERSITY OF CAPE TOWN
IYUNIVESITHI YASEKAPA • UNIVERSITEIT VAN KAAPSTAD

Department of Mechanical Engineering

BLAST IMPACT & SURVIVABILITY RESEARCH UNIT

BISRU

Dynamic Response of Aluminium Foams

Richard Peter Merrett

Submitted to the University of Cape Town in partial
fulfilment of the degree of MSc in Mechanical Engineering

May 2011

DECLARATION

I know the meaning of plagiarism and declare that all the work in the document, save for that which is properly acknowledged, is my own.

Richard Peter Merrett

May 2011

ABSTRACT

This thesis presents the results of an investigation into the response of two types of aluminium foam (ALPORAS and Cymat) to quasi-static, impact, and blast loading. The design of experiments and experimental results are reported.

The main objective of this investigation is to investigate strength enhancement phenomena known to be present in some cellular materials such as aluminium foam.

Uni-axial quasi-static compressive tests were performed on the foams in order to determine their characteristic plateau stress and densification strain. Power laws describing the plateau stress as a function of density were determined for each material, allowing the calculation of a theoretical quasi-static strength for each specimen used in direct impact and blast testing.

The direct impact testing technique consisted of a short tubular striker fired from a gas gun, and a long Hopkinson output tube as a stress measurement device. The tube was necessary as the foam specimens were relatively weak, and were larger than normal Hopkinson bar specimens. Both striker and tube had flat end caps.

Two testing configurations were used, with the specimen mounted on the output tube, and impacted by the striker (a 'forward' test), and the specimen mounted on the striker and fired at the output bar (a 'reverse' test). Both tests are needed to investigate the so-called 'shock' phenomenon, in which a densification front propagates from the impacted end of the specimen above a certain critical velocity. A displacement sensor and high-speed camera were used to measure strain. Tests over a velocity range from 17m/s to 77m/s were conducted. A series of Taylor impact tests in which the specimen alone is fired from the barrel was conducted in order to obtain clearer evidence of the densification front.

The dynamic plateau stresses and initial yield stresses in the forward and reverse direction were compared, as they varied with velocity. For ALPORAS, the plateau stress and initial yield stress were found to stay relatively constant in the forward direction, whereas in the reverse direction both were found to increase with increasing velocity. This is consistent with the theoretical shock model. There was good correlation between the predicted dynamic plateau stress for ALPORAS in the reverse direction and the

theoretical plateau stress according to the shock model. For Cymat, the material was not densified sufficiently to be compared to theoretical predictions. The testing of Cymat is complicated by significant through-thickness variation in material properties.

In blast testing, specimens were prepared by placing foam panels between a face plate and rigid back plate. The blast was generated by detonating plastic explosive. The blast wave travelled down a square blast tube and impinged on the face plate, which then compressed the foam specimen.

The blast and direct impact tests were compared by calculating the momentum per unit area for both series. It was determined that the blast specimens were not undergoing shock.

ACKNOWLEDGEMENTS

First and foremost, the author would like to thank Assoc. Prof. Genevieve Langdon for her guidance and support in supervising this project, and to Dr Matthew Theobald for his assistance and knowledge in many aspects of design, testing and data analysis.

Thanks must also go to the following people: To Trevor Cloete and Reuben Govender for their advice and expertise in Hopkinson bar testing, to Melchior Stander for his research into the design of reflective object sensors, to Prof. Dora Kariagazova for her insight into the material behaviour, and to Ms Penny Park-Ross for her assistance in material testing.

Thanks must go to Mr Glen Newins and his workshop staff for their hard work in machining specimens and testing equipment components.

Finally the author would like to thank Prof. Gerald Nurick, and all the staff and students at the Blast and Impact Survivability Research Unit for their support during the duration of this project.

TABLE OF CONTENTS

DECLARATION i

ABSTRACT iii

ACKNOWLEDGEMENTS v

TABLE OF CONTENTS vii

LIST OF FIGURES xii

LIST OF TABLES xviii

NOTATION xix

1 INTRODUCTION 1

2 LITERATURE REVIEW 5

- 2.1 Cellular Materials 5
  - 2.1.1 General 5
  - 2.1.2 Aluminium foam 6
- 2.2 Quasi-Static Testing Of Cellular Metals 10
  - 2.2.1 Deformation Characteristics in Cellular Metals 10
- 2.3 Dynamic Compressive Testing Techniques 14
  - 2.3.1 Split Hopkinson Pressure Bars 14
  - 2.3.2 Direct Impact 16
  - 2.3.3 The Use of Viscoelastic Bars 17
  - 2.3.4 The use of thin-walled Hopkinson tubes 19
- 2.4 Dynamic Testing of Cellular Materials 21
  - 2.4.1 Sources of Rate Sensitivity 22
  - 2.4.2 Shock Phenomenon 22

2.5 Blast Testing 30
2.5.1 Background 30
2.5.2 Protective Cladding Structures 32
2.5.3 Blast testing of Aluminium Foam 33
2.6 Summary of literature 36
3 QUASI-STATIC MATERIAL CHARACTERIZATION 37
3.1 Testing Programme 37
3.2 Results 38
3.2.1 ALPORAS 39
3.2.2 Cymat 45
3.2.4 Comparison of results 51
3.3 Summary 53
4. DYNAMIC TESTING PROCEDURE 55
4.1 Design of Experimental Rig 55
4.1.1 Hopkinson Tube 58
4.1.2 Gas gun and striker 62
4.1.3 Reflective Object Sensor 65
4.2 Experimental Procedure 67
4.2.1 Calibration of the Experimental Rig 67
4.2.2 Direct impact testing procedure 68
4.2.3 Taylor testing procedure 68
5 DYNAMIC MATERIAL TEST RESULTS 71
5.1 Overview of experiments 71

5.2 Data processing 72

5.3 ALPORAS direct impact results 75

5.2.1 Effect of velocity on stress-strain behaviour 75

5.2.2 Comparison of forward and reverse tests 78

5.2.3 Comparison of quasi-static and dynamic tests 80

5.2.4 Taylor test results 81

5.4 Discussion of ALPORAS direct impact results 84

5.3.1 Effect of velocity on initial yield stress 84

5.3.2 Effect of velocity on plateau stress 86

5.5 Cymat direct impact results 89

5.4.1 Effect of velocity on stress-strain behaviour 89

5.4.2 Comparison of forward and reverse tests 92

5.6 Discussion of Cymat direct impact results 94

5.5.1 Effect of velocity on initial yield stress 94

5.5.2 Effect of velocity on plateau stress 95

6 BLAST TESTING 97

6.1 Experimental Setup 97

6.1.1 The Ballistic Pendulum 97

6.1.2 Blast Rig 98

6.2 Blast Test Specimen Preparation 100

6.2.1 Introduction 100

6.2.2 Bonded Specimens 100

6.2.3 Unbonded Specimens 101

6.3 Blast Testing Programme 102

    - 6.3.1 Test Procedure ... 102
    - 6.3.2 Test Programme ... 102
  - 6.4 Blast test results ... 105
    - 6.4.1 ALPORAS blast test results ... 106
    - 6.4.2 Cymat blast test results ... 111
- 7. DISCUSSION ... 119
  - 7.1 Comparison of failure mechanism ... 119
  - 7.2 Comparison of strain hardening behaviour ... 120
  - 7.3 Effect of Cymat non-homogeneity ... 122
  - 7.4 Shock development under dynamic testing ... 123
    - 7.4.1 Shock development in ALPORAS ... 123
    - 7.4.2 Discussion of Taylor test results ... 124
    - 7.4.3 Shock development in Cymat ... 126
  - 7.5 Shock development under blast loading ... 128
- 8 CONCLUSIONS ... 137
  - Failure mechanisms ... 137
  - Effect of velocity on dynamic compressive response – forward direction ... 137
  - Effect of velocity on dynamic compressive response – reverse direction ... 138
  - Shock development under Taylor cylinder testing ... 138
  - Effect of charge mass on blast response ... 138
  - Methods of comparing direct impact and blast loading results ... 139
- 9 RECOMMENDATIONS ... 141
- 10 REFERENCES ... 143

APPENDIX A: QUASI-STATIC STRESS STRAIN CURVES A-1

A-1: ALPORAS A-1

A-2: Cymat.. A-3

APPENDIX B: DYNAMIC STRESS-STRAIN CURVES B-1

B-1: ALPORAS B-1

B-1.1: ALPORAS cubes B-1

B-1.2: ALPORAS Cylinders... B-3

B-2 Cymat.. B-7

B-2.1 Cymat cubes.. B-7

B-2:2 Cymat cylinders B-8

APPENDIX C: DYNAMIC TEST SPECIMEN DETAILS C-1

APPENDIX D: SUPPORTING THEORY D-1

APPENDIX E: DRAWINGS E-1

LIST OF FIGURES

Figure 1: Aluminium foam panels used as noise protection during tunnel construction blasting (2) 1

Figure 2: ALPORAS (left) and Cymat (right) aluminium foams (3), (4) 2

Figure 3: Examples of truss-type cellular structures (8) 6

Figure 4: The production of aluminium foam by direct foaming, used to manufacture Cymat foam (16) 7

Figure 5: Foaming of powdered aluminium by a blowing agent, used to manufacture ALPORAS foam (16) 8

Figure 6: Progressive buckling of a tube with aluminium foam insert (17) 9

Figure 7: Use of aluminium foam as a component in ballistic armour (6) 9

Figure 8: The characteristic stress-strain curve of a cellular material (18) 10

Figure 9: Schematic of a split Hopkinson bar setup (26) 15

Figure 10: Forward and reverse impact tests (29) 17

Figure 11: Measurement of the displacement of a projectile (42) 20

Figure 12: Signal recorded by a reflective object sensor (42) 21

Figure 13: Characteristic stress-strain curve of a cellular material (solid curve), and the idealised r-p-p-l model (dashed curve) (28) 23

Figure 14: Nominal stress-strain curve and its idealisation (46) 24

Figure 15: Collapse mechanism of a polyhedral cell under static and dynamic loading (20) 26

Figure 16: Experiments conducted by Zhao, et al. to measure the stresses ahead of (a) and behind (b) the shock propagation front (28). 27

Figure 17: Taylor test specimens showing ‘frozen’ densification front (9) 28

Figure 18: Pressure histories (actual and theoretical) 11% (460m/s) and 17% (430m/s) foams (47) 29

Figure 19: Pressure-time history of a far-field blast wave (49) 30

Figure 20: Schematic of a ballistic pendulum (50) 31

Figure 21: Measurement of blast pressure using pressure transducers (51).................. 32

Figure 22: The principle behind a sacrificial cladding (52) 33

Figure 23: Experimental setup used by Hanssen et al. (52)... 34

Figure 24: Test specimen used by Langdon, et al (54) 35

Figure 25: Test rig and ballistic pendulum used by Langdon et al. (54) 35

Figure 26: Typical stress-strain curve for an ALPORAS specimen (AC1, density 9.06%) 40

Figure 27: Energy absorption efficiency versus strain for a 9% density ALPORAS specimen.. 41

Figure 28: Stress ratio versus relative density – ALPORAS... 43

Figure 29: Densification strain versus relative density – ALPORAS............................... 44

Figure 30: Stress-strain curve for a Cymat specimen of relative density 16.3%............. 46

Figure 31: Energy absorption efficiency curve Cymat specimen CL1, showing a less well-defined maximum.. 47

Figure 32: Stress ratio versus relative density for all Cymat tests 49

Figure 33: Densification strain versus relative density for all Cymat tests 50

Figure 34 Comparison of quasi-static stress-strain curves for the two different materials 51

Figure 35: Experimental setup for direct impact and Taylor tests.................................. 55

Figure 36: Striker, striker end cap and displacement sensor 56

Figure 37: Strain gauge placement on output tube 59

Figure 38: Schematic of direct impact specimen and end cap placement (forward direction) 60

Figure 39: Tube mounting, with white inner Teflon ring and outer bronze ring 61

Figure 40: Schematic of 50mm diameter tube, with fluting holes 63

Figure 41: 50mm striker with 2mm end cap (left) and 36mm striker with heavier 5mm end cap (right) 64

Figure 42: The Fairchild QRB1134 Reflective Object Sensor (60) 65

Figure 43: The three reflective object sensors comprising the displacement sensor 67

Figure 44: Raw signal output for a typical direct impact test 72

Figure 45: Comparison of displacement-time signals from the reflective object sensor and high-speed camera footage 73

Figure 46: Comparison of velocity measurement techniques – high-speed camera and Reflective Object Sensor 74

Figure 47: Comparison of of stress-strain curves for ALPORAS cylinders at varying velocties - forward direction 75

Figure 48: Comparison of stress-strain curves for ALPORAS cylinders at varying velocies - reverse direction 77

Figure 49: Stress-strain curves for forward and reverse tests at comparable velocities (high velocity) 78

Figure 50: Stress-strain curves for forward and reverse tests at comparable velocities (low velocity) 79

Figure 51: Stress-strain curves for quasi-static and dynamic forward and reverse tests 80

Figure 52: Taylor test A29T (V_0 = 183.3m/s) at time t = 0s, 86μs, and 229μs 82

Figure 53: Stress-time plot for Taylor test A29T (V_0 = 183.3m/s) 83

Figure 54: Taylor test A33T (V_0 = 147.8m/s), showing densification front 84

Figure 55: Yield stress ratio vs impact velocity for all ALPORAS cylinders 85

Figure 56: Yield stress ratio vs impact velocity for all ALPORAS tests 86

Figure 57: Comparison of two methods of calculating the plateau stress for all quasi-static ALPORAS tests 87

Figure 58: Plateau stress ratio vs impact velocity – ALPORAS cylinders 88

Figure 59: Plateau stress ratio vs impact velocity for all ALPORAS tests 89

Figure 60: Stress-Strain curves for all Cymat cylinders – forward direction 90

Figure 61: Stress-strain curves for all Cymat cylinders – reverse direction 91

Figure 62: Comparison of Cymat forward and reverse tests – dense side toward striker, nominal velocity 33m/s 92

Figure 63: Comparison of Cymat forward and reverse tests – dense side toward bar, nominal velocity 70m/s 93

Figure 64: Initial peak stress ratio vs impact velocity – all Cymat tests 94

Figure 65: Plateau stress ratio vs impact velocity – all Cymat tests 95

Figure 66: The ballistic pendulum...97

Figure 67: Blast test specimen, blast tube and explosive charge 99

Figure 68: Impulse versus charge mass for all blast test specimens 105

Figure 69: Percentage crush versus impulse for all 25mm ALPORAS specimens 108

Figure 70: Percentage crush versus damage number for all 25mm thick ALPORAS specimens..108

Figure 71: Increase in crush distance with increasing charge mass for ALPORAS blast test specimens 109

Figure 72: Specimen A8, charge mass 4g, ρ=8.2% 110

Figure 73: Specimen A9, charge mass 5g, ρ=8.2% 110

Figure 74: Specimen A11, charge mass 8g, ρ=7.3% 110

Figure 75: Specimen A13, charge mass 10g, ρ=7.3% 111

Figure 76: Specimen A14, charge mass 11g, ρ=7.4% 111

Figure 77: Crush distance versus impulse for all Cymat specimens 113

Figure 78: Percentage crush versus damage number for all Cymat specimens...........113

Figure 79: Increase in crush distance with charge mass (Cymat) –16-26 grams 114

Figure 80: Increase in crush distance with charge mass (Cymat) –8-15 grams 115

Figure 81: Cymat specimen C12 – charge mass 8g, ρ=14.9% 116

Figure 82: Cymat specimen C15 – charge mass 11g, ρ=19.1% 116

Figure 83: Cymat specimen C17 – charge mass 15g, ρ=16.2% 116

Figure 84: Cymat specimen C1 – charge mass 18g, ρ=15.7% 117

Figure 85: Cymat specimen C6 – charge mass 22g, ρ =18.9% 117

Figure 86: Cymat specimen C11 – charge mass 26g, ρ=15.3% 117

Figure 87: Specimen fracture in bonded specimen C4 (18 grams) 118

Figure 88: Specimen fracture in unbonded specimen C9 (20 grams) 118

Figure 89: Brittle collapse of Cymat foam under quasi-static compression. Note fragments around specimen due to brittle fracture. 119

Figure 90: Ductile collapse of ALPORAS foam under quasi-static compression 120

Figure 91: Comparison of strain hardening for ALPORAS and Cymat specimens, at sub-critical velocities. Forward direction. 121

Figure 92: Comparison of strain hardening for ALPORAS and Cymat specimens, at sub-critical velocities. Reverse direction. 121

Figure 93: Dependence of Cymat foam response on specimen orientation. Reverse direction. 122

Figure 94: Dynamic plastic collapse stress, plateau stress and theoretical shock stress versus impact velocity for all ALPORAS cylinders, reverse direction. 124

Figure 95: Crush distance versus impact velocity for all Taylor tests 125

Figure 96: Progressive crush distances of Taylor test specimens...............................125

Figure 97: Initial peak stress ratio versus impact velocity for Taylor tests 126

Figure 98: Limitations of r-p-p-l model for a strain-hardening material. Modified from (21) 127

Figure 99: Crush distances of comparable direct impact and blast tests......................131

Figure 100: Comparison of crush distance for comparable blast and direct impact tests (normalised) 132

Figure 101: Percentage crush versus specific impulse for all blast test and ALPORAS cylinder forward direct impact tests 133

Figure 102: Percentage crush distance (normalised) versus specific impulse for all ALPORAS direct impact and blast tests 133

Figure 103: Corner of ALPORAS panel, showing differing cell structure toward top/left edges of panel.. 134

Figure 104: Percentage crush versus specific impulse for all Cymat direct impact and blast tests.. 135

Figure 105: Percentage crush (normalised) versus specific impulse for all forward cylinder Cymat DI tests and Cymat blast tests.. 136

LIST OF TABLES

Table 1: ALPORAS specimen information 39

Table 2: Summary of ALPORAS quasi-static test results 42

Table 3: Cymat specimen information 45

Table 4: Summary of Cymat quasi-static test results 48

Table 5: Comparison of constants A and B 52

Table 6: Overview of test programme 71

Table 7: Taylor test specimen details 81

Table 8: Blast test specimen details - ALPORAS 103

Table 9: Blast test specimen details - Cymat 104

Table 10: ALPORAS blast test measurements 106

Table 11: Cymat blast test measurements 112

Table 12: Theoretical maximum face plate velocities and specific impulses for all ALPORAS blast tests 128

Table 13: Theoretical maximum face plate velocities and specific impulses for all Cymat blast tests 129

Table 14: Comparable blast and direct impact tests, based on specific impulse 131

NOTATION

E_f	Young’s Modulus of the foam material
E_s	Young’s Modulus of the parent/cell wall material
ρ_f	Density of the foam
ρ_S	Density of the parent/cell wall material
P_0	Internal cell pressure
P_{ATM}	Atmospheric pressure
σ_{pl}	Plateau stress
σ_{YS}	Yield stress of the parent /cell wall material
ε_D	Densification strain
σ_{CR}	Initial peak stress/yield stress
V_0	Initial velocity/impact velocity
V_{CRIT}	Critical velocity
E_d	Energy dissipation efficiency
I	Impulse
I^*	Specific impulse

1 INTRODUCTION

Cellular metals are a relatively modern class of material that exhibits a wide range of attractive properties that allow them to be used in a variety of engineering applications. As the materials and their associated production processes are refined, their continued development broadens the range of fields in which they can be used. A great deal of research and material testing must be carried out on these materials in order for them to become commercially useful (1).

Figure 1: Aluminium foam panels used as noise protection during tunnel construction blasting (2)

Aluminium foams are a particular type of cellular metal that are formed by solidifying a mixture of molten aluminium and gas bubbles. Aluminium foams may be ‘open’ or ‘closed’, depending on whether the cells are open to the atmosphere or not. They were first produced in the 1940’s, and are starting to become commercially popular due to their properties, which include:

- High specific stiffness
- Low density
- Noise reduction (shown in Figure 1)
- Low thermal conductivity
- Electro-magnetic wave shielding
- Machinability
- Recyclability

A property of aluminium foams that suggests great potential in the fields of blast mitigation and impact protection is their ability to absorb energy by undergoing large strains at relatively constant stresses under compression. Aluminium foams have been proposed as a sacrificial cladding material that could be fitted to existing structures or vehicles that would provide protection during a blast event, and as a component material in the impact zones of passenger vehicles.

This thesis reports on the results of an experimental investigation into two types of aluminium foams (ALPORAS and Cymat), and their behaviour under uni-axial compression using three different testing techniques. The two foams are shown in Figure 2.

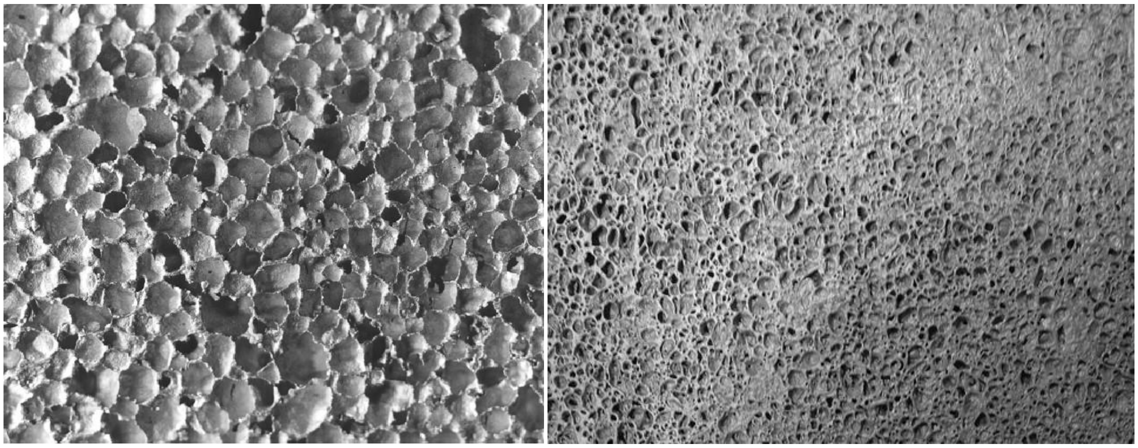

Figure 2: ALPORAS (left) and Cymat (right) aluminium foams (3), (4)

Both foams are closed-cell, and are manufactured using two different techniques. ALPORAS has a nominal density of 240kg/m^3, and an average cell diameter of 3mm. Cymat has a nominal density of 430kg/m^3, and an average cell size of 4mm. The materials are to be tested under quasi-static, dynamic impact, and blast loading.

The principle objectives of this report are to:

- Investigate the response of two types of aluminium foam to quasi-static, dynamic and blast loading.
- Design a testing technique to enable the testing of aluminium foams under dynamic compression.
- Consider the development of shock within two different aluminium foams under various impact and blast conditions.
- Draw conclusions and make recommendations based on the results.

The report begins by presenting and discussing a review of the literature published on aluminium foams, and on relevant experimental work done and testing techniques used by various authors. The quasi-static testing programme and the results thereof are presented in Chapter 3. The details of the dynamic testing equipment, and the dynamic testing procedure, are discussed in Chapter 4. The dynamic material test results, along with initial discussions, are presented in Chapter 5. Chapter 6 details the blast test programme, including the use of the ballistic pendulum, along with the blast test results. Chapter 7 discusses the results of the three test programmes. Conclusions are drawn and recommendations are made in Chapters 8 and 9 respectively.

2 LITERATURE REVIEW

2.1 Cellular Materials

2.1.1 General

A cellular material is a material that is composed of a number of hollow sub-structures (cells) in a regular or irregular array. A detailed description of cellular materials and their properties is given in (1). It may also be described as a composite material composed of a phase of solid (cell wall) and gaseous phases (5). This definition encompasses a wide and constantly growing range of materials with an equally wide range of applications. The most commonly cited advantage of a cellular material is the fact that it has a lower density than the parent or constituent material that the cell walls are composed of (due to the inclusion of the gaseous phase). This has seen the widespread use of cellular materials as a core material in sandwich structures, where a panel of the cellular material is combined with solid face sheets. The purpose of using a sandwich structure is primarily to reduce the weight of a structure whilst maintaining strength or stiffness, but the core material can be chosen to meet any type of design requirement such as sound or heat insulation, cost saving, electro-magnetic shielding or recyclability.

Of particular interest to the present study is the ability of many cellular materials to absorb energy under compaction. This has significant potential in the fields of crashworthiness and protecting structures from impact and blast. Applications range from packaging (such as polystyrene), to use as a component in composite armour (6) and protective cladding materials (7).

Figure 3 shows a truss-type cellular material, consisting of two face sheets, and a regular array of trusses forming the cellular core (8).

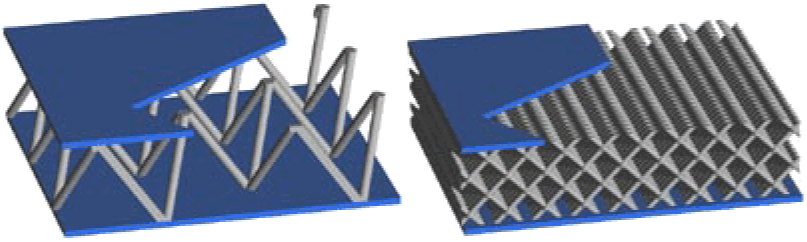

Figure 3: Examples of truss-type cellular structures (8)

2.1.2 Aluminium foam

Aluminium foams are a particular type of cellular material in which the cell wall material is an aluminium alloy, and the cells are polyhedral in shape (9). The cell morphology is limited by the fact that solid foams are manufactured from liquid metallic foams, and thus adhere to the principle of minimisation of surface energy of the bubbles/cells. The cells may be open or closed and filled with a gas such air. Attempts were first made to manufacture metallic foams as early as the 1940's (10), but it has only been more recently in the early 1990's that a concerted effort was made to develop a reliable manufacturing process in which cell size and distribution could be controlled accurately. Since then, a number of companies have started producing aluminium foam on a commercial basis, such as the Shinko Wire Company (ALPORAS) (11), Cymat (Cymat) (12), the Frauenhoefer institute (IFAM) (13), Alulight International GmbH (Alulight) (14), and ERG Materials and Aerospace Corporation (Duocel) (15).

Banhart (16) provides an extensive overview of the advances in production and applications of aluminium foams. The two production processes relevant to the current work are direct foaming through gas injection (used to manufacture Cymat foam), and foaming of powdered aluminium by a blowing agent (used to manufacture ALPORAS).

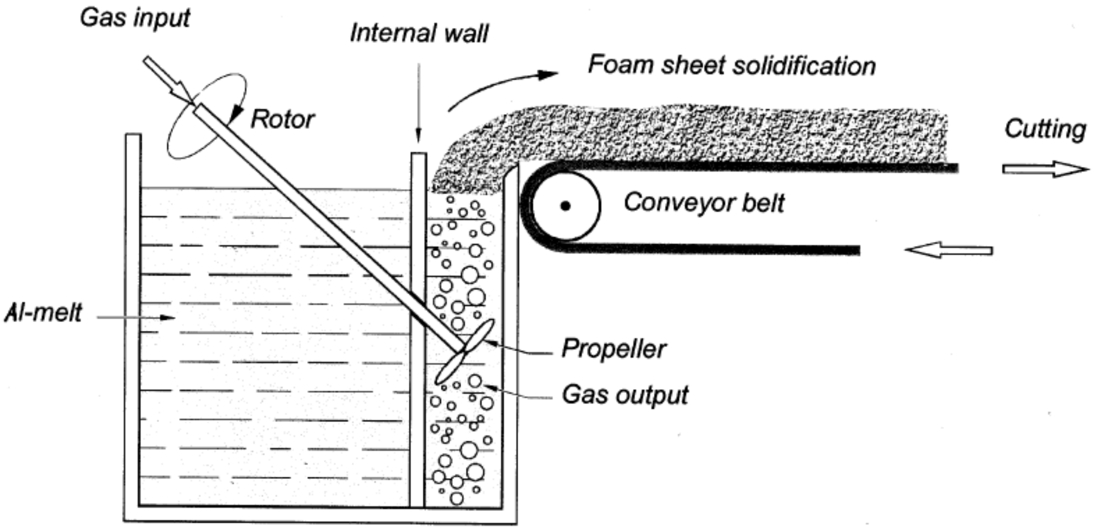

Figure 4: The production of aluminium foam by direct foaming, used to manufacture Cymat foam (16)

A schematic of the direct foaming process is shown in Figure 4. An aluminium alloy is liquefied in the melt, during which ceramic particles are added. The function of the particles is to stabilise the cell walls by increasing their viscosity (12). Gas bubbles are then added, with the impellor creating an even distribution of very fine bubbles. The liquid foam then rises and can be pulled off by a conveyor belt on which it solidifies. As it solidifies on the conveyor, the resulting foam becomes anisotropic due to:

- Shearing forces from the conveyor, elongating the cells in the cast direction.
- Gravitationally induced drainage, creating a through-thickness variation in density, cell size, cell elongation and volume fraction of ceramic particles.

This anisotropy is regarded as undesirable, as it is not a controlled part of the manufacturing process, and the relatively high concentration of ceramic particles makes machining the foam difficult.

The 'ALPORAS' process is shown in Figure 5. The Shinko Wire Co. has used this process since 1986 for small-scale commercial production, and can produce up to 1000kg per day (16).

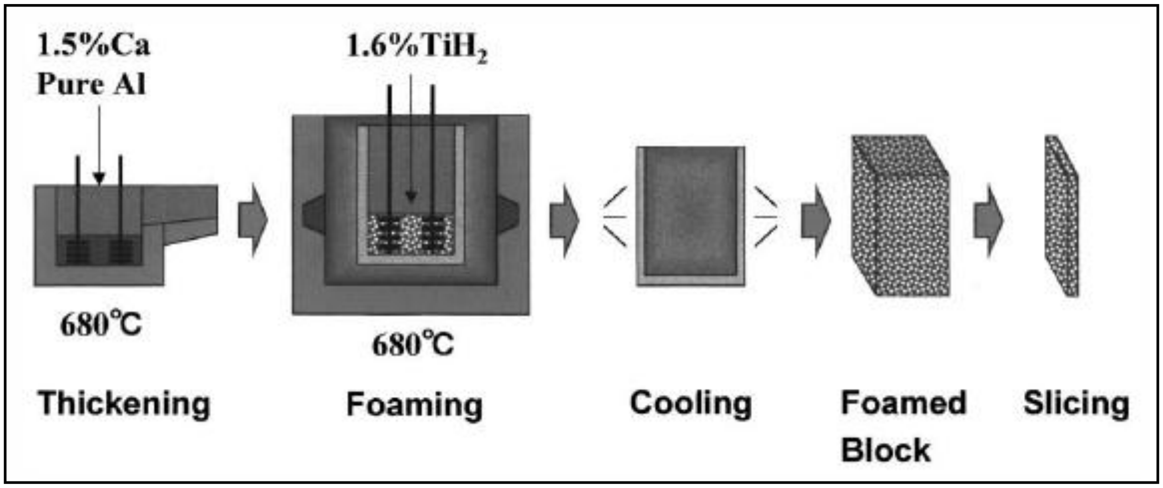

Figure 5: Foaming of powdered aluminium by a blowing agent, used to manufacture ALPORAS foam (16)

Calcium is added to molten aluminium, increasing its viscosity with the formation of various compounds that thicken the metal. At a certain viscosity, TiH_2 particles are added, which decompose, releasing hydrogen gas and creating bubbles in the molten metal. The metal foams and expands to fill the foaming vessel before the vessel is cooled and the foam solidifies. The solid foam can then be removed and machined. Foams produced in this way result in a more homogeneous product than with the direct foaming process (16).

While aluminium foam is often proposed as a material that has good energy-absorbent properties in the fields of impact and blast protection, it has yet to find widespread commercial application in this regard. It has been used in experimental applications, for example in impact tests on aluminium tubes filled with Cymat foam (17), increasing the energy absorption of the tube and developing progressive buckling (as shown in Figure

6). Alulight foam has been tested as part of a lightweight composite ballistic armour, shown in Figure 7. The addition of the foam was found to cause lower dynamic deflections of the armour backing plate (6).

There have been numerous studies conducted in order to characterise the behaviour of aluminium foam under high rates of compressive strain (as opposed to testing it as part of a structure in a specific application). These studies are mentioned in more detail in section 2.4 and 2.5.

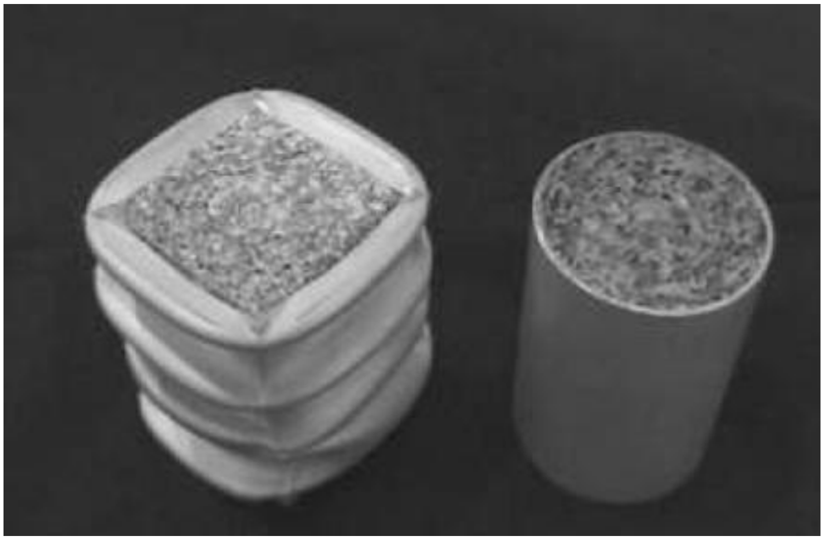

Figure 6: Progressive buckling of a tube with aluminium foam insert (17)

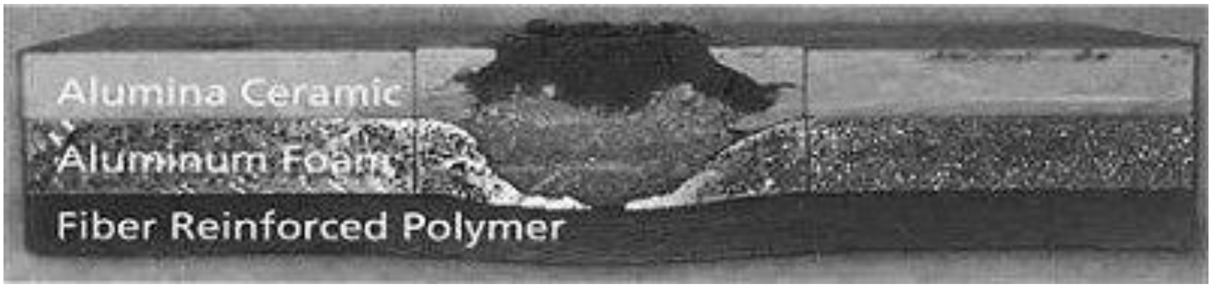

Figure 7: Use of aluminium foam as a component in ballistic armour (6)

2.2 Quasi-Static Testing Of Cellular Metals

2.2.1 Deformation Characteristics in Cellular Metals

Gibson and Ashby (1) have described the deformation modes of elastomeric, elastic-plastic, and elastic-brittle foams. Under quasi-static uni-axial compression, all cellular materials show a characteristic stress-strain curve, similar to the one shown in Figure 8.

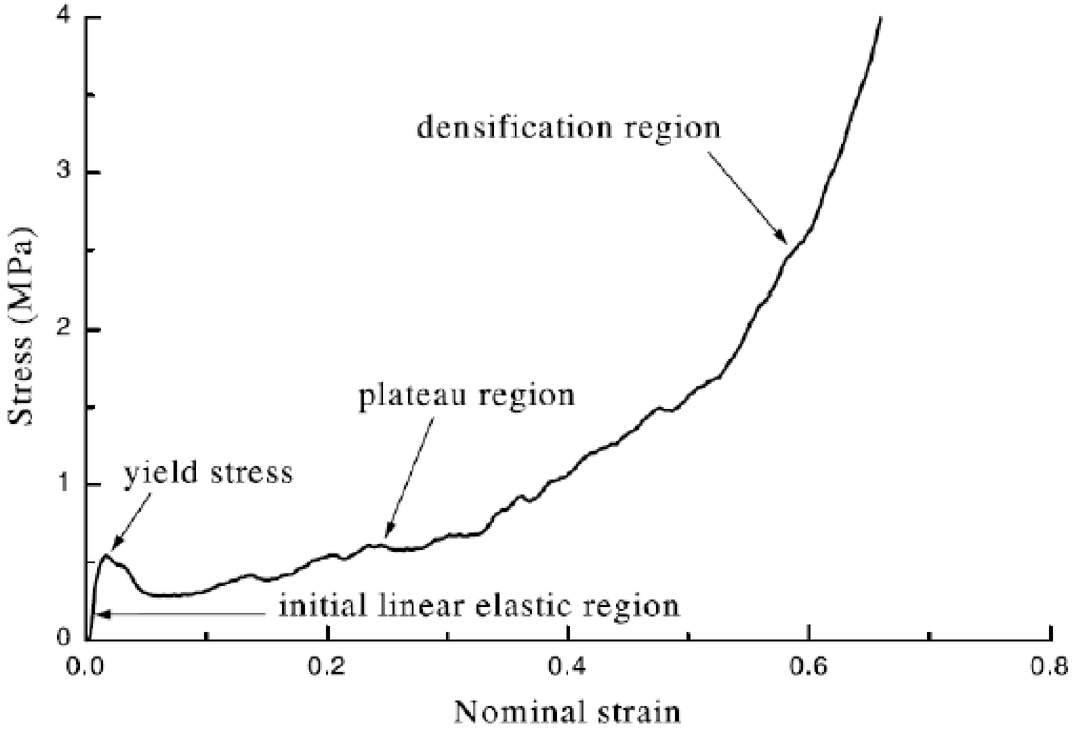

Figure 8: The characteristic stress-strain curve of a cellular material (18)

The curve comprises three distinct regions, namely the initial linear elastic region, plateau region, and densification region.

In the linear elastic region, the material undergoes non-permanent deformation. The mode of deformation is cell wall bending, and in the case of closed-cell foams, cell face stretching. The Young's modulus of the material in this region, as with many properties of cellular materials, can be described by a power function of the relative density of the material, as shown in equation 1 (for closed-cell foams) and equation 2 (for open-cell foams).

$$\frac{E_f}{E_S} = C_1\Phi^2\left(\frac{\rho_f}{\rho_S}\right)^2 + C_1^{'}(1-\Phi)\frac{\rho_f}{\rho_s} \tag{1}$$

$$\frac{E_f}{E_S} = C_1\left(\frac{\rho_f}{\rho_S}\right)^2 \tag{2}$$

The subscripts f and S refer to the foam and solid cell wall material respectively. C_1 and C_1' are geometric constants of proportionality, and Φ is the fraction of solid in the cell faces. Idris et al. (19) have reported studies that give the yield stress of the cell wall material of ALPORAS variously as 120, 172 and 130 MPa, as well as determining it to be 99.8 MPa based on their own experiments. Shen et al (20) have reported the yield stress to be 172MPa. Tan et al. (21) have reported the yield stress of the cell wall material of CYMAT foam to be 185MPa.

As the material reaches its initial yield point, the weakest cells in the material yield permanently, followed by progressively stronger bands of cells. In ductile materials, this progressive collapse is via the formation of plastic hinges; in brittle materials, by the brittle crushing of cell walls (1). The stress in the plateau region may be relatively constant, in the case of a more homogeneous, ductile foam such as ALPORAS foam, or may increase significantly, as is the case with Cymat foam which undergoes brittle crushing and is less homogeneous.

The plateau region is characteristic of the ability of a cellular material to undergo large strains at relatively constant stress, and in doing so absorb large amounts of energy.

The plateau stress (the average stress in the plateau region) is therefore an important factor to determine in characterising a material under quasi-static compression. Tan et al. (21) have noted that there is a lack of consistency in the method used to determine the plateau stress. Various methods include taking the average stress from a strain of 0.1 to 0.5 (18), calculating the integral of the plastic engineering stress-strain curve from 0 to 0.4 (22), and converting the strain to time, and using the time-average value of the σ(t) function (21). Another method is by locating the densification strain (discussed later), and calculating the experimental plateau stress using equation 3 (20):

$$\sigma_{pl} = \frac{\int_0^{\varepsilon_d} \sigma(\varepsilon) d\varepsilon}{\varepsilon_d} \tag{3}$$

The theoretical plateau stress of closed-cell foams is (1):

$$\frac{\sigma_{pl}}{\sigma_{ys}} = 0.3\left(\varphi \frac{\rho_f}{\rho_s}\right)^{3/2} + (1-\varphi)\frac{\rho_f}{\rho_s} + \frac{p_0 - p_{atm}}{\sigma_{ys}} \tag{4}$$

where p_0 is the fluid pressure in the cells, and p_{atm} is atmospheric pressure. In practice this internal pressure has little or no effect on the strength of the material, both quasi-statically or dynamically. The first term accounts for cell wall bending/buckling and the second term for cell face yielding. φ is once again the fraction of solid in the cell edges. Tan et al. (21) have found that the membrane stress (term 2) also has little influence on the plateau stress. The plateau stress has also been shown empirically to obey the power law described by equation 5.

$$\frac{\sigma_{pl}}{\sigma_{ys}} = A\left(\frac{\rho_f}{\rho_s}\right)^B \tag{5}$$

where A and B are constants for a given type of material. This has the same form as the first term of the expression in equation 4, although A and B vary. It assumes that cell face yielding and fluid pressure in the cells have no effect on the plateau stress.

Once the majority of cells in the material have collapsed, the material begins to densify, and the slope of the stress-strain curve begins to increase rapidly. As many of the applications of cellular materials in energy absorption depend on its behaviour in the plateau region, it is important to be able to define a strain at which the onset of densification can be said to occur, and to have a consistent method of locating this densification strain. One method, described by Shen et al. (20), requires the calculation of the energy dissipation efficiency (E_d) of the material under compression. E_d at a particular strain ε_a is defined as:

$$E_d(\varepsilon_a) = \frac{\int_0^{\varepsilon_a} \sigma(\varepsilon)d\varepsilon}{\sigma_a},\ 0 \le \varepsilon_a \le 1 \tag{6}$$

where σ_a is the stress at ε_a. The densification strain ε_d is then defined as the stationary point of the efficiency-strain curve, or point of maximum efficiency:

$$\left.\frac{dE_d(\varepsilon_a)}{d\varepsilon}\right|_{\varepsilon_a=\varepsilon_i} = 0 \tag{7}$$

The plateau stress σ_{pl} is defined as shown in equation 3.

The densification strain can be described by (1):

$$\varepsilon_d = A - B\left(\frac{\rho_f}{\rho_s}\right) \tag{8}$$

where A and B are constants. Gibson and Ashby (1) reported values of 1 and 1.4 for A and B respectively, while Shen et al. (20) reported values of 1 for A, and 4.8 or 5 for B depending on whether loading was quasi-static or dynamic.

2.3 Dynamic Compressive Testing Techniques

2.3.1 Split Hopkinson Pressure Bars

The pressure-time relation of stress waves travelling through elastic bars were first studied by Bertram Hopkinson (23), who used the technique to study the change in shape of the pulses as they travelled along the bars. This technique was then developed be Kolsky (24) and Davies (25) to investigate the dynamic compression of a sample held between two pressure bars. This testing apparatus then became known as the Split Hopkinson Pressure Bar (SHPB), or the Kolsky Bar. A schematic of the apparatus is shown in Figure 9.

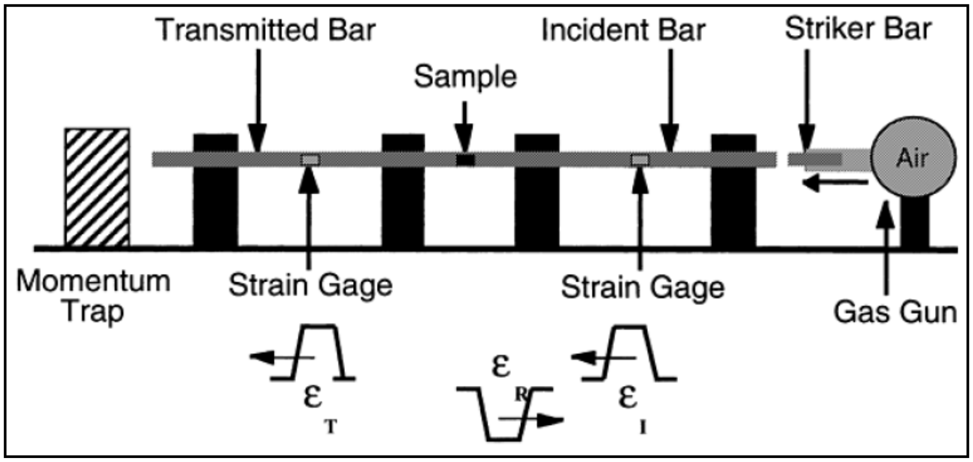

Figure 9: Schematic of a split Hopkinson bar setup (26)

This technique has become popular in the testing of materials at strain rates of the order of 10^3-10^4 s^{-1}. This is to characterize the behaviour of materials undergoing high-speed dynamic or impact loading, such as those used in high strain-rate manufacturing processes or those that are exposed to such loading during their service life (25). The SHPB technique has become popular for dynamic testing as the behaviour of one-dimensional stress wave propagation in thin cylindrical bars is relatively well understood.

The experimental procedure described by Gray (26) is summarised as follows: The standard SHPB apparatus consists of a striker, an input/incident bar and an output/transmitted bar. The striker is fired from a gas gun which then impacts the input bar. This generates a compressive wave (called the incident wave, ε_I) in the input bar which then propagates along the bar until it reaches the specimen, which is sandwiched between the input and output bars. Part of the wave is then reflected from the specimen-input bar interface, as a tensile wave. This is called the reflected wave (ε_R). The other part of the wave is transmitted through the specimen and into the output bar as a compressive wave. This is called the transmitted wave (ε_T).

The magnitudes of the stress waves are calculated from the voltage recorded by the strain gauges (typically one pair of diametrically opposite gauges mounted on the input and output bars each). In order to prevent the incident and reflected waves overlapping in the input bar, the distance between the strain gauges and the ends of the bar must be more than half the wave length. The length of the incident, reflected and transmitted waves is determined by the length and material of the striker.

2.3.2 Direct Impact

In the dynamic testing of cellular materials, the higher strain rates required to investigate some phenomena are beyond the capabilities of the conventional SHPB setup. One may require an impact velocity (i.e. a particle velocity in the input bar) of up to $200m.s^{-1}$, and at this particle velocity, the stress in the input bar would be far beyond the yield stress of the bar material. In the direct impact method, there is no input bar, and the striker or projectile impacts the output bar, with the specimen mounted between the striker and output bar. One inherent drawback of this method is that, while a stress history can be recorded by the output bar, as there is no input bar the strain or displacement reading must be done by indirectly, for example by using a high-speed camera or optical sensing device.

The direct impact technique (and the similar Taylor cylinder – Hopkinson bar technique) has been used extensively in recent years to investigate the dynamic properties of many kinds of cellular metals, initially by Reid et al. (27) in the uni-axial crushing of wood specimens. Elnasri et al. (28) and Lee et al. (29) have used forward and reverse direct impact tests to investigate the so-called ‘shock’ phenomenon that occurs in cellular metals under dynamic compression. This phenomenon, as well as the forward and reverse testing technique, is described further in section 2.4.2.

Schematics of the forward and reverse tests are shown in Figure 10. In the forward test, the specimen is mounted on the output bar, and the striker impacts the specimen. In the reverse test, the specimen is mounted on the striker, and the specimen and striker together impact the output bar. This enables stress measurements on the impacted and stationary faces of specimens respectively.

During dynamic compression cellular materials undergo highly non-uniform deformation (i.e. different forces are recorded on the two faces of the specimen), and the aim of the forward and reverse tests is record these different force histories.

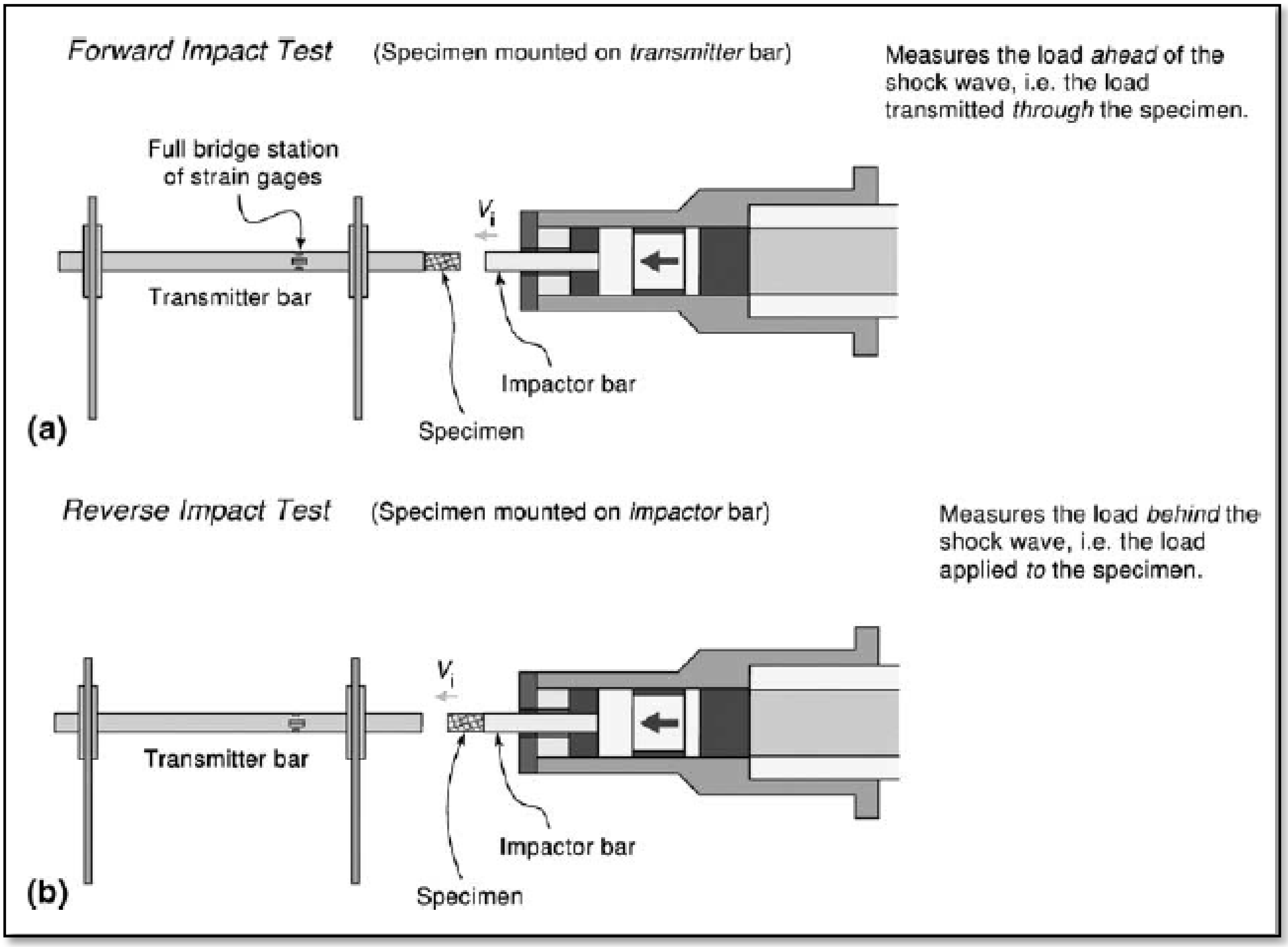

Figure 10: Forward and reverse impact tests (29)

2.3.3 The Use of Viscoelastic Bars

When testing low-impedance impedance materials (materials that require low stresses to compress), the use of low-impedance Hopkinson bars (30) or a Hopkinson tube is required. This is relevant to the present study as many cellular materials are considered to be low-impedance materials. During testing, a low-impedance specimen will generate small stresses and hence small strains in a metal bars. This is problematic, as the ratio of the amplitude of the signal measured to that of the noise inherent in the signal becomes too low. Further amplification of the signal does not help as this would amplify the noise as well.

There are two solutions to the problem of small stresses in the Hopkinson bars. The first is to use a more sensitive semiconductor strain gauge. Semiconductor strain gauges have a gauge factor of 120 to 225, as opposed to about 2 for a constantan strain gauge (31). This gives a proportionally bigger output signal for a given strain. They are, however, considerably more expensive. The second solution is to increase the strain in the output bar (for a given input force) through the use of a low impedance bars, made from a material with a lower elastic modulus than a metal, such as nylon. These materials are always viscoelastic (30), as opposed to metals, which can be assumed to be perfectly elastic. There arise two problems when analysing the propagation of stress waves in viscoelastic materials; wave attenuation, and wave dispersion. Wave attenuation can be described as the reduction in amplitude of a stress wave as it travels along a bar. Wave dispersion is a phenomenon in which the waves of different frequencies that constitute a disturbance (such as an impact) in a bar propagate through a material at different speeds (and hence reach the strain gauge at different times). Wave dispersion occurs in bars made from viscoelastic materials (viscoelastic dispersion) as well as any large diameter bars (elastic geometric dispersion). In large-diameter viscoelastic bars the two different causes of dispersion cannot be separately accounted for when performing the wave shifting, but must be simultaneously accounted for in a single means of data reduction (32).

Pochammer (33) and Chree (34) developed solutions for the equation of motion in an infinitely long elastic cylinder, appropriate assumptions for metal Hopkinson bars. These solutions where then modified by Coquin (35) and Zhao and Gary (36) to describe wave propagation in an infinitely long cylindrical solid made from a linear viscoelastic material (the solutions for a finite elastic or viscoelastic cylinder, or non-linear viscoelastic solid do not exist).

2.3.4 The use of thin-walled Hopkinson tubes

An alternative to using polymer output bars to measure stresses in low impedance materials is to use a thin-walled metal tube as the output ‘bar’. For a given stress in a specimen, a thin-walled tube of a certain outer diameter will experience a larger strain than a solid cylindrical bar of the same outer diameter and material (due to the smaller cross-sectional area of the tube). A metal tube has advantages when compared to a viscoelastic bar, as the effects of attenuation and dispersion on wave propagation are not as great, and the material is not affected by ageing factors such as creep and moisture absorption.

Campbell and Fergusson (37) and Klepaczko (38) utilised Hopkinson tubes in the shear testing of mild steel, although this was to accommodate the ‘top-hat’ shaped shear specimen, and not for the suitability of tubes in testing low-impedance materials. Klepaczko (38) noted that the effects of dispersion in a thin-walled tube are much smaller than in a solid cylindrical bar of the same external diameter.

Chen et al. (39, 40) used an experimental technique for compressive testing of low impedance materials at high strain rates using a thin-walled aluminium output tube in a split Hopkinson pressure bar setup (both studies use a similar technique). The use of high-strength aluminium instead of steel allows for a larger strain for a given input force, due to the lower elastic modulus of aluminium. The rise time of the incident pulse was lengthened (this is known as ‘pulse shaping’) to ensure that the amplitude of the stress pulse did not reach the yield strength of the material being tested before the specimen is loaded homogeneously. Another advantage of the longer rise time is that it has the effect of filtering out high-frequency components of the incident pulse, and reduces the amount of dispersion (the smaller the range of frequencies, the less the range of frequencies in the wave form will disperse). It is noted that the end cap on the tube (on which the specimen is mounted) could interfere with the wave propagation in the tube, and the increased rise time apparently negates this problem. There is therefore no need to correct for the effects of wave attenuation and dispersion in an elastic metal tube, as there is in a viscoelastic polymer bar.

Segreti et al. (41) and Rusinek et al. (42) have utilised Hopkinson tubes in direct impact setups in the perforation testing of PMMA and mild steel plates respectively. The use of a tube was again due to its suitability in attaching the circular plate specimens. In both of these studies, the displacement of the specimen was calculated by measuring the displacement of the projectile, as the light signal reflected from alternate black and white stripes on the projectile was recorded. This use of a reflective object sensor overcomes the difficulty of measuring average strain of a specimen in direct impact tests. Figure 11 is a schematic of the test rig used in (42). On the right, the striped projectile is exiting the gas gun barrel. Light sources, and diametrically opposite optical fibres are used to measure the initial velocity of the projectile, and light sources and adjacent optical fibres mounted in the barrel wall are used to measure displacement. The projectile then impacts the specimen on the left, and the strain in the wall of the output tube is detected by the resistance gauge.

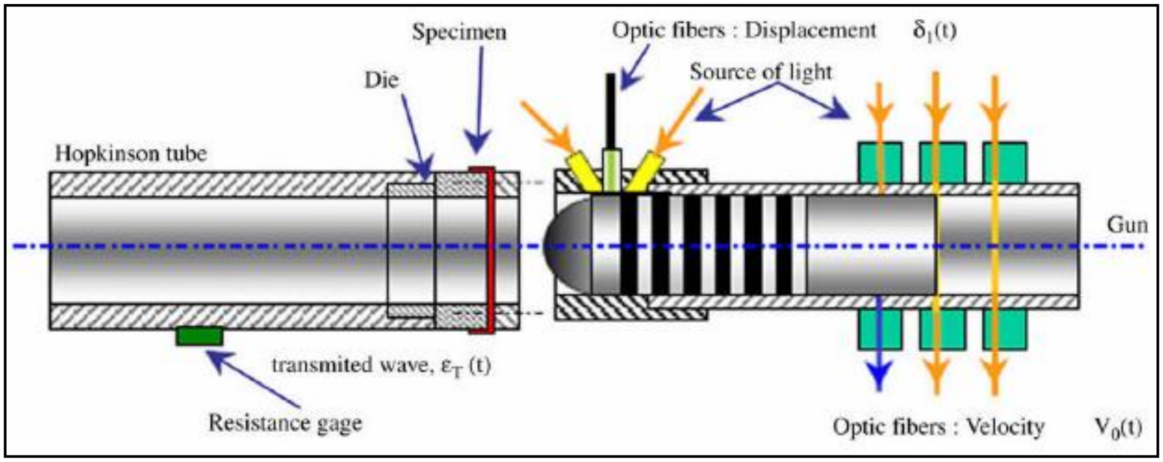

Figure 11: Measurement of the displacement of a projectile (42)

The signal recorded by the displacement sensor is shown in Figure 12, as a function of time. Voltage peaks occur as light from the light source is reflected off the shiny surfaces and detected by the optic fibres. As the projectile slows down, the peaks become progressively further apart. As the distance between the shiny stripes is known, the displacement can then be calculated.

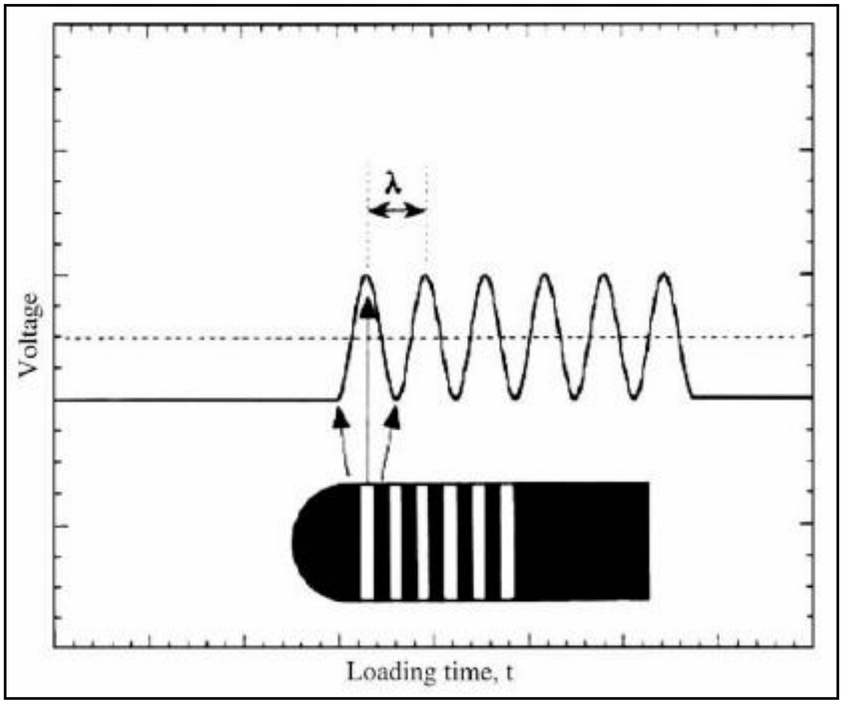

Figure 12: Signal recorded by a reflective object sensor (42)

2.4 Dynamic Testing of Cellular Materials

Dynamic tests on cellular materials are conducted to determine the influence of strain rate and the ‘shock’ phenomenon on the response of the material, and to determine the sources of any effects.

2.4.1 Sources of Rate Sensitivity

Deshpande and Fleck (43) have tested Alulight and Duocel foams at strain rates of up to 5000s^{-1} (corresponding to an impact velocity of 50$m.s^{-1}$) and found no significant difference in plateau stress when compared to quasi-static tests. Danneman and Lankford (44) and Yu et al. (45) have also recorded rate-independent behaviour under dynamic compression of aluminium foams.

Zhao et al. (32) have identified four possible contributing factors for the increased strength observed during the dynamic testing of some cellular materials, when compared to quasi-static testing. These are:

- Pressure increase due to trapped air within the cells
- Strain rate sensitivity of the cell wall material
- Shock enhancement (global inertia)
- Microinertia of cell walls/constituent particles of material

It must be noted that the second factor is a property of the parent material, while the other three factors are due to the structure of the cellular material. It was determined that microinertia during the buckling of the cell walls may be an important factor in strength enhancement. Internal pressure of closed-cell materials is not thought to be an important factor – in fact in man-made foams the internal pressure of the foam is equal to atmospheric pressure, and theoretically would then have no effect (32).

2.4.2 Shock Phenomenon

Reid and Peng (27) observed strength enhancement in the dynamic testing of wood specimens during Taylor cylinder – Hopkinson bar tests, and determined that this was due to the propagation of a densification front through the material from the impact side. This propagation front causes a step change in material properties as it moves through the material, and is therefore analogous to a shock wave travelling through a hydraulic fluid. It does not travel at sonic velocities as a hydraulic shock wave does. A simple analytical model was developed based on the idealisation of wood as a rate-independent, rigid, perfectly plastic, locking (densifying) material, along with equations to predict the increased plateau stress, using data from quasi-static tests. A constant plateau stress is assumed, as shown in Figure 13. This model worked well for predicting results of tests on wood in the in-grain direction, but not for tests across the grain. Any cellular material that exhibits the characteristic quasi-static stress-strain curve shown in Figure 13 has the potential to experience the shock phenomenon under high-speed impact or impulsive blast loading.

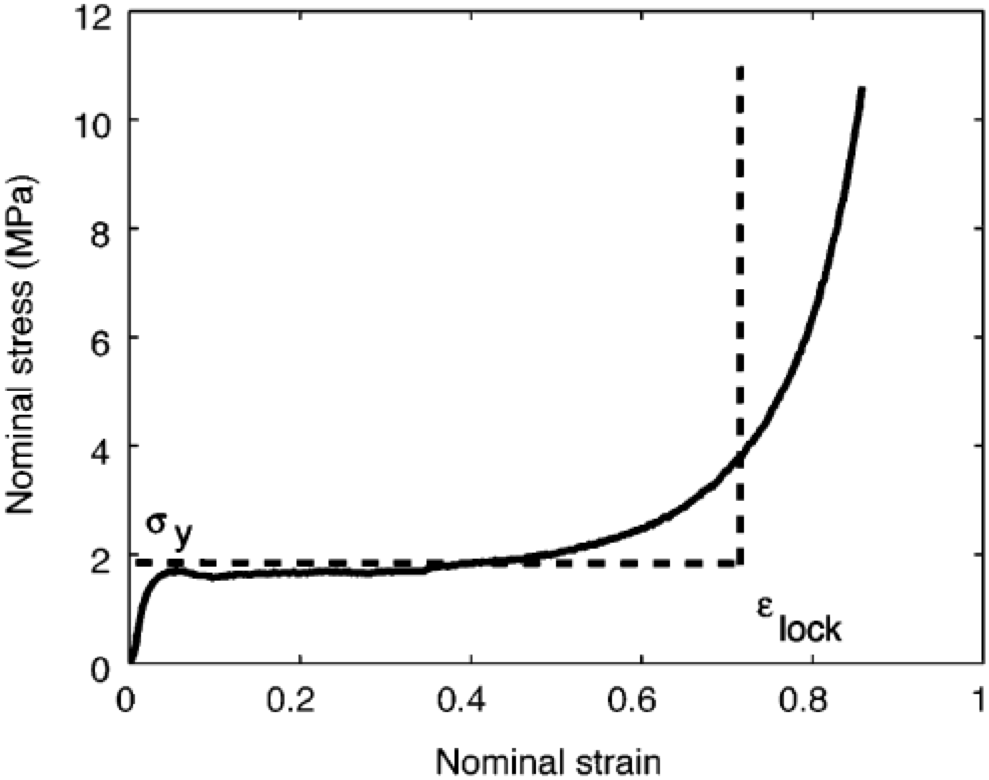

Figure 13: Characteristic stress-strain curve of a cellular material (solid curve), and the idealised r-p-p-l model (dashed curve) (28)

Figure 14 shows a nominal stress-strain curve (described by a function g(ε)) and the r-p-p-l approximation. In theory, as the shock front propagates through a material, the material properties jump from State 1 to State 2.

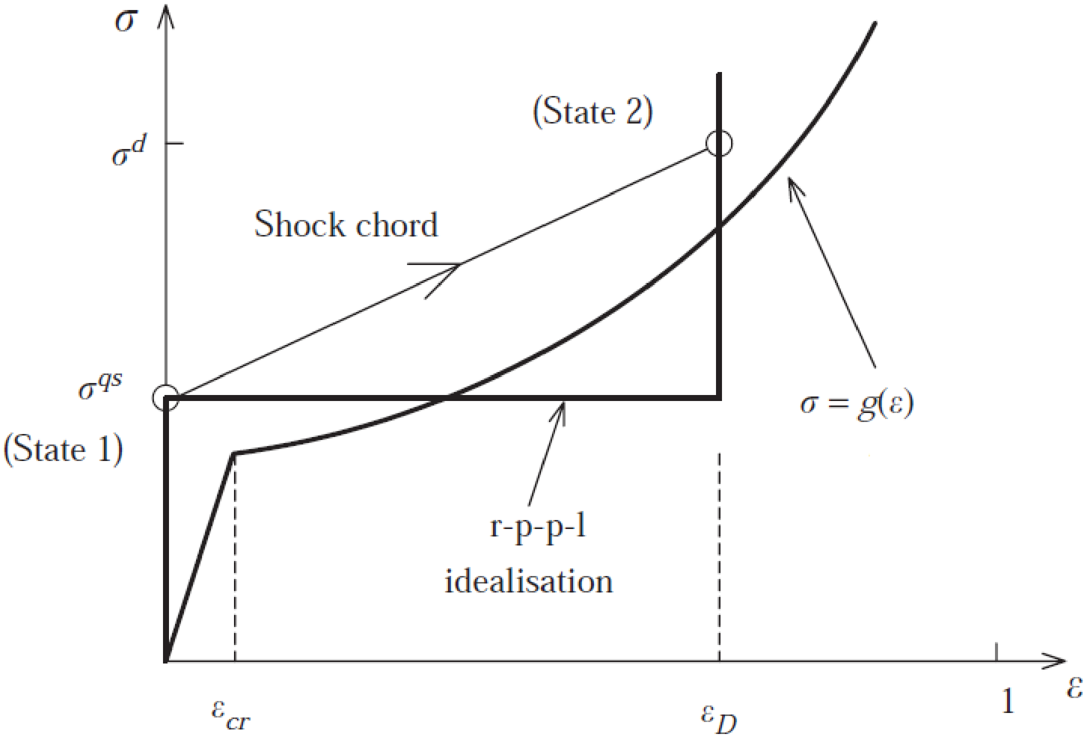

Figure 14: Nominal stress-strain curve and its idealisation (46)

Based on the r-p-p-l model, Reid, et al. (27) predicted the initial crushing stress ($\sigma_{0,DYN}$) of a material due to shock could be estimated by equation 9:

$$\sigma_{0,DYN} = \sigma_{0,QS} + \frac{\rho_0 v^2}{\varepsilon_D} \tag{9}$$

A focus of studies on the shock phenomenon is the determination of the critical velocity (the velocity at which shock begins to occur in a material). The critical velocity for ALPORAS has been estimated at between 46m/s and 55m/s (28), and for Cymat as 108m/s and 42m/s for specimens with 4mm and 14mm diameter cells respectively (the Cymat foam used in the current study has 4mm diameter cells). The critical velocity for an r-p-p-l material can be estimated using equation 10 (21):

$$V_{CRIT} = \left(2A\sigma_{ys} / \rho_S\right)^{1/2} \left(\rho_f / \rho_S\right)^{1/4} \varepsilon_D{}^{1/2} \tag{10}$$

A is a constant determined from the quasi-static response of the material. Tan et al. (21) have found that this equation works well in estimating the dynamic crushing (initial plastic collapse) stress for Cymat foams.

Shen et al. (20) noted that for tests conducted on ALPORAS foam at impact velocities of up to 8m/s, the shock term in equation 9 has a negligible contribution to the dynamic plateau stress of the material. Stress enhancement and decrease in densification strain with increasing strain rate are attributed to a change in the cell deformation mechanism, shown in Figure 15. This is stress enhancement due to microinertia (inertia of the cell walls under impact, as opposed to shock.

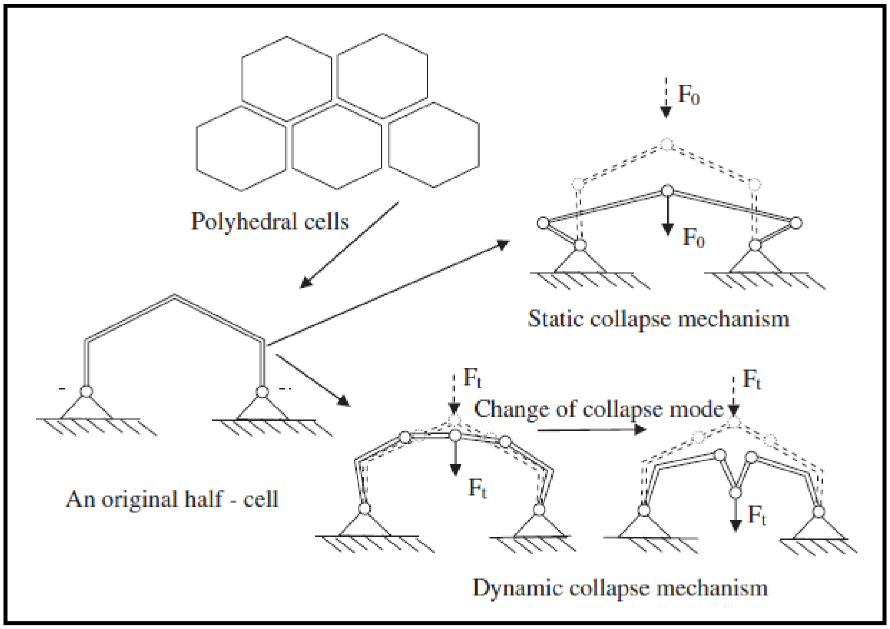

Figure 15: Collapse mechanism of a polyhedral cell under static and dynamic loading (20)

Zhao et al. (28) and Lee et al. (29) have conducted forward and reverse direct impact tests to measure the stresses in front of and behind the shock front (see Figure 16). Lee (29) focused on the development of the experimental technique using a 60mm diameter nylon Hopkinson bar. The use of a high-speed camera allowed the average strain of the specimen as well as the velocity of the shock front to be measured, and the velocity range in which the shock effect began to occur was determined.

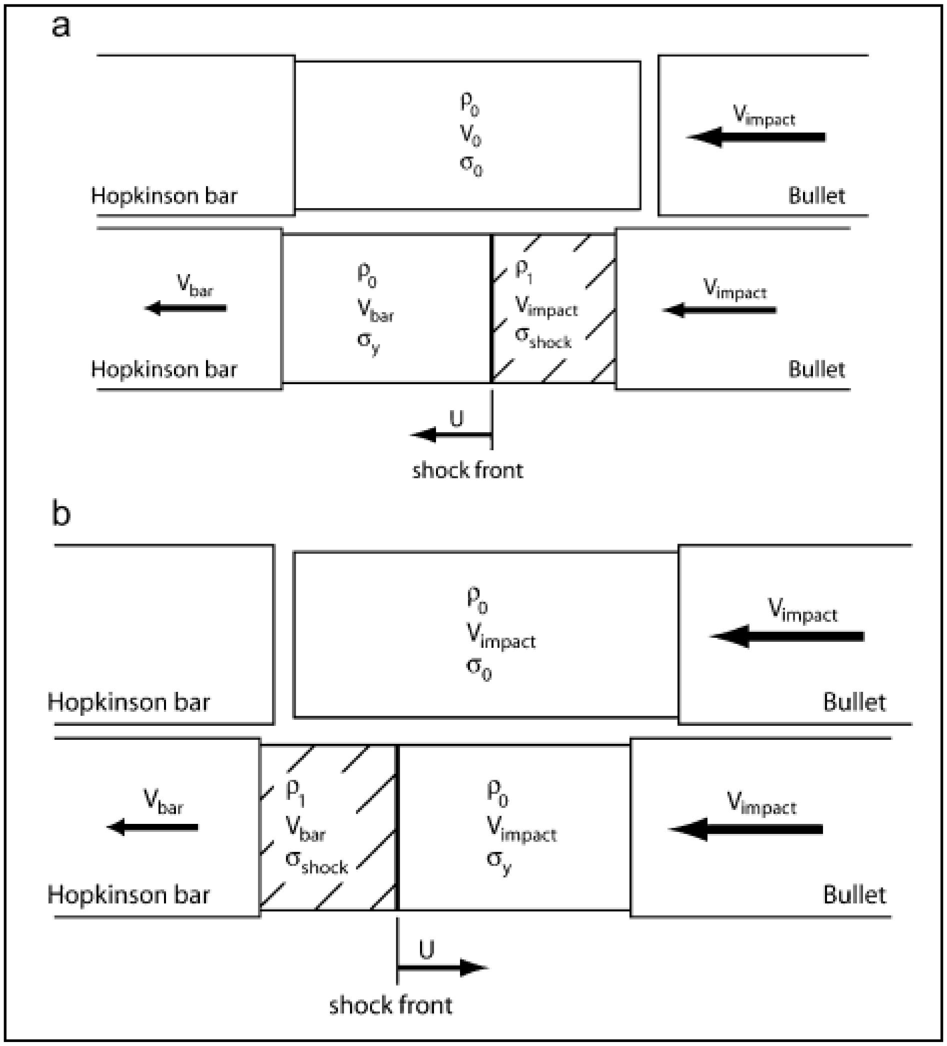

Figure 16: Experiments conducted by Elnasri, et al. to measure the stresses ahead of (a) and behind (b) the shock propagation front (28).

Lopatnikov et al. (9) have developed an elastic, perfectly plastic, rigid model to predict the behaviour of IFAM aluminium foam under Taylor cylinder – Hopkinson bar testing. In these tests, the foam specimen itself is the projectile, and as such allow for high-speed, low-energy tests. This results in a specimen with a ‘frozen’ shock front (see Figure 17), as opposed to the whole specimen being densified, as occurs with direct impact tests. It was shown that this testing method is a simple and reliable method for determining the compression of foam under high-speed impact, and further use of the technique would allow the critical stresses of cellular materials to be determined.

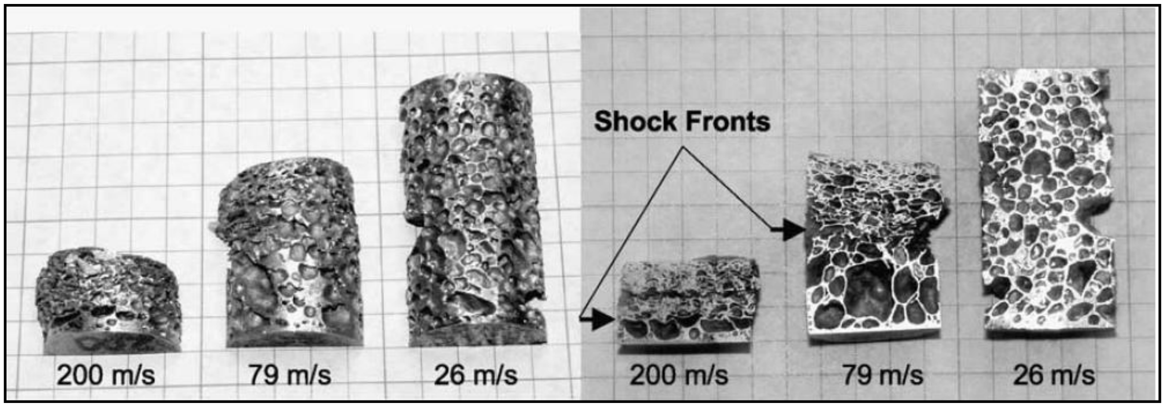

Figure 17: Taylor test specimens showing 'frozen' densification front (9)

Radford et al. (47) have investigated the use of metal foam projectiles to simulate shock loading on a structure using the Taylor cylinder technique, and used foam projectiles in simulating blast loading on foam-cored sandwich panels and monolithic plates (48). The pressure-time plots from the impact of ALPORAS foam specimens are shown in Figure 18.

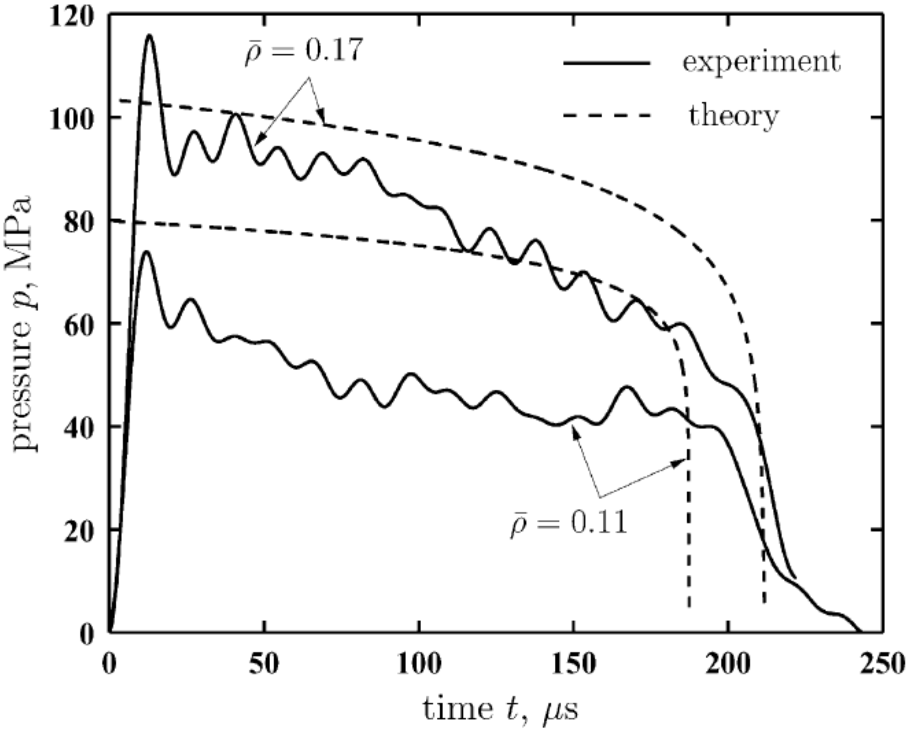

Figure 18: Pressure histories (actual and theoretical) 11% (460m/s) and 17% (430m/s) foams (47)

The ‘shock’ phenomenon is still not a well-understood one, despite the work that has been done in the field in the past 15 years, and experimental proof of the densification front. The velocity range at which strength enhancement due to shock starts to occur (the critical velocity range), the degree to which shock is observed, and the contribution of shock to strength enhancement when compared to the other possible sources of strength enhancement in section 2.4.1 all depend on the specific material being tested. While the r-p-p-l model provides a model for first-order analysis of shock, it does not describe the behaviour of all cellular materials at high strain rates.

2.5 Blast Testing

2.5.1 Background

A blast is an event whereby the detonation of an explosive material generates a high-pressure shock wave in the surrounding air. This is due to the very rapid combustion of the explosive material, and the expansion of the combustion products. The loading on a structure that a blast event causes is characterised by relatively high stresses and short duration and is known as impulsive loading. An impulsive load is defined as a load that acts over a period that is much shorter than the natural period of the structure experiencing the load (49). The typical pressure-time history of a blast event is shown in Figure 19.

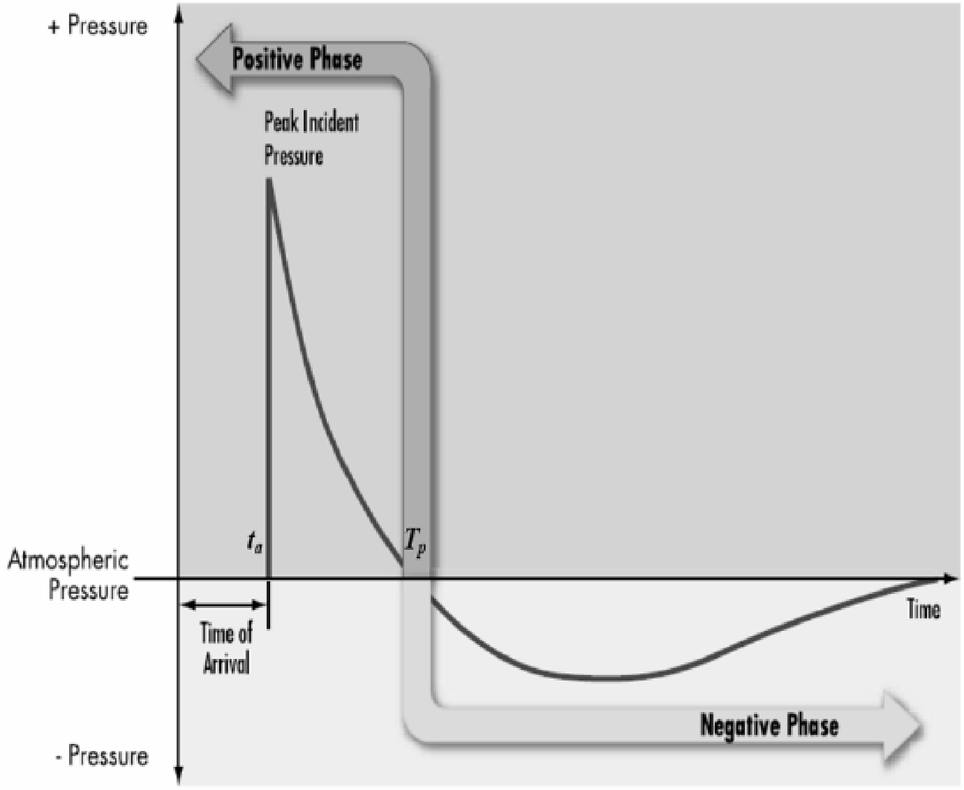

Figure 19: Pressure-time history of a far-field blast wave (49)

The area between the pressure curve and the line of atmospheric pressure is defined as the impulse of the blast, with the unit Newton-seconds. The impulse is given by equation 11:

$$I = A_0 \times \int P(t)dt \tag{11}$$

where A_0 is the area over which the impulse is imparted. The recording of the impulse of a blast during a blast test is done by mounting the test specimen on a ballistic pendulum. A schematic of a ballistic pendulum is shown below in Figure 20. The swing of the pendulum is proportional to the impulse of the blast. Another method of calculating the impulse of the blast without a pendulum is by placing pressure transducers at a distance away from the explosive, as in Figure 21 overleaf, and assuming that the blast pressure is the same at the equidistant specimen face. This may work well at large stand-off distances.

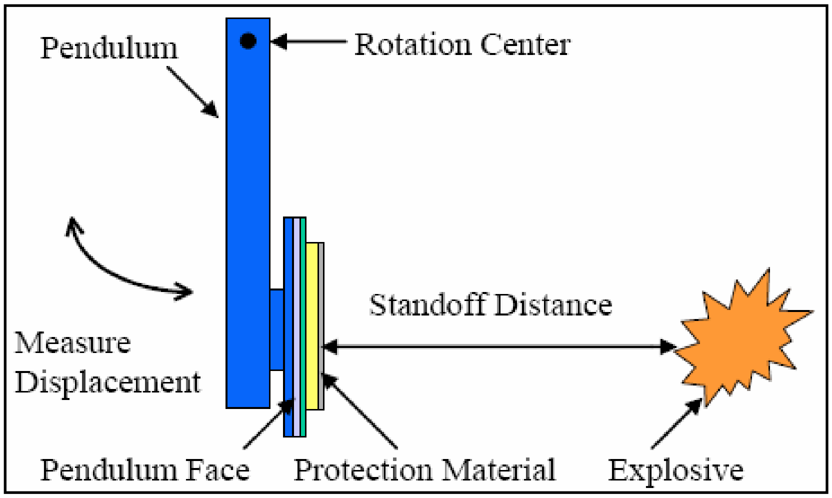

Figure 20: Schematic of a ballistic pendulum (50)

Figure 21: Measurement of blast pressure using pressure transducers (51)

2.5.2 Protective Cladding Structures

A protective, or sacrificial cladding structure, is a layer of material placed on the exterior of a building or vehicle in order to protect it from projectile impact or blast. The cladding is designed to be damaged in a blast or impact event, thereby mitigating the amount of damage done to the main structure. The theory behind sacrificial cladding is shown in Figure 22. Cladding structures have been used for many years for military applications, such as in the composite armour of combat vehicles.

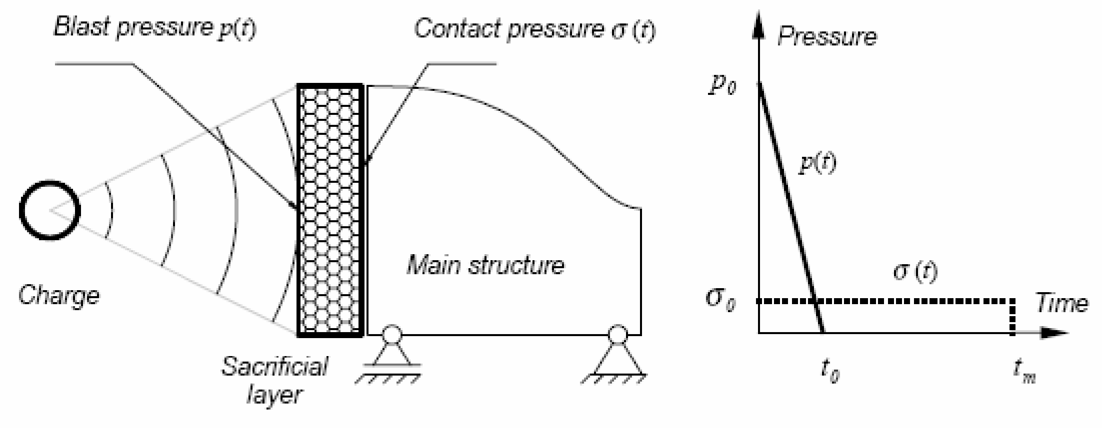

Figure 22: The principle behind a sacrificial cladding (52)

Although the total impulse transferred to the structure remains the same, the peak pressure is reduced, ideally to below the material yield stress of the structure being protected, for the duration of the blast. A study by Li and Meng (53) has shown that in theory a protective cladding of cellular material may in fact lead to stress enhancement under intensive loading.

2.5.3 Blast testing of Aluminium Foam

Hanssen et al. (52) investigated the response of Hydro (Cymat) foam panels to blast loading by conducting full-scale field tests using 1 to 2.5kg of PE4 at a standoff distance of 500mm on a ballistic pendulum, shown in Figure 23 below. Foams of approximate relative density of 15% and 35% were tested, with and without face plates. Contrary to expectations, the addition of a foam panel increased the energy and impulse transferred to the pendulum. A possible reason for this was thought to be “the continuous changing of the shape of the initially plane panel surface into a double-curved shape” (52). They note that the global response of the structure being protected should depend on the value of the impulse alone, and be unaffected by the shape of the impulse. Numerical and analytical results support this.

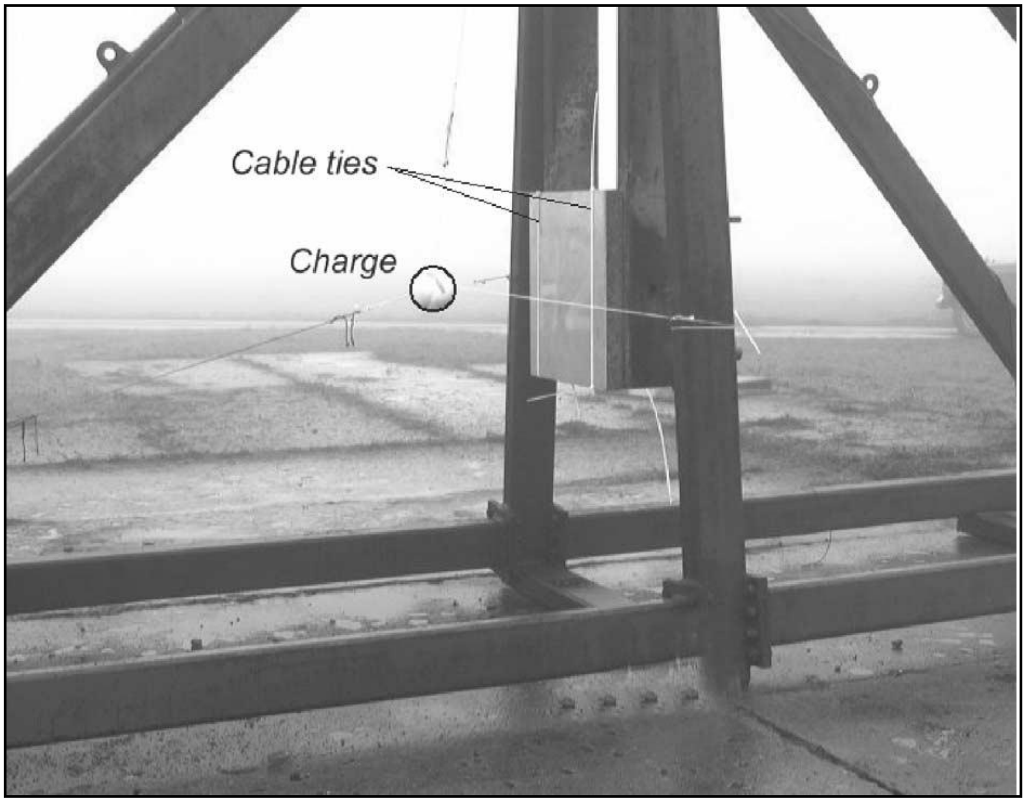

Figure 23: Experimental setup used by Hanssen et al. (52)

Previous work by Langdon et al. (54) studied the small-scale blast testing of Cymat foams of varying densities. The rig and ballistic pendulum used for the experiments is shown in Figure 25, and an example of a test specimen in Figure 24.

Figure 24: Test specimen used by Langdon, et al (54)

Figure 25: Test rig and ballistic pendulum used by Langdon et al. (54)

Foams with relative densities of 10, 15, 17 and 20% were tested. Specimens were initially bonded to the face and back plates. Face plates of 2mm and 4mm thickness were used. Brittle fracture through the cores of all bonded specimens was observed, and in some cases fragmentation of the specimen. Specimens with 2mm face plates showed plastic deformation due to non-homogeneity of the foam. Unbonded specimens showed brittle fracture under compression, but did not fragment. It was concluded that the specimens were fragmenting under tensile load due to the rebounding of the face plate. Numerical analysis was able to predict the failure mechanism and fragmentation observed experimentally.

2.6 Summary of literature

- Cellular materials are a class of materials with a wide range of properties and applications, notably their low density when compared to solid materials, and their ability to absorb energy under compaction.
- Aluminium foams have been well-characterised under quasi-static compression, showing a characteristic stress-strain curve. The plateau stress and densification strain are two important properties that are determined from these tests, and trends for how these properties vary as a function of density for a given material can be determined for use in dynamic testing.
- The direct impact technique, a modification of the split Hopkinson bar technique, has been used to investigate the behaviour of aluminium foams under high-speed impact. Due to the 'shock' phenomenon (propagation of a densification front from the impact side through the specimen, resulting in highly non-uniform strain), tests in the forward and reverse directions need to be conducted to measure the stresses in front of and behind the shock front. Strain needs to be measured indirectly, such as with the use of a reflective object sensor.
- Cellular materials have been tested under blast loading as protective cladding structures, and cores in sandwich materials. Protective cladding structures theoretically reduce the peak impulse that the protected structure experiences, although analysis has shown that the cladding may in fact result in stress enhancement. There is a need for additional experimental work to investigate the performance of aluminium foam as a cladding material.

3 QUASI-STATIC MATERIAL CHARACTERIZATION

This chapter describes the quasi-static material characterisation method, and the material properties (plateau stress and densification strain) that were determined from the tests. These properties are compared to those in the literature, as well as to existing theoretical and empirical formulae.

3.1 Testing Programme

Quasi-static uni-axial compression tests were conducted on CYMAT foam and ALPORAS foam using a Zwick universal testing machine in the Centre for Materials Engineering at the University of Cape Town. Tests were conducted at a strain rate of 10^{-3} per second. The cross-head displacement and force measured by the machine are recorded. The specimens were not constrained radially during the tests, and as such slight variation in the cross-sectional area of the specimens was to be expected during testing.

The nomenclature for each series of aluminium foam specimens is as follows: First letter denotes material (A = ALPORAS, C = CYMAT). The second letter denotes the size or shape of the specimen (L = large (50mm square), S = small (25mm square), C = cylindrical (Φ40mm)). The third letter denotes whether the specimen was 40mm thick (T) as opposed to 25mm thick, or had undergone heat treatment (H). No third letter denotes 25mm thickness and no heat treatment. For example, the specimen ALT1 was made from ALPORAS foam, had planar dimensions of 50x50mm, and was 40mm thick.

For both aluminium foam materials, specimens of different aspect ratios (ratio of width to thickness) and shape were tested. All aluminium foam specimens were nominally 25mm thick, except for the specimens in the ACT series, which were 40mm thick.

The specimens in the ALH series were heat treated in an oven at 400°C for one hour.

Preparation of a number of the ALPORAS blast test specimens required the material to be heated to 185°C for 1 hour. The effect of this heat treatment on the material's strength properties needed to be investigated. According to Ashby et al. (55) the melting point of ALPORAS foam is 910-920K (637-647°C), and the maximum service temperature 400-420K (127-147°C). Lehmus and Banhart (56) investigated 9 different heat-treatments for AlSiMg foams (similar to Cymat), and reported that the strength of AA6061 alloy foams could be varied between 7MPa and 20.5MPa. No studies for heat treatment of ALPORAS (AlCaTi) foams were found.

It was decided to heat a number of quasi-static specimens to 400°C, a temperature significantly above that that the blast specimens would be heated to during preparation, for the same period of time (one hour). The behaviour of the heat-treated quasi-static specimens could then be compared to that of the untreated specimens.

3.2 Results

As described in section 2.2, the densification strain for a particular specimen can be determined by locating the stationary point on the efficiency-strain curve, and the experimental plateau stress then calculated using equation 3:

$$\sigma_{pl} = \frac{\int_0^{\varepsilon_d} \sigma(\varepsilon)\, d\varepsilon}{\varepsilon_d} \tag{3}$$

In the following three sections, the densification strains and plateau stresses for each material are calculated, and their relation to the relative density of the foams compared to that in the literature. The data from the tests were processed using a script written in MATLAB. Graphs were plotted using MATLAB or Excel.

3.2.1 ALPORAS

A summary of the ALPORAS specimen details is given in Table 1.

Table 1: ALPORAS specimen information

Specimen	Nominal planar dimensions	Thickness (mm)	Relative density (%)
AS1	25 x 25	25.20	8.50
AS2	25 x 25	25.10	8.65
AS3	25 x 25	25.12	9.16
AS5	25 x 25	25.28	9.85
AS4	25 x 25	25.16	11.47
AL5	50 x 50	25.10	8.40
AL3	50 x 50	25.10	8.43
AL2	50 x 50	25.10	8.82
AL4	50 x 50	25.10	8.84
AL1	50 x 50	25.10	9.00
ALH1	50 x 50	25.14	8.85
ALH5	50 x 50	25.16	10.52
ALH4	50 x 50	25.16	10.74
ALH3	50 x 50	25.16	11.07
ALH2	50 x 50	25.14	12.32
AC4	Φ40	25.02	8.68
AC3	Φ40	25.10	8.88
AC2	Φ40	25.08	8.94
AC5	Φ40	24.86	9.05
AC1	Φ40	25.04	9.06

Table 1: (Continued)

Specimen	Nominal planar dimensions	Thickness (mm)	Relative density (%)
AS1	25 x 25	25.20	8.50
AS2	25 x 25	25.10	8.65
AS3	25 x 25	25.12	9.16
AS5	25 x 25	25.28	9.85
AS4	25 x 25	25.16	11.47

Figure 26 shows a typical stress-strain curve for an ALPORAS test. The shape of the plateau region is typical of a cellular material that undergoes ductile yielding. The relatively constant stress in the plateau region is indicative of a homogeneous material.

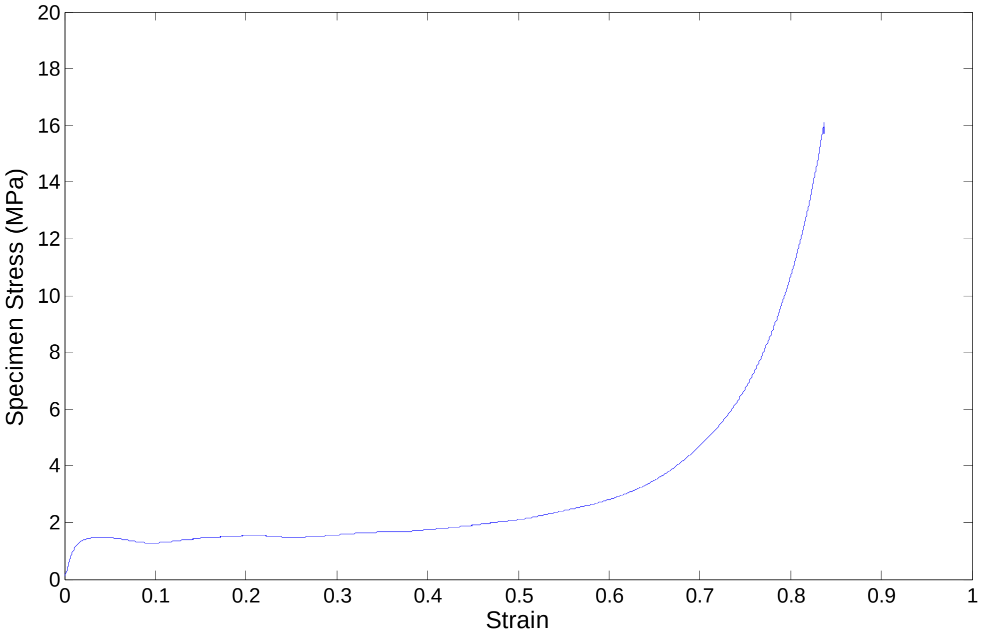

Figure 26: Typical stress-strain curve for an ALPORAS specimen (AC1, density 9.06%)

In the raw data, there is a region of ‘bedding-in’, as the specimen becomes uniformly loaded, and enters the linear elastic region. In order to zero the strain at the start of the linear elastic region, a linear plot is fitted through this region, and the data shifted so that the x-intercept of the linear fit goes through zero.

The energy-absorption efficiency (as defined by equation 6) versus strain curve for the same test is plotted in Figure 27 for a 9% density ALPORAS foam. For ALPORAS, the stationary point (point of maximum efficiency, and densification strain) on the efficiency-strain curve is readily identifiable. Table 2 shows a summary of the densification strains and plateau stresses for all ALPORAS tests.

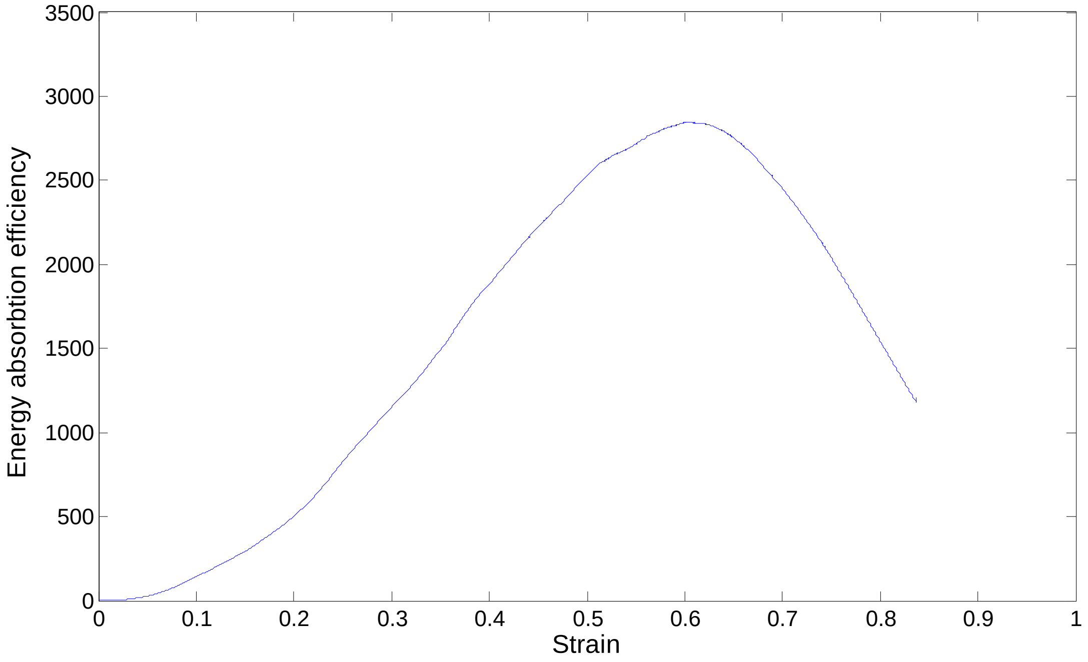

Figure 27: Energy absorption efficiency versus strain for a 9% density ALPORAS specimen

Table 2: Summary of ALPORAS quasi-static test results

Specimen	Relative density (%)	Densification strain	Plateau stress (MPa)
AS1	8.50	0.59	1.46
AS2	8.65	0.61	1.62
AS3	9.16	0.57	1.66
AS5	9.85	0.64	2.14
AS4	11.47	0.59	2.33
AL5	8.40	0.60	1.54
AL3	8.43	0.62	1.60
AL2	8.82	0.61	1.66
AL4	8.84	0.61	1.67
AL1	9.00	0.61	1.69
ALH1	8.85	0.62	1.78
ALH5	10.52	0.61	2.35
ALH4	10.74	0.62	2.24
ALH3	11.07	0.60	2.37
ALH2	12.32	0.60	2.81
AC4	8.68	0.60	1.58
AC3	8.88	0.61	1.70
AC2	8.94	0.58	1.65
AC5	9.05	0.60	1.67
AC1	9.06	0.61	1.70
ACT4	6.93	0.62	1.09
ACT5	7.00	0.62	1.15

Table 2: (Continued)

Specimen	Relative density (%)	Densification strain	Plateau stress (MPa)
ACT3	7.05	0.63	1.30
ACT2	7.67	0.63	1.30
ACT1	8.21	0.61	1.43

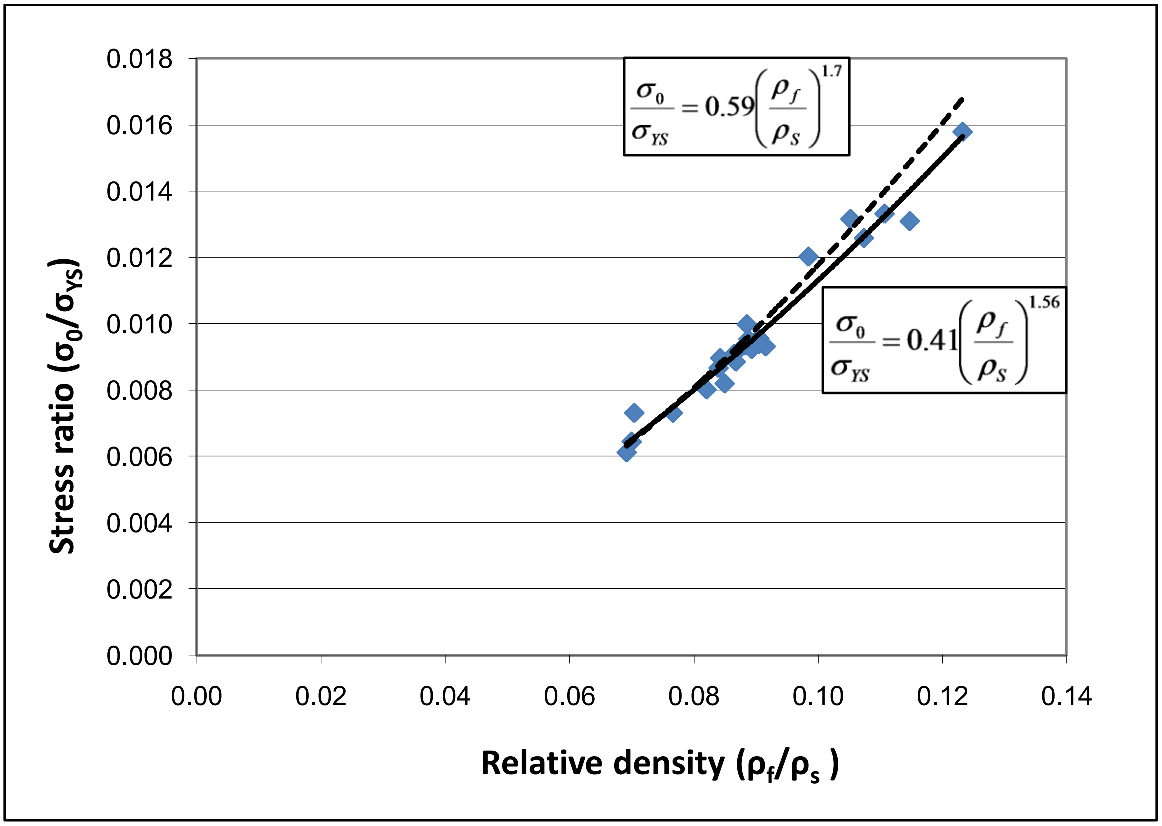

Figure 28: Stress ratio versus relative density – ALPORAS

A graph of stress ratio versus relative density is shown in Figure 28. A power law trend has been fitted to the data, as described in section 2.2.1, using equation 5:

$$\frac{\sigma_{pl}}{\sigma_{ys}} = A\left(\frac{\rho_0}{\rho_s}\right)^B \tag{5}$$

The constants A and B were determined from the power law fit to be 0.41 and 1.56 respectively. Shen et.al (57) performed similar tests and determined A and B to be 0.59 and 1.7 respectively. This trend is indicated in Figure 28 as a dotted line. It is evident that the Shen trend is very similar to the experimental data in the current work.

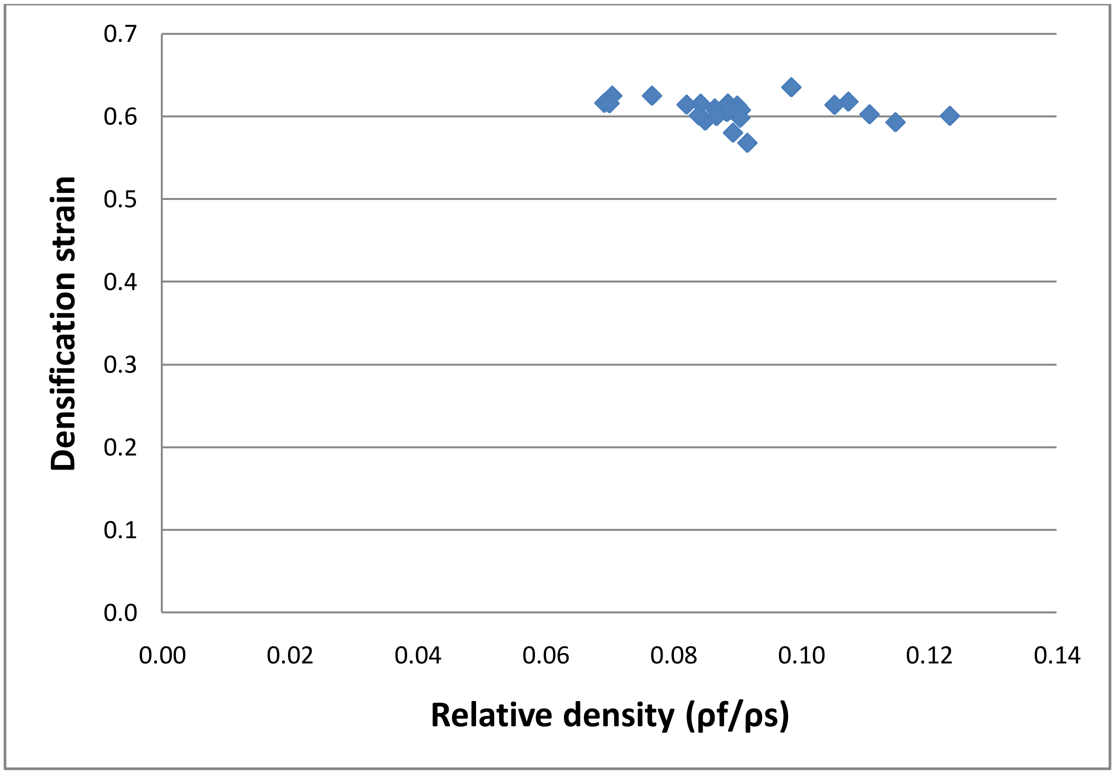

Figure 29: Densification strain versus relative density – ALPORAS

A commonly cited expression relating densification strain, ε_D, to relative density is shown in equation 12, which is for cellular materials in general (1).

$$\varepsilon_D = 1.4 - \alpha\left(\frac{\rho_f}{\rho_S}\right) \tag{12}$$

From inspection of Figure 29, it is apparent that the data for ALPORAS do not conform to the expression. The densification strain for ALPORAS can be assumed to be invariant within the density range considered herein.

3.2.2 Cymat

A summary of the Cymat quasi-static test specimen details is given in Table 3.

Table 3: Cymat specimen information

Specimen	Nominal planar dimensions (L x B, or diameter)	Thickness (mm)	Relative density (%)
CL1	50 x 50	25	16.3
CL5	50 x 50	25	16.4
CL3	50 x 50	25	16.5
CL2	50 x 50	25	17.0
CL4	50 x 50	25	17.4
CC3	Φ40	25	14.1
CC2	Φ40	25	14.3

Table 3: (Continued)

Specimen	Nominal planar dimensions (L x B, or diameter)	Thickness (mm)	Relative density (%)
CC1	Φ40	25	14.8
CC5	Φ40	25	14.9
CC4	Φ40	25	17.8
CS3	25 x 25	25	15.4
CS2	25 x 25	25	15.9
CS5	25 x 25	25	15.9
CS4	25 x 25	25	16.2
CS1	25 x 25	25	16.4

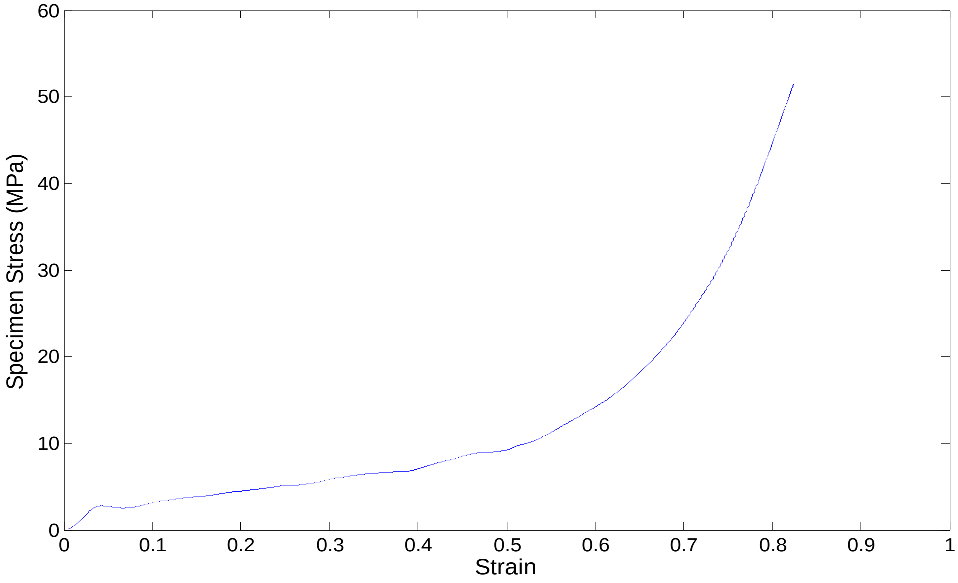

Figure 30: Stress-strain curve for a Cymat specimen of relative density 16.3%

The graphs of stress versus strain and energy-absorption efficiency versus strain for a typical Cymat specimen are shown in Figure 30 and Figure 31 respectively. The strain hardening in the plateau region indicates that Cymat is a less homogeneous material than ALPORAS, with progressively stronger cells buckling as the specimen is compressed.

In the energy-absorption efficiency versus strain curve (Figure 31), it can be seen that a clearly defined point of maximum efficiency was not as obvious with Cymat as it was with ALPORAS. Although the densification strain is still taken as the maximum point on the curve, there is a larger range of uncertainty with Cymat than ALPORAS.

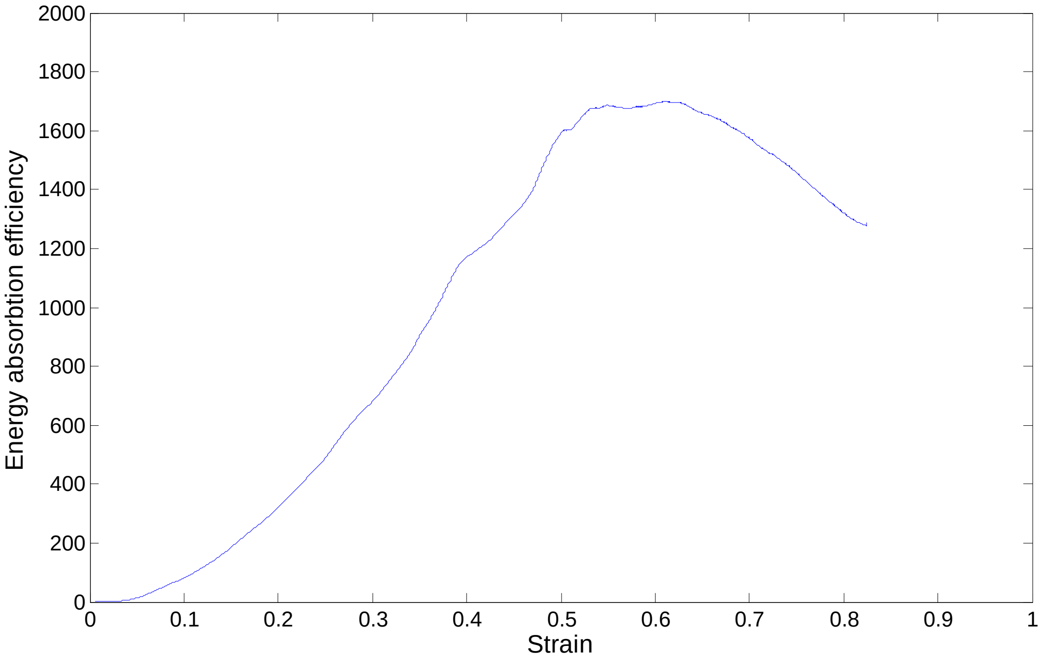

Figure 31: Energy absorption efficiency curve Cymat specimen CL1, showing a less well-defined maximum.

Table 4 summarises the densification strains and plateau stresses calculated for all Cymat tests. The densification strain for test CS3 is omitted as no clearly defined maximum was found.

Table 4: Summary of Cymat quasi-static test results

Specimen	Relative density (%)	Densification strain	Plateau stress (MPa)
CL1	16.34	0.61	6.33
CL5	16.41	0.65	6.7
CL3	16.47	0.61	5.96
CL2	17.03	0.6	7.28
CL4	17.42	0.62	7.42
CC3	14.1	0.6	4.29
CC2	14.34	0.58	4.34
CC1	14.84	0.59	4.82
CC5	14.87	0.55	5.41
CC4	17.84	0.62	7.82
CS3	15.4	-	4.3
CS5	15.93	0.61	5.6
CS4	16.23	0.61	5.97
CS1	16.38	0.59	5.51
CS2	17.27	0.61	7.37

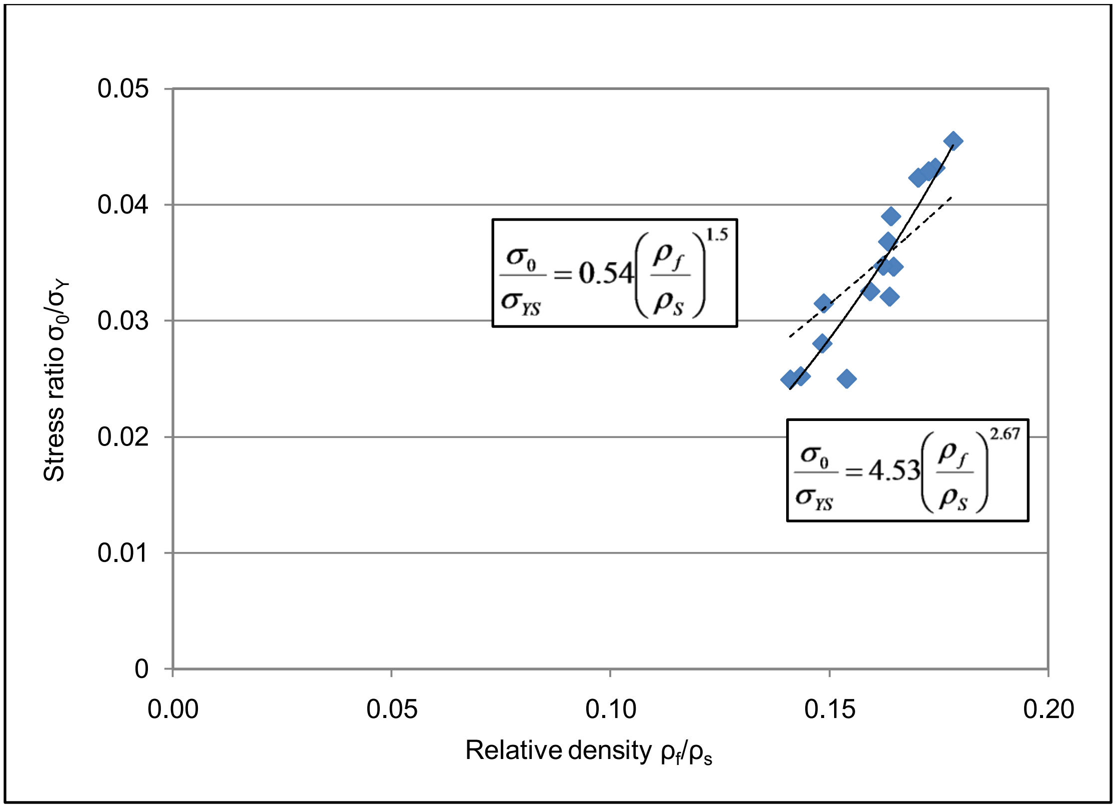

Figure 32: Stress ratio versus relative density for all Cymat tests

A graph of stress ratio versus relative density data for all Cymat tests is plotted in Figure 32. Equation 5 is once again used to fit the data. The power law fitted to the data is shown in equation 13.

$$\frac{\sigma_0}{\sigma_{ys}} = 4.53\left(\frac{\rho_f}{\rho_S}\right)^{2.67} \tag{13}$$

For comparison, the power law from the data in the literature (21) is also shown in equation 14.

$$\frac{\sigma_0}{\sigma_{ys}} = 0.54\left(\frac{\rho_f}{\rho_S}\right)^{1.5} \tag{14}$$

The densification strain versus relative density shows an increasing trend, contrary to the trend expected for a cellular material. The limitations with calculating a precise densification strain for Cymat specimens are mentioned in section 2.2.4, as a realistic trend may not be observed for the data from a small number of tests over a small density range. Given the narrow range of densities, the densification strain for Cymat could also be considered to be constant.

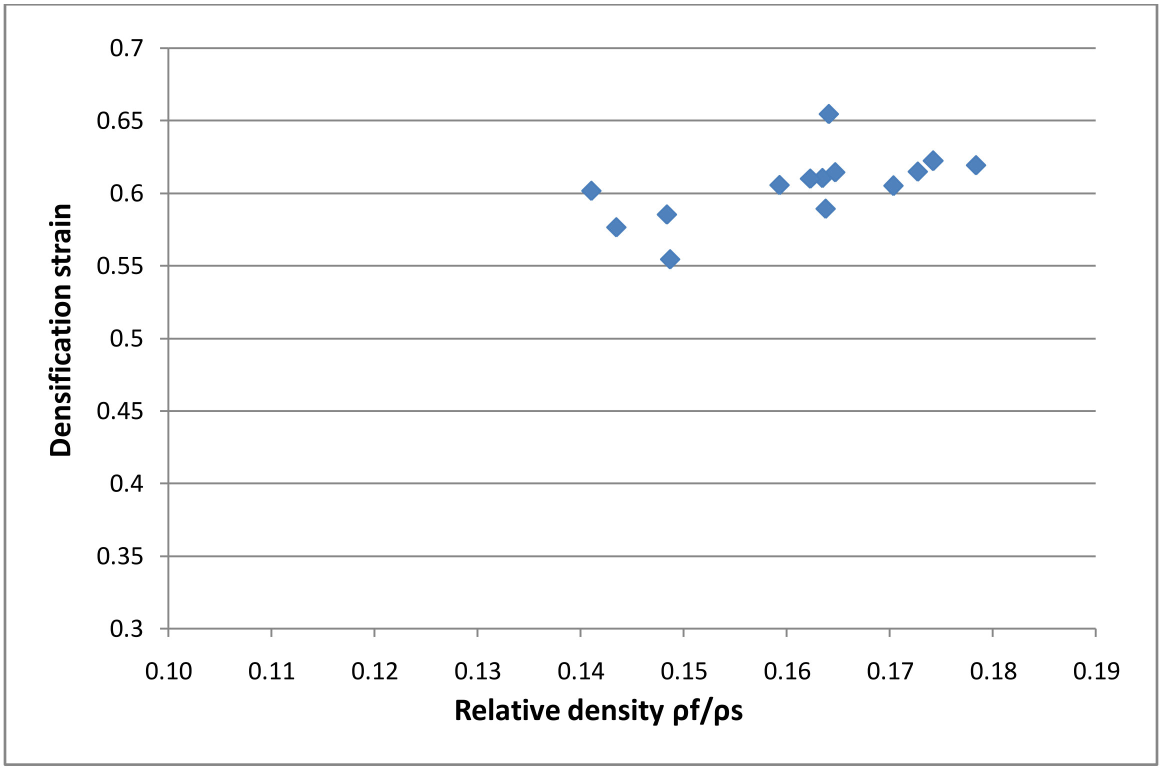

Figure 33: Densification strain versus relative density for all Cymat tests

3.2.4 Comparison of results

Typical stress-strain curves for the two materials are shown in Figure 34 for comparison.

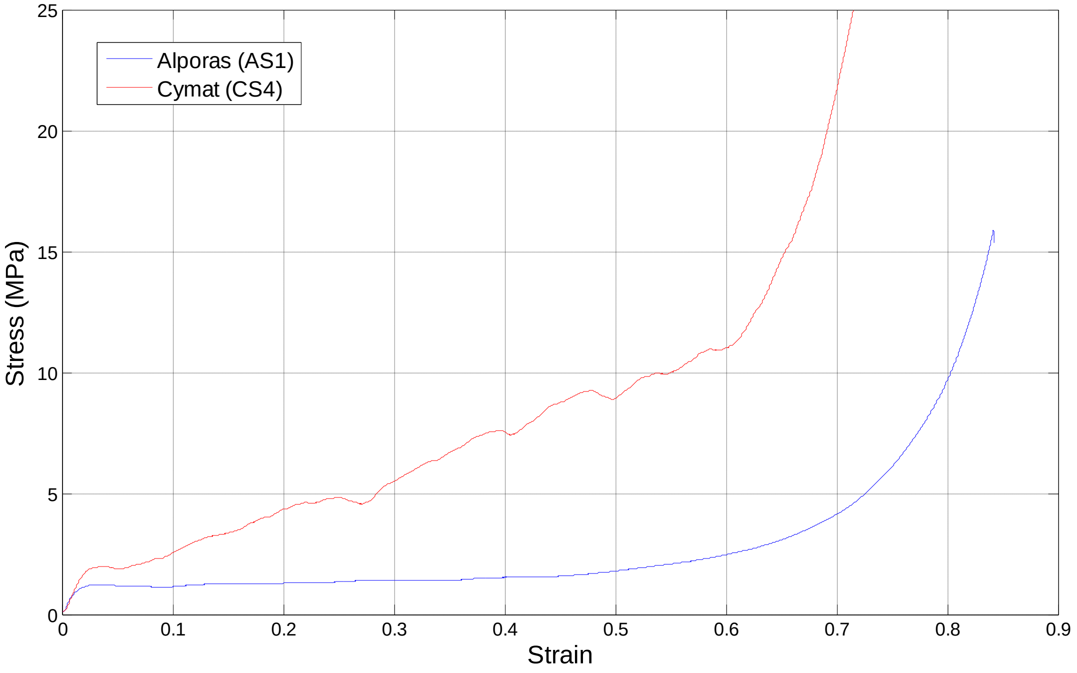

Figure 34 Comparison of quasi-static stress-strain curves for the two different materials

It is evident that Cymat is the stronger of the two materials, with a higher yield stress and more strain hardening than ALPORAS. This is in part due to the higher average density of Cymat. Cymat specimens exhibit a roughly fivefold increase in stress in the plateau region (the area from a strain of approximately 0.1 to 0.6), as opposed to ALPORAS which has a relatively constant stress in the plateau region. Figure 34 shows the effect of material homogeneity on the plateau region, as the increasing stress in the plateau region of the Cymat specimen (the less homogenous of the two materials) is attributable to the collapse of progressively stronger cells.

The shape of the typical Cymat stress-strain curve highlights the limitations of characterising a cellular material as having a plateau region and a densification strain, which has implications in the predicting of strength enhancement under dynamic loading using the ‘shock’ model discussed later.

In the table below, constants A and B determined for each material in the current study are shown, along with those for aluminium foam determined by experiment in previous studies. The values determined by Gibson and Ashby (1) are also shown.

Table 5: Comparison of constants A and B

	Current study		Gibson and Ashby (1)		Shen, Ruan, et. al (20), (18)		Tan, et. al (21)		Langdon, et. al (54)	
Constant	A	B	A	B	A	B	A	B	A	B
ALPORAS	0.41	1.56	0.3	1.5	0.59	1.7				
Cymat	4.53	2.67			0.95	2.19	0.541	1.5	0.93	2.74

The value of the constant A for the current study is high compared to that in the literature. Cymat is a less homogeneous material than Alporas, and as such differences in strength, cell morphology, and density can be expected between specimens from different panels. The trend for a given study is often based on a small density range, and cannot necessarily be compared to other studies.

3.3 Summary

- ALPORAS exhibits a stress-strain curve typical of those for cellular materials.
- Cymat shows considerable strain hardening, whereas ALPORAS has a relatively constant plateau stress.
- Plateau stress increases with relative density according to a power law fit, and constants have been obtained for use in data analysis in chapters 5 and 6.
- Densification strain appears constant across the range of densities considered.
- Cymat offers the greatest energy absorption.
- ALPORAS has a ductile failure mechanism, whereas Cymat appears more brittle.

4. DYNAMIC TESTING PROCEDURE

This chapter details the modification and use of the experimental equipment used in the dynamic material characterisation of the various cellular metals.

4.1 Design of Experimental Rig

A series of dynamic compression tests were carried out on both materials on the Hopkinson bar testing bed at the BISRU, using the Direct Impact testing technique. The experimental arrangement is shown in Figure 35.

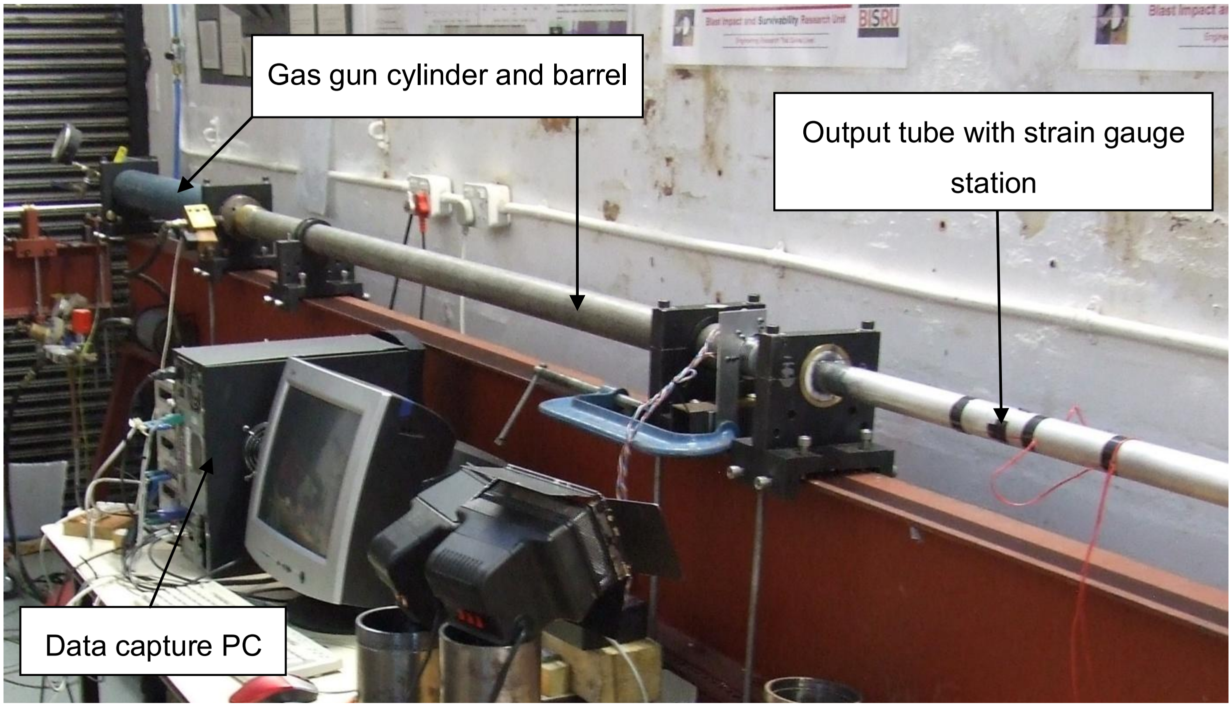

Figure 35: Experimental setup for direct impact and Taylor tests

Modifications were needed to convert the existing equipment (used for standard split Hopkinson bar compression testing of materials) for use with low-impedance cellular materials requiring a larger representative volume. Specimens up to 40mm in diameter were to be tested in the modified arrangement.

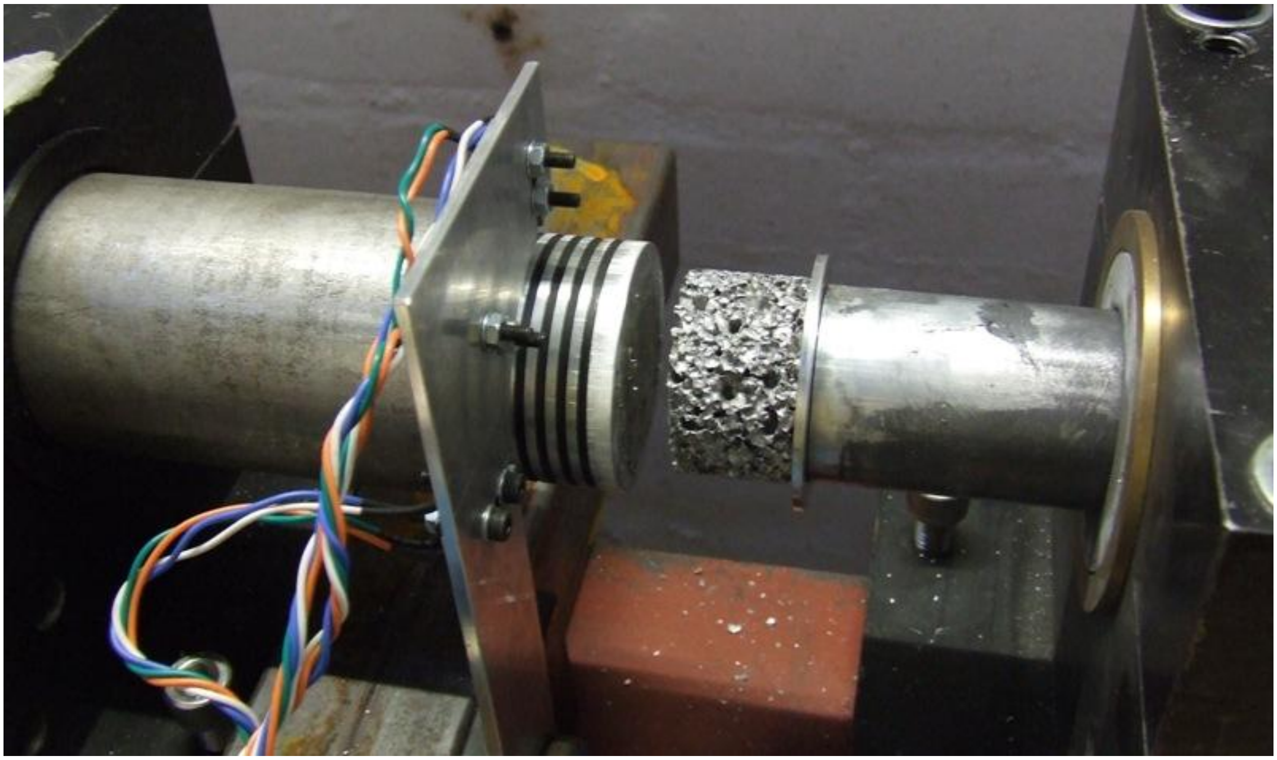

Figure 36: Striker, striker end cap and displacement sensor

A list of the requirements for the test rig was produced, as follows:

1. **A specimen large enough to be a representative sample of the material being tested must be able to be mounted on the output bar and/or projectile:**

To mount the 40mm diameter cylindrical specimens (the largest specimens tested), and end cap was placed on the output bar (see Figure 36). The diameter of the end cap (and the projectile) was 50mm.

2. **The length of the bar should be such that the entire duration of the test could be recorded:**

The length available for the output bar was 5m. An output bar of 5m was more than sufficient for the test duration required. Assuming an impact velocity of 20m/s for a 25mm thick specimen, the test duration would be 1ms. A 5m bar would give a test duration of approximately 2ms.

3. **The output bar should be suitable for the recording of stresses encountered in the testing of low-impedance materials:**

In order to record stress in the order of 1MPa (the lowest plateau stress recorded during quasi-static testing), a thin-walled aluminium tube was used as the output bar. The lower elastic modulus of aluminium (compared to steel), and the lower cross-sectional area of the tube compared to a solid bar of the same diameter result in a larger recorded strain in the output bar for a given input force. A hollow tube is stiffer than a solid bar of the same cross-sectional area.

4. **It must be accommodated by the existing Hopkinson bar bed:**

The existing Hopkinson bar mounts are large enough to accommodate a tube of more than 40mm diameter (the diameter of the largest specimen to be tested).

5. **The projectile must be as light as possible, while still being of a large enough diameter to uniformly compress the specimen, and be long enough to maintain stability as it is propelled along the gas gun barrel:**

The strikers comprised a section of thin-walled aluminium tube, with a threaded end cap that would impact the specimen (or that the specimen would be mounted on). The ratio of length to diameter of the strikers was at least 1:1. 36mm diameter strikers of length 36 and 80mm were made and 50mm diameter strikers of length 50mm and 80mm were made.

6. **The gas gun barrel must attach to the existing gas gun cylinder, and be of sufficient size to accommodate the projectiles used:**

Two barrels (a 36mm and 50mm internal diameter) were used. The 50mm barrel required an adaptor to connect it to the existing gas gun.

Further details on the individual components of the test arrangement are given in the sections that follow.

4.1.1 Hopkinson Tube

For the reasons outlined in section 2.3.2, a solid output bar is not ideal for the testing of low-impedance materials, as the noise to output signal ratio is too high. An additional factor when selecting an output bar is that, for cellular materials, a large diameter specimen is ideal as this will give a more representative sample of the material. This requires a large diameter Hopkinson bar, or a method of mounting the specimen on a small diameter bar. Following the quasi-static testing of the materials to determine plateau stresses, ALPORAS was found to be the weaker material, with a plateau stress of approximately 2 MPa for the weakest specimen. Although strength enhancement of the materials was expected, this figure was used as the limiting factor in the choice of output bar. A thin-walled aluminium tube (outer diameter 38mm, wall thickness 1.8mm) was therefore used. It was predicted that an output tube of this material and cross-sectional area will give an acceptable signal-to-noise ratio for the stresses expected during the compression of cellular metals. The length of the tube is 5 metres, and determined by the length of the test bed. This length is more than sufficient to prevent overlapping of the transmitted wave with itself as it reflects off the distal end of the tube. The tube was standard extruded aluminium of 6061-T6 grade.

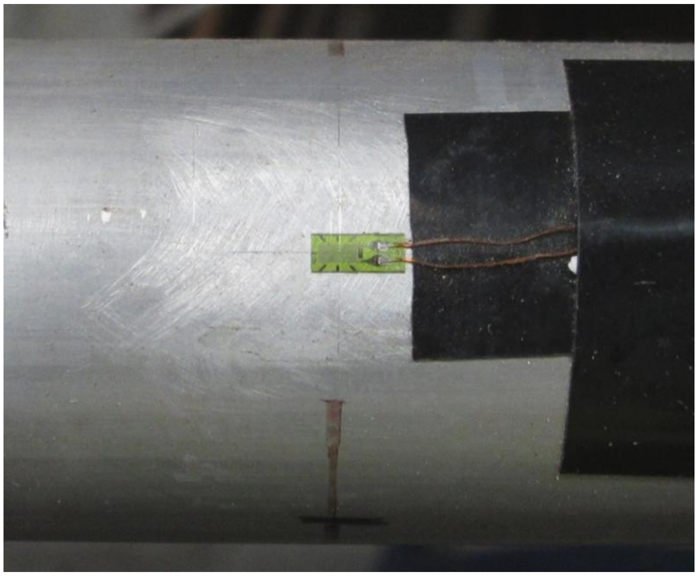

Figure 37: Strain gauge placement on output tube

A pair of diametrically opposite strain gauges (one of which is shown in Figure 37) was placed on the output tube to record the strain history due to the compressive stress wave. The strain gauge bridge used is for the measurement of uni-axial strain, while standard practice for solid bars is to place the strain gauges at a distance from the impact end of the bar equivalent to ten bar diameters, as this is the distance required for the stress wave to become a planar one-dimensional wave (25). Although a wave undergoes less dispersion in a tube than a solid bar of the same diameter (38), and the gauges could be placed closer to the end of the tube, for the current arrangement they were mounted at ten bar diameters from the end to ensure sufficient distance from the mounting at the end of the tube. For large-diameter bars, placing the strain gauges at a greater distance than this is not desirable, as dispersion of different frequencies due to geometric effects may become a factor (30).

An end cap was placed on the end of the tube to facilitate the placement of the specimen. The use of an end cap also allows specimens with a diameter slightly larger than that of the output tube to be tested. As it was not certain how strong the end caps needed to be, several different end caps of different designs and thicknesses were manufactured. The end caps were machined from 6063 grade aluminium, and were designed to be as light and stiff as possible. The end caps were designed to be lightly press-fitted into the end of the tube. A schematic of the tube end cap is shown in Figure 38.

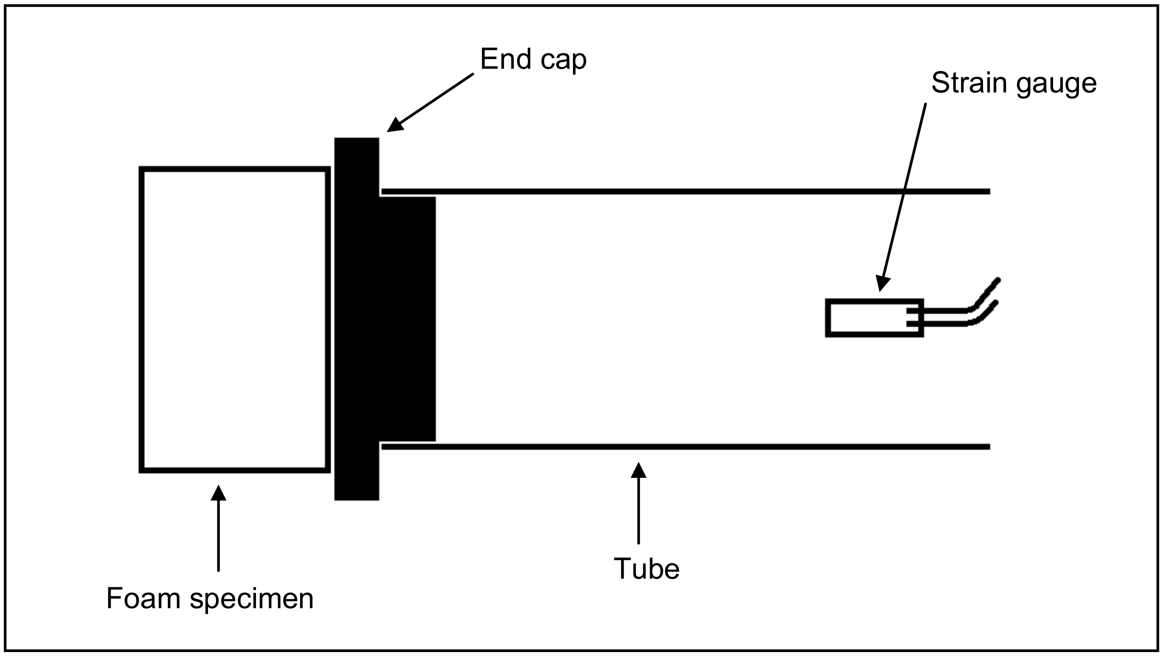

Figure 38: Schematic of direct impact specimen and end cap placement (forward direction)

Preliminary tests were conducted on foam specimens mounted on the various end caps, and it was determined that an end cap with a 2mm thick face would be the lightest end cap that would not yield at the expected impact velocities.

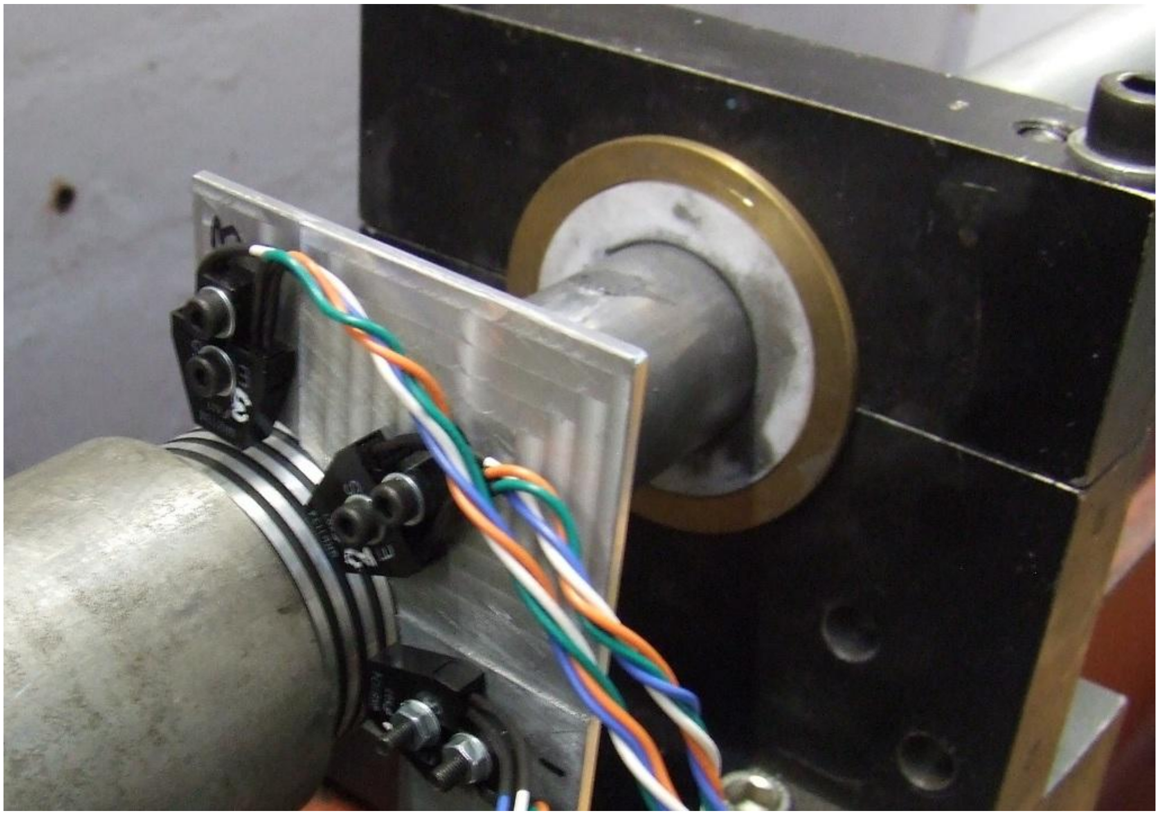

Figure 39: Tube mounting, with white inner Teflon ring and outer bronze ring

In order for the tube to be aligned axially on the test bed, and be unconstrained in the axial direction, it is placed in mounts with bushes (visible in Figure 39). The mounts are adjustable, which allows the tube to be aligned. The bushes comprise an outer bronze ring and an inner Teflon ring. The Teflon ring allows the metal tube to run smoothly, and the bronze collar allows the bushes to be clamped in place by the mounts without the Teflon (with its relatively low elastic modulus) being compressed enough to restrict the movement of the tube. To ensure that the Teflon bushes have the correct fit with respect to the tube, they were press-fit into the bronze collars and then bored out to achieve a smooth running fit with the aluminium tube.

4.1.2 Gas gun and striker

The gas gun on the test bed is driven by compressed nitrogen, and is designed to be able to fire at pressures of up to 20 bar. The gas gun cylinder was originally designed so that it could accommodate barrels of different diameters and lengths. The largest existing barrel was of 36mm internal diameter, and while this would be sufficient for some of the material specimens in the current study to be tested, for the larger cylindrical aluminium foam specimens a larger diameter striker, and hence larger diameter barrel was needed.

Standard schedule steel is not of sufficient quality in terms of internal finish and consistent internal diameter to allow a striker to move freely along it, and bored and honed hydraulic pipe was instead selected. The tube is two metres long, with a 50 mm internal diameter and 5mm wall thickness. The tube is designed to withstand internal pressures of up to 80 bar (58).

Three pairs of diametrically opposite 5mm diameter fluting holes were drilled in the distal end of the barrel, 50, 100 and 150mm from the end respectively. A schematic of the barrel is shown in Figure 40. This ensures that there is not a significant pressure driving the striker once it leaves the barrel. The velocity of the striker is measured as it leaves the barrel, and any excess pressure after this could alter the striker's velocity after it leaves the barrel, but before it impacts the specimen.

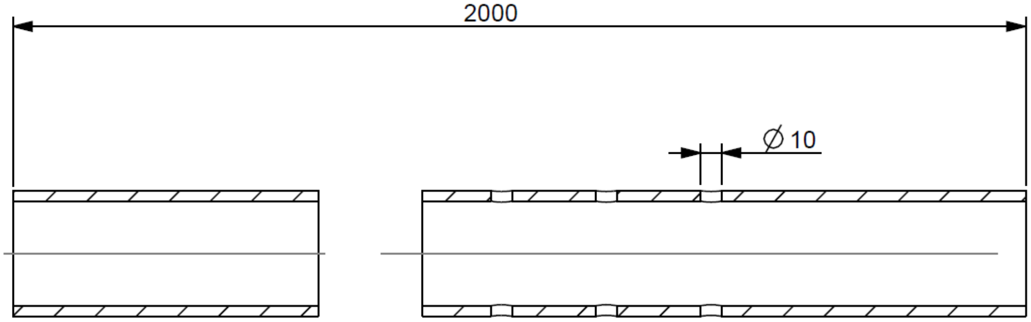

Figure 40: Schematic of 50mm diameter tube, with fluting holes

In split Hopkinson bar tests, the size, material and shape (and hence mass) of the striker is determined by the length and shape of input pulse required, and is fired at a velocity to give the required specimen strain rate, while not exceeding the limiting stress in the input bar (usually determined by the bonding of the strain gauges). The mass of the striker is therefore not itself important.

During a direct impact test, however, the mass of the striker projectile is critical. The desired velocity regime is predetermined (in the region of 100 $m.s^{-1}$ for the current tests), and the initial kinetic energy (and therefore the mass) of the striker is limited by how much energy the specimen can absorb in compression. If the striker has too much initial energy, once the specimen has densified, the striker may still be going at a high enough velocity to exceed the yield stress in the output bar. In direct impact tests, the specimen can be thought of as protecting the output bar, in the same way that the material would be protecting a structure in a real-world application.

Although degrees of strength enhancement and increased energy absorption were expected under dynamic conditions when compared to quasi-static conditions, the energy absorbed during quasi-static tests of the weaker material (ALPORAS) was used when calculating the minimum mass a striker should have when fired at $100m.s^{-1}$. By integrating the quasi-static force-displacement data, this mass was calculated to be 8 grams. The striker would therefore need to be as light as possible, yet strong and rigid enough to compress the specimen, and fit the required barrel (36mm or 50mm diameter). Strikers of different masses would also be needed, depending on the material and size of specimen being tested.

Figure 41: 50mm striker with 2mm end cap (left) and 36mm striker with heavier 5mm end cap (right)

In order to be stable as it is propelled along the barrel, a striker generally needs to have a length-to-width ratio of 1:1 (59). A solid striker of this size would have been far too heavy for the current experiments, and it was decided to use a section of thin-walled aluminium tubing, with a threaded cap to be placed on the impact end of the tube. End caps of different masses could be used on the same striker to provide the different energies needed for the different materials. The strikers used are shown in Figure 41.

4.1.3 Reflective Object Sensor

As discussed previously, the overall strain of the specimen cannot be calculated from the recorded strain gauge signals during a direct impact test as it can be in a split Hopkinson bar test. A reflective object sensor similar to that used by Rusinek (42) was designed. This necessitated a sensor and accompanying circuit to be sourced and designed, and a striker with an alternately reflective and non-reflective surface. As the striker passes the sensor, a varying voltage signal is recorded with the peaks of the signal corresponding to known displacements, as described in section 2.3.4.

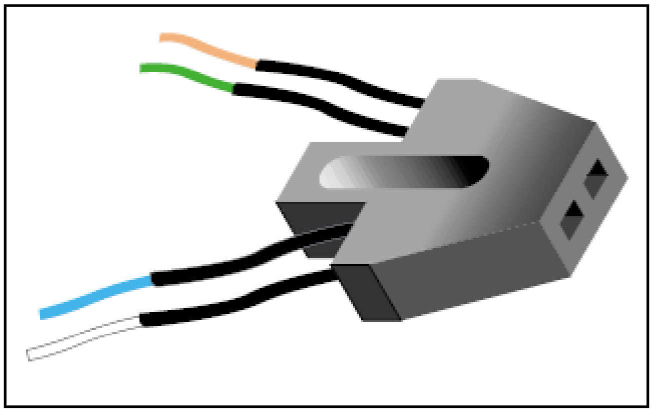

Figure 42: The Fairchild QRB1134 Reflective Object Sensor (60)

The sensor used was a Fairchild QRB1114, which comprises an infra-red light-emitting diode (LED) and photo-transistor, positioned so that when light from the LED is reflected off a surface, it is collected by the photo-transistor, through which a current then flows. The rise and fall times of the current flow through the photo-transistor (the time taken for the current to rise to a peak when light is detected, and for the current to return to zero when no light is detected) are each 8 microseconds, which is well within the response time needed for tests at 100 m.s^{-1}. The sensor has an approximately 5mm diameter 'footprint' (area exposed to light from the LED). The width of the reflective stripes on the tube of the striker therefore needed to be 2mm wide (separated by 2mm non-reflective stripes) in order to ensure that little more than one reflective stripe at a time was picked up by the sensor. This would ensure the largest magnitude voltage signal possible to be recorded. In order to explore the effect of smaller stripes, and whether this voltage signal would still be useful, a striker with 1mm reflective stripes was also made. The stripes were applied by machining 2mm wide, 0.4mm deep circumferential grooves in the outer surface of the striker barrels, spray-painting the barrels, and sanding the layer of paint off the raised surfaces.

One sensor measuring reflective stripes with a 4mm pitch would emit a signal with peaks 4mm apart. This would give a resolution of 4mm (that is, one would get a displacement reading every 4mm). As the specimens were only 20 to 25mm thick, a higher resolution was needed. If one used the local minima as well as local maxima in the signal, this increases the resolution to 2mm. Three sensors, offset by 0.5mm were used, thus increasing the resolution to 0.5mm. The sensor circuit would therefore emit three voltage signals, with the three peaks corresponding to a certain stripe offset by 0.5mm. A mounting plate, which could be placed adjacent to the gas gun barrel, was designed so that the sensors could be adjusted to match a 36mm or 50mm diameter striker. The strikers were designed to be long enough so that the tail of the striker would still be in the barrel once the specimen had been fully compressed. This would prevent the striker from moving sideways away from the specimen after the test, and possibly being damaged. The striker and displacement sensor are shown in Figure 43.

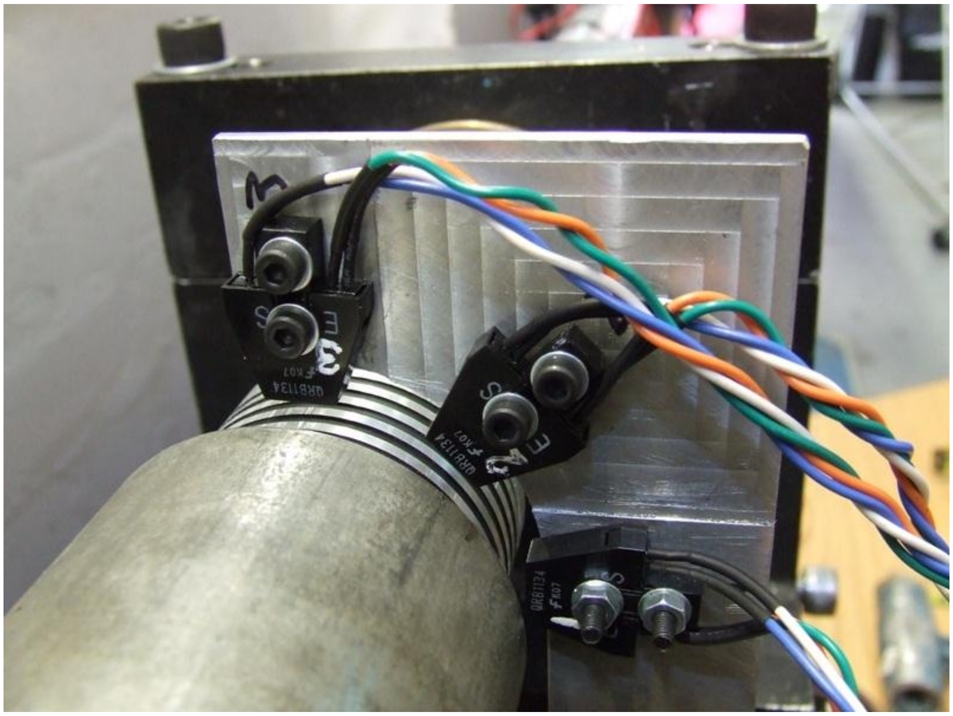

Figure 43: The three reflective object sensors comprising the displacement sensor

4.2 Experimental Procedure

4.2.1 Calibration of the Experimental Rig

Before conducting experiments using a Hopkinson bar, calibration tests need to be carried out to determine the wave speed (speed of sound) in the bar. This is to calculate the time taken for the wave to travel from the specimen-bar interface to the strain gauges, and to calculate the elastic modulus of the bar material. As even materials of the same grade, but from different production batches may differ slightly in their material properties, these calibration tests need to be conducted for any set of bars. The determining of the elastic modulus of the bar allows the calibration factor K for the bar to be calculated. This is the factor that the voltage signal from the strain gauges needs to be multiplied by to convert it to stress in the output bar.

The theoretical calibration factor is calculated using the theoretical stress given by a strain gauge voltage signal. It is known that the stress σ in the bar can be related to the voltage output from the strain gauges (V_{READ}) by equation 15:

$$\sigma(t) = \left[\frac{4E_{BAR}}{G_{AMP} K_{GF} N V_{IN}} \right] V_{READ}(t) \qquad (15)$$

where E_{BAR} is the elastic modulus of the output bar, G_{AMP} is the gain of the voltage signal amplifier, K_{GF} the gauge factor of the strain gauge, N the number of active arms in the strain gauge circuit, and V_{IN} the bridge or excitation voltage of the strain gauge circuit. For the current setup, the gain is 1000, the gauge factor is 2.14, and N = 4.

4.2.2 Direct impact testing procedure

The placement of the specimen for a forward test is shown in Figure 36. The specimen is attached to the bar end cap using a small piece of double-sided tape. The specimen was placed in the correct position for the high-speed camera, and the striker was positioned in the gas gun barrel, 600mm or 900mm from the end. The position of the striker was varied along with the pressure in the gas gun cylinder in order to attain the required projectile velocity. The procedure for a reverse test is the same, except the specimen is attached to the striker end cap. The impact velocity of the striker is calculated from the ROS signal.

4.2.3 Taylor testing procedure

A series of Taylor cylinder – Hopkinson bar tests was conducted, similar to those done by Lopatnikov, et al. (9). This technique is a combination of a Taylor cylinder test (in which the specimen is fired from a gas gun against a rigid surface, and the initial velocity and final thickness of the specimen recorded) (27), and a Hopkinson bar test. By firing the specimen against an instrumented bar instead of a rigid surface, a stress history of the impact can also be recorded.

For a Taylor test, the specimen is placed in the barrel, but is not attached to a striker (the specimen itself is the striker). A polystyrene disk, the same diameter as the barrel, is placed behind the specimen as a backing of negligible mass. This ensures that the specimen cells are not damaged by the high pressure of the gas. The velocity of the specimen is calculated using a light trap mounted on the end of the barrel, comprising two opposing sets of photodiodes and phototransistors. As it exits the barrel the specimen interrupts the light from the first, and then the second photodiode reaching their opposing phototransistors. This causes successive voltage drops in the transistors. The time between the successive voltage drops in the transistors is recorded.

5 DYNAMIC MATERIAL TEST RESULTS

5.1 Overview of experiments

Direct impact tests were conducted on both materials, with the focus being on ALPORAS foam. Cubic and cylindrical specimens were tested for ALPORAS and Cymat foam.

A series of Taylor tests was also conducted on cylindrical specimens machined from ALPORAS foam, at velocities ranging from 17 to 183m/s.

Table 6 summarises the dynamic testing programme.

Table 6: Overview of test programme

MATERIAL	SPECIMEN GEOMETRY	VELOCITY RANGE (FORWARD DIRECTION)	VELOCITY RANGE (REVERSE DIRECTION)	VELOCITY RANGE (TAYLOR TESTS)
ALPORAS	Cube	51 – 81m/s	54 - 79 m/s	
	Cylinder	35 – 77m/s	34 - 75 m/s	17 - 183 m/s
Cymat	Cube	70 – 81m/s	64 - 69 m/s	
	Cylinder	33 – 74m/s	33 - 70 m/s	

Details of all the direct impact and Taylor test specimens tested are given in Appendix C.

5.2 Data processing

This section describes the data processing procedure for plotting a stress-strain curve from the signals obtained during the dynamic tests.

The raw signal output from the reflective object sensor (ROS) and strain gauges is shown in Figure 44. The three oscillating signals are the three offset sensors that comprise the reflective object sensor. The strain gauge signal is shown in red.

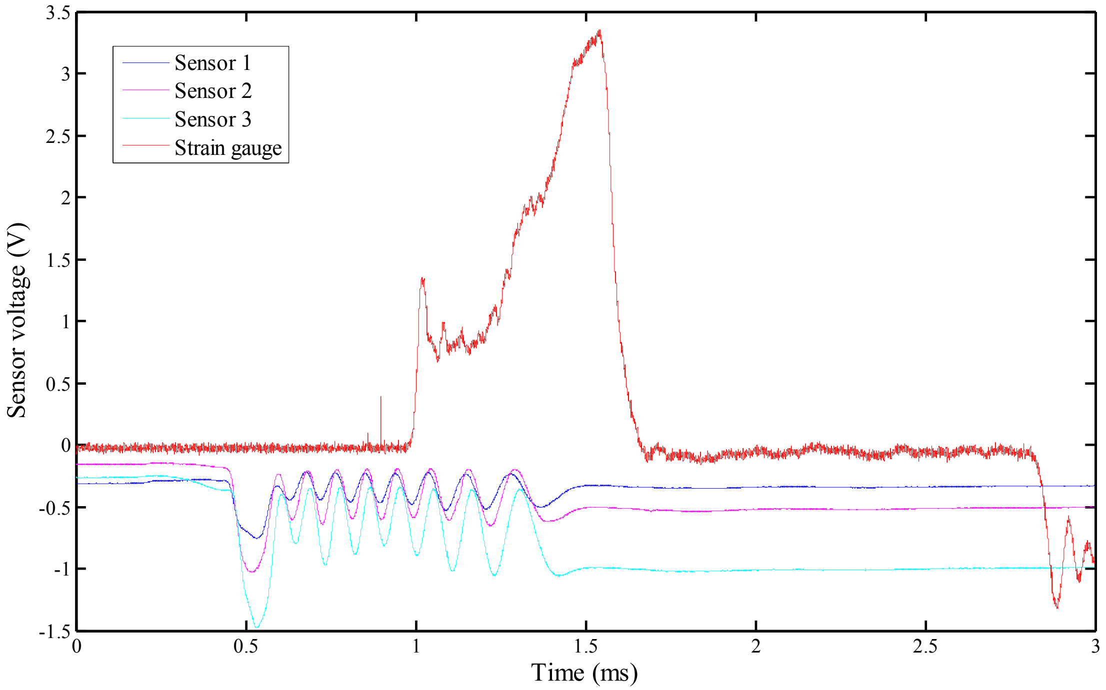

Figure 44: Raw signal output for a typical direct impact test

The strain gauge signal is shifted by 79μs in order for it to correspond to the ROS signal in the time domain, as the strain gauge reading is delayed by the time taken for the stress wave to travel from the specimen-bar interface to the strain gauges. The time at the start of the strain gauge signal then corresponds to the point of impact of the striker (the start of the displacement-time curve). As the distance between the sensors (and hence the distance between the peaks) is known, the displacement-time curve from the point of impact onwards can be plotted. The specimen stress is calculated from the strain gauge signal using equation 18.

The displacement-time history for each test was also recorded using the high-speed camera footage. The camera footage was deemed more reliable, on the occasion when the peaks on the ROS signal were not clearly defined due to signal noise. With clearly defined peaks, however, the displacement-time plots correspond well. A graph comparing the displacement histories from the reflective object sensor and high-speed camera is shown in Figure 45.

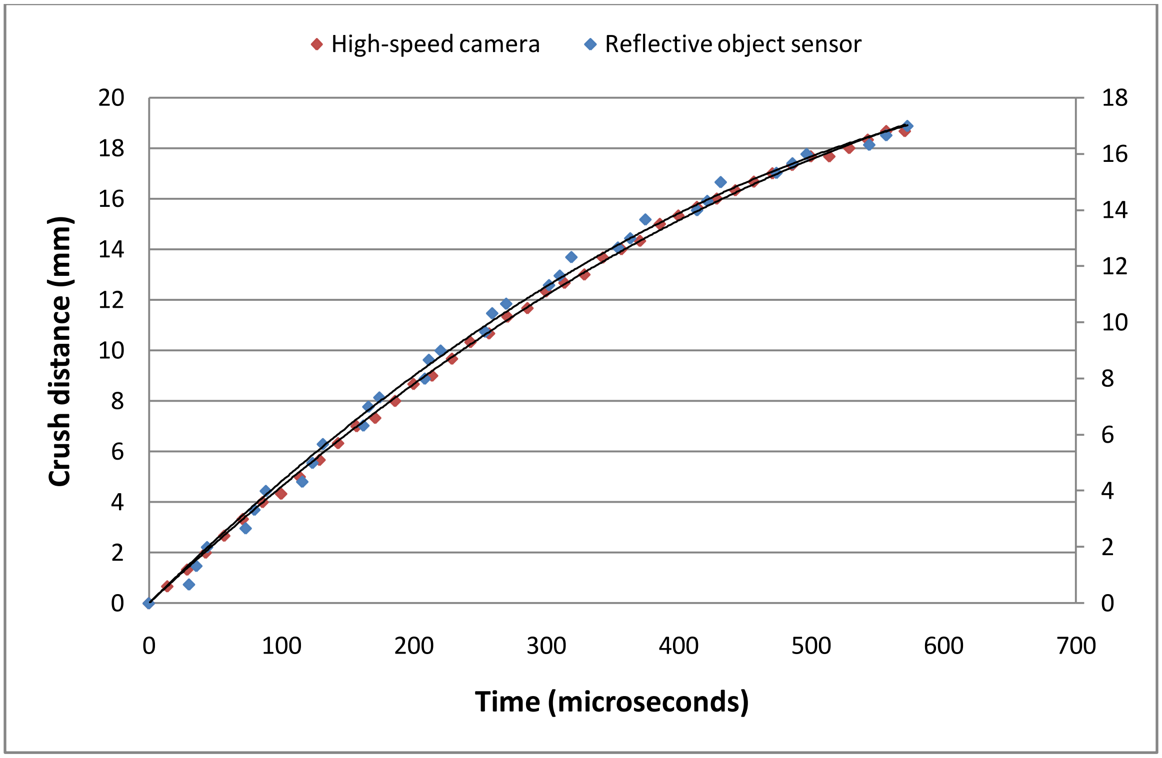

Figure 45: Comparison of displacement-time signals from the reflective object sensor and high-speed camera footage

The initial velocity of the striker can be measured from the high-speed camera footage, or by taking the time difference of the first two peaks of one signal of the ROS (the distance between the peaks being the pitch of the stripes on the striker). The measurements for which both methods were used are compared in Figure 46.

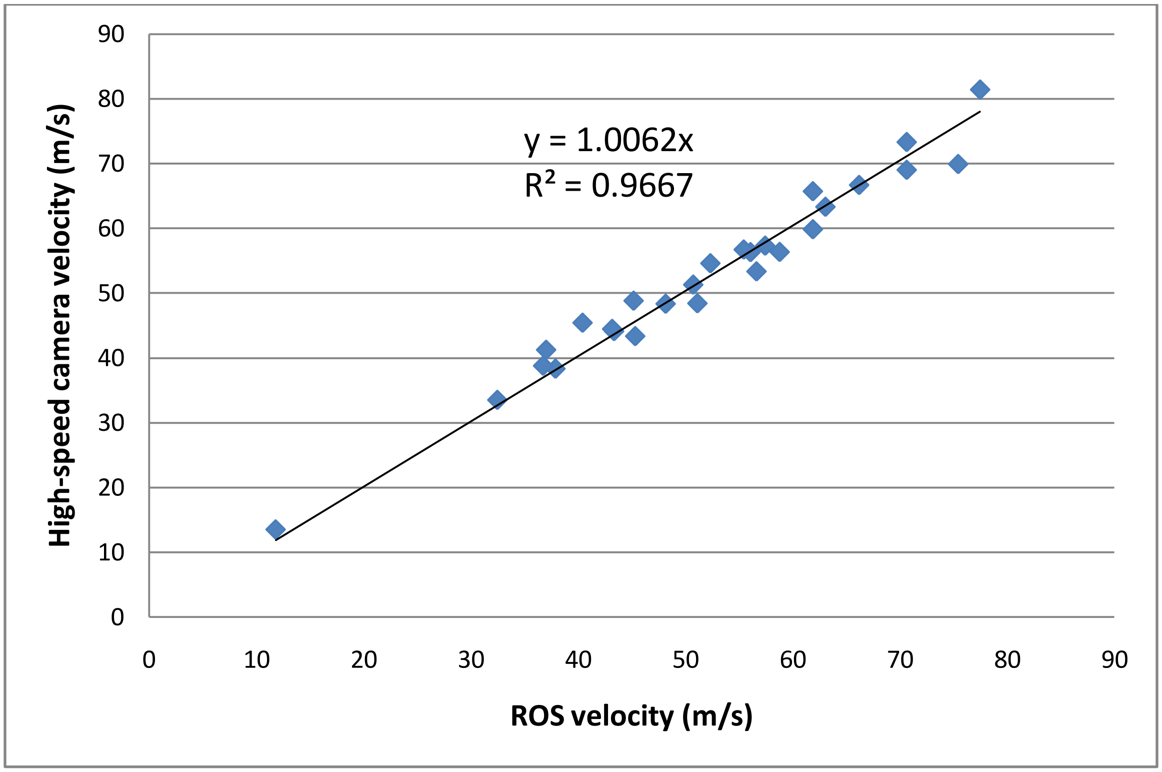

Figure 46: Comparison of velocity measurement techniques – high-speed camera and Reflective Object Sensor

The measurement from the ROS was deemed more accurate, due to the sources of possible error inherent in the HS camera technique (error of parallax, low resolution, and small displacements over which to calculate the velocity). For tests for which there was HS camera footage, but no ROS data, the trend in Figure 46 can be used as a calibration curve to approximate the corresponding ROS velocity.

5.3 ALPORAS direct impact results

5.2.1 Effect of velocity on stress-strain behaviour

In Figure 47, four stress-strain curves from tests of varying velocities in the forward direction are compared. Some variation in the characteristics of the curves can be expected due to the slight differences in cell morphology and density for each specimen.

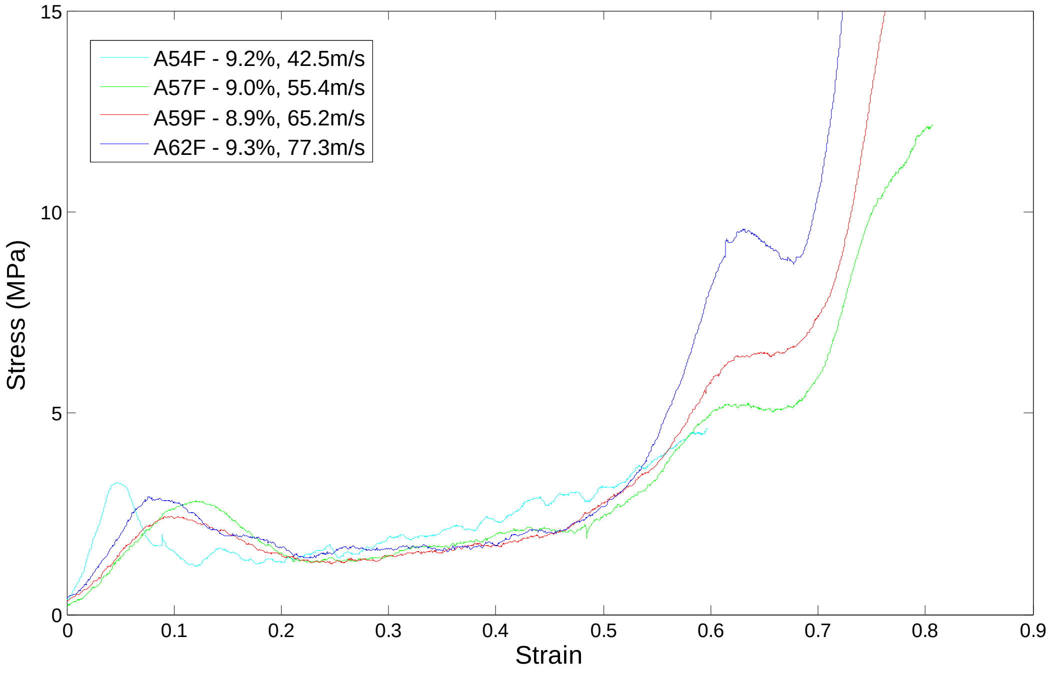

Figure 47: Comparison of of stress-strain curves for ALPORAS cylinders at varying velocities - forward direction

For the purposes of the current study, the plateau region of a stress-strain curve is defined as the average stress between the strains of 0.2 and 0.5. This is to avoid the initial peak, which occurs prior to 0.2 strain, and the densification region, which tends to occur subsequent to a strain of 0.5. The energy-efficiency method of locating the densification strain could not be used, as the point of maximum efficiency was not identifiable. The two methods of calculating the plateau stress were compared for all ALPORAS quasi-static tests, and gave very similar results.

According to shock theory, the plateau stresses for all the forward tests should be independent of the impact velocity, and should be equal for identical specimens. This is because the stress ahead of the propagating densification front is being measured, and this is theoretically equal to the quasi-static yield stress (not the plateau stress) of the specimen. In Figure 47, the stresses in the plateau regions of the curves do not appear to be increasing as the velocity increases.

There is variation in the shape, peak broadness and strain at which the initial peak occurs, but no consistent correlation between these characteristics and the impact velocity is observed.

In the densification region, however, there is significant difference in the curve characteristics. The onset of densification occurs at lower strains as velocity increases, and the gradient of the slope also becomes steeper with increasing velocity. Between the strains of 0.6 and 0.7, there appears to be a decrease in the stress, before it begins to increase again as densification continues. This momentary unloading of the specimen may be associated with the arrival of the densification front at the specimen-bar interface, as this is the region in which the densification front reaches the distal end of the specimen (where the stress is being recorded).

In Figure 48, the stress-strain curves of four tests conducted in the reverse direction are shown. As with the forward tests, there will be again be some variation depending on the density and cell morphology of the individual specimens.

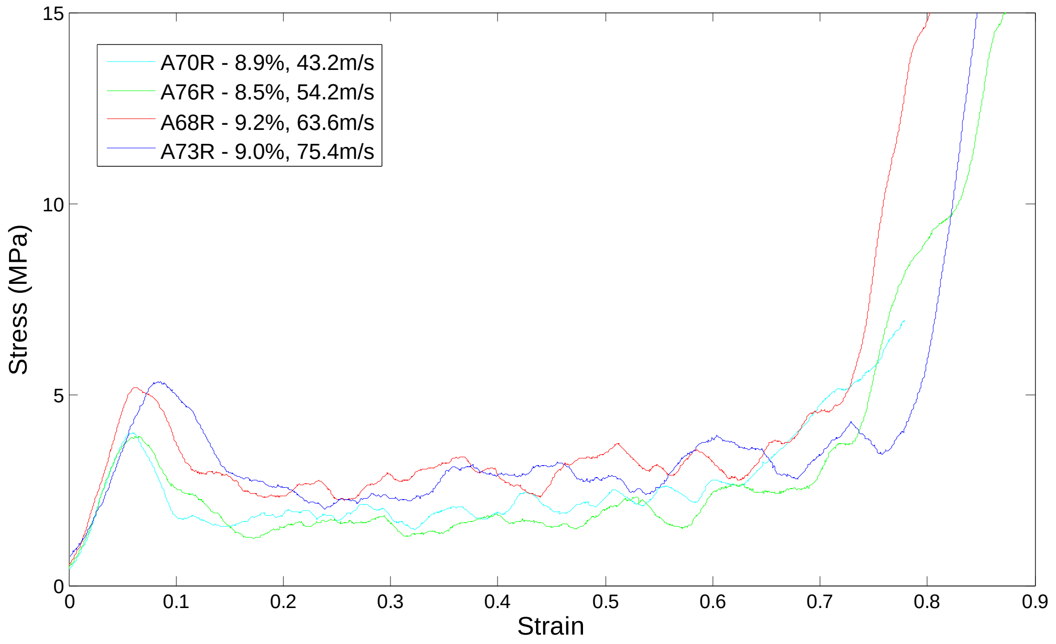

Figure 48: Comparison of stress-strain curves for ALPORAS cylinders at varying velocities - reverse direction

The stress measured in the reverse tests is the stress behind the densification front which, according to shock theory, is dependent on the impact velocity (the higher the velocity, the higher the stress in the densified region of the foam). Two measurements from each test that can be compared quantitatively are the initial peak stress, and the plateau stress.

The initial peaks of the two higher-velocity tests are markedly higher than those of the two lower-velocity tests. The same difference is observed with the plateau stresses of the two pairs of tests, although the difference is not as great. Although the densification strains differ, they do not differ depending on velocity. Velocity dependence is discussed in greater detail in section 5.3.1.

5.2.2 Comparison of forward and reverse tests

The stress-strain curves of forward (blue) and reverse (red) direct impact tests are shown in Figure 49 and Figure 50. Each comparison is between tests at similar velocities, on specimens of similar density.

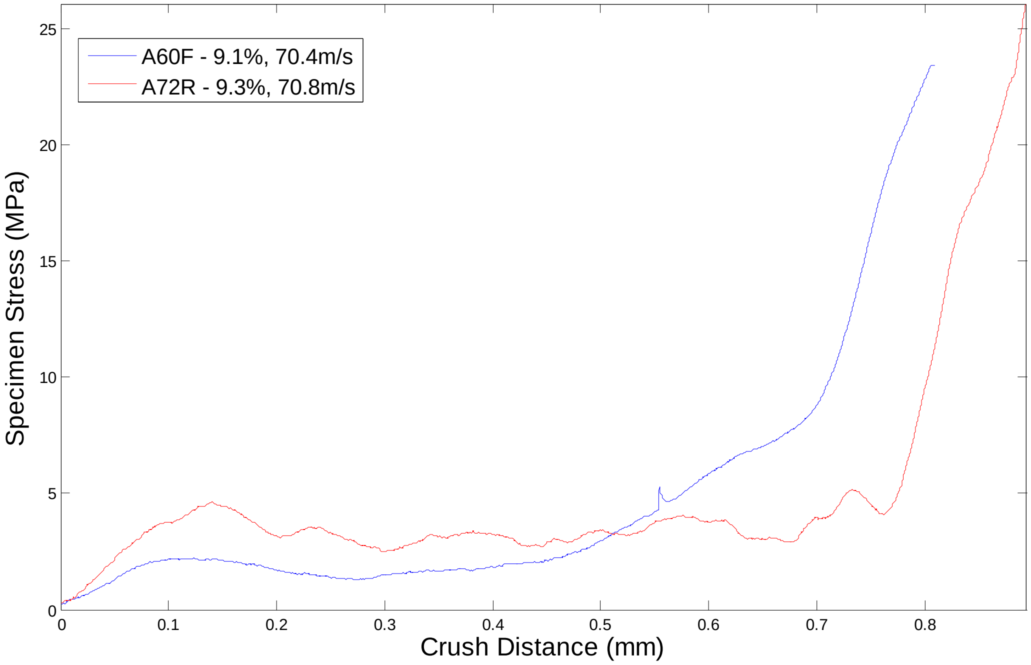

Figure 49: Stress-strain curves for forward and reverse tests at comparable velocities (high velocity)

In Figure 49, the tests were conducted at a nominal impact velocity of 70m/s. According to the literature (28), this is above the ‘critical velocity’ at which one should begin to see the effects of stress enhancement due to shock (i.e. a higher stress recorded in the reverse direction, for a specimen of the same density tested at the same velocity). Two observations can be made, namely:

- The forward test has a lower initial peak stress, and lower plateau stress, than the reverse test.
- The reverse test has a higher densification strain than the forward test.

The first observation is in accordance with shock theory (28).

Figure 50 shows the stress-strain curves of forward and reverse tests, at a nominal impact velocity of 46m/s. At this velocity the effects of shock should not be as evident, as this is below the critical velocity.

The initial peak stress of the reverse test is slightly higher than the peak of the forward test. There appears to be no difference in the plateau stresses.

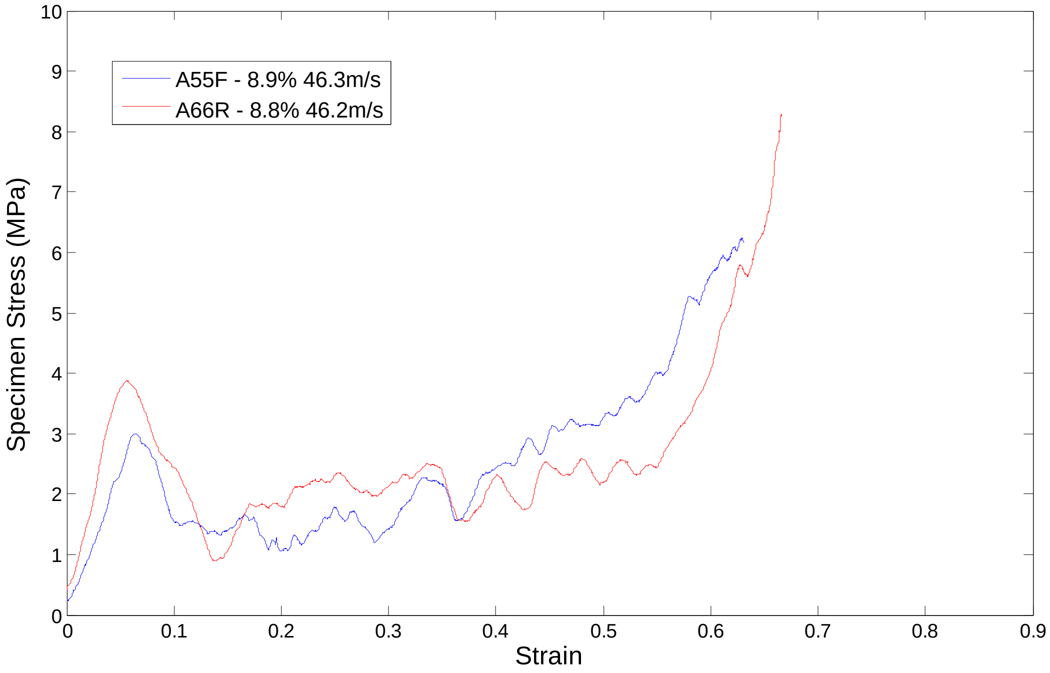

Figure 50: Stress-strain curves for forward and reverse tests at comparable velocities (low velocity)

5.2.3 Comparison of quasi-static and dynamic tests

In Figure 51, the stress-strain curves of quasi-static, forward and reverse direct impact tests of specimens of similar density are compared. Both dynamic tests are at a nominal impact velocity of 70m/s.

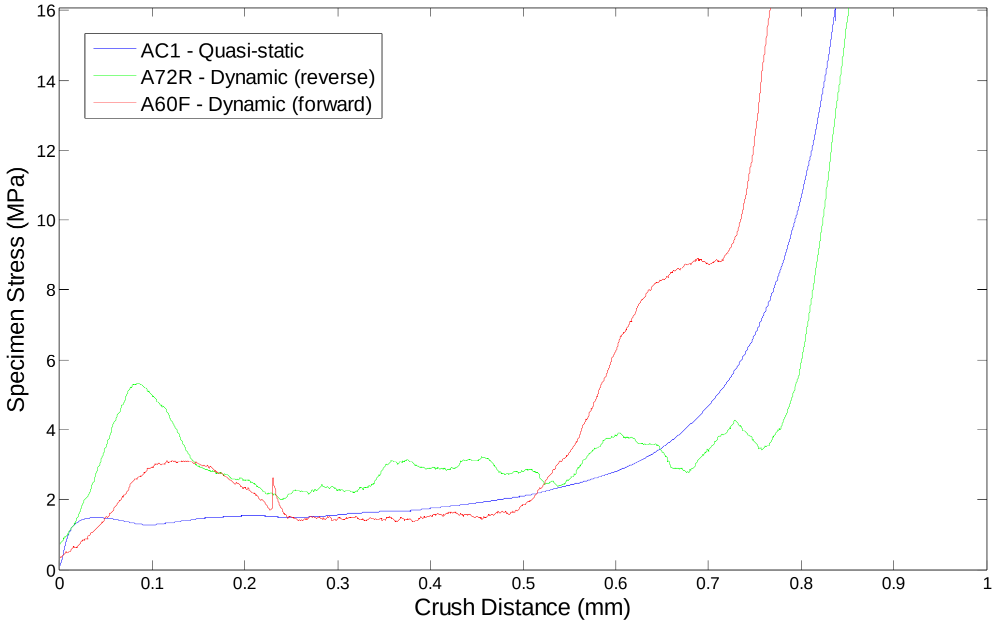

Figure 51: Stress-strain curves for quasi-static and dynamic forward and reverse tests

The quasi-static test is shown in blue. The quasi-static curve has the following characteristics when compared to the dynamic tests:

- A steeper linear elastic region.
- A lower initial yield stress, and no initial yield peak.
- A smoother plateau region.
- A plateau stress approximately equal to that of the forward dynamic test.

- A densification strain approximately equal to that of the reverse dynamic test.

5.2.4 Taylor test results

Table 7 summarises the Taylor tests conducted. All specimens were cylinders, nominally 40mm thick, and 35mm in diameter.

Table 7: Taylor test specimen details

Specimen	Mass (g)	Relative density (%)	Impact velocity (m/s)	Final thickness (mm)	Crush distance (mm)
A34T	No data	No data	17.00	39.5	0.5
A36T	No data	No data	28.4	38.26	1.74
A35T	No data	No data	29.3	37.98	2.02
A37T	No data	No data	36.85	37.2	2.8
A38T	No data	No data	42.90	36.3	3.7
A39T	No data	No data	45.05	35.94	4.06
A40T	No data	No data	57.47	32.22	7.78
A30T	8.77	8.50	63.0	31.62	8.72
A27T	8.73	8.22	75.5	28.86	11.90
A31T	7.98	8.00	86.2	27.20	13.68
A32T	7.76	7.80	105.1	21.67	19.70
A28T	8.81	8.43	122.5	19.89	21.44
A33T	7.60	7.43	147.8	20.16	20.44
A29T	8.29	8.02	183.3	12.00	27.62

The lowest velocity test (A30T, V_0 = 63.0m/s) underwent permanent deformation (i.e. experienced shock), which is consistent with 63m/s being above the critical velocity. The specimens show clearly defined densified and non-densified regions.

Figure 52 shows three frames from the high-speed camera footage of test A29T. The polystyrene backing disk has separated from the specimen, as it only propels the specimen as far as the fluting holes (where the back pressure is reduced).

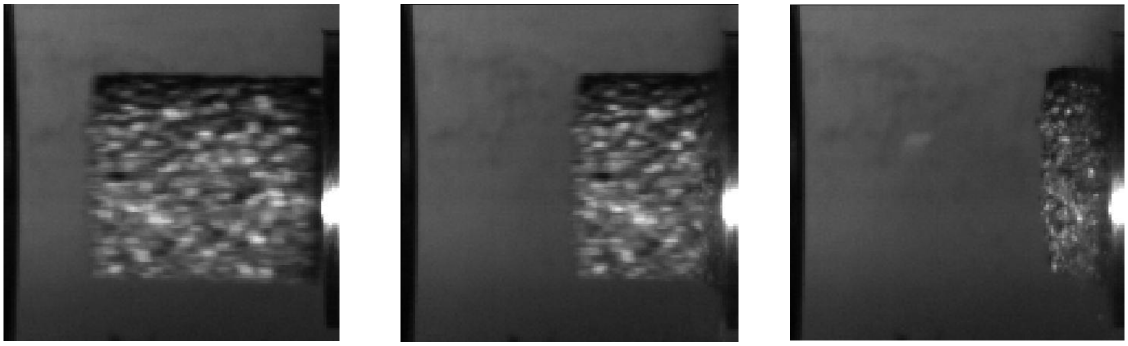

Figure 52: Taylor test A29T (V_0 = 183.3m/s) at time t = 0s, 86μs, and 229μs

The stress-strain history for test A29T is shown in Figure 53.

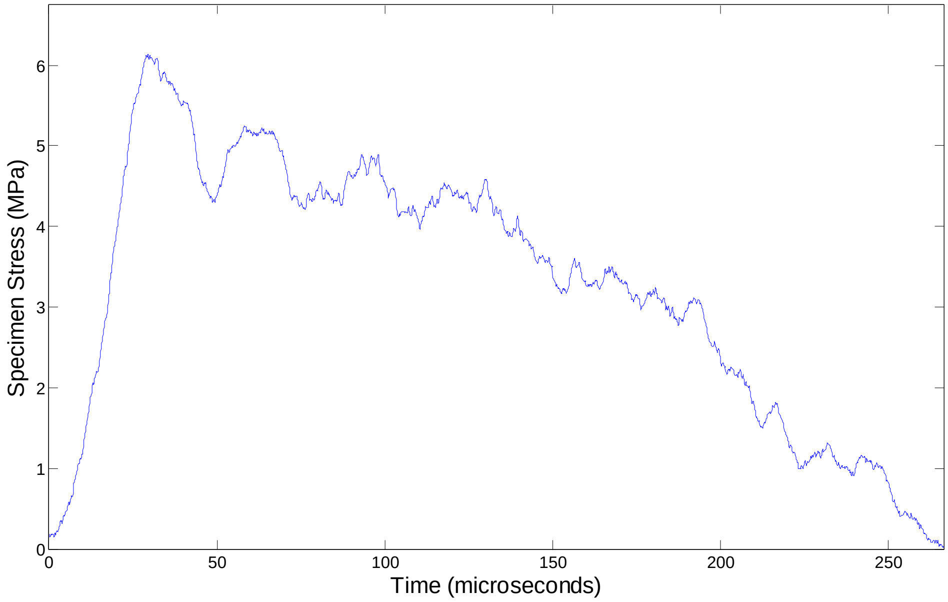

Figure 53: Stress-time plot for Taylor test A29T (V_0 = 183.3m/s)

The initial elastic region demonstrates a period of ‘bedding-in’ after the specimen has impacted, as the impact face of the specimen compacts to its maximum density. After the initial impact the specimen decelerates, until at the point of coming to rest the densification front ceases to propagate through the specimen. The force recorded at the specimen-bar interface decreases as the velocity of the specimen decreases.

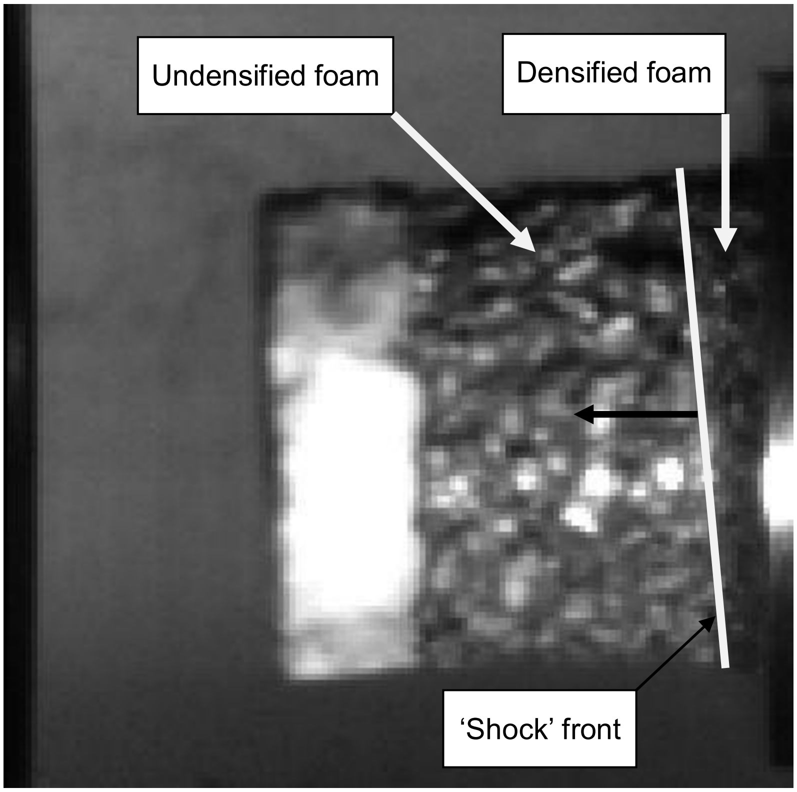

Figure 54: Taylor test A33T (V_0 = 147.8m/s), showing densification front

5.4 Discussion of ALPORAS direct impact results

5.3.1 Effect of velocity on initial yield stress

The influence of velocity on the yield stress (the yield point being the initial peak at the end of the approximately linear elastic region) is illustrated in Figure 55, which is a graph of initial peak stress ratio versus impact velocity. The initial peak stress ratio is the ratio between the yield stress and the theoretical quasi-static plateau stress at that specimen density. The quasi-static stress was determined using equation 13, developed from the test data in chapter 3.

The yield stresses for all tests on ALPORAS cylinder specimens, in both forward and reverse directions, are shown in Figure 55. The forward (blue) and reverse (red) tests are plotted as different series. A large amount of scatter is observed, after the recorded yield stress has been divided by the theoretical quasi-static plateau stress to remove the effect of density on the specimen strength from the data.

Three observations can be made from the data:

- The peak stress ratio in the forward tests does not appear to be increasing as the impact velocity increases.
- The yield stresses recorded for the reverse tests are all higher than those recorded for the forward tests.
- The yield stresses recorded for the reverse tests show a linearly increasing trend as the impact velocity increases.

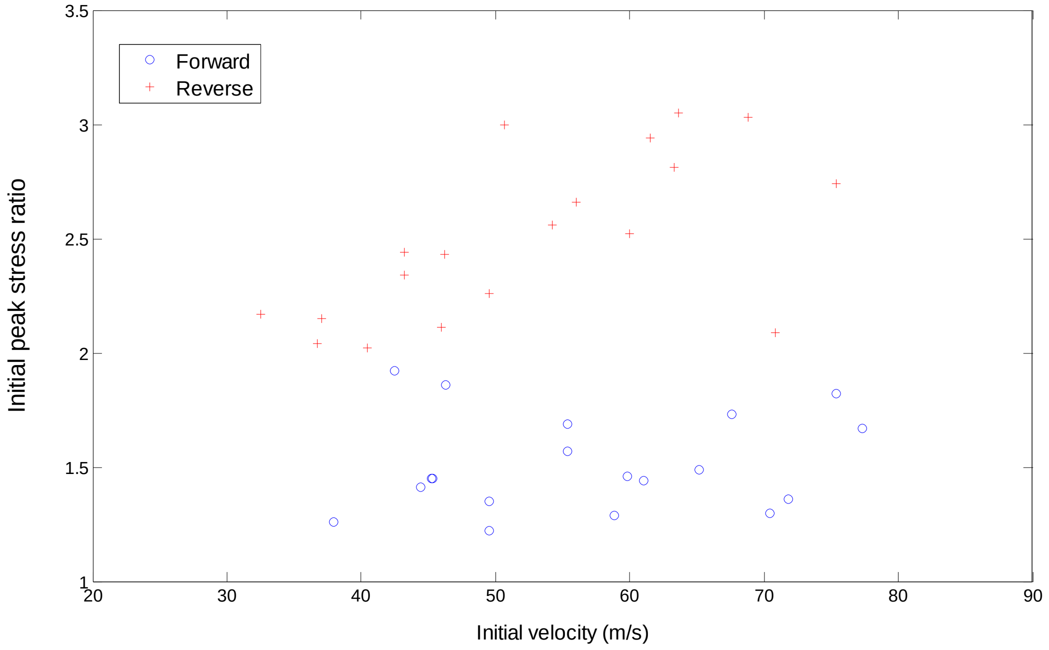

Figure 55: Yield stress ratio vs impact velocity for all ALPORAS cylinders

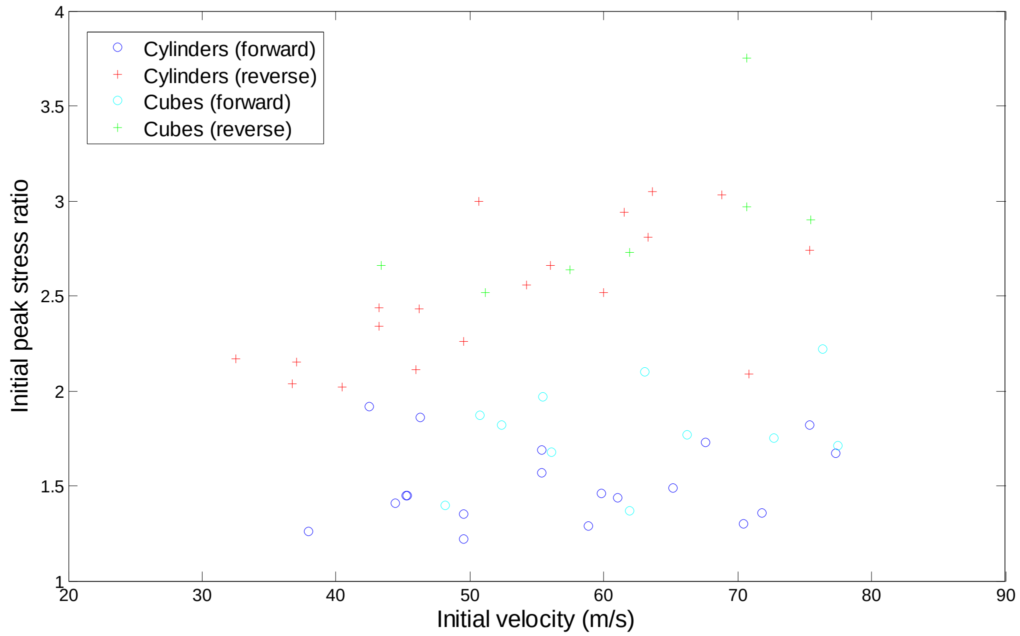

Figure 56: Yield stress ratio vs impact velocity for all ALPORAS tests

Figure 56 is a graph of yield stress ratio versus impact velocity, with data from the cube tests included.

The same observations can be made for the forward and reverse series of tests conducted on the cubes. The forward series shows the same amount of scatter as the forward series of the cylinders, and the linearly increasing trend of the reverse series follows that of the reverse cylinder series.

5.3.2 Effect of velocity on plateau stress

Two methods of calculating the plateau stresses for the ALPORAS quasi-static data are compared in Figure 57. The two methods are:

1. The average stress between zero strain and the densification strain corresponding to the point of maximum energy absorption efficiency.
2. The average stress between the strains of 0.2 and 0.5

The first method is that used in calculating the plateau stress for all quasi-static tests; the second is that which is used in calculating the plateau stresses for all dynamic tests. The stress ratio in Figure 57 is the ratio between the actual plateau stress and the yield stress for the cell wall material.

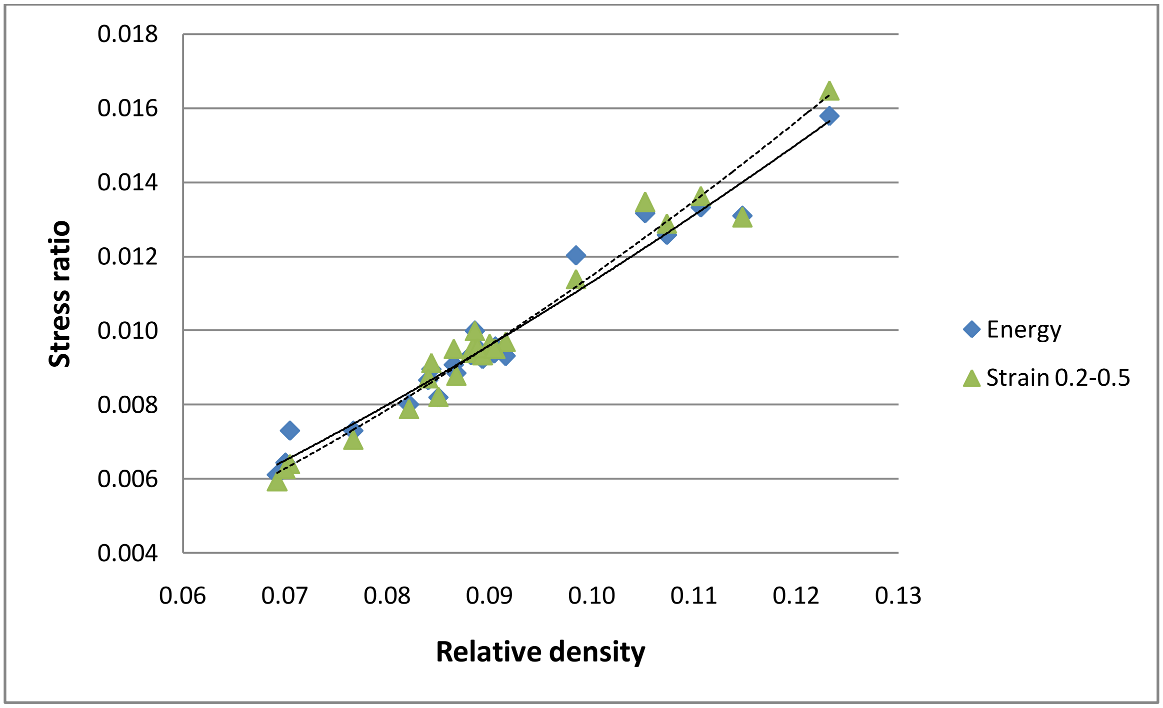

Figure 57: Comparison of two methods of calculating the plateau stress for all quasi-static ALPORAS tests

The power trend determined from method 1 in chapter 3 is used to calculate the theoretical quasi-static plateau stress for the dynamic tests. The two methods are compared here, as method 1 is used to calculate the quasi-static plateau stress (in chapter 3), and method two is used for to calculate the dynamic plateau stress (in this section). This is because the point of maximum efficiency of the energy absorption efficiency curve (i.e. the densification strain) is not readily identifiable for the dynamic tests. The difference between the two methods for the density range of the dynamic test specimens needs to be quantified. For the lowest and highest density dynamic specimens (8.5% and 11.0% relative density), the difference between the two methods is 0.7% and 2.8% respectively.

The ratio of actual dynamic plateau stress to theoretical quasi-static plateau stress is plotted against impact velocity for all ALPORAS cylinders in Figure 58.

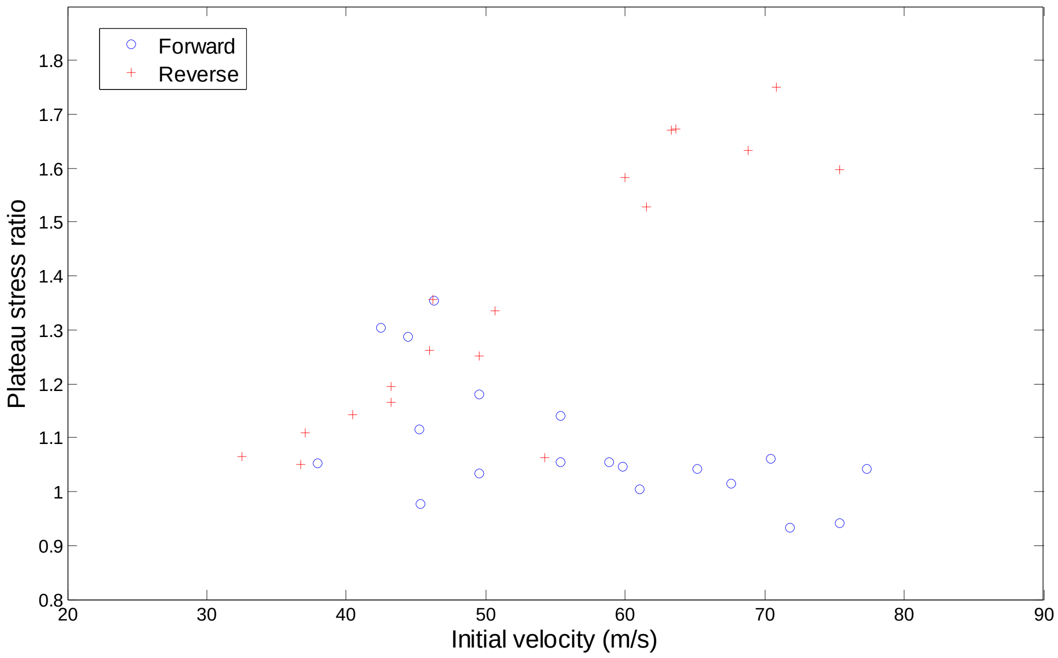

Figure 58: Plateau stress ratio vs impact velocity – ALPORAS cylinders

As with the initial peak stress ratio, the plateau stress ratio shows scatter in both the forward and reverse series. The forward series does not increase as the impact velocity increases, whilst the reverse series follows a linearly increasing trend.

From Figure 58 the critical velocity for the current series of ALPORAS tests can be determined. Although the reverse data below 50m/s appear to follow the increasing trend, there is no clear difference in the stress ratio between the forward and reverse tests (that is, for a given velocity, the stress in the reverse direction is not necessarily higher than that in the forward direction). Above 60m/s, however, there is a marked difference in the stress ratio as the reverse series continues to increase. The critical velocity for ALPORAS for the current series of tests is therefore 50-60m/s.

In Figure 59, the data for the ALPORAS cubes are added to the cylinder data. The cubes follow similar trends but show considerably more scatter, and are not included in the determination of critical velocity.

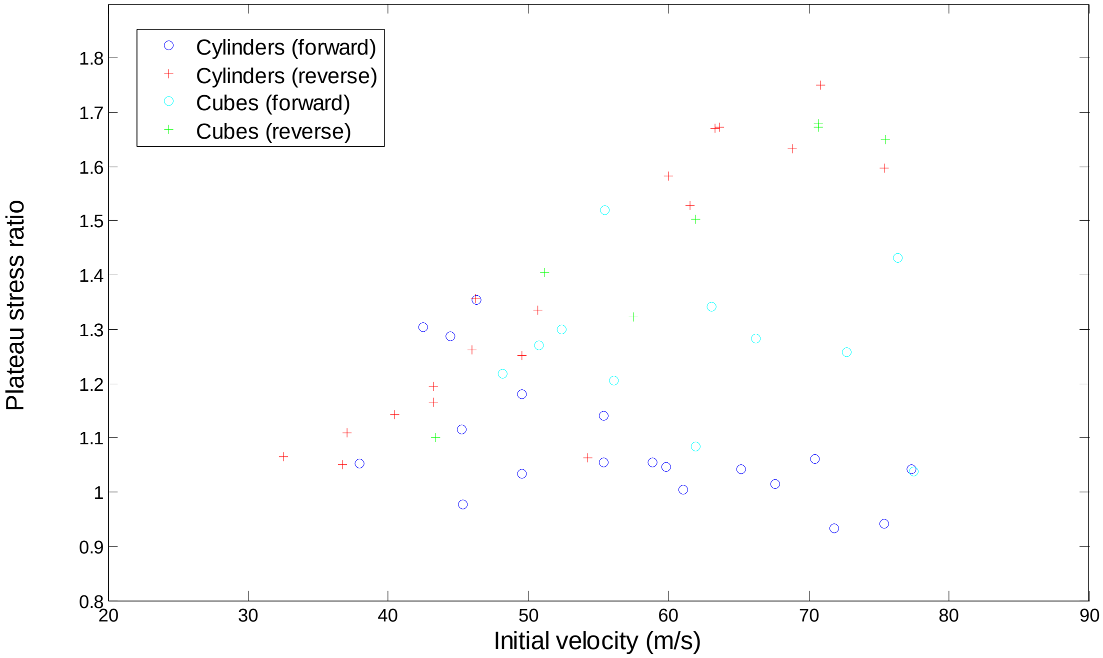

Figure 59: Plateau stress ratio vs impact velocity for all ALPORAS tests

5.5 Cymat direct impact results

5.4.1 Effect of velocity on stress-strain behaviour

The stress-strain curves for all Cymat cylinders in the forward direction are plotted in Figure 60.

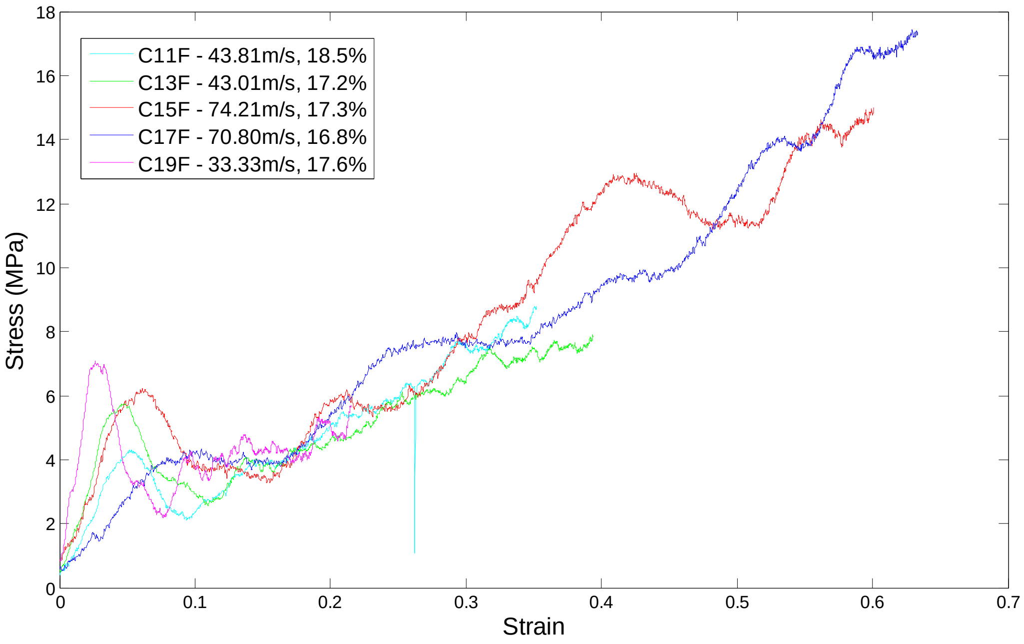

Figure 60: Stress-Strain curves for all Cymat cylinders – forward direction

While the curves show the specimens yielding at varying stresses, the magnitude does not appear to depend on the impact velocity (for example, the lowest velocity test has the highest initial peak stress). This indicates that variation in the initial peak stress depends on the specific density and cell structure of each specimen.

The stress-strain curves for Cymat specimens do not show the same distinct plateau region as the ALPORAS specimens do. This is the same difference between the materials that is observed in the quasi-static stress-strain behaviour, and is once again indicative of the less homogeneous cell structure of the Cymat foam. The stress strain curves in Figure 60 show approximately the same gradient in the plateau region, and the plateau stress does not appear to be dependent on impact velocity.

Unlike the ALPORAS specimens, which are almost all compressed into the densification region, for a given velocity and striker mass the denser (and hence stronger) Cymat specimens are compressed to a lower strain, as the energy of the striker is absorbed in the initial yielding and plateau regions.

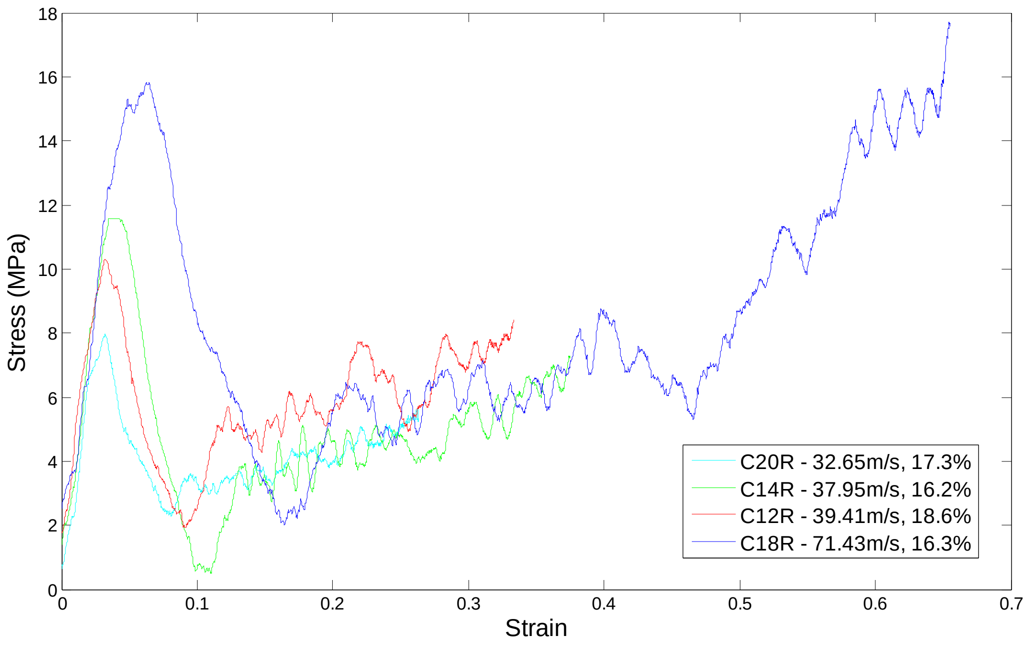

Figure 61: Stress-strain curves for all Cymat cylinders – reverse direction

Figure 61 shows the stress-strain curves of four cylindrical Cymat specimens tested in the reverse direction, over a velocity range of 32.7 to 71.4m/s. Two observations can be made from the figure:

- The initial peak stress increases as the impact velocity increases.
- The strain to which the specimen is crushed increases as the velocity increases.

The peak stress of specimen C14R is not the actual peak stress, as the signal exceeded the maximum voltage that the data card could record (known as 'clipping'). The test is included as it still indicates the increasing trend in yield stress. The actual stress is approximately 13MPa.

5.4.2 Comparison of forward and reverse tests

In Figure 62 and Figure 63, two pairs of forward and reverse tests are compared. As Cymat shows significant through-thickness variation in density, a forward and reverse pair needs to have specimens in the same orientation.

Figure 62 shows a forward and reverse pair of tests at relatively low velocity. For both tests, the dense side of the specimen is facing toward the striker (i.e. the stress is being measured on the less-dense side of the foam). Although the initial peak of the reverse test is slightly higher, there is no significant difference between the stress-strain curves at this velocity. The specimens were only crushed to strains of 0.21 and 0.26 respectively.

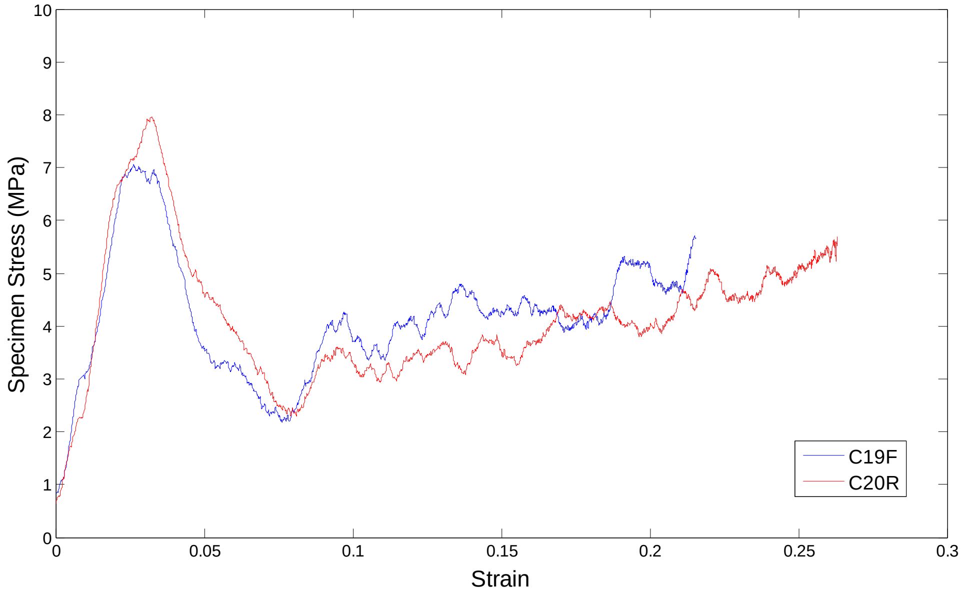

Figure 62: Comparison of Cymat forward and reverse tests – dense side toward striker, nominal velocity 33m/s

Figure 63 shows a pair of forward and reverse tests conducted at higher velocity. In this case the dense side of the material is facing the bar. At this higher velocity, there is a difference between the plastic collapse stresses of the two curves, with that of the reverse test being significantly higher. The lack of a definite initial peak for the forward test could indicate an area of particular weakness within the specimen.

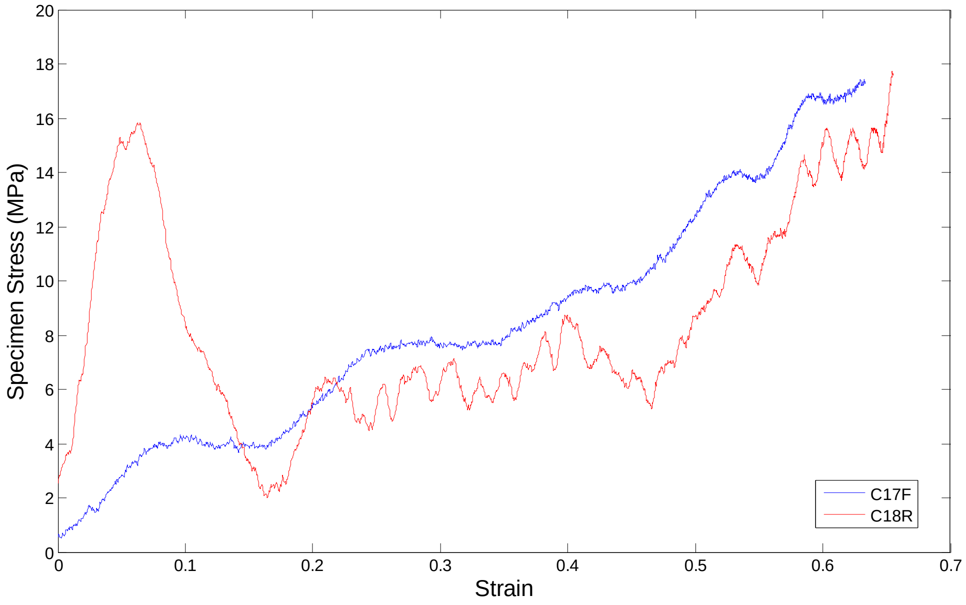

Figure 63: Comparison of Cymat forward and reverse tests – dense side toward bar, nominal velocity 70m/s

5.6 Discussion of Cymat direct impact results

5.5.1 Effect of velocity on initial yield stress

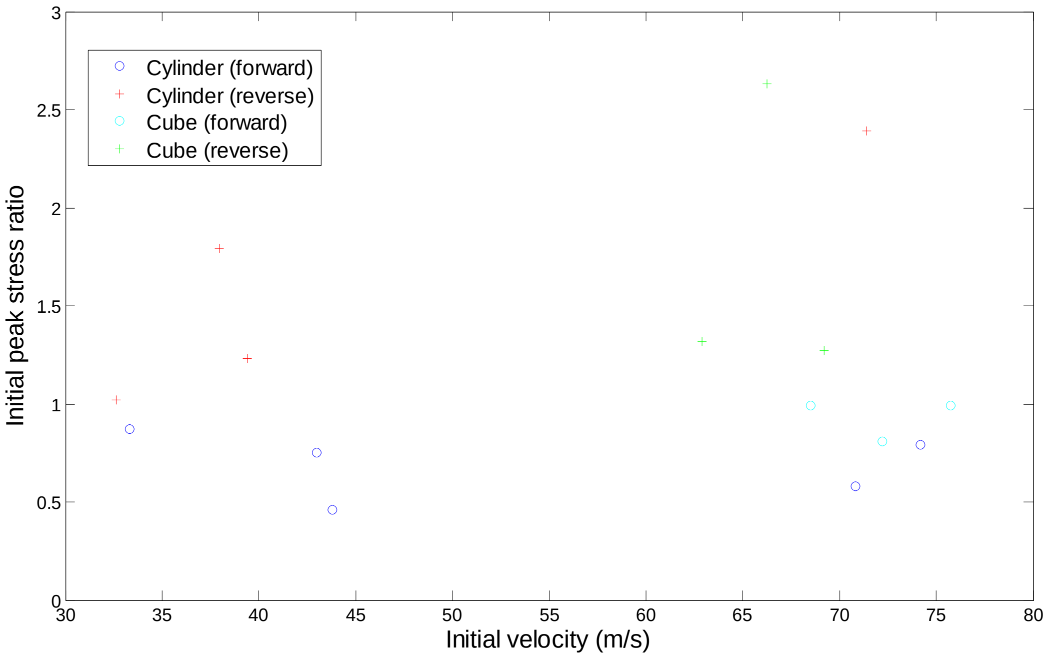

Figure 64: Initial peak stress ratio vs impact velocity – all Cymat tests

Fewer tests were conducted on Cymat specimens than on ALPORAS specimens. Therefore the data from the cylinders and cubes need to be plotted together in order to examine trends. Forward test data appears to show a constant initial peak stress ratio, similar to ALPORAS.

5.5.2 Effect of velocity on plateau stress

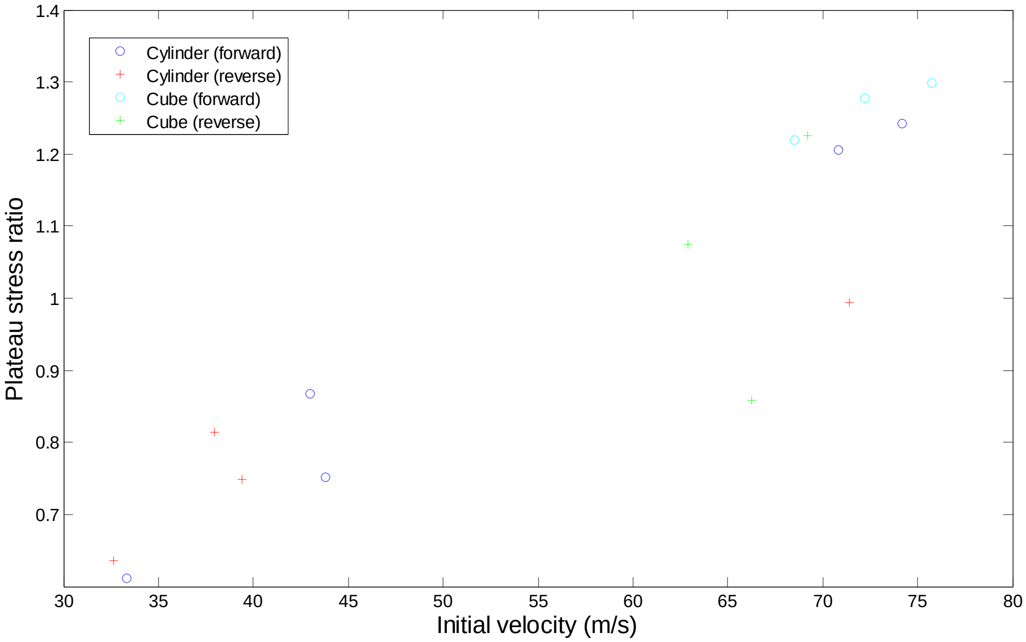

Figure 65: Plateau stress ratio vs impact velocity – all Cymat tests

The plateau stresses for both forward and reverse tests appear to follow an increasing trend with increasing velocity, in contrast to the ALPORAS. This may be due to the considerable strain hardening exhibited by Cymat. As all Cymat specimens were not crushed beyond a strain of 0.5 (for calculation purposes, the end of the plateau region), the plateau stress was calculated as the average stress between a strain of 0.2 and the maximum strain. As higher impact velocity leads to a higher maximum strain, this, in conjunction with strain hardening, would lead to a higher calculated plateau stress with a higher velocity.

6 BLAST TESTING

6.1 Experimental Setup

6.1.1 The Ballistic Pendulum

The ballistic pendulum used for the blast testing program is located in a blast chamber at the Blast Impact and Survivability Research Unit, at the University of Cape Town. A photograph of the pendulum is shown in Figure 66.

Figure 66: The ballistic pendulum

The pendulum is a steel I-beam suspended from a frame by four cables in such a way that it can swing freely, in the lengthwise direction of the I-beam. When an impulse is applied to one end, the pendulum undergoes a displacement. The magnitude of the impulse can then be calculated from the displacement of the pendulum, as described in Appendix D. During a blast test, the horizontal displacement of a trace pen attached to the pendulum was recorded, from which the displacement of the pendulum can be calculated. Although the impulse of a blast is approximately proportional to the mass of explosive detonated, two charges of the same mass will not give the same impulse due to the fact that the explosive may not detonate uniformly. Due to the conservation of momentum, a given impulse will always result in the same pendulum displacement, irrespective of how much energy is absorbed by the specimen being tested.

The blast rig and charge are placed at the proximal (blast) end of the pendulum; at the other end is a pen which indicates the horizontal displacement of the pendulum for each test. A mass is placed on the distal end of the pendulum to counterbalance the mass of the blast rig. The pendulum is balanced by adjusting turnbuckles at the end of each of the cables until it is level, and parallel to the wall of the blast chamber. This ensures as far as possible that the assumptions of simple pendulum motion required for the calculation of the impulse are satisfied.

6.1.2 Blast Rig

During a blast test, it is important that the test specimen is subjected to as uniform a load as possible. To achieve this, the specimen was placed at the end of a blast tube or shroud, similar to that used by Theobald (61), and used by Langdon (54) in a previous study. The explosive charge was placed at the proximal end of the tube at the centre of a polystyrene pad, and the specimen was located at the distal end of the tube. The blast tube was attached to a specimen mounting plate using threaded rods. This allowed the blast tube to be removed between tests while a new specimen was mounted on the blast rig. The blast tube and specimen mounting plate was attached to the pendulum by spacer rods. The experimental rig, attached to the pendulum, is shown in Figure 67.

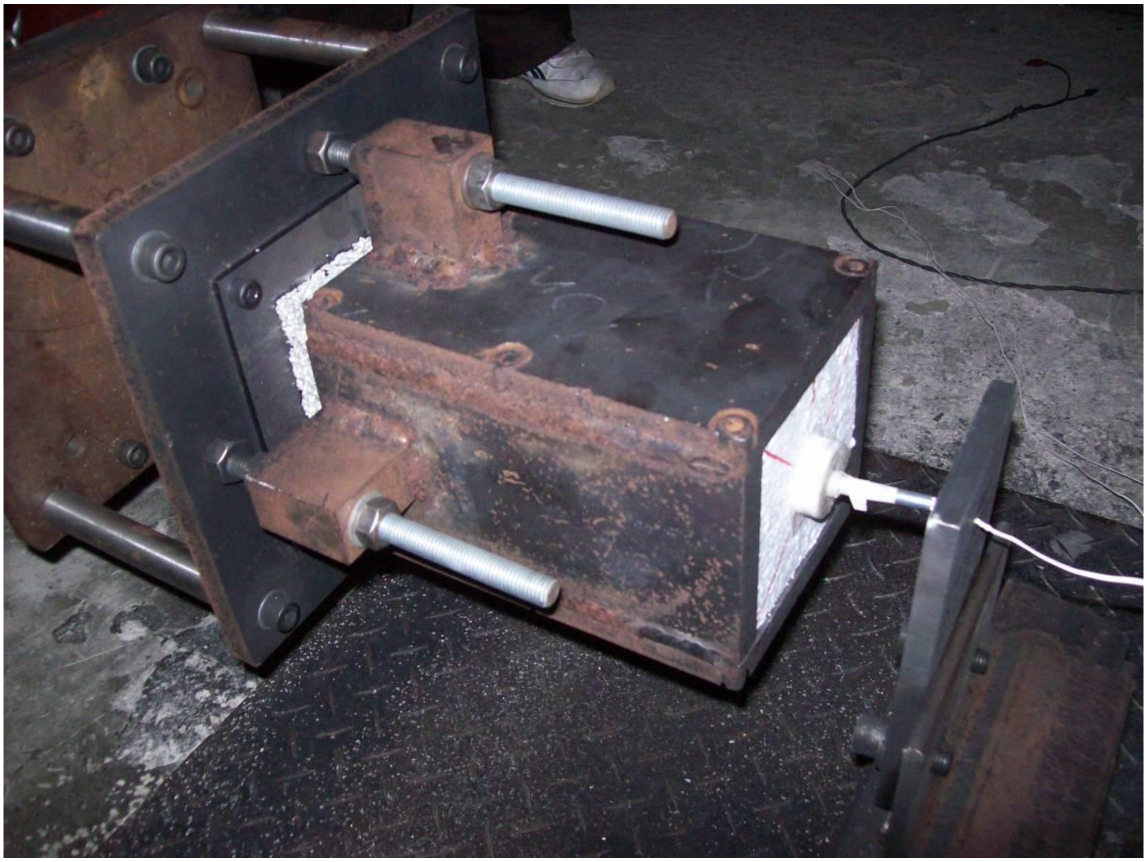

Figure 67: Blast test specimen, blast tube and explosive charge

It is important that the impulse that is transferred to the pendulum via the specimen, i.e. that no part of the pressure wave generated by the blast bypasses the specimen and impinges on the pendulum. In order to ensure that this did not happen, the blast tube is constructed with a slightly smaller width than the specimen, allowing the specimen to overlap the tube, and directing any “leaked” pressure to the side, away from the pendulum.

6.2 Blast Test Specimen Preparation

6.2.1 Introduction

The specimens used in the blast test programme were all 105x105x25mm square panels of foam, cut from larger foam panels, and 25mm in thickness. The mass of each foam panel was measured. These square panels were placed between 4mm thick mild steel plates. The front plate was referred to as the face plate, and the purpose of the face plate was to apply a uniform compressive load to the foam panel, as the face plate was accelerated by the force (pressure) of the blast. The face plates have the same dimensions as the foam panel (105x105mm), while the back plates are larger (156x156mm) and have holes drilled in each corner to enable the specimen to be bolted to the specimen mounting plate. Some specimens were prepared by bonding the foam panel to the face and back plates, while others were not bonded.

In a previous study using Cymat foam (54), it was found that bonding the panels to the face and back plates caused the foam panel to be partially or completely fragmented during testing. This was determined to be due to the Cymat specimens (which fail under brittle fracture, as opposed to ductile yielding of ALPORAS foam) fracturing under tension as the specimen unloaded after being fully compressed by the blast. In terms of measuring the final thickness of the specimen after testing, this is undesirable.

While it is understood that sacrificial cladding in a real-world scenario would likely be constructed by bonding the aluminium foam to face and/or back plates, in an experimental environment some unbonded specimens were tested to remove the effect of the face plate during tensile rebound of the specimen.

6.2.2 Bonded Specimens

Three Cymat specimens and seven ALPORAS specimens were bonded to their face and back plates before being tested. The specimens were bonded using Xiro polypropylene film adhesive. The surfaces of the steel plates were abraded, and two sheets of Xiro (the same size as the specimen) placed at each foam-plate interface. The specimen was then placed in an oven. The polypropylene layer was heated to between 180 and 190 °C for 20 minutes to promote flow of the polypropylene and initiate bonding between the steel plates and the foam. A thermocouple placed in between the back plate and foam panel was used to check that the temperature stays in this range for the full 20 minutes. After 20 minutes, the oven was turned off, and the specimen left to oven-cool.

6.2.3 Unbonded Specimens

The remainder of the foam specimens were tested without bonding the foam panel to the face and back plates. The specimens were held together by masking tape prior to being tested. Masking tape was used as this will hold the specimen together while it is being placed on the pendulum, but will not have any significant effect while the specimen is deforming.

Whether the specimen is bonded or unbonded does not have an effect on the axial compressive load during testing, only during tensile unloading (rebound) of the specimen, during which the energy of the rebounding face plate may be enough to deform or destroy the specimen. During the compressive stage loading, a disadvantage of the specimen being unbonded is that it is difficult to ensure that the specimen or the face plate are not shifting vertically or horizontally (with respect to the loading direction) during the test. Shifting would result in non-uniform loading of the specimen, and would also cause some of the blast pressure to bypass the specimen and impinge on the pendulum, resulting in an incorrect impulse-deflection measurement for the specimen.

6.3 Blast Testing Programme

6.3.1 Test Procedure

The procedure for each blast test was as follows: The test specimen (bonded or unbonded) was secured to the specimen mounting plate using cap screws. The blast tube was then mounted on the threaded rods and located against the specimen face plate, with care being taken not to load the specimen while securing the blast tube. The polystyrene pad with the 30mm diameter explosive was placed at the proximal end of the blast tube. The detonator was placed at the centre of the explosive, and the measuring pen placed on the tracing sheet. The explosive was detonated (during which the door to the blast lab was closed), after which the pen was raised, and the blast tube and specimen removed. The thickness of the four corners of each specimen was then measured to determine the mean post-test thickness for each specimen.

6.3.2 Test Programme

Table 8 and Table 9 detail the number of each type of foam that was tested, as well as the corresponding explosive mass for each test. All specimens were nominally 25mm in thickness, except specimens A20 and A21, which were 40mm in thickness. The density of each specimen (ρ_f) is quoted in kg.m^{-3} and the density as a percentage of the density of solid aluminium (the relative density) is also shown. The indicated specimen mass is the mass of the foam panel only, with no face and back plates. The plateau stress is a theoretical value calculated using equation 13. The charge mass includes the 1 gram leader to the detonator.

Table 8: Blast test specimen details - ALPORAS

Spec. no	Bonding	Mass (g)	ρ_f (kg.m^{-3})	ρ_f/ρ_s (%)	σ_0 (MPa)	Charge (g)
A17	-	54.81	198.9	7.4	1.2	3
A8	-	60.69	220.2	8.2	1.4	4
A9	-	61.16	221.9	8.2	1.4	5
A10	-	53.06	192.5	7.1	1.2	6
A1	-	60.93	221.1	8.2	1.4	7
A2	-	61.37	222.7	8.2	1.4	7
A3	Xiro	60.95	221.1	8.2	1.4	7
A6	Xiro	60.09	218	8.1	1.4	7
A7	Xiro	62	224.9	8.3	1.4	7
A11	-	54.42	197.4	7.3	1.2	8
A12	-	61.38	222.7	8.2	1.4	9
A13	-	54.13	196.4	7.3	1.2	10
A5	Xiro	61.08	221.6	8.2	1.4	11
A14	-	55.38	200.9	7.4	1.2	11
A20	-	89.7	203.4	7.5	1.3	11
A15	-	54.07	196.2	7.3	1.2	12
A4	Xiro	53.09	192.6	7.1	1.2	14
A21	-	97.6	221.3	8.2	1.4	16

Table 9: Blast test specimen details - Cymat

Spec. no	Bonding	Mass (g)	ρ_f (kg.m^{-3})	ρ_f/ρ_s (%)	σ_0 (MPa)	Charge (g)
C5	Xiro	129.71	470.6	17.4	6.8	7
C12	-	110.91	402.4	14.9	4.8	8
C13	-	114.56	415.6	15.4	5.1	9
C14	-	107.05	388.4	14.4	4.4	10
C15	-	142.4	516.6	19.1	8.4	11
C2	-	118.25	429	15.9	5.5	12
C16	-	125.6	455.7	16.9	6.3	13
C3	Xiro	115.65	419.6	15.5	5.3	14
C7	-	124.52	451.8	16.7	6.2	14
C17	-	120.91	438.7	16.2	5.8	15
C8	-	131.72	477.9	17.7	7	16
C18	-	125.2	454.2	16.8	6.3	17
C1	-	116.92	424.2	15.7	5.4	18
C4	Xiro	135.44	491.4	18.2	7.5	18
C19	-	127.05	461	17.1	6.5	19
C9	-	138.02	500.8	18.5	7.8	20
C10	-	140.53	509.9	18.9	8.2	20
C20	-	123.83	449.3	16.6	6.1	21
C6	-	140.44	509.5	18.9	8.1	22
C21	-	127.89	464	17.2	6.6	23
C11	-	113.53	411.9	15.3	5	26

6.4 Blast test results

Figure 68 show the increase of measured impulse versus charge mass graph for all blast tests. The Cymat, 25mm thick ALPORAS specimens and 40mm thick ALPORAS specimens are shown as separate series. It can be observed that the impulse transferred to the pendulum is independent of the energy absorbed by the specimen (i.e. a given charge mass will result in approximately the same impulse for tests on different specimens). This is demonstrated by the tests with a charge mass of 11 grams, where tests on specimens of different material and thickness results in similar impulses.

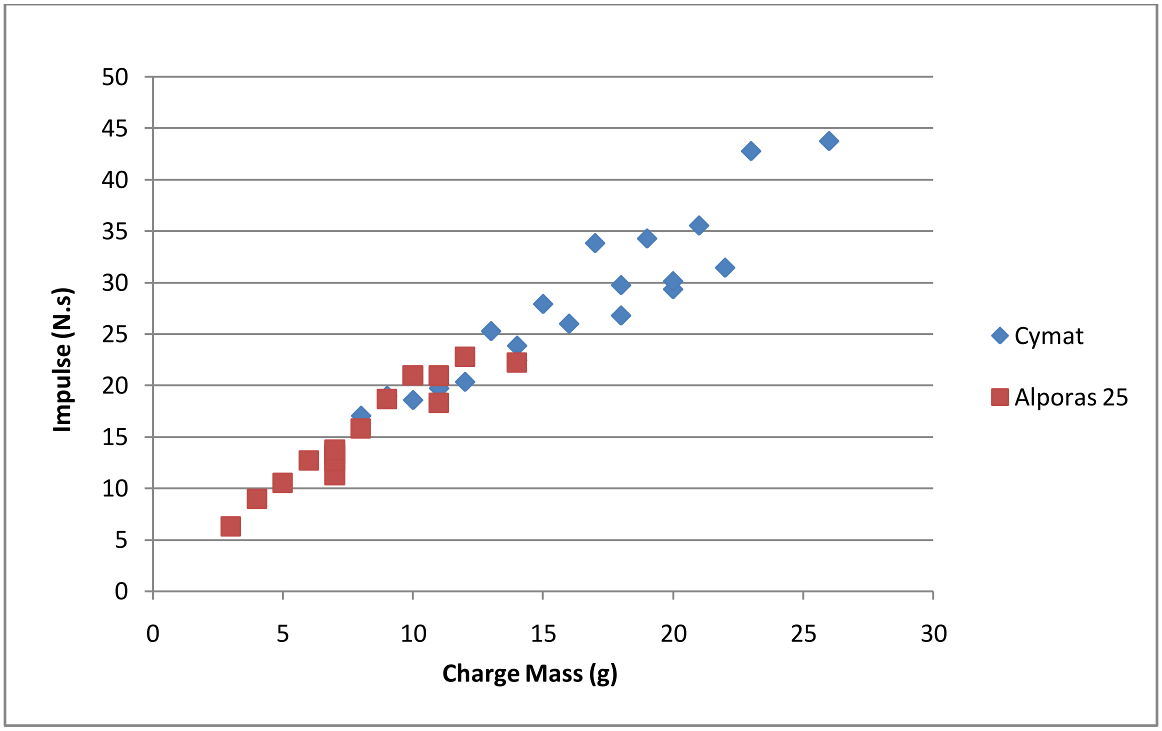

Figure 68: Impulse versus charge mass for all blast test specimens

6.4.1 ALPORAS blast test results

In order to compare tests on specimens of different densities, the impulse needs to be normalised using a modified damage number Φ_q, used by Nurick and Martin (62), defined by equation 16:

$$\phi_q = \frac{I}{2t^2\sqrt{BL\rho_f\sigma_0}} \tag{16}$$

where t, B and L are the thickness, length and width of the specimen respectively, I is the calculated impulse, and ρ_f and σ_0 are the density and theoretical plateau stress of the foam specimen. The test results for all ALPORAS specimens are shown in Table 10.

Table 10: ALPORAS blast test measurements

Specimen	Bonding	Mass (g)	ρ_f/ρ_s (%)	σ_0 (MPa)	Charge (g)	Impulse (N.s)	Φ_q	Crush (%)
A17	-	54.81	7.37	1.21	3	6.3	3.08	9.1
A8	-	60.69	8.16	1.39	4	9.0	3.90	16.4
A9	-	61.16	8.22	1.40	5	10.5	4.55	25.6
A10	-	53.06	7.13	1.16	6	12.7	6.46	39.4
A1	-	60.93	8.19	1.39	7	13.2	5.72	42.0
A2	-	61.37	8.25	1.41	7	13.4	5.75	38.5
A3	Xiro	60.95	8.19	1.40	7	11.3	4.90	28.4
A6	Xiro	60.09	8.07	1.37	7	12.6	5.57	38.7
A7	Xiro	62.00	8.33	1.43	7	13.7	5.84	35.9

Table 10: (Continued)

Specimen	Bonding	Mass (g)	ρ_f/ρ_s (%)	σ_0 (MPa)	Charge (g)	Impulse (N.s)	Φ_q	Crush (%)
A11	-	54.42	7.31	1.20	8	15.8	7.82	58.1
A12	-	61.38	8.25	1.41	9	18.7	8.04	57.8
A13	-	54.13	7.27	1.19	10	21.0	10.44	69.0
A5	Xiro	61.08	8.21	1.40	11	18.3	7.92	63.5
A14	-	55.38	7.44	1.23	11	21.0	10.16	71.4
A15	-	54.07	7.27	1.19	12	22.8	11.36	73.0

In Figure 69 and Figure 70, graphs of percentage crush versus impulse and damage number respectively are shown. As the ALPORAS specimens have a low variation in density, there is no significant difference between the trends of the two series. Both follow an initially linear trend as impulse/damage number increases, which begins to level off as the foam reaches its densification strain (at about 60% crush).

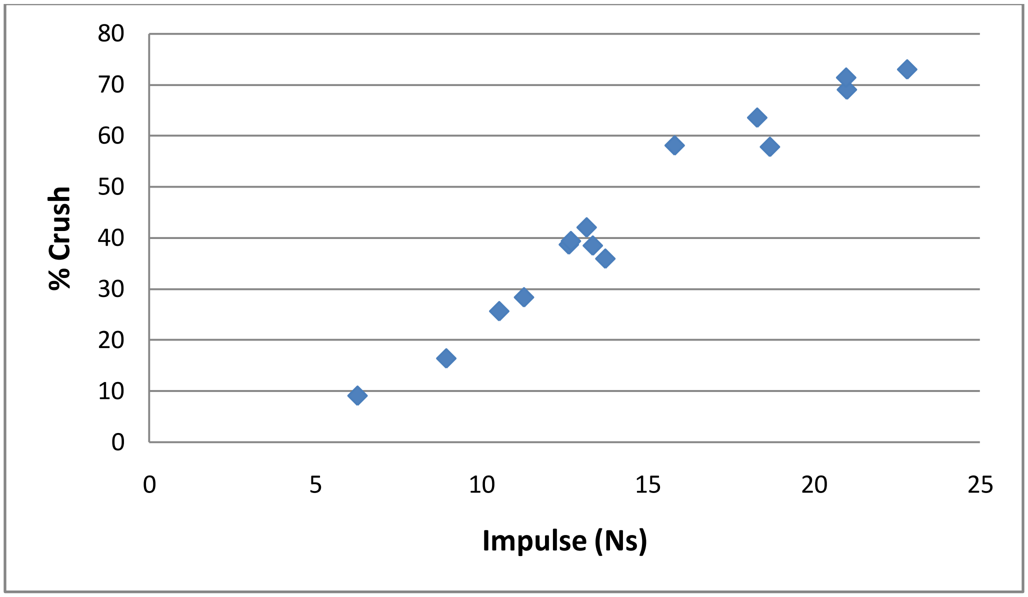

Figure 69: Percentage crush versus impulse for all 25mm ALPORAS specimens

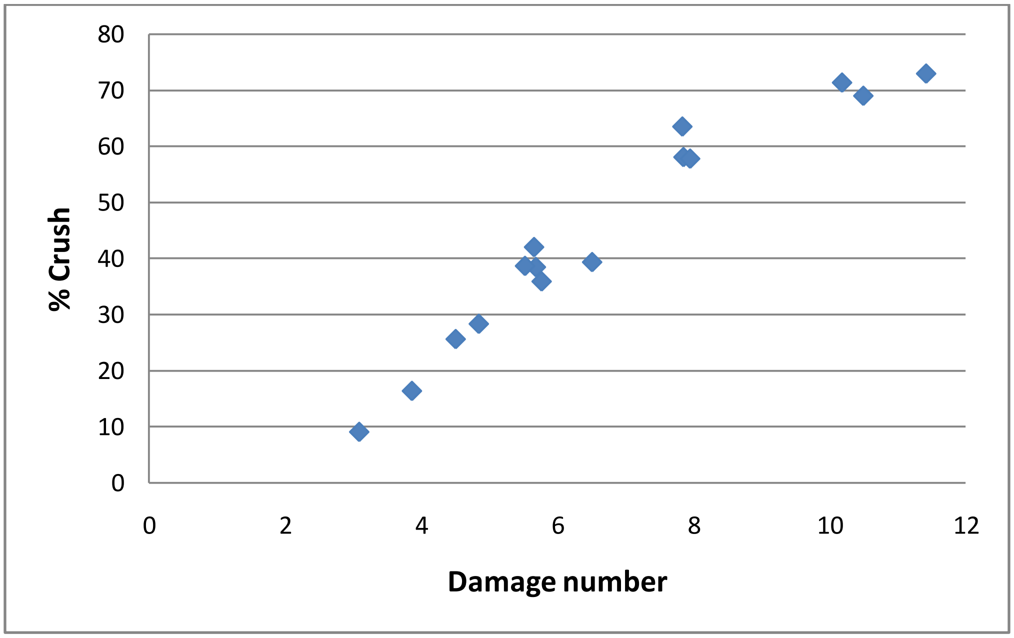

Figure 70: Percentage crush versus damage number for all 25mm thick ALPORAS specimens

The progressive increase in crush distance with increase in charge mass is shown in Figure 71. The charge mass used varies from 3 grams (for the topmost specimen) to 12 grams.

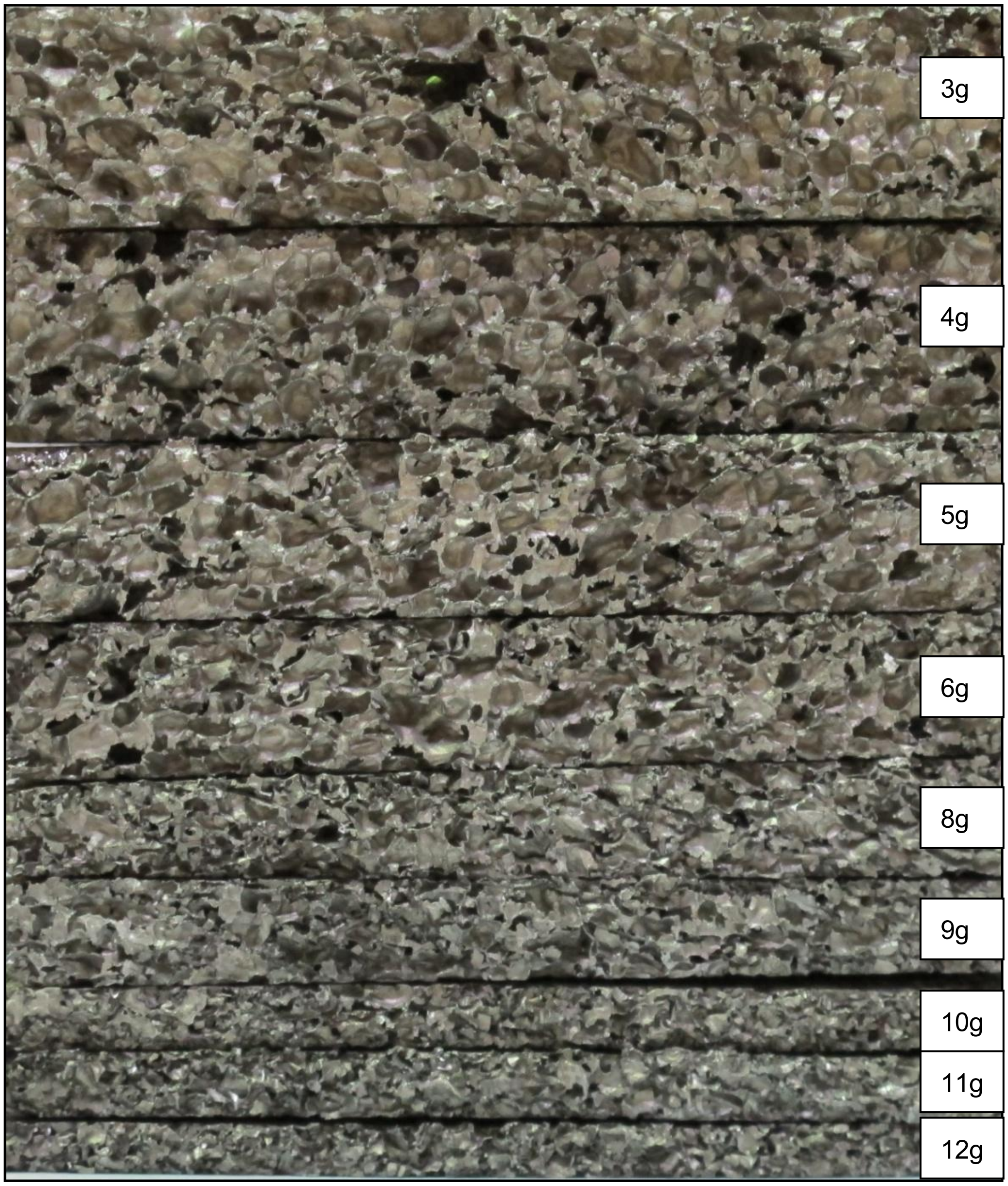

Figure 71: Increase in crush distance with increasing charge mass for ALPORAS blast test specimens

In Figure 72 to Figure 76 individual ALPORAS blast specimens are shown, also indicating the progressivly increasing deflection with increasing charge mass.

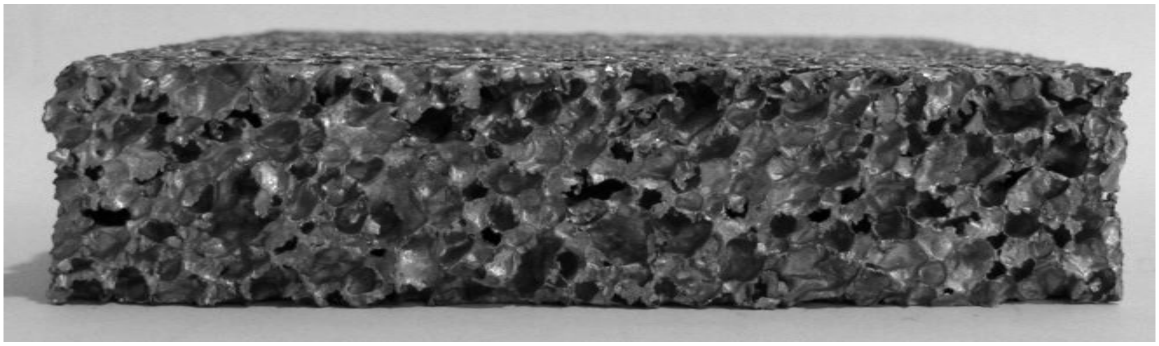

Figure 72: Specimen A8, charge mass 4g, ρ=8.2%

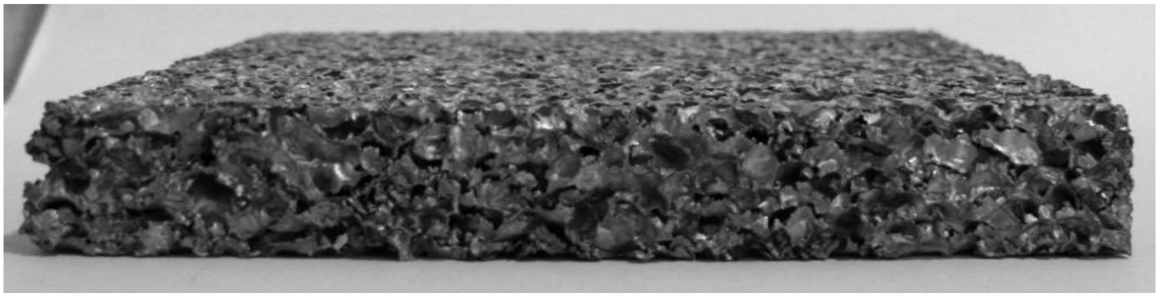

Figure 73: Specimen A9, charge mass 5g, ρ=8.2%

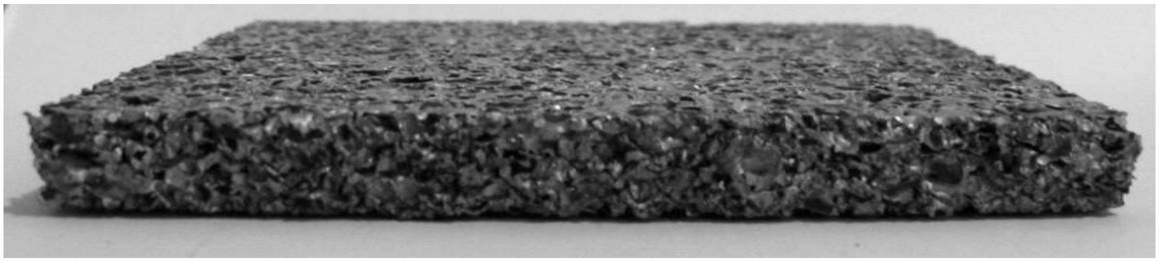

Figure 74: Specimen A11, charge mass 8g, ρ=7.3%

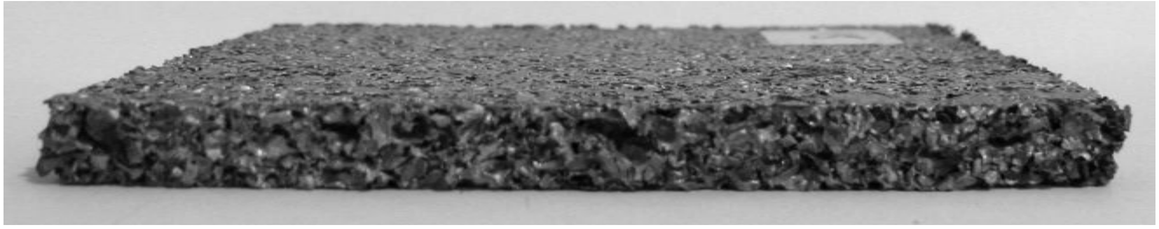

Figure 75: Specimen A13, charge mass 10g, ρ=7.3%

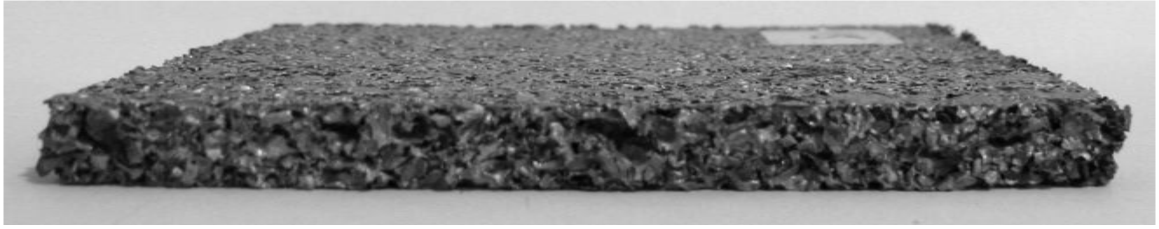

Figure 76: Specimen A14, charge mass 11g, ρ=7.4%

6.4.2 Cymat blast test results

The results for all Cymat blast tests are summarised in Table 11.

As the Cymat specimens have a wider range in density than the ALPORAS specimens, there is much more scatter in the crush distance versus impulse plot (Figure 77). The damage number is necessary here to be able to compare the specimens of different densities, and the graph of percentage crush versus damage number (Figure 78) shows a similar linear trend as the impulse increases. As the Cymat is denser and therefore stronger than the ALPORAS, the specimens are not compressed into the densification region, thus no plateau is observed in Figure 78.

Table 11: Cymat blast test measurements

Specimen	Bonding	Mass (g)	ρ_f/ρ_s (%)	σ_0 (MPa)	Charge (g)	Impulse (N.s)	Φ_q	Crush (%)
C5	Xiro	129.71	4.8	0.37	7	12.9	14.14	7.0
C12	-	110.91	4.1	0.26	8	17.0	24.12	19.5
C13	-	114.56	4.2	0.28	9	19.0	25.50	20.8
C14	-	107.05	4.0	0.24	10	18.6	27.84	27.6
C15	-	142.4	5.3	0.46	11	19.7	18.58	16.1
C2	-	118.25	4.4	0.30	12	20.3	25.94	27.1
C16	-	125.6	4.7	0.35	13	25.3	29.22	24.6
C3	Xiro	115.65	4.3	0.29	14	23.9	31.55	-
C7	-	124.52	4.6	0.34	14	22.5	26.32	31.4
C17	-	120.91	4.5	0.32	15	27.9	34.34	34.2
C8	-	131.72	4.9	0.39	16	26.0	27.82	31.6
C18	-	125.2	4.6	0.34	17	33.9	39.32	36.0
C1	-	116.92	4.3	0.29	18	29.8	38.65	44.9
C4	Xiro	135.44	5.0	0.41	18	26.8	27.40	-
C19	-	127.05	4.7	0.36	19	34.3	38.91	38.4
C9	-	138.02	5.1	0.43	20	29.4	29.11	33.5
C10	-	140.53	5.2	0.45	20	30.1	29.01	33.2
C20	-	123.83	4.6	0.34	21	35.6	42.06	44.4
C6	-	140.44	5.2	0.45	22	31.5	30.32	35.0
C21	-	127.89	4.7	0.36	23	42.8	48.04	45.0
C11	-	113.53	4.2	0.28	26	43.8	59.65	56.5

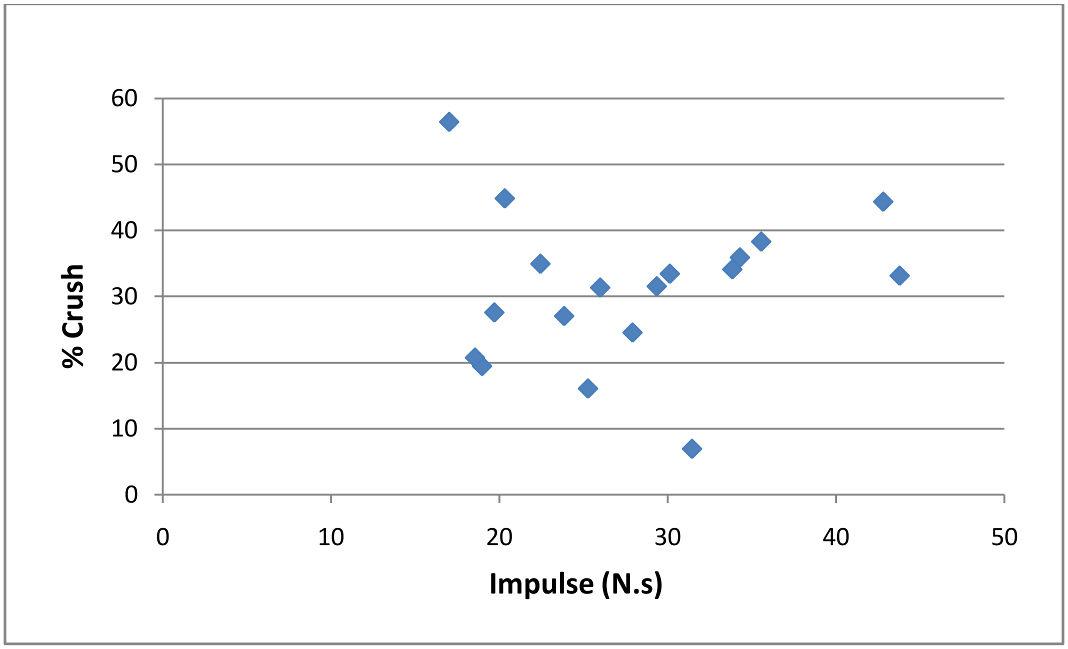

Figure 77: Crush distance versus impulse for all Cymat specimens

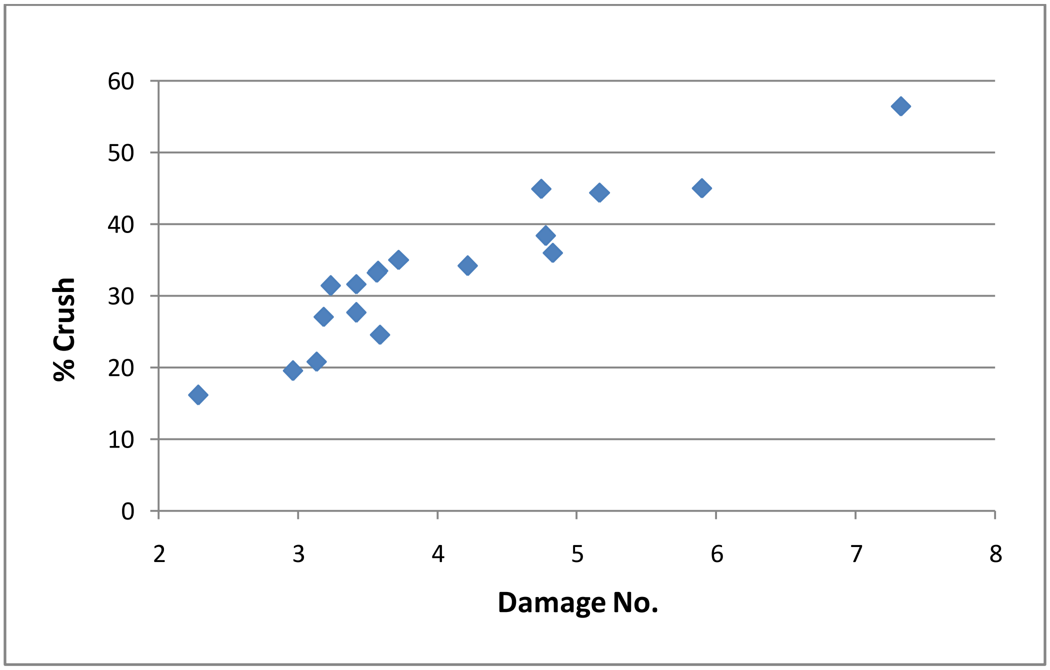

Figure 78: Percentage crush versus damage number for all Cymat specimens

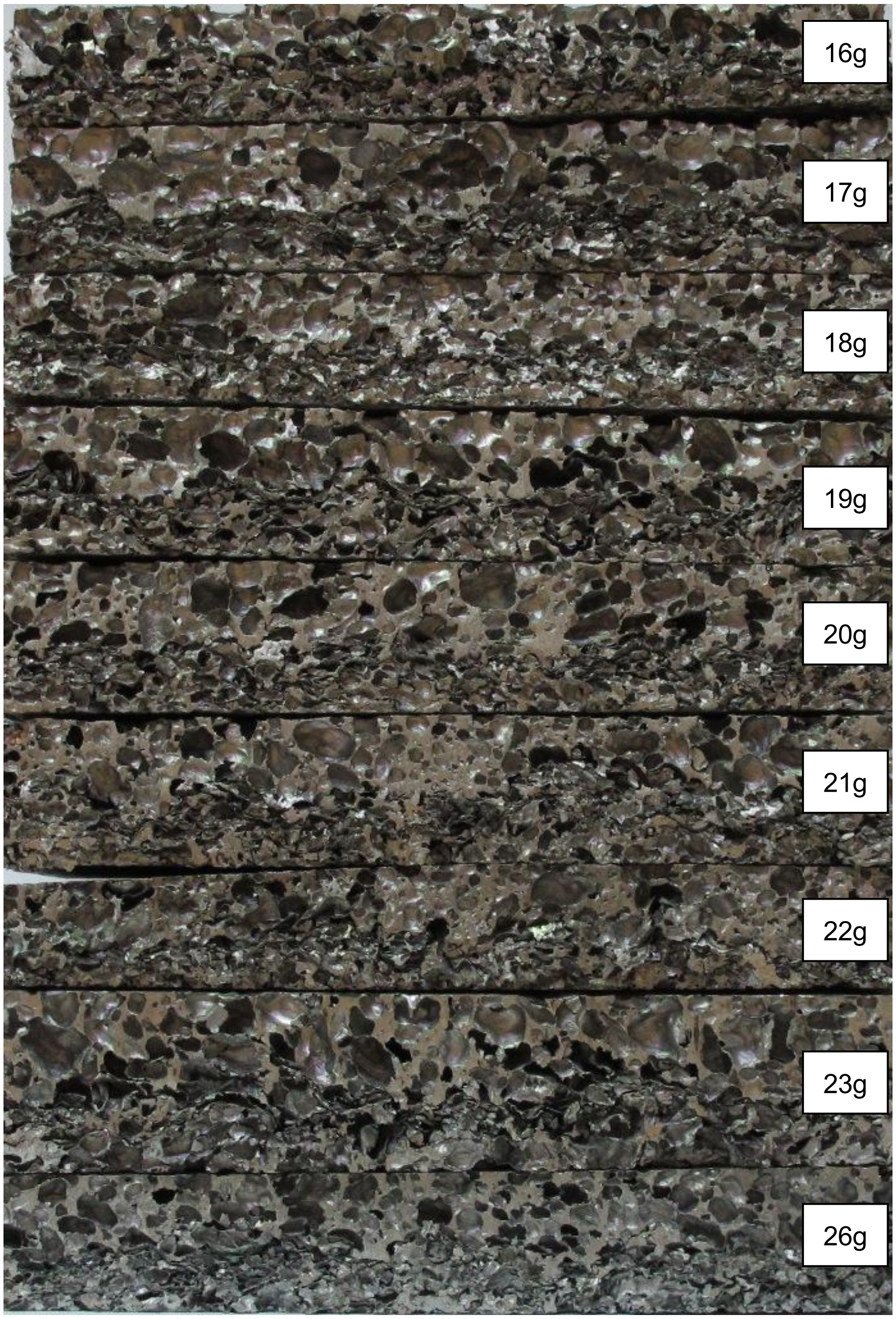

Figure 79: Increase in crush distance with charge mass (Cymat) –16-26 grams

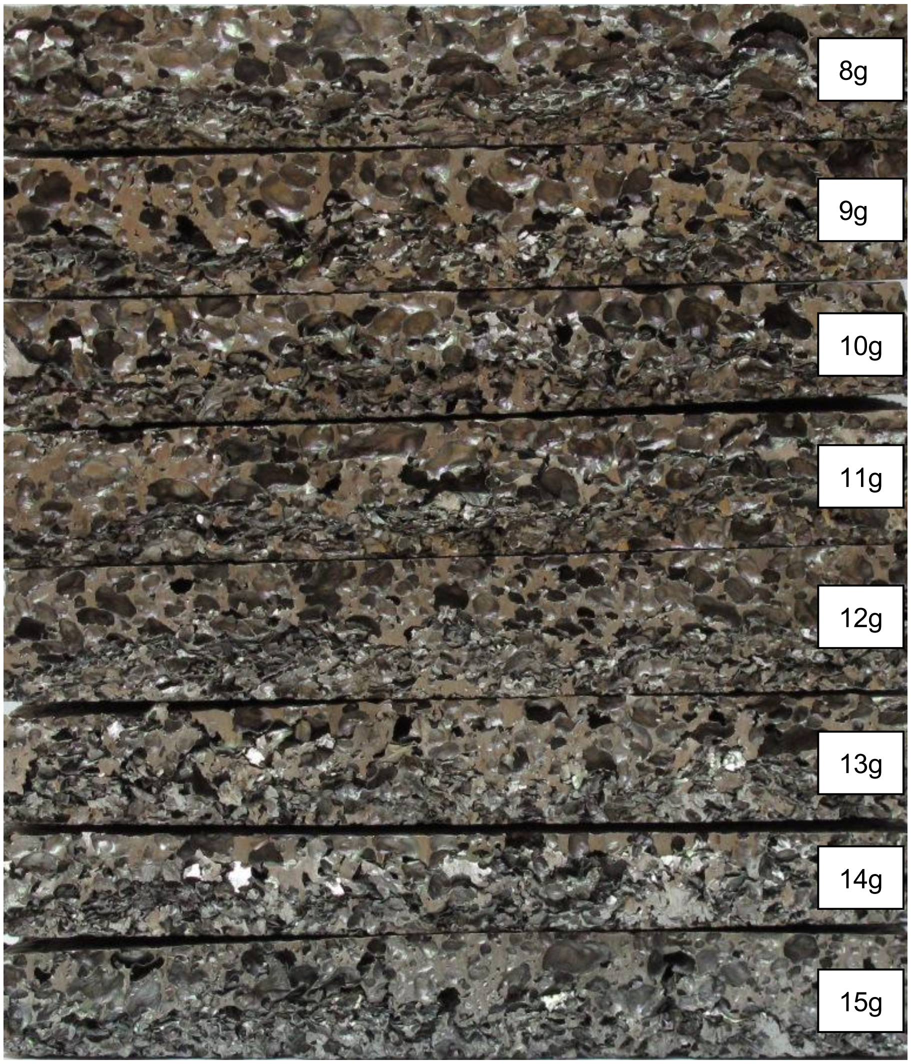

Figure 80: Increase in crush distance with charge mass (Cymat) –8-15 grams

Figure 81 to Figure 86 show a selection of individual Cymat specimens. The effect of the through-thickness variation in cell structure and variation in areal density can be seen. The crushing in the specimens has initiated in weaker bands of cells, and areas of lower density (and hence strength) within the specimens have undergone greater compaction, resulting in uneven deformation.

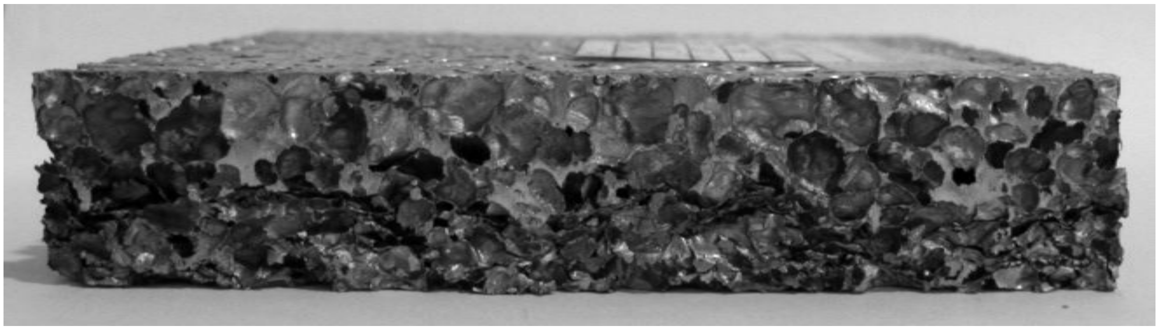

Figure 81: Cymat specimen C12 – charge mass 8g, ρ=14.9%

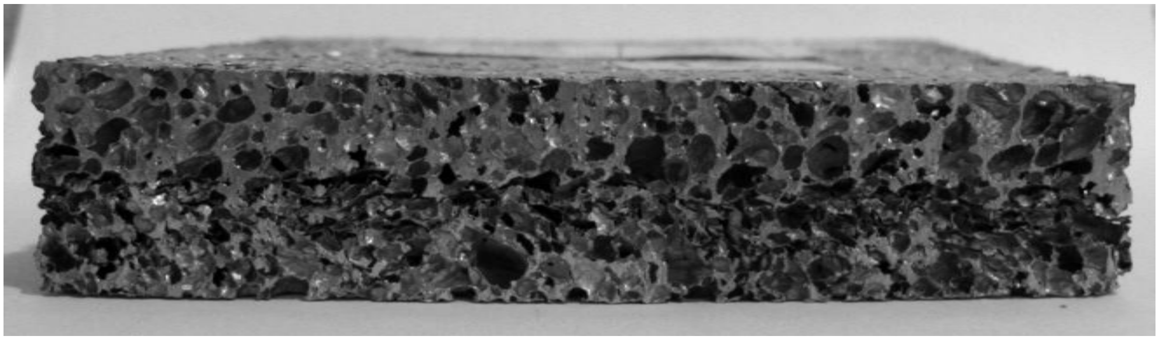

Figure 82: Cymat specimen C15 – charge mass 11g, ρ=19.1%

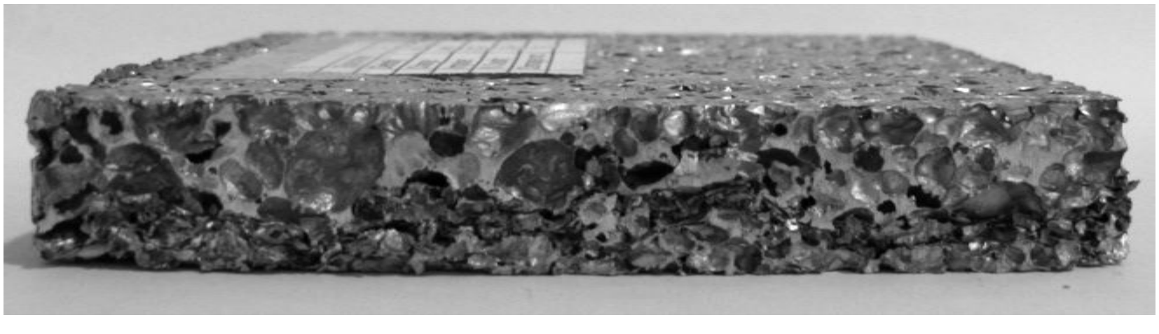

Figure 83: Cymat specimen C17 – charge mass 15g, ρ=16.2%

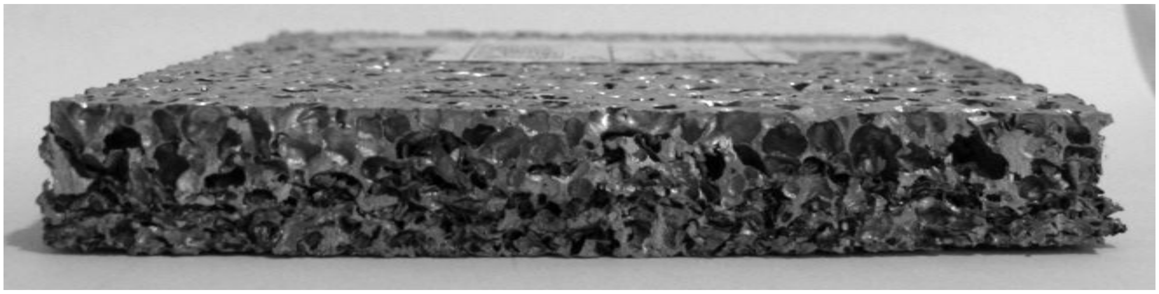

Figure 84: Cymat specimen C1 – charge mass 18g, ρ=15.7%

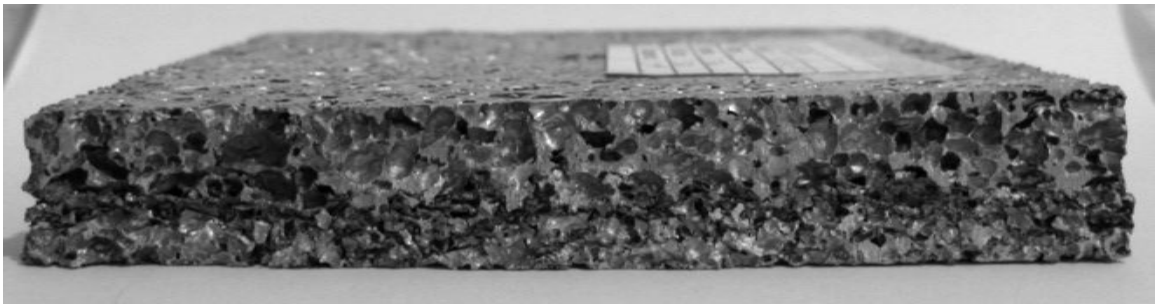

Figure 85: Cymat specimen C6 – charge mass 22g, ρ =18.9%

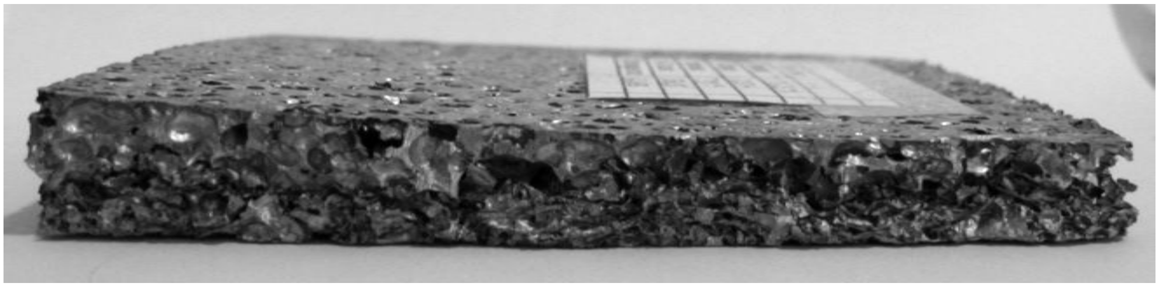

Figure 86: Cymat specimen C11 – charge mass 26g, ρ=15.3%

In Figure 87 and Figure 88, the fracture of bonded and unbonded Cymat specimens is compared. In Figure 87, the attached face plate has caused the specimen to fracture through its core, due to recoil of the face plate after the blast event. In Figure 88, the unbonded specimen shows signs of crack initiation, but has not disintegrated. This is consistent with the findings by Langdon et al. (54).

Figure 87: Specimen fracture in bonded specimen C4 (18 grams)

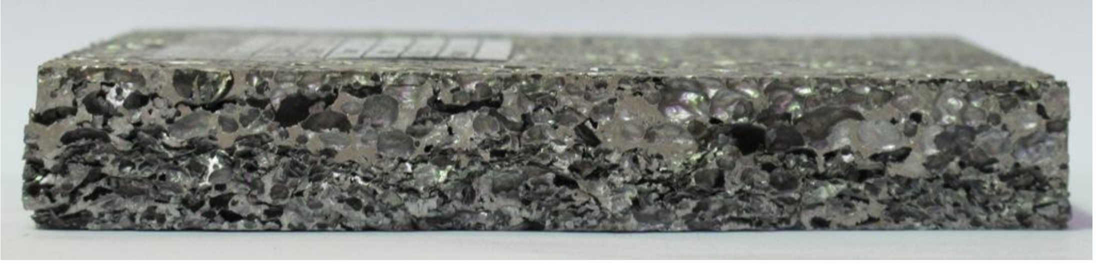

Figure 88: Specimen fracture in unbonded specimen C9 (20 grams)

7. DISCUSSION

7.1 Comparison of failure mechanism

Figure 89 and Figure 90 show photographs of Cymat and ALPORAS cubes subjected to QS compression. Both specimens have densified. Cymat exhibits a brittle failure, with considerable fracture and foam fragmentation observed at the edges of the test specimen.

In contrast, the ALPORAS exhibits ductile failure, with little fracture observed in the foam.

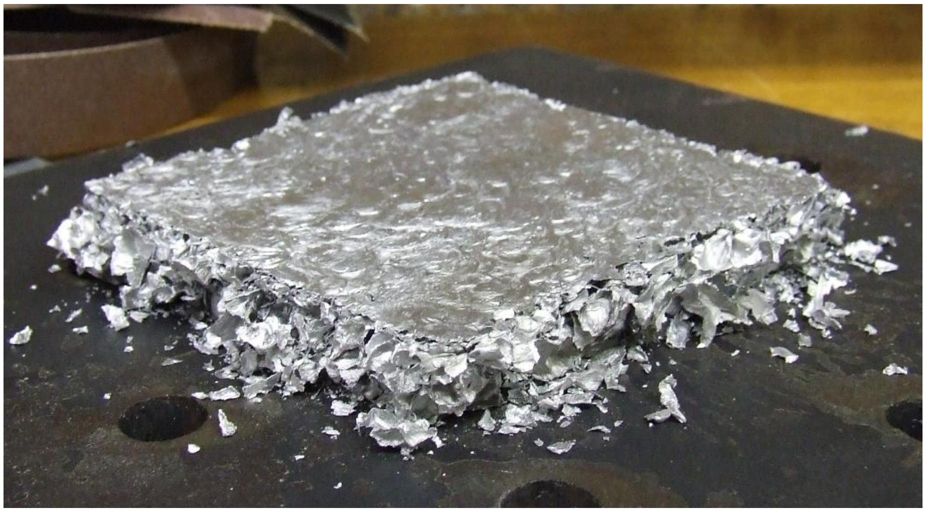

Figure 89: Brittle collapse of Cymat foam under quasi-static compression. Note fragments around specimen due to brittle fracture.

Figure 90: Ductile collapse of ALPORAS foam under quasi-static compression

7.2 Comparison of strain hardening behaviour

Figure 91 and Figure 92 compare the stress-strain curves of Cymat and ALPORAS direct impact specimens in the forward and reverse direction respectively. All tests were at sub-critical velocities, implying that the shock effect would have little influence on the plateau stresses. In each figure, the two tests are being compared based on their velocities relative to their respective critical velocities. Their relative absolute velocities are not being compared.

In both figures, the Cymat test shows significantly greater strain-hardening in the plateau region than the corresponding ALPORAS test.

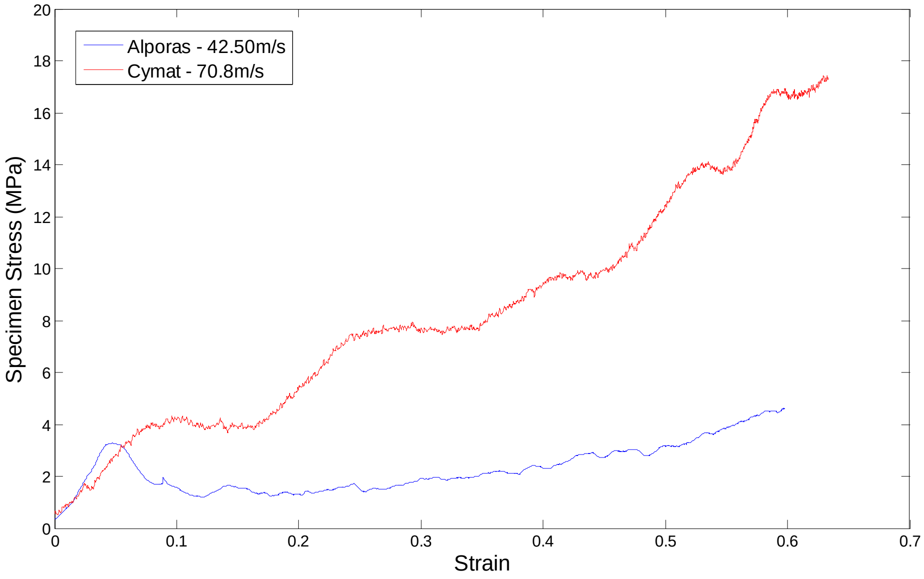

Figure 91: Comparison of strain hardening for ALPORAS and Cymat specimens, at sub-critical velocities. Forward direction.

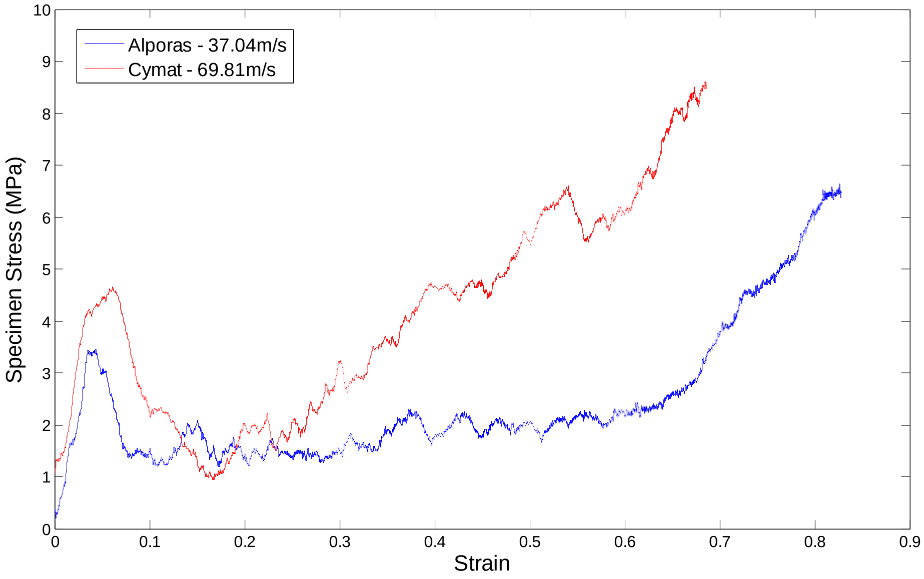

Figure 92: Comparison of strain hardening for ALPORAS and Cymat specimens, at sub-critical velocities. Reverse direction.

7.3 Effect of Cymat non-homogeneity

Figure 93 demonstrates the dependence of the response of Cymat direct impact foam specimens on the specimen orientation. Specimen C18R was placed with the dense side of the foam facing the output tube, and specimen C19R with the dense side facing the striker. The tests were conducted at similar velocities.

The significantly higher initial peak stress of test C18R is due to the higher density region of foam striking the output tube end cap.

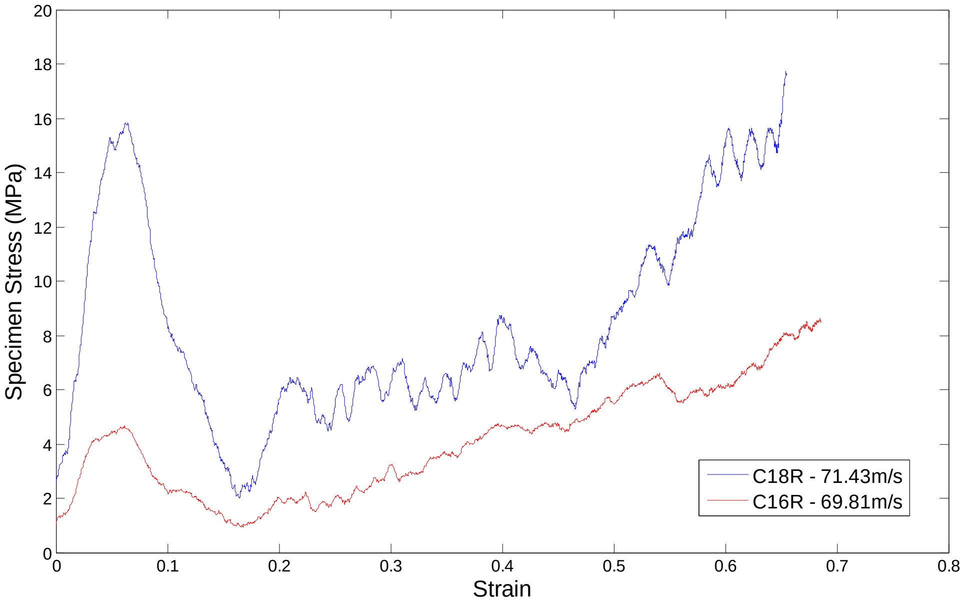

Figure 93: Dependence of Cymat foam response on specimen orientation. Reverse direction.

7.4 Shock development under dynamic testing

7.4.1 Shock development in ALPORAS

Figure 94 compares the theoretical shock stress with the experimental dynamic plastic collapse stress (also called the initial peak stress), and experimental dynamic plateau stress, for all ALPORAS cylinders in the reverse direction. The average quasi-static plateau stress, along with the upper and lower bounds of scatter, are shown as solid and dashed lines respectively. A power law trend is fitted to the experimental dynamic plateau stress data. All stresses are divided by the theoretical quasi-static plateau stress, according to equation 14.

A criterion for the velocity at which the dynamic strength can said to be enhanced is the velocity at which the plateau stress exceeds the upper limit of the scatter of the quasi-static plateau stress for the material (21). The velocity at which this occurs in Figure 94 is approximately 40m/s. Assuming that shock is the dominant source of strength enhancement, this is the critical velocity for ALPORAS.

According to the r-p-p-l model, the plastic collapse stress is the same as the plateau stress. In practice the plastic collapse stress is an initial ‘spike’ in the stress that, unlike the quasi-static stress-strain response of ALPORAS, is higher than the plateau stress. In Figure 94, the shock theory slightly over-predicts the actual dynamic plateau stress, and under-predicts the initial peak stress.

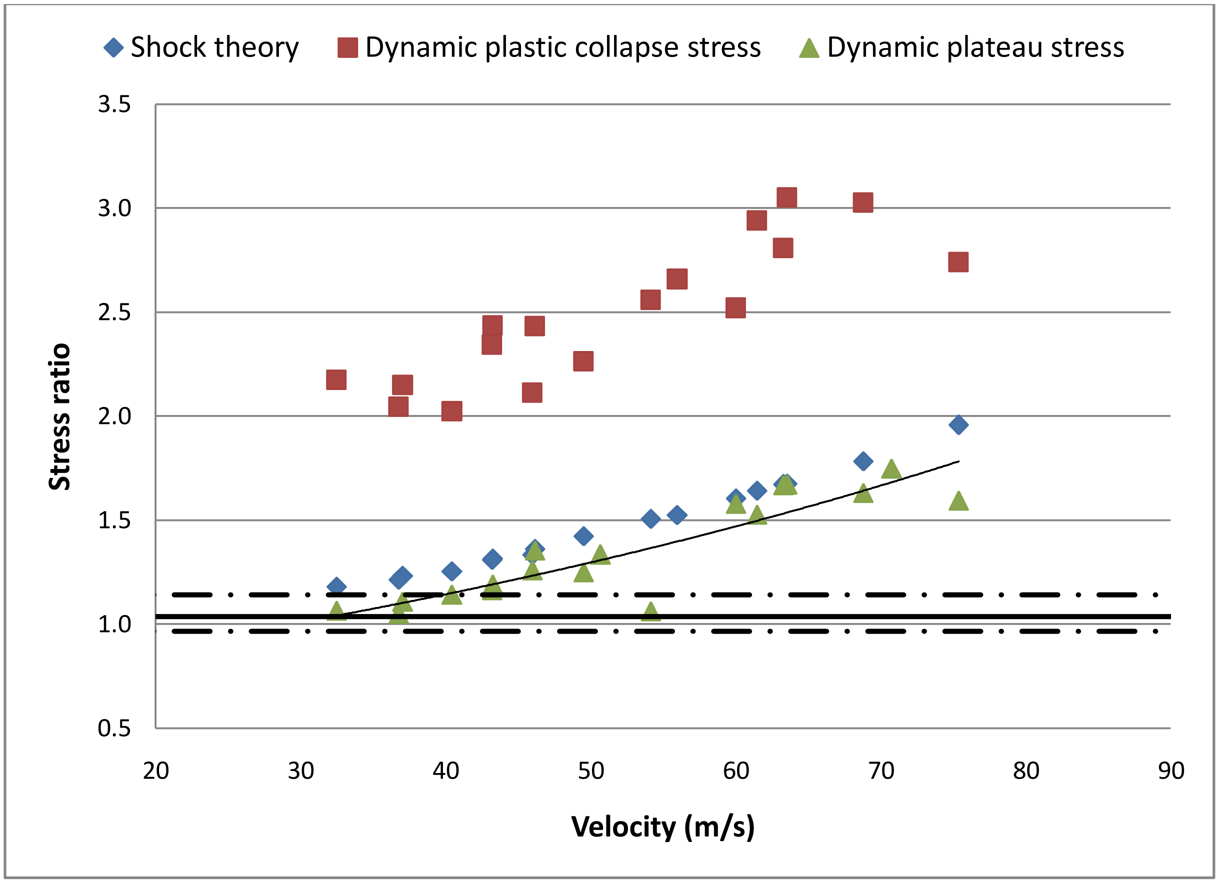

Figure 94: Dynamic plastic collapse stress, plateau stress and theoretical shock stress versus impact velocity for all ALPORAS cylinders, reverse direction.

7.4.2 Discussion of Taylor test results

A plot of crush distance versus impact velocity for the Taylor test specimens is shown in Figure 95. As expected, the crush distance increases as the impact velocity increases. Some scatter due to the varying density of the specimens can be expected.

The initial peak of the characteristic curve shown in Figure 53 is dependent on the initial velocity. The initial peak stress ratio (the initial peak stress divided by the theoretical plateau stress) versus initial impact velocity for the Taylor test series is shown in Figure 97.

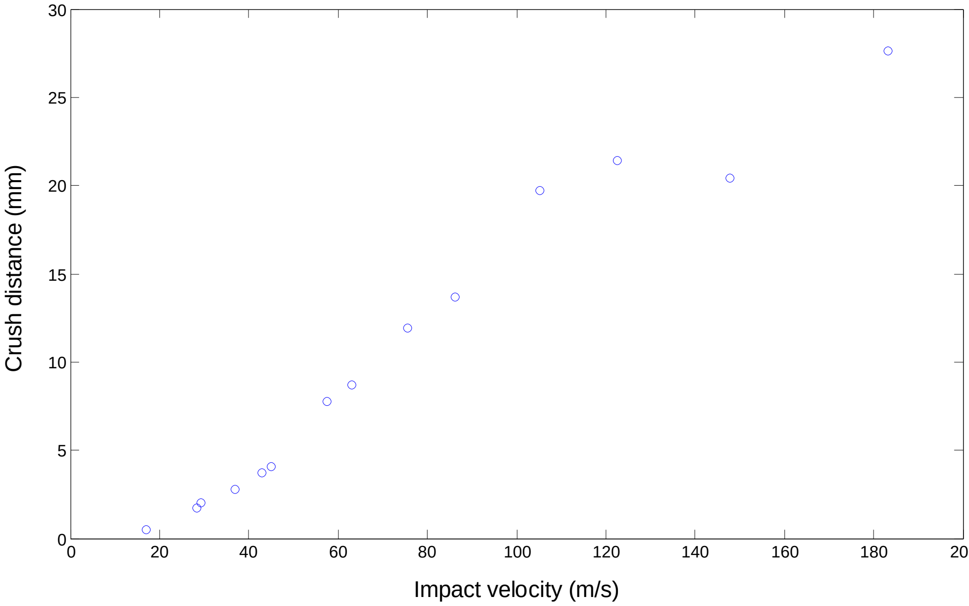

Figure 95: Crush distance versus impact velocity for all Taylor tests

In Figure 96, the progressively larger crush distance with increase in velocity can be seen.

A30T	A27T	A31T	A32T	A28T	A33T	A29T
63.0m/s	75.6m/s	86.2m/s	105.1m/s	122.5m/s	147.9m/s	183.3m/s

Figure 96: Progressive crush distances of Taylor test specimens

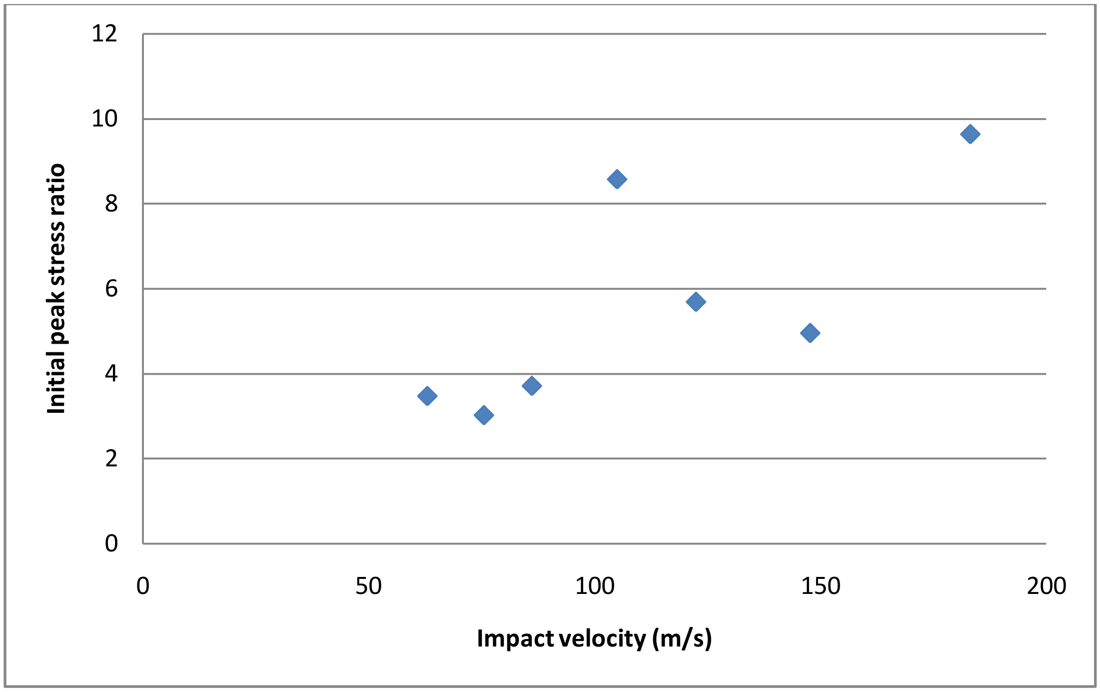

Figure 97: Initial peak stress ratio versus impact velocity for Taylor tests

7.4.3 Shock development in Cymat

Figure 98 demonstrates how the shock behaviour of a material that exhibits significant strain hardening may not be well described by the r-p-p-l model. The figure shows the stress-strain curve of an ideal r-p-p-l material, as well as a function *g(ε)* that approximates the stress-strain curve of a strain-hardening cellular material.

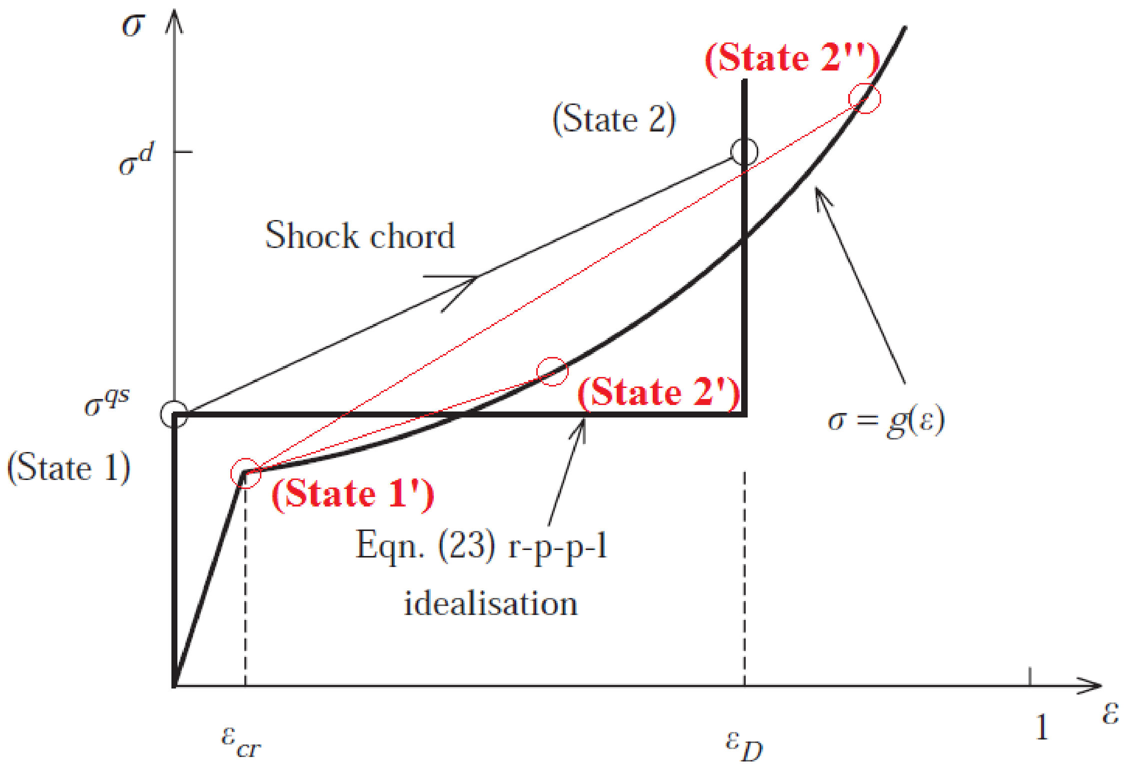

Figure 98: Limitations of r-p-p-l model for a strain-hardening material. Modified from (21)

Theoretically, under shock, the properties of the material experience a sudden change as the shock front passes (a jump from State 1 to State 2). In an ideally r-p-p-l material, this will be a jump (shown in black) from the quasi-static elastic limit to the densification strain. In reality, however, it will be a jump from the quasi-static elastic limit (State 1'), which is less than the plateau stress. The state to which the material properties jump will depend on the impact velocity (63). At a lower impact velocity, they will jump to State 2', while at a higher impact velocity they would jump to State 2'', both shown in red. As the there is no clear densification strain on the curve g(ε), there will be a gradual increase in the density that the material jumps to as the velocity increases. There will not be a specific critical velocity at which shock will start to occur. Under direct impact and blast testing, it is therefore more difficult to initiate shock development in a material that exhibits significant strain-hardening, such as Cymat, than it is with a material such as ALPORAS.

7.5 Shock development under blast loading

To understand whether the blast test specimens experience shock during compaction, the face plate velocities need to be estimated. This can be done using the momentum (impulse) transferred to the pendulum, which is the same as the momentum transferred to the face plate. This will give the theoretical maximum face plate velocity. In practice the foam specimen will prevent the face plate from reaching this maximum velocity. The theoretical maximum velocities and specific impulses for all blast tests are shown in Table 12 (ALPORAS) and Table 13.

Table 12: Theoretical maximum face plate velocities and specific impulses for all ALPORAS blast tests

Specimen	Bonding	Charge mass (g)	Face Plate Velocity (m/s)	Specific Impulse	Percentage crush
A17	-	3	8.3	570	9.1
A8	-	4	11.8	812	16.4
A9	-	5	13.9	956	25.6
A10	-	6	16.7	1152	39.4
A1	-	7	17.4	1195	42.0
A2	-	7	17.6	1211	38.5
A11	-	8	20.8	1435	58.1
A12	-	9	24.6	1694	57.8
A13	-	10	27.7	1904	69.0
A14	-	11	27.6	1902	71.4

Table 12: (Continued)

Specimen	Bonding	Charge mass (g)	Face Plate Velocity (m/s)	Specific Impulse	Percentage crush
A15	-	12	30.0	2069	73.0
A4	Xiro	14	29.3	2020	-
A3	Xiro	7	14.9	1024	28.4
A6	Xiro	7	16.6	1146	38.7
A7	Xiro	7	18.1	1246	35.9
A5	Xiro	11	24.1	1660	63.5

Table 13: Theoretical maximum face plate velocities and specific impulses for all Cymat blast tests

Specimen	Bonding	Charge mass (g)	Face Plate Velocity (m/s)	Specific Impulse	Percentage crush
C12	-	8	22.5	1546	19.5
C13	-	9	25.0	1723	20.8
C14	-	10	24.5	1685	27.6
C15	-	11	26.0	1789	16.1
C2	-	12	26.8	1845	27.1
C16	-	13	33.3	2293	24.6
C7	-	14	29.6	2037	31.4
C17	-	15	36.8	2533	34.2
C8	-	16	34.3	2359	31.6
C18	-	17	44.6	3070	36.0
C1	-	18	39.2	2700	44.9

Table 13: (Continued)

Specimen	Bonding	Charge mass (g)	Face Plate Velocity (m/s)	Specific Impulse	Percentage crush
C19	-	19	45.2	3111	38.4
C9	-	20	38.7	2663	33.5
C10	-	20	39.7	2734	33.2
C20	-	21	46.9	3226	44.4
C6	-	22	41.4	2854	35.0
C21	-	23	56.4	3883	45.0
C11	-	26	57.7	3971	56.5
C5	Xiro	7	17.0	1169	7.0
C3	Xiro	14	31.4	2165	-
C4	Xiro	18	35.3	2431	-

The theoretical maximum face plate velocities are all below the critical velocity required to induce shock (46m/s for Alporas, and 108 m/s for Cymat, according to the literature). The specific impulse (impulse per unit area) can be calculated for each blast test, and compared to the specific momentum for each forward direct impact test (as the face plates are initially stationary, the impulse transferred to the plates equals the momentum of the plate). The direct impact tests in the forward direction, as opposed to the reverse direction, most closely resemble the loading condition of the blast test. The specific momentum in the direct impact tests is hereafter referred to as the specific impulse. In order to account for the effect of foam density on the crush distance, the specific impulse for each test is multiplied by the theoretical plateau stress of the test specimen.

When comparing the specific impulses of the blast test series and the direct impact test series, there are four tests (three Cymat and one ALPORAS) from the blast test series that have comparable specific impulses to tests from the direct impact series. These four pairs of tests are shown in Table 14, and Figure 100.

Table 14: Comparable blast and direct impact tests, based on specific impulse

Blast test				Direct impact test			
Test	Specific impulse (Pa.s)	Density (%)	Percentage crush	Test	Specific impulse (Pa.s)	Density (%)	Percentage crush
A13	1904	7.3	69	A43F	1958	8.5	58.8
C7	2037	16.7	31.4	C19F	2077	17.5	17.2
C1	2700	15.7	44.9	C11F	2703	18.5	32
C9	2663	18.5	33.5	C13F	2667	17.2	33.2

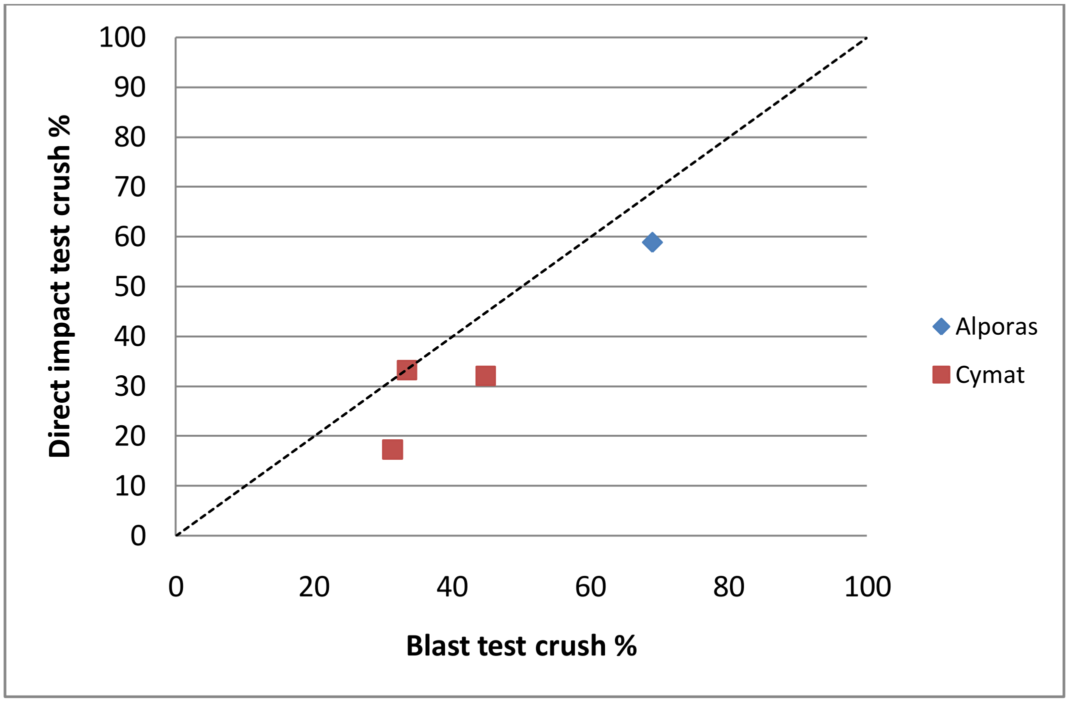

Figure 99: Crush distances of comparable direct impact and blast tests

In order to account for the effect of varying density on crush distance, the data can be normalised by multiplying the crush distance by the theoretical quasi-static plateau stress. The data in Figure 99 is re-plotted in Figure 100 with the normalised crush distances.

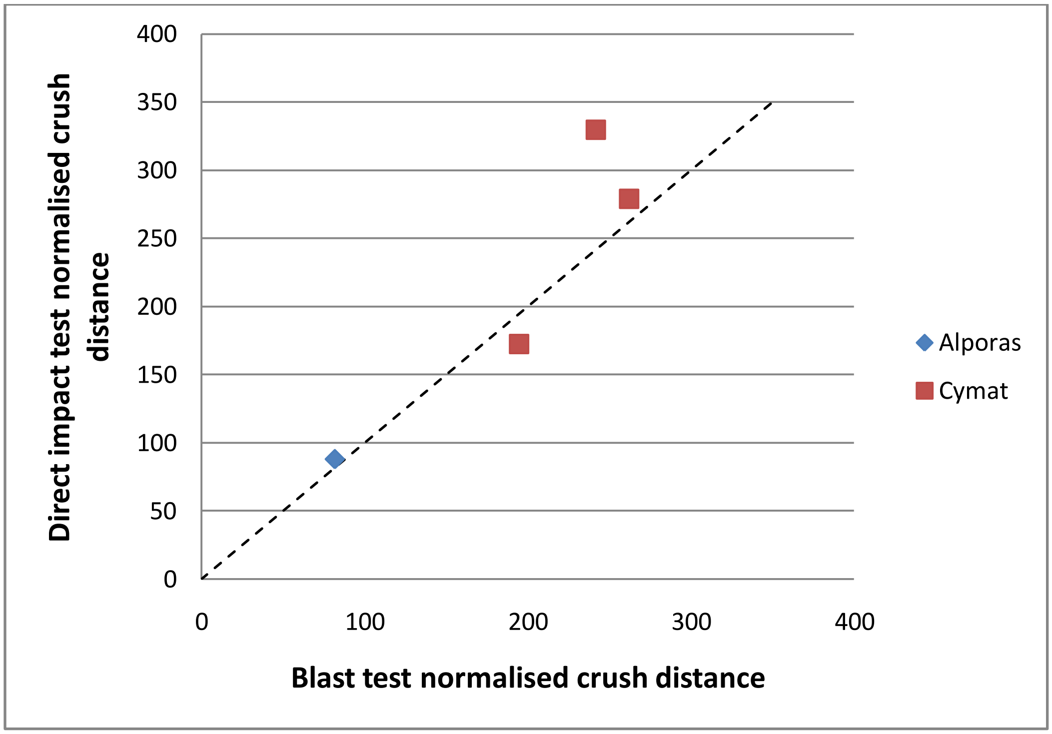

Figure 100: Comparison of crush distance for comparable blast and direct impact tests (normalised)

Figure 100 shows good correlation between the normalised direct impact crush distance and normalised blast test crush distance.

The ranges of specific impulses for all ALPORAS blast tests and forward cylinder tests are shown in Figure 101 and Figure 102. Figure 101 shows percentage crush distance versus specific impulse, and Figure 102 shows normalised percentage crush distance versus specific impulse.

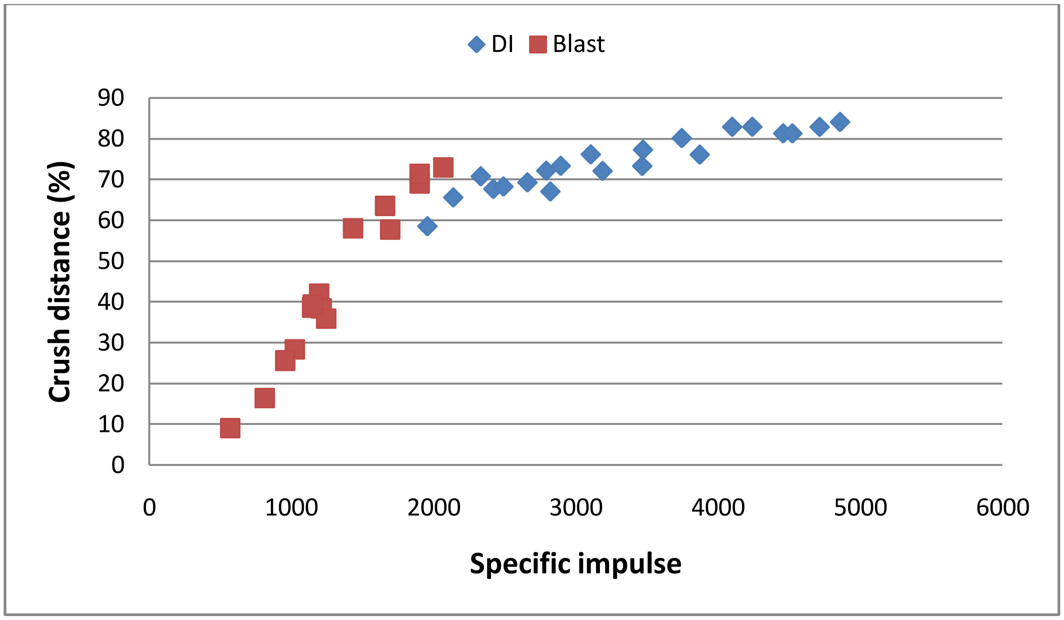

Figure 101: Percentage crush versus specific impulse for all blast test and ALPORAS cylinder forward direct impact tests

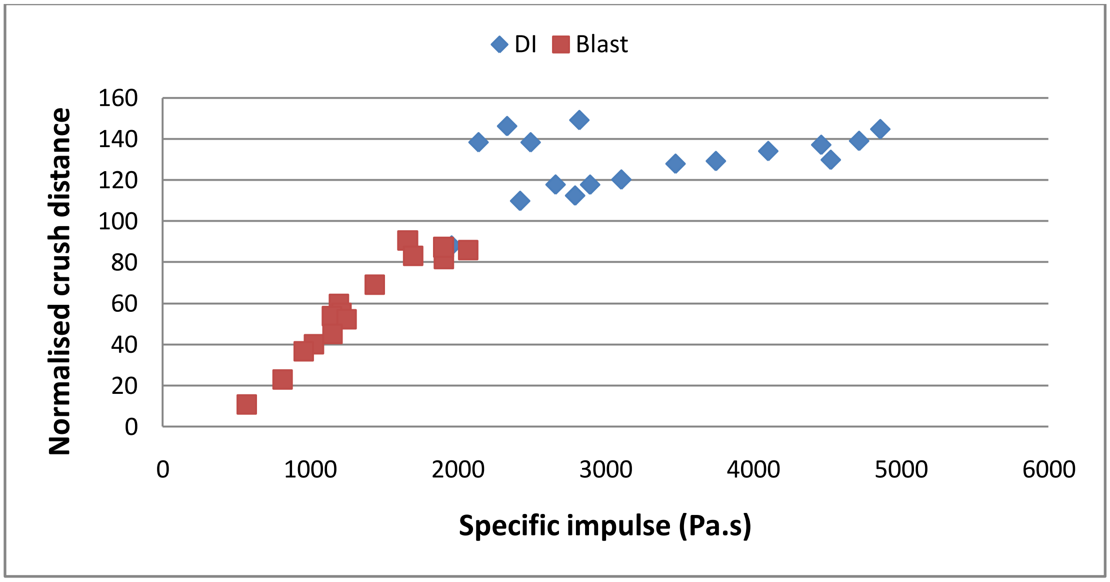

Figure 102: Percentage crush distance (normalised) versus specific impulse for all ALPORAS direct impact and blast tests

Figure 102 shows a smooth transition from the blast test series to the direct impact test series. There are four data points from the direct impact series that show an unusually high crush distance for the corresponding specific impulse. A possible explanation for this is that these specimens were cut from a region of the foam sheet near the edge that had different material properties than the rest of the sheet. The material in this region has a different colour and more irregular cell structure. In Figure 103, this differing cell structure is noticeable towards the left and top sides of the panel.

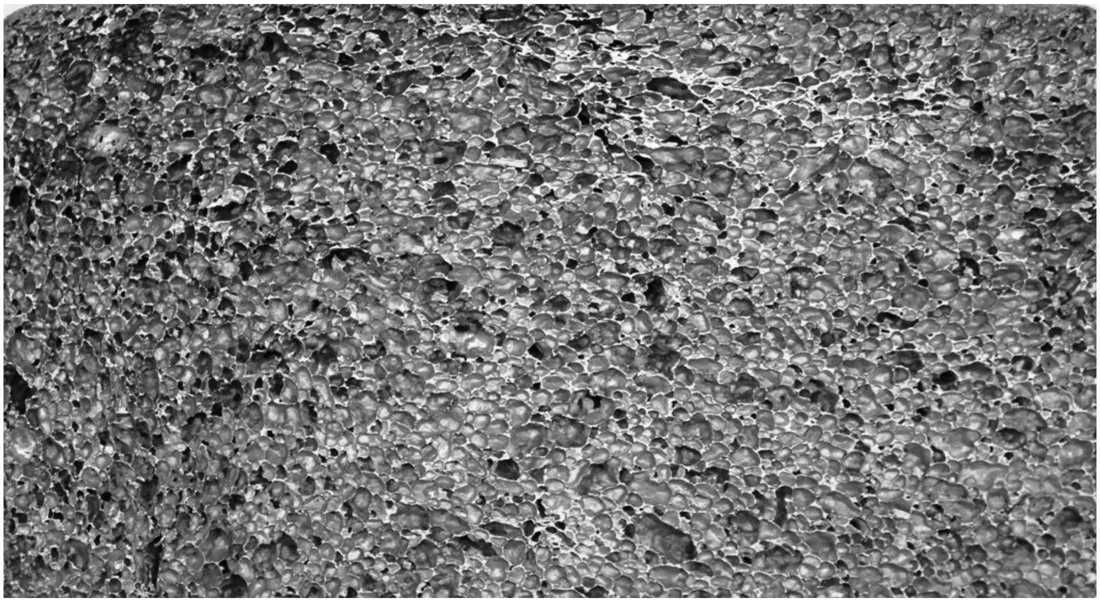

Figure 103: Corner of ALPORAS panel, showing differing cell structure toward top/left edges of panel

It is clear from Figure 102 that the specific impulse of the blast tests needs to be increased in order to induce shock under blast loading by generating a higher face plate velocity (the specific impulse for the blast test series does not extend into the region needed to induce shock, which the direct impact series does) . In order to do this, the mass (i.e. thickness) of the face plate needs to be reduced, or the charge mass needs to be increased. Both of these would result in face plate deformation. Langdon, et al. (54)

noted significant face plate deformation in 2mm thick face plates under blast loading. This would complicate the analysis of the blast tests, as a significant amount of the energy of the blast would be absorbed by the deformation of the face plate (and not by crushing of the foam). The loading of the specimen could no longer be assumed to be uniform uni-axial loading, and comparison of the blast and direct impact tests by means of comparing the specific impulses would not useful.

The same process is followed for comparing the Cymat direct impact and blast tests. Figure 104 and Figure 105 show percentage crush and normalised crush distance respectively versus specific impulse for all Cymat forward cylinder direct impact and blast tests.

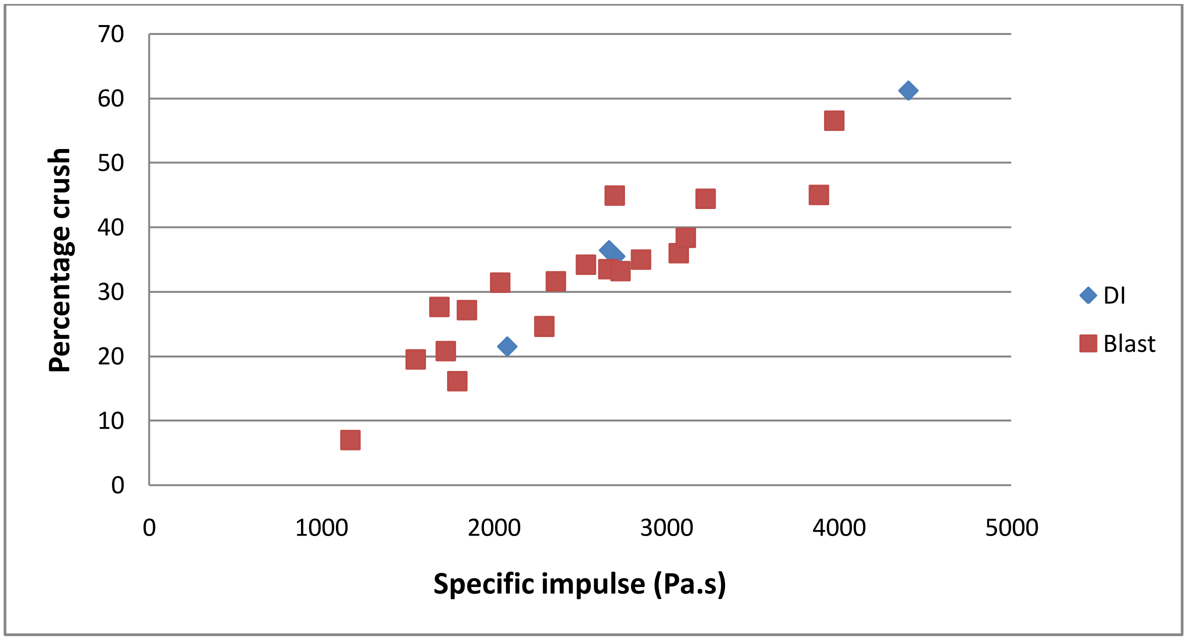

Figure 104: Percentage crush versus specific impulse for all Cymat direct impact and blast tests

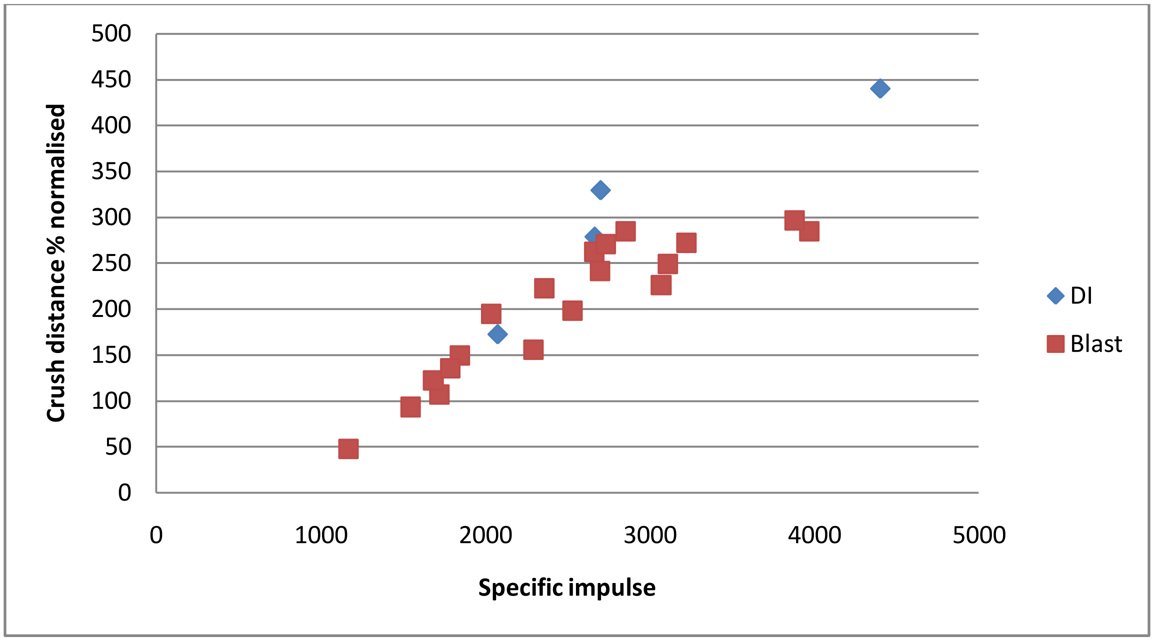

Figure 105: Percentage crush (normalised) versus specific impulse for all forward cylinder Cymat DI tests and Cymat blast tests

8 CONCLUSIONS

Failure mechanisms

Under quasi-static compression, ALPORAS and Cymat showed different failure mechanisms, with the cells undergoing ductile and brittle collapse respectively. ALPORAS exhibited the typical stress-strain curve for a cellular material, with a relatively constant stress in the plateau region. Cymat exhibited considerable strain hardening in the plateau region, and no definitive densification region. This affects the analysis of the material behaviour when using the rigid-perfectly-plastic-elastic model, as the model assumes a constant plateau stress, equal to the plastic collapse stress, and a definite densification strain.

Due to the different production processes, ALPORAS was a more homogeneous material, and showed a more consistent response than Cymat. Cymat specimens showed significant through-thickness variation in density and cell morphology.

The plateau stresses of both materials varied with density according to power law fits, similar to those found in previous work. The densification strains for both materials were approximately constant over the density ranges tested, in contrast to the findings in the literature.

Effect of velocity on dynamic compressive response – forward direction

Under direct impact, in the forward direction (with the stationary specimen attached to the output bar and impacted with the striker), neither material showed an increasing trend in plastic collapse stress or plateau stress as the velocity was increased. The strength response of the material measured in the forward direction is therefore independent of impact velocity, in the velocity range over which the tests were conducted.

Effect of velocity on dynamic compressive response – reverse direction

For both materials, the initial plastic collapse and plateau stresses increased with increasing impact velocity. The dynamic plateau stress of ALPORAS was well predicted by a shock approximation; therefore the strength enhancement is attributed to shock. The critical velocity (velocity at which strength enhancement due to shock becomes significant) for ALPORAS was determined to be approximately 42m/s. This is comparable to the figure in the literature of 46m/s (28).

The Cymat specimens were not tested at a high enough impact velocity to induce shock, nor to compress them well into the densification region. The response of Cymat in the reverse direction was highly dependent on the specimen orientation, due to the through-thickness variation in specimen density. The denser side of the material resulted in a higher plastic collapse stress when impacting the output bar than the less dense side of a material with the same overall density. No critical velocity was determined for Cymat.

Shock development under Taylor cylinder testing

The Taylor test specimens showed evident of a strain discontinuity that supports the conclusion that shock was induced in the reverse direct impact specimens. Taylor test specimens clearly showed a densified region distinct from an undensified region that showed little or no permanent deformation.

Effect of charge mass on blast response

Increasing the charge mass produced greater percentage crush in both the ALPORAS and Cymat cladding specimens. No evidence of shock was apparent in the post-test inspection. The maximum theoretical initial face plate velocities ranged from 8.3 and 30.0m/s for ALPORAS, and 17.0 and 57.7m/s for Cymat, which are below the critical velocity thought to produce shock. The Cymat specimens showed non-uniform deformation; however this was due to the non-uniform density of the foam, not the presence of shock.

In order to induce shock, the charge mass would need to be increased, which may lead to unwanted face plate deformation. Using a thicker face plate for a given charge mass would result in a lower face plate velocity.

Methods of comparing direct impact and blast loading results

In order to compare the direct impact and blast tests, the specific impulses (impulse per unit specimen area) for the blast test series and forward direct impact series for both materials were calculated, from the recorded impulse, and projectile mass and velocity respectively. The forward direct impact tests, as opposed to the reverse, were equivalent to the blast test loading condition. The specific impulse range for the ALPORAS blast series was lower than that for the direct impact series, with the exception of one comparable pair of tests which had a similar specific impulse. The Cymat series had three comparable points.

The crush distances (normalised, to account for the effect of density on crush distance) of the four comparable pairs of tests were compared. They showed good correlation, i.e. a blast specimen subject to a given impulse will experience a similar crush distance to a direct impact specimen of the same density subject to the same impulse.

9 RECOMMENDATIONS

Based on this investigation, and the results and conclusions thereof, the following recommendations are made:

- The direct impact experimental technique must be verified, by comparison to tests on ALPORAS and Cymat using viscoelastic and solid metal bars, as opposed to a hollow tube. Any effect of the end cap or tube on the material response should be accounted for.
- The behaviour of a foam specimen mounted on an end cap and tube should be modelled numerically, as this could give greater insight into the material response.
- The Reflective Object Sensor should be refined to provide a more reliable and consistent displacement measurement tool. Ideally one sensor should be used.
- The output bar should be instrumented with two strain gauge stations, each with a different bridge voltage. This would allow the plateau region and the densification region of the stress-strain curve to be recorded without the signal ‘clipping’.
- Validation of analytical models with experimental data should be done with materials that closely match the assumptions of the analytical model.
- A technique should be determined to initiate shock in aluminium foam panels under blast loading.

10 REFERENCES

1. **Gibson LJ, Ashby MF.** *Cellular solids: Structure and properties, 2nd ed.* Oxford : s.n., 1997. 0521 49560.

2. Alporas (eng). *shinko-wire.* [Online] [Cited: 10 May 2011.] http://www.shink-wire.co.jp/product/alporas-eng.pdf.

3. Types of materials for metalfoam ceilings. *AlCarbon.* [Online] [Cited: 25 May 2011.] http://www.alcarbon.de/jcms/content/view/72/1/lang,en/.

4. Stabilised aluminium foam. *Universal Metaltek.* [Online] [Cited: 25 May 2011.] http://www.universalmetaltek.com/afp.htm.

5. **Youssef S, Maire E, Gaertner R.** *Finite element modelling of the actual structure of cellular materials determined by X-ray tomography.* Acta Materia., Vol. 53, pp. 719-730. 2005.

6. Fraunhofer USA centre, Delaware. *Fraunhofer IFAM.* [Online] [Cited: 3 May 2011.] http://www.ifam.fraunhofer.de/jahresberichte/jb01/d_jb01_delaware.html.

7. SmartMetal features. *Cymat.* [Online] [Cited: 3 May 2011.] www.cymat.com.

8. Periodic cellular materials: Topology. [Online] [Cited: 29 April 2011.] http://www.ipm.virginia.edu/newres/pcm.topo/.

9. **Lopatnikov SL, Gama BA, Hague J, Krauthauser C, Gillespie JW, Guden M, Hall IW.** *Dynamics of metal foam deformation during Taylor cylinder - Hopkinson bar experiment.* Compos. Struct., Vol. 61, pp. 61-71. 2003.

10. **Yu H, Guo Z, Li B, Yao G, Luo H, Liu Y.** *Research into the effect of cell diameter of aluminium foam on its compressive and energy absorption properties.* Materi. Sci. and Eng. A, Vols. 454-455, pp. 454-455. 2007.

11. *Shinko Wire Company, Ltd.* [Online] [Cited: 3 May 2011.] http://www.shinko-wire.co.jp/product/alporas.html.

12. Cymat. [Online] [Cited: 3 May 2011.] www.cymat.com.

13. Fraunehofer IFAM. [Online] 3 May 2011. http://www.ifam.fraunhofer.de/index.php?seite=&lang=en.

14. Alulight International Gmbh. [Online] [Cited: 3 May 2011.] http://www.alulight.com/index2.html.

15. Duocel Aluminium Foam. *ERG Materials and Aerospace Corporation.* [Online] [Cited: 3 May 2011.] http://www.ergaerospace.com/foamproperties/aluminumproperties.htm.

16. **Banhart, J.** *Manufacture, characterisation and application of cellular metals and metal foams.* Progress in Materi. Sci., Vol. 46, pp. 559-632. 2001.

17. Aluminum foam technology applied to automative design. *Cymat.* [Online] [Cited: 3 May 2011.] http://www.cymat.com/PDFs/Cymat%20SAF%20Automotive%20Applications.pdf.

18. **Ruan D, Lu G, Chen FL, Siores E.** *Compressive behaviour of aluminium foams at low and medium strain rates.* Compos. struct., Vol. 57, pp. 331-336. 2002.

19. **Idris MI, Vodenitcharova T, Hoffman M.** *Mechanical behaviour and energy absorption of closed-cell aluminium panels in uniaxial compression.* Materi. Sci. and Eng. A, Vol. 517, pp. 37-45. 2009.

20. **Shen J, Lu G, Ruan D.***Compressive behaviour of closed-cell aluminium foams at high strain rates.* Compos. B: Eng., Vol. 41, pp. 678-685. 2010.

21. **Tan PJ, Reid SR, Harrigan JJ, Zou Z, Li S.** *Dynamic compressive strength properties of aluminium foams. Pt I - experimental data and observations.* J. Mech. Phys. Solids, Vol. 53, pp. 2174-2205. 2005.

22. **Theobald MD, Langdon GS, Nurick GN, Pillay S, Heyns A, Merrett RP.** *Inelastic response of undonded metallic foam and honeycomb core sandwich panels to blast loading.* Compos. Struct., Vol. 92, pp. 2465-2475. 2010.

23. **B, Hopkinson.** *A method of measuring the pressure produced in the detonation of high explosives or by the impact of bullets.* Phil. Trans. Royal Soc. London: Series A, Vol. 213, pp. 437-456. 1914.

24. **H, Kolsky.** *An investigation of the mechanical properties of materials at very high rates of loading*. Proc. Phys. Soc. B, Vol. 62, pp. 679-700. 1949.

25. **JM, Davies.** *A critical study of the Hopkinson pressure bar.* Phil. Trans. Royal Soc. London, Vol. 240, pp. 375-457. 1948.

26. **GT, Gray III.** Classic split-Hopkinson bar pressure testing. *ASM Handbook.* 2000. Vols. 8, Mechanical Testing and Evaluation, pp. 462-476.

27. **Reid SR, Peng C.** *Dynamic uniaxial crushing of wood.* Int. J. Impact Eng., Vol. 19, pp. 531-570. 1997.

28. **Elnasri I, Pattofatto S, Zhao H, Tsitsiris H, Hild F, Girard Y.** *Shock enhancement of cellular structures under impact loading: Part I Experiments.* J. Mech. Phys. Solids., Vol. 55. pp. 2652-2671. 2007.

29. **Lee S, Barthelat F, Moldovan N, Espinosa HD, Wadley HNG.** *Deformation rate effects on failure modes of open-cell Al foams and textile materials.* Int. J. Solids and Struct., Vol. 43, pp. 53-73. 2006.

30. **Zhao H, Gary G, Klepaczko JR.** *On the use of a viscoelastic split Hopkinson pressure bar.* Int. J. Impact Eng., Vol. 19, pp. 319-330. 1996.

31. Micro-strain measuring gauges. *www.kyowa.com.* [Online] [Cited: 24 May 2011.] http://www.kyowa-ei.co.jp/english/products/gages/pdf/ksp.pdf.

32. **Zhao H, Elnasri I, Abdennadher S.** *An experimental study under impact loading of metallic cellular materials.* Int. J. Materi. Sci., Vol. 47, pp. 757-774. 2005.

33. **L, Pochammer.** *Uber die fortpflanzungsgeschwindigkeiten kleiner schwingungen in einem unbergrenzten isotropen kreiszylinder.* J. fiir die Reine und Angewande Mathematic, Vol. 81, pp. 324-336. 1876.

34. **C, Chree.** *The equations of an isotropic elastic solid in polar and cylindrical co-ords, their solutions and applications.* Cambridge Phil. Soc. Trans, Vol. 14, pp. 250-369. 1889.

35. **GA, Coquin.** *Attenuation of guided waves in isotropic viscoelastic materials.* J. Ac. Soc. Am., Vol. 36(6), pp. 1074-1080. 1964.

36. **Zhao H, Gary G.** *A three dimensional analytical solution of the wave propagation in an infinite linear viscoelastic cylindrical bar. Application to experimental techniques.* J. Mech. Phys. Solids, Vol. 43, pp. 1335-1348. 1995.

37. **Campbell JD, Fergusson WG.** *The temperature and strain-rate dependence of the shear strength of mild steel.* Philosphical Magazine, Vol. 21, pp. 63-82. 1970.

38. **JR, Klepaczko.** *An experimental technique for shear testing at high and very high strain rates. The case of mild steel.* Int. J. Imact Eng, Vol. 15, pp. 25-39. 1994.

39. **Chen W, Zhang B, Forrestal MJ.***A split Hopkinson bar technique for low-impedence materials.* Exp. Mech., Vol. 39(2), pp. 81-85. 1999.

40. **Chen W, Lu F, Cheng M.** *Tension and compression tests on two polymers under quasi-static and dynamic loading.* Polymer Testing, Vol. 21, pp. 113-121. 2002.

41. **Segreti M, Rusinek A, Klepaczko JR.** *Experimental study on puncture of PMMA at low and high velocities, effect on the failure mode.* Polymer Testing, Vol. 23, pp. 703-718. 2004.

42. **Rusinek A, Rodriguez-Martinez JA, Zaera R, Klepaczko JR, Arias A, Sauvelet C.** *Experimental and numerical study on the perforation process of mild steel sheets subjected to perpendicular impact by hemispherical projectiles.* Int. J. of Impact Eng., Vol. 36, pp. 565-587. 2009.

43. **Deshpande VS, Fleck NA.** *High strain rate compressive behaviour of aluminium alloy foams.* Int. J. Impact Eng., Vol. 24, pp. 277-298. 2000.

44. **Lankford J, Dannemann KA.** *Strain rate effects in porous materials.* Proc. Sympo. Materi. Res. Soc., Vol. 521. 1998.

45. **Yu JL, Wang X, Wei ZG, Wang EH** *Deformation and failure mechanism of dynamically loaded sandwich beams with aluminum-foam core.* Int. J. of Impact Eng., Vol. 28(3), pp. 331-347. 2003.

46. **Tan PJ, Reid SR, Harrigan JJ, Zou Z, Li S.** *Dynamic compressive strength properties of aluminium foams. Pt II - 'shock' theory and comparison with experimental data and numerical models.* J. Mech. Phys. Solids. Vol. 53, pp. 2206-2230. 2005.

47. **Radford DD, Deshpande VS, Fleck NA.** *The use of metal foam projectiles to simulate shock loading on a structure.* Int. J. Impact Eng., Vol. 31, pp. 1152-1171. 2005.

48. **Radford DD, McShane GJ, Deshpande VS, Fleck NA.** *The response of clamped sandwich panel with metallic foam cores to simulated blast loading.* Int. J. Solids Struct.. Article in press. 2005.

49. **Institute, The Steel Construction.** *The effects of simplification of the explosion pressure-time history.* British Gas Research and Technology. Technical report. 1992.

50. **Yen CF, Skaggs R, Cheeseman BA.** *Modeling of shock mitigation sandwich structures for blast protection.* 3rd First Int. Conf. Struct. Stab. Dyn. 2005.

51. **Guruprasad S, Mukherjee A.** *Layered sacrificial claddings under blast loading part II - experimental studies.* Int. J. Impact Eng., Vol. 24(9), pp. 975-984. 2000.

52. **Hanssen AG, Enstock L, Langseth M.** *Close-range blast loading of aluminium panels.* Int. J. Impact Eng., Vol. 27, pp. 593-618. 2002.

53. **Li QM, Meng H.** *Attenuation or enhancement - a one-dimensional analysis on shock transmission in the solid phase of a cellular material.* Int. J. Impact Eng., Vol. 27, pp. 1049-1065. 2002.

54. **Langdon GS, Karagiozova D, Theobald MD, Nurick GN, Lu G, Merrett RP.** *Fracture of aluminium foam core sacrificial cladding subjected to air-blast loading.* Int. J. Impact Eng., Vol. 37, pp. 638-651. 2010.

55. **Ashby MF, Evans AG, Fleck NA, Gibson LJ, Hutchinson JW, Wadley HNG.** *Metal foams: A design guide.* s.l. : Warrendale: Butterworth-Heinemann, 2000.

56. **Lehmus D, Banhart J.** *Properties of heat-treated aluminium foams.* Materi. Sci. Eng. A, Vol. A349, pp. 98-110. 2002.

57. **Shen J, Lu G, Ruan D.** *Compressive behaviour of closed-cell aluminium foams at high strain rates.* Compos. Pt B Eng., Vol. 41, pp. 678-685. 2010.

58. Tubes & Pipes. *GS Hydro*. [Online] [Cited 25 May 2011.] http://www.gshydro.com/GSH/gshweb.nsf/0/E28EC47C06E82D69C225781C00496818/$FILE/03_Pipes_LOW_rev1_2011.pdf

59. Private communication, Dr M Theobald, February 2010.

60. Phototransistor reflective object sensors. *DatasheetDir.* [Online] [Cited: 25 May 2011.] http://www.datasheetdir.com/QRB1134+Phototransistors.

61. **MD, Theobald.** *Blast loading of sandwich panels with thin-walled tube cores.* PhD Thesis. 2007.

62. *Deformation of thin plates subject to blast loading - a review.* **Nurick GN, Martin JM.** Int. J. Impact Eng., Vol. 8, pp. 171-186. 1989.

63. **Karagiazova, Prof. Dora.** 15 April 2011. Private communication.

APPENDIX A: QUASI-STATIC STRESS STRAIN CURVES

A-1: ALPORAS

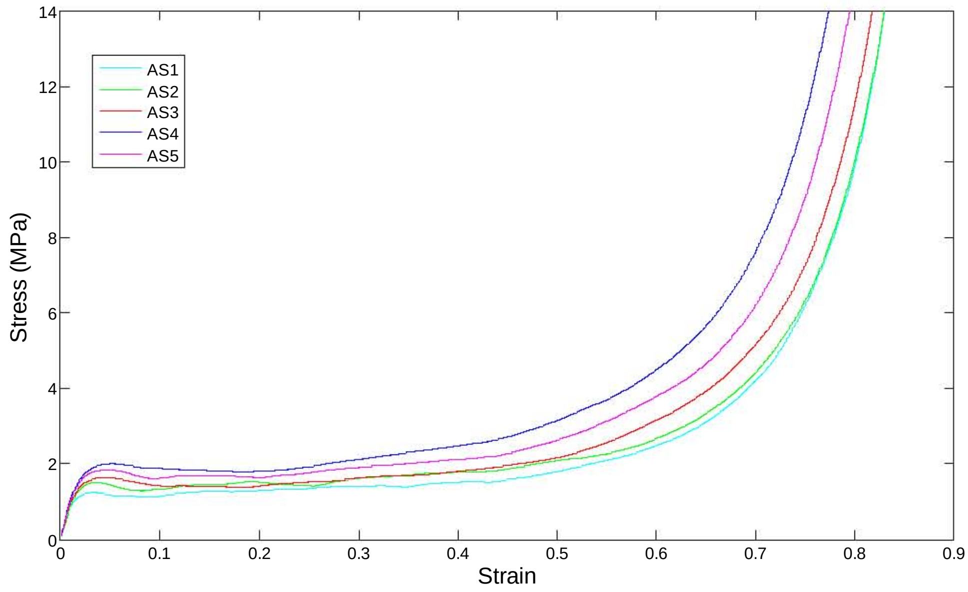

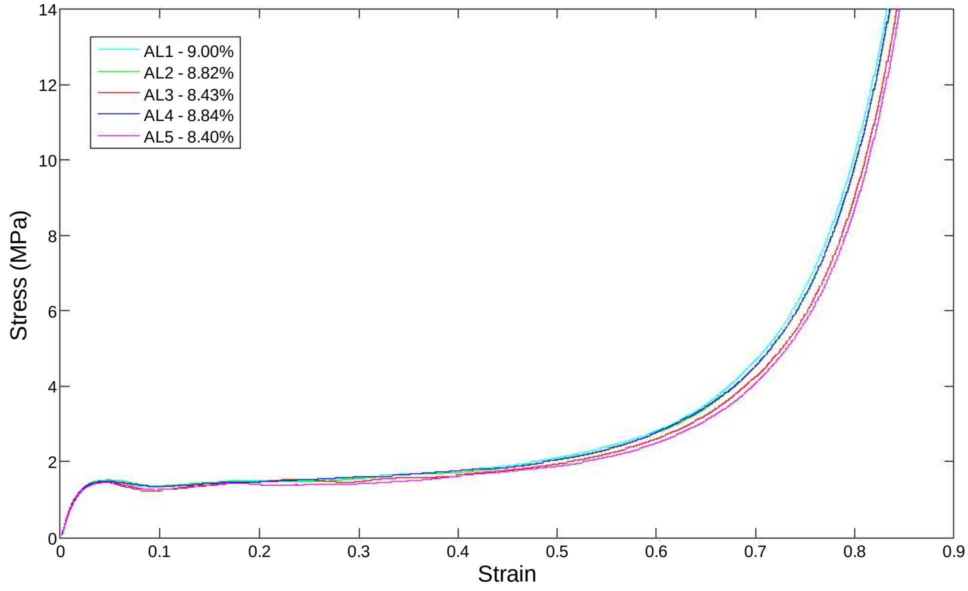

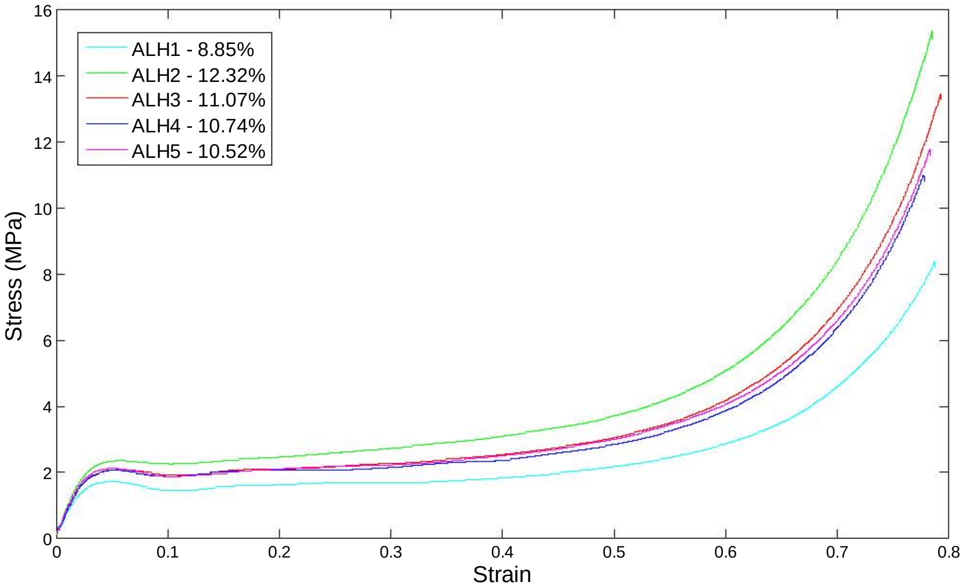
ALH1 - 8.85%
ALH2 - 12.32%
ALH3 - 11.07%
ALH4 - 10.74%
ALH5 - 10.52%
Stress (MPa)
Strain
0
2
4
6
8
10
12
14
16
0
0.1
0.2
0.3
0.4
0.5
0.6
0.7
0.8

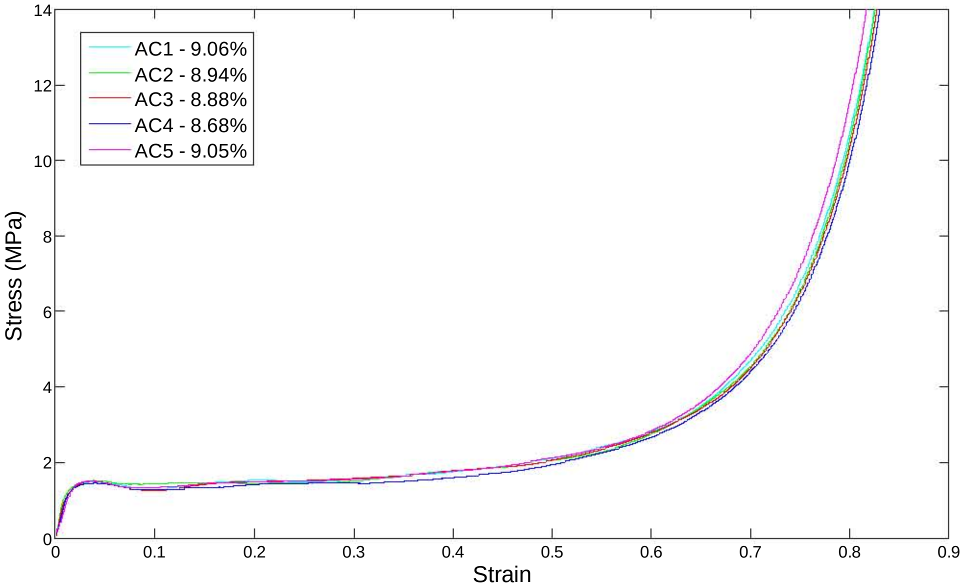
AC1 - 9.06%
AC2 - 8.94%
AC3 - 8.88%
AC4 - 8.68%
AC5 - 9.05%
Stress (MPa)
Strain
0
2
4
6
8
10
12
14
0
0.1
0.2
0.3
0.4
0.5
0.6
0.7
0.8
0.9

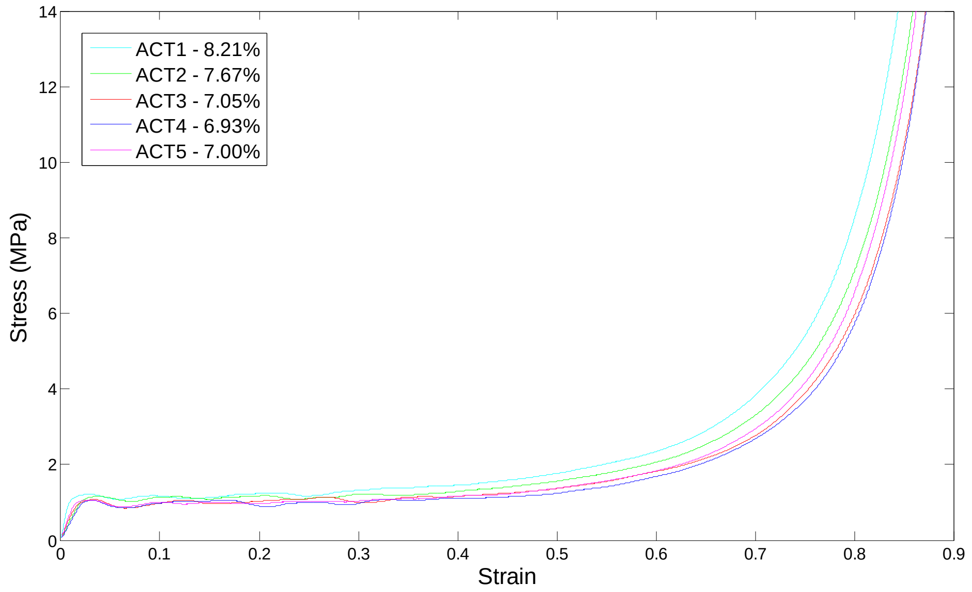
ACT1 - 8.21%
ACT2 - 7.67%
ACT3 - 7.05%
ACT4 - 6.93%
ACT5 - 7.00%
Stress (MPa)
Strain
0
2
4
6
8
10
12
14
0
0.1
0.2
0.3
0.4
0.5
0.6
0.7
0.8
0.9

A-2: Cymat

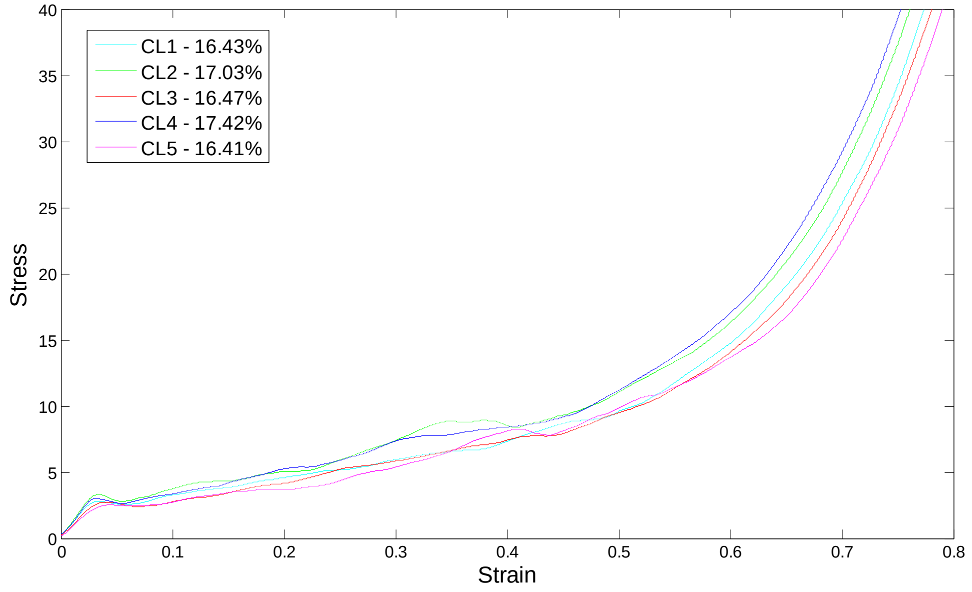
CL1 - 16.43%
CL2 - 17.03%
CL3 - 16.47%
CL4 - 17.42%
CL5 - 16.41%
Stress
Strain
0
5
10
15
20
25
30
35
40
0
0.1
0.2
0.3
0.4
0.5
0.6
0.7
0.8

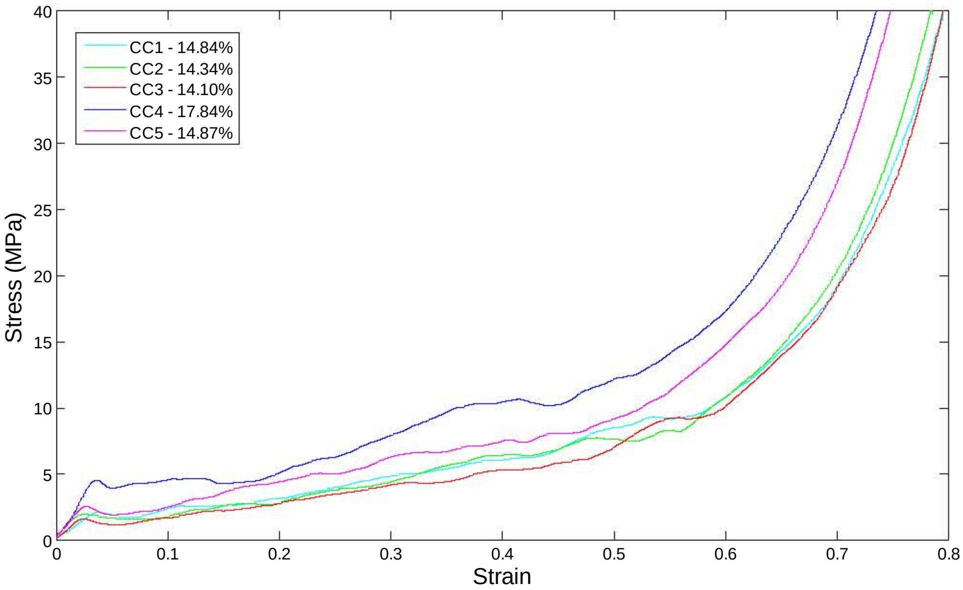
CC1 - 14.84%
CC2 - 14.34%
CC3 - 14.10%
CC4 - 17.84%
CC5 - 14.87%
Stress (MPa)
Strain
0
5
10
15
20
25
30
35
40
0
0.1
0.2
0.3
0.4
0.5
0.6
0.7
0.8

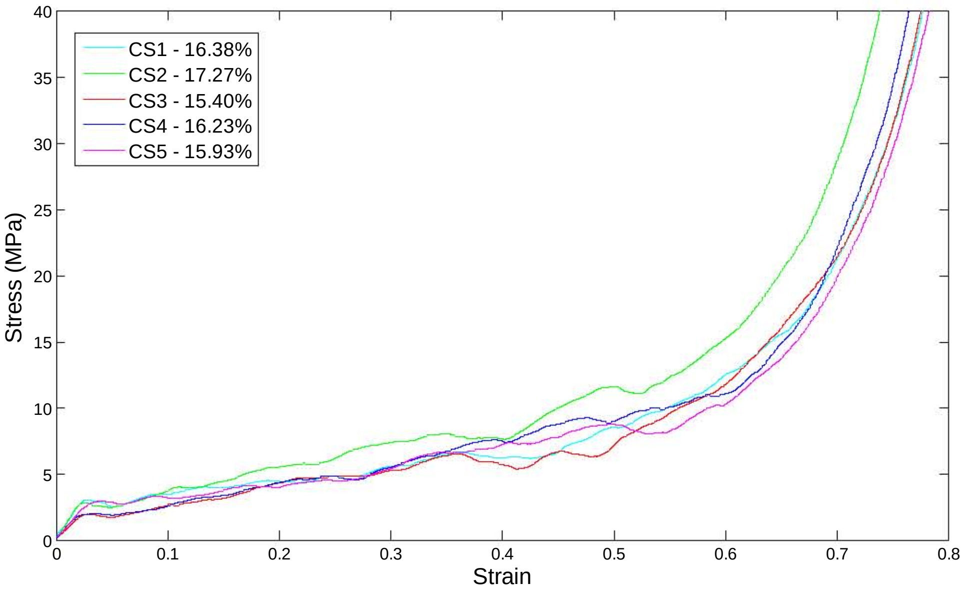
CS1 - 16.38%
CS2 - 17.27%
CS3 - 15.40%
CS4 - 16.23%
CS5 - 15.93%
Stress (MPa)
Strain
0
5
10
15
20
25
30
35
40
0
0.1
0.2
0.3
0.4
0.5
0.6
0.7
0.8

APPENDIX B: DYNAMIC STRESS-STRAIN CURVES

B-1: ALPORAS

B-1.1: ALPORAS cubes

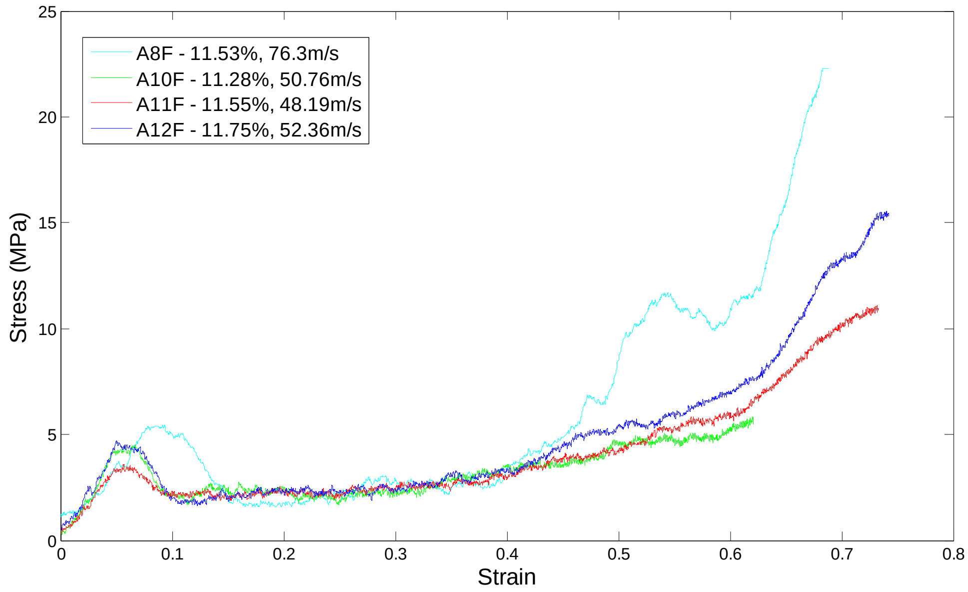

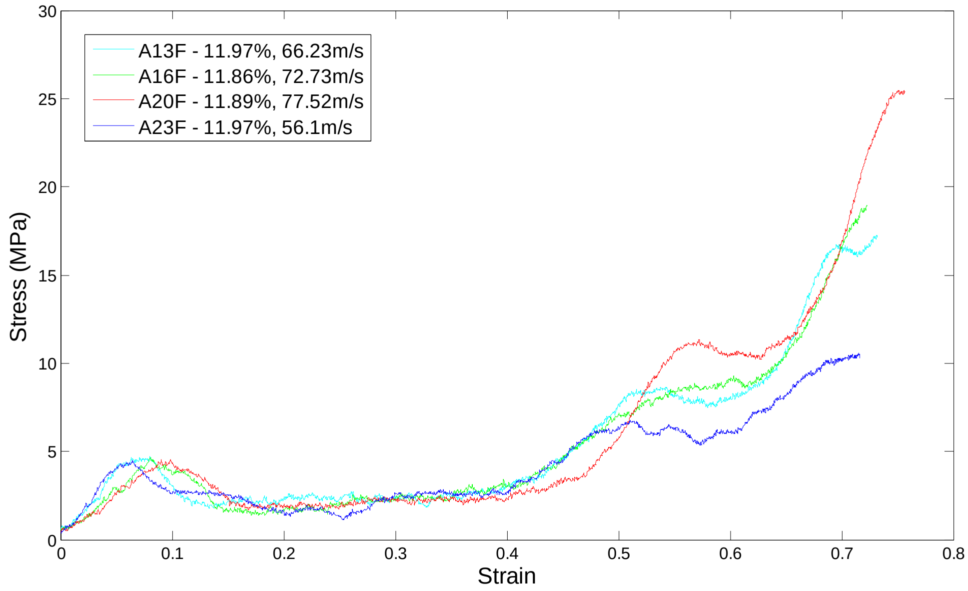

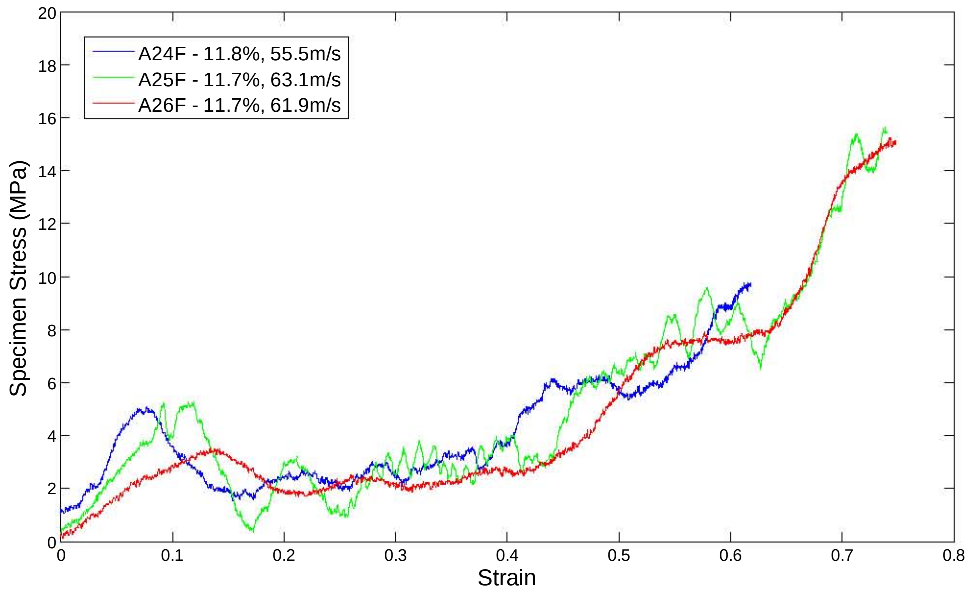
A24F - 11.8%, 55.5m/s
A25F - 11.7%, 63.1m/s
A26F - 11.7%, 61.9m/s
Specimen Stress (MPa)
Strain
0
2
4
6
8
10
12
14
16
18
20
0
0.1
0.2
0.3
0.4
0.5
0.6
0.7
0.8

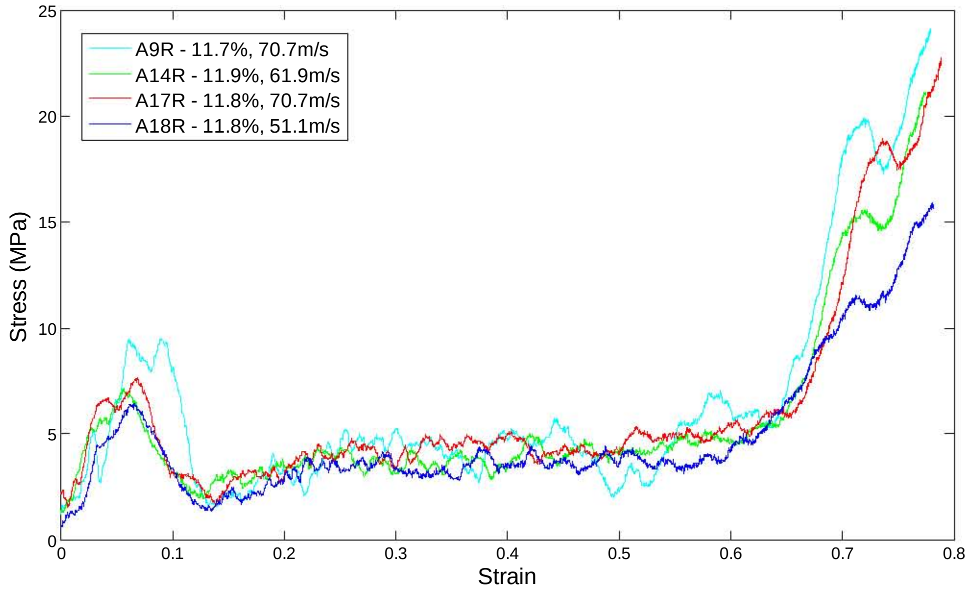
A9R - 11.7%, 70.7m/s
A14R - 11.9%, 61.9m/s
A17R - 11.8%, 70.7m/s
A18R - 11.8%, 51.1m/s
Stress (MPa)
Strain
0
5
10
15
20
25
0
0.1
0.2
0.3
0.4
0.5
0.6
0.7
0.8

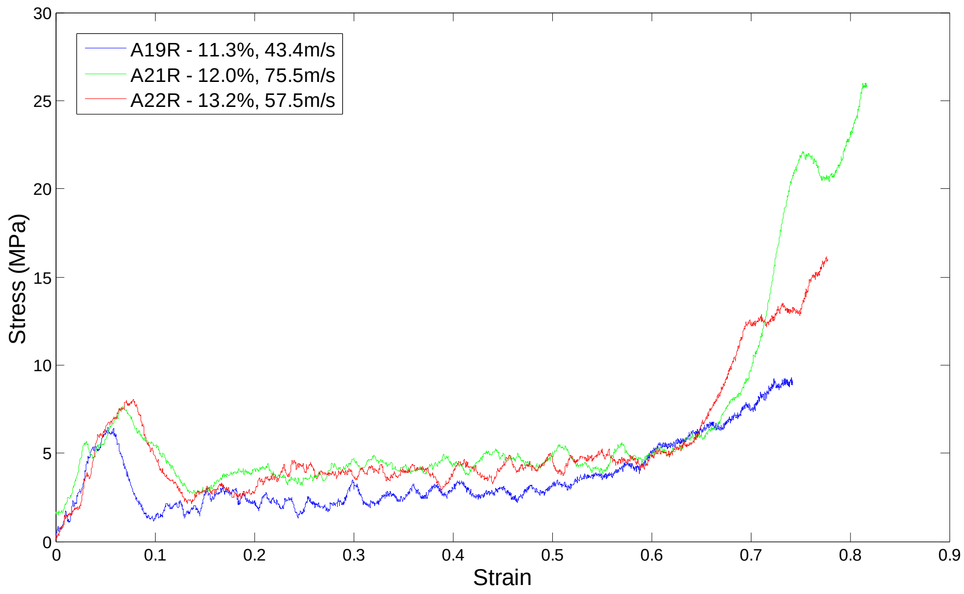

B-1.2: ALPORAS Cylinders

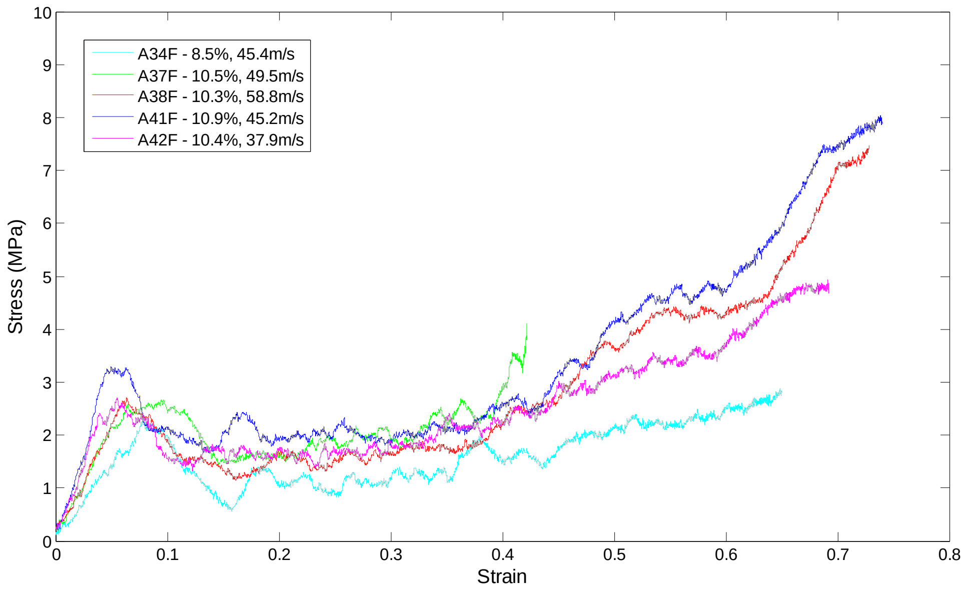

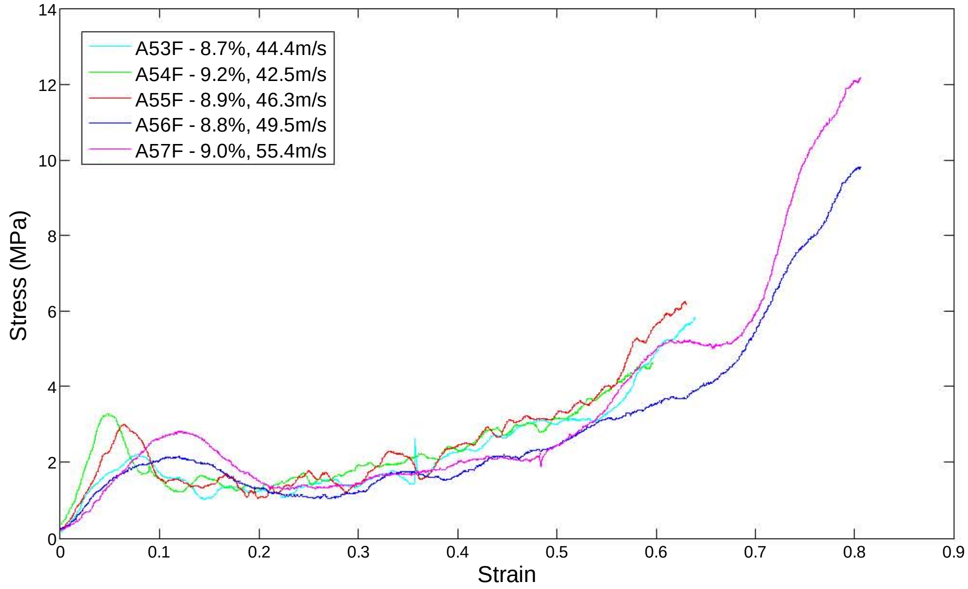
A53F - 8.7%, 44.4m/s
A54F - 9.2%, 42.5m/s
A55F - 8.9%, 46.3m/s
A56F - 8.8%, 49.5m/s
A57F - 9.0%, 55.4m/s
Stress (MPa)
Strain
0
2
4
6
8
10
12
14
0
0.1
0.2
0.3
0.4
0.5
0.6
0.7
0.8
0.9

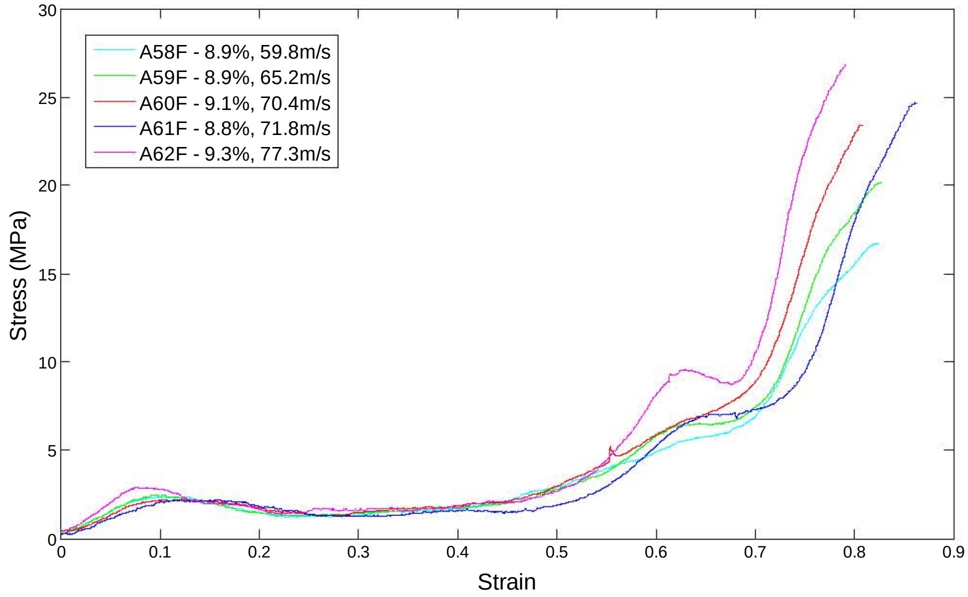
A58F - 8.9%, 59.8m/s
A59F - 8.9%, 65.2m/s
A60F - 9.1%, 70.4m/s
A61F - 8.8%, 71.8m/s
A62F - 9.3%, 77.3m/s
Stress (MPa)
Strain
0
5
10
15
20
25
30
0
0.1
0.2
0.3
0.4
0.5
0.6
0.7
0.8
0.9

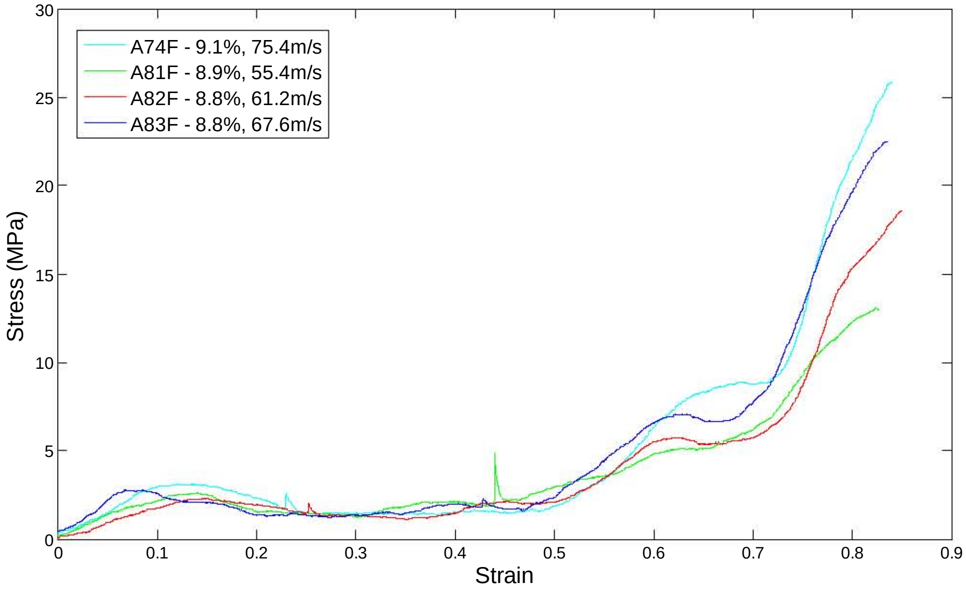
A74F - 9.1%, 75.4m/s
A81F - 8.9%, 55.4m/s
A82F - 8.8%, 61.2m/s
A83F - 8.8%, 67.6m/s
Stress (MPa)
Strain
0
5
10
15
20
25
30
0
0.1
0.2
0.3
0.4
0.5
0.6
0.7
0.8
0.9

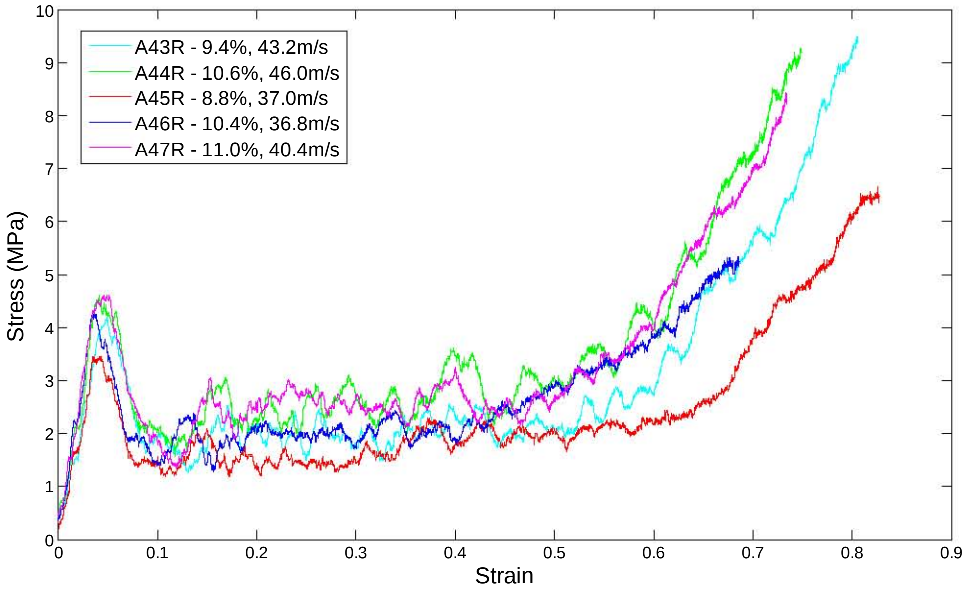
A43R - 9.4%, 43.2m/s
A44R - 10.6%, 46.0m/s
A45R - 8.8%, 37.0m/s
A46R - 10.4%, 36.8m/s
A47R - 11.0%, 40.4m/s
Stress (MPa)
Strain
0
1
2
3
4
5
6
7
8
9
10
0
0.1
0.2
0.3
0.4
0.5
0.6
0.7
0.8
0.9

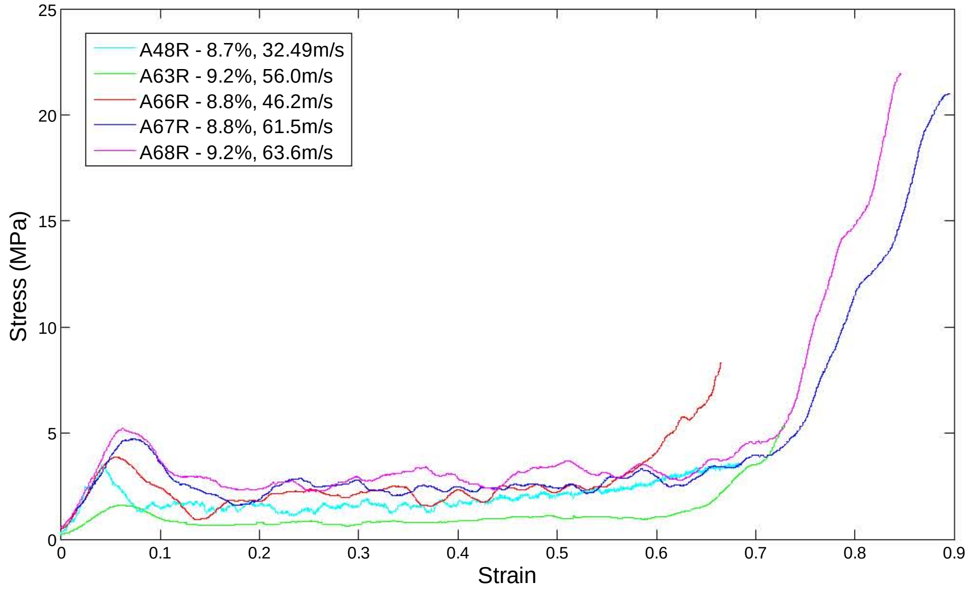

A48R - 8.7%, 32.49m/s
A63R - 9.2%, 56.0m/s
A66R - 8.8%, 46.2m/s
A67R - 8.8%, 61.5m/s
A68R - 9.2%, 63.6m/s
Stress (MPa)
Strain
0
5
10
15
20
25
0
0.1
0.2
0.3
0.4
0.5
0.6
0.7
0.8
0.9

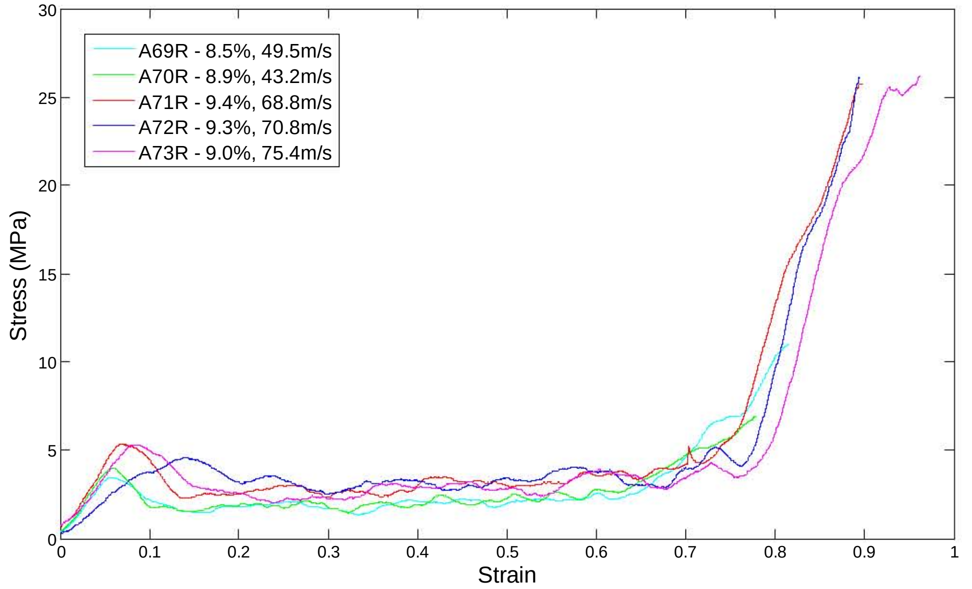

A69R - 8.5%, 49.5m/s
A70R - 8.9%, 43.2m/s
A71R - 9.4%, 68.8m/s
A72R - 9.3%, 70.8m/s
A73R - 9.0%, 75.4m/s
Stress (MPa)
Strain
0
5
10
15
20
25
30
0
0.1
0.2
0.3
0.4
0.5
0.6
0.7
0.8
0.9
1

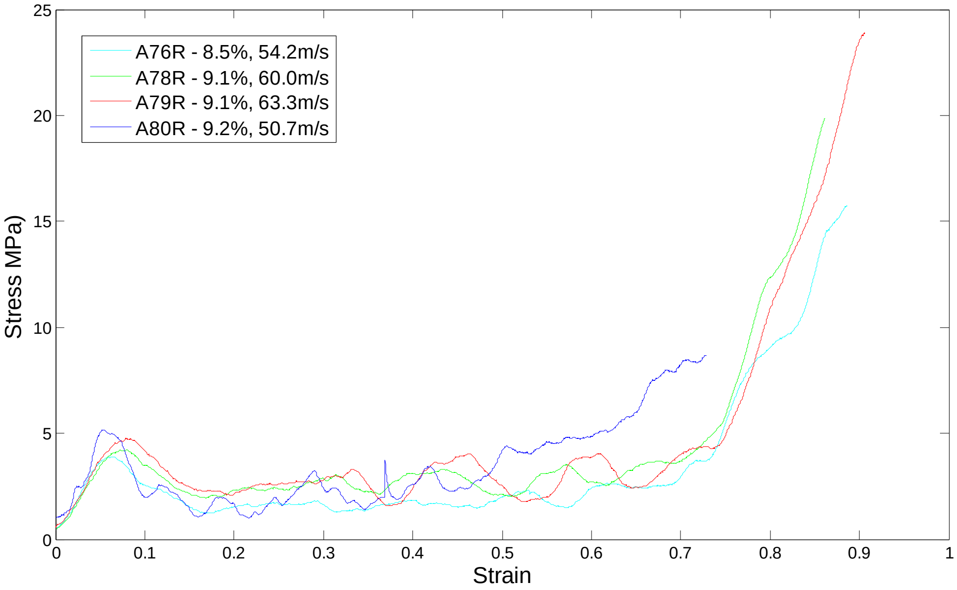

B-2 Cymat

B-2.1 Cymat cubes

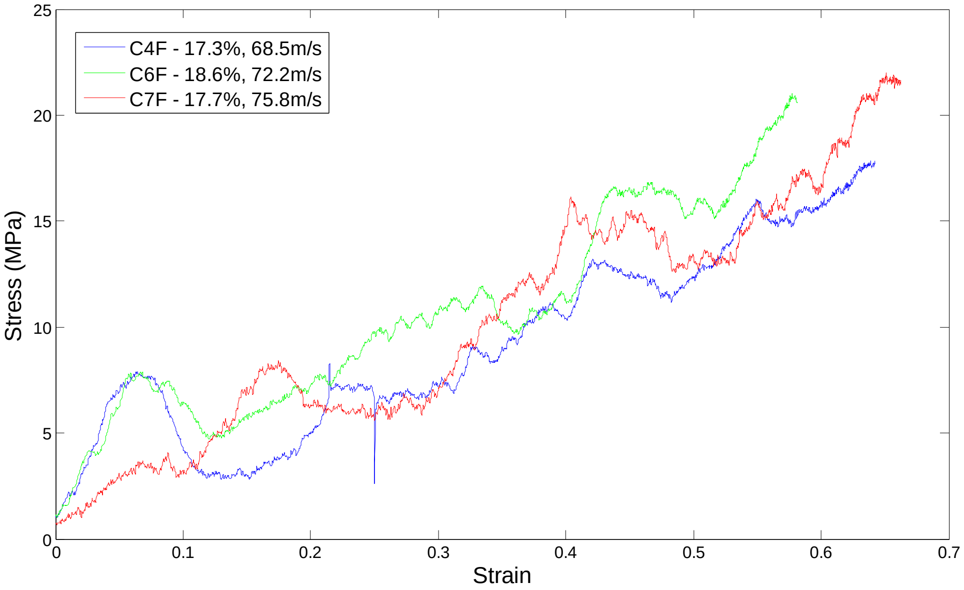

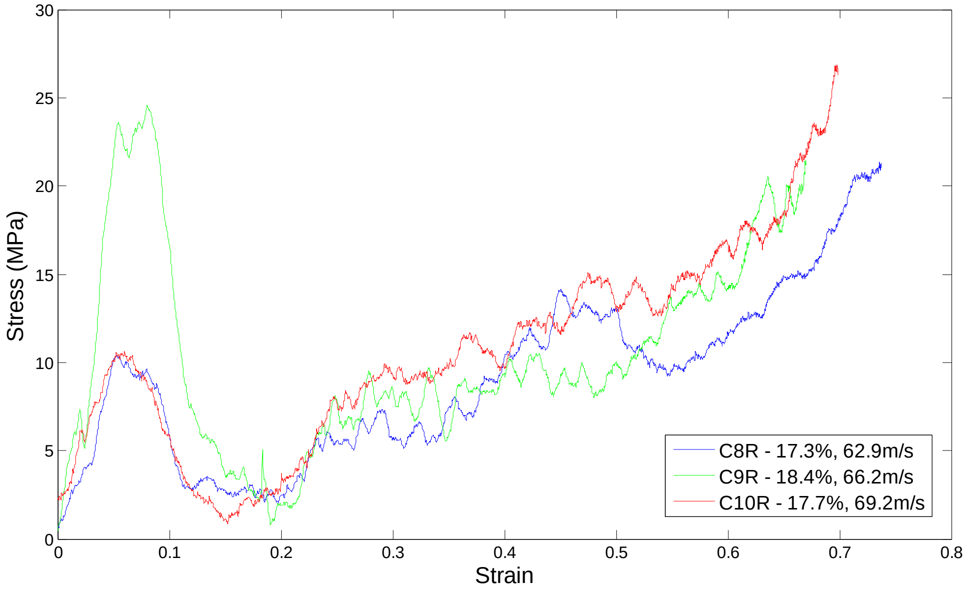

B-2:2 Cymat cylinders

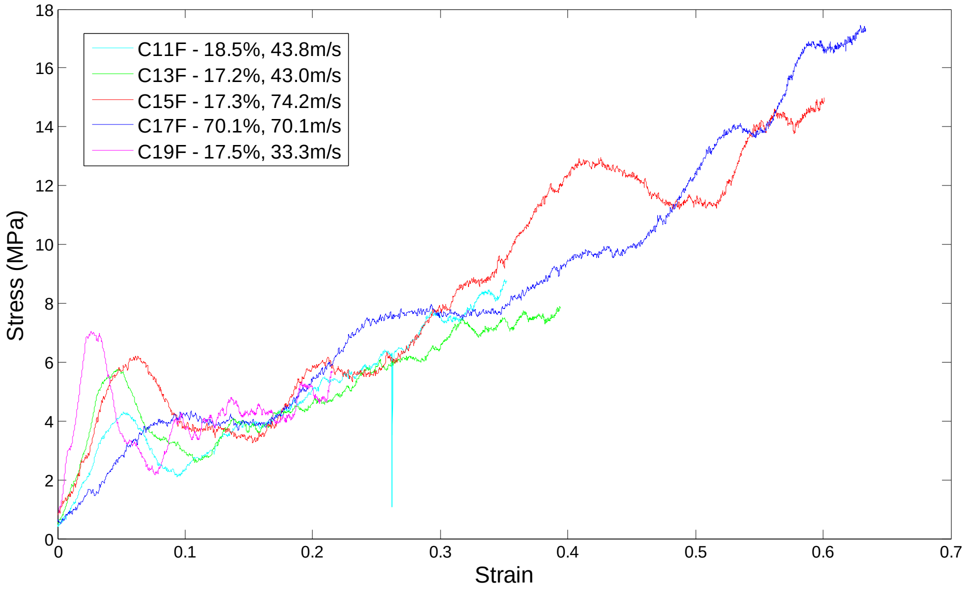

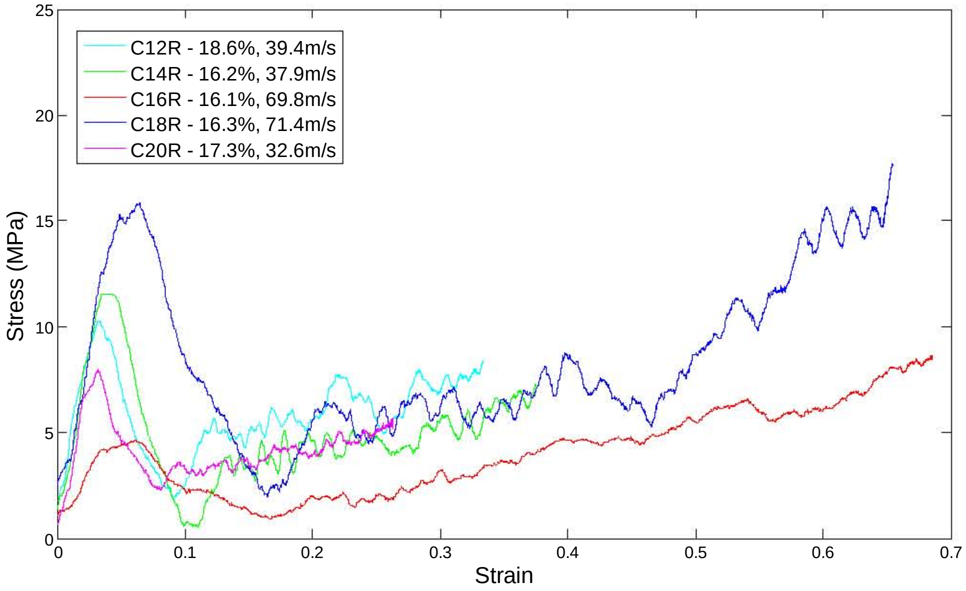
C12R - 18.6%, 39.4m/s
C14R - 16.2%, 37.9m/s
C16R - 16.1%, 69.8m/s
C18R - 16.3%, 71.4m/s
C20R - 17.3%, 32.6m/s
Stress (MPa)
Strain
0
5
10
15
20
25
0
0.1
0.2
0.3
0.4
0.5
0.6
0.7

APPENDIX C: DYNAMIC TEST SPECIMEN DETAILS

Specimen #	Nom. dimensions (lxb, or Φ)	Thickness (mm)	Mass (g)	Relative density (%)
ALPORAS DIRECT IMPACT CUBES				
A10F	25x25	25.16	5.02	11.28
A8F	25x25	25.16	5.05	11.53
A11F	25x25	25.16	5.14	11.55
A25F	25x25	25.08	5.16	11.65
A26F	25x25	25.14	5.18	11.74
A12F	25x25	25.14	5.16	11.75
A24F	25x25	25.16	5.3	11.79
A16F	25x25	25.16	5.15	11.86
A20F	25x25	25.1	5.24	11.89
A13F	25x25	25.18	5.34	11.97
A23F	25x25	25.16	5.31	11.97
A19R	25x25	25.1	4.97	11.26
A9R	25x25	25.18	5.22	11.73
A18R	25x25	25.18	5.18	11.78
A17R	25x25	25.1	5.25	11.83
A14R	25x25	25.18	5.33	11.91
A21R	25x25	25.1	5.26	11.99
A22R	25x25	25.1	5.79	13.21
ALPORAS TAYLOR TEST CYLINDERS				
a33t	Φ35	39.50	7.60	7.4
a32t	Φ35	38.26	7.76	7.8

Specimen #	Nom. dimensions (lxb, or Φ)	Thickness (mm)	Mass (g)	Relative density (%)
a31t	Φ35	38.68	7.98	8.0
a29t	Φ35	39.24	8.29	8.0
a27t	Φ35	39.86	8.73	8.2
a28t	Φ35	39.26	8.81	8.4
a30t	Φ35	39.10	8.77	8.5
ALPORAS DIRECT IMPACT CYLINDERS				
A34F	Φ40	24.86	7.16	8.5
A53F	Φ40	25.14	7.32	8.7
A56F	Φ40	25.16	7.41	8.8
A83F	Φ40	25.14	7.42	8.8
A82F	Φ40	25.1	7.33	8.8
A61F	Φ40	25.12	7.42	8.8
A55F	Φ40	25.14	7.51	8.9
A58F	Φ40	25.16	7.52	8.9
A59F	Φ40	25.12	7.5	8.9
A81F	Φ40	25.1	7.56	8.9
A57F	Φ40	25.1	7.62	9.0
A74F	Φ40	25.1	7.71	9.1
A60F	Φ40	25.12	7.65	9.1
A54F	Φ40	25.08	7.76	9.2
A62F	Φ40	25.12	7.81	9.3
A38F	Φ40	24.28	8.62	10.3
A42F	Φ40	23.96	8.55	10.4
A37F	Φ40	24.14	8.62	10.5

Specimen #	Nom. dimensions (lxb, or Φ)	Thickness (mm)	Mass (g)	Relative density (%)
A41F	Φ40	24.3	8.96	10.9
A69R	Φ40	25.14	7.15	8.5
A76R	Φ40	25.12	7.17	8.5
A48R	Φ40	24.1	7.05	8.7
A45R	Φ40	25	7.47	8.8
A66R	Φ40	25.16	7.44	8.8
A67R	Φ40	25.12	7.43	8.8
A70R	Φ40	25.14	7.52	8.9
A73R	Φ40	25.12	7.59	9.0
A78R	Φ40	25.14	7.66	9.1
A79R	Φ40	25.12	7.68	9.1
A68R	Φ40	25.18	7.71	9.2
A63R	Φ40	25.1	7.72	9.2
A80R	Φ40	25.08	7.77	9.2
A72R	Φ40	25.12	7.92	9.3
A43R	Φ40	24.34	7.78	9.4
A71R	Φ40	25.1	7.9	9.4
A46R	Φ40	24.38	8.48	10.4
A44R	Φ40	24.2	8.73	10.6
A47R	Φ40	24.28	9.06	11.0
CYMAT DIRECT IMPACT CUBES				
C4F	25x25	25.02	7.83	17.3
C7F	25x25	24.92	7.82	17.7
C6F	25x25	25.26	8.03	18.6

Specimen #	Nom. dimensions (lxb, or Φ)	Thickness (mm)	Mass (g)	Relative density (%)
C8R	25x25	25.26	7.57	17.3
C9R	25x25	25.28	7.99	17.7
C10R	25x25	25.06	8.24	18.4
CYMAT DIRECT IMPACT CYLINDERS				
C11F	Φ40	24.98	14.27	16.8
C13F	Φ40	26.26	15.4	17.2
C15F	Φ40	26.36	15.36	17.3
C17F	Φ40	26.36	15.66	17.5
C19F	Φ40	26.34	16.69	18.5
C12R	Φ40	26.3	14.48	16.1
C14R	Φ40	26.28	14.58	16.2
C16R	Φ40	25.96	14.26	16.3
C18R	Φ40	26.42	15.65	17.3
C20R	Φ40	26.42	16.82	18.6

APPENDIX D: SUPPORTING THEORY

This appendix describes in detail the method used to calculate the theoretical impulse of a blast, using the measurements of the maximum deflection of the ballistic pendulum. The method described is that used by Theobald (61).The ballistic pendulum is assumed to maintain its orientation throughout its swing, and is assumed to have simple pendulum motion. These are reasonable assumptions if the pendulum is properly balanced.

The measurements required for the calculation of the impulse, and shown in figure A.1, are the pen displacements ΔL and ΔR (which are measured for each blast), the cable length l_w, the height of the pendulum above the pen tip a_1 and the length of the pen Z. The natural frequency T and pendulum mass m_p are also required.

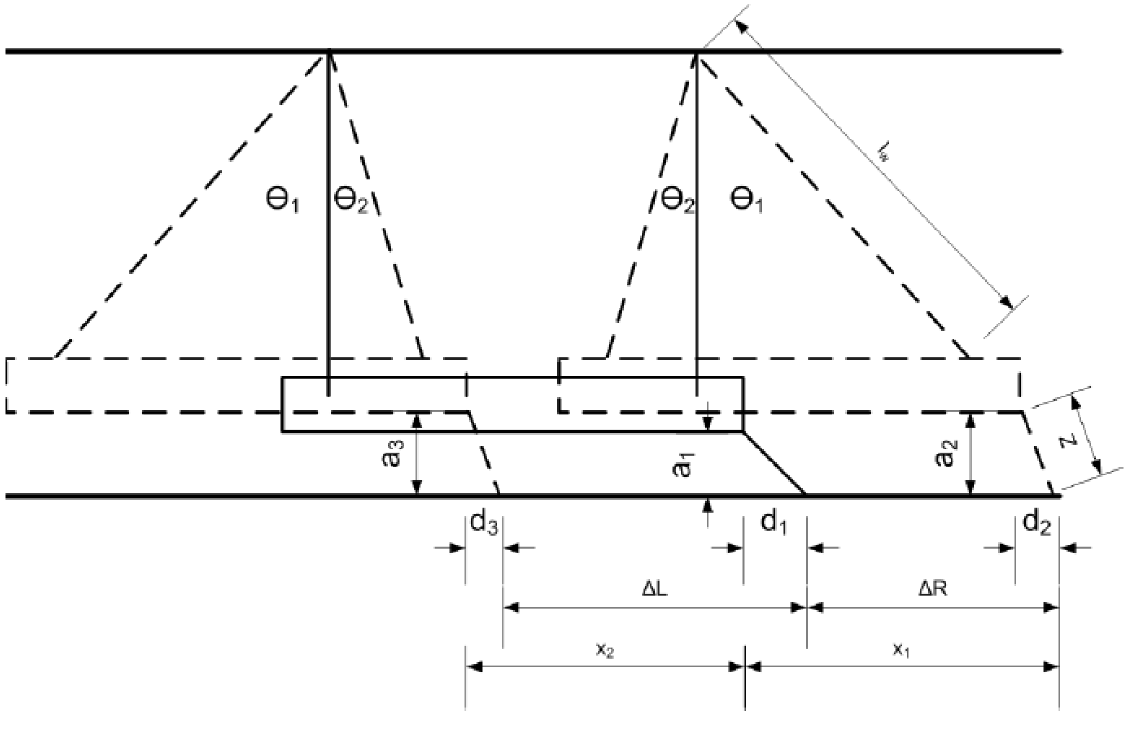

Figure A-1: Schematic of the ballistic pendulum (61)

The difference between the initial position of the pendulum and the tip of the pen (d_1) is

$$d_1 = \sqrt{Z^2 - a_1^2} \qquad \text{(A.1)}$$

d2, the difference between the forward swing of the pendulum (to the right in Figure) and the forward displacement of the pen is

$$d_2 = \sqrt{Z_2 - a_2^2} \qquad \text{(A.2)}$$

where

$$a_2 = l_w(1 - \cos\theta_1) + a_1 \qquad \text{(A.3)}$$

Likewise, d3, the difference in displacement between the backward swing of the pendulum and the backward displacement of the pen, is given by

$$d_3 = \sqrt{Z^2 - a_3^2} \qquad \text{(A.4)}$$

where

$$a_3 = l_w(1 - \cos\theta_2) + a_1 \qquad \text{(A.5)}$$

Let x_1 and x_2 be the maximum forward and backward displacements of the pendulum respectively. x_1 and x_2 are then given by

$$x_1 = l_w \sin\theta_1 \qquad \text{(A.6)}$$

and

$$x_2 = l_w \sin\theta_2 \qquad \text{(A.7)}$$

Therefore the measured displacements ΔL and ΔR are defined as

$$\Delta R = x_1 - d_1 + d_2 = l_w \sin\theta_1 - \sqrt{Z^2 - a_1^2} + \sqrt{Z^2 - (l_w(1 - \cos\theta_1) + a_1)^2} \qquad \text{(A.8)}$$

and

$$\Delta L = x_2 + d_1 - d_3 = l_w \sin\theta_2 - \sqrt{Z^2 - a_1^2} + \sqrt{Z^2 - (l_w(1 - \cos\theta_2) + a_1)^2} \qquad \text{(A.9)}$$

All the variables in equations A.8 and A.9 above are measured or calculated from these measurements, except for θ_1 and θ_2. These angles are determined in Excel by using the Solver function. x1 and x2 can then be calculated.

The motion of a simple pendulum is described by the following equation:

$$\ddot{x} + 2\beta\dot{x} + \omega_n^2 = 0 \qquad \text{(A.10)}$$

Where

$$\beta = C/2m_p \qquad \text{(A.11)}$$

and

$$\omega_n = 2\pi/T \qquad \text{(A.12)}$$

where C is the damping coefficient, m_p is the total mass of the pendulum and T is the natural period of the pendulum. In this case, the mass of the pendulum is 95.58kg and the natural period is 3.41s. The period is measured by allowing the pendulum to swing freely and measuring the time taken for ten oscillations.

The solution of the differential equation A.10 is given by

$$x(t) = \frac{(e^{-\beta t})\,\dot{x}_0 \sin\omega_d t}{\omega_d} \qquad \text{(A.13)}$$

where $_{x0}$ is the initial velocity of the pendulum and ω_d is given by

$$\omega_d = \sqrt{\omega_n^2 - \beta^2} \qquad \text{(A.14)}$$

x_1 and x_2 occur at t=T/4 and t=3T/4 respectively. They can now be given by the equations

$$x_1 = \frac{\dot{x}_0}{2\pi} e^{-\beta T/4} \qquad \text{(A.15)}$$

and

$$x2 = -\frac{\dot{x}_0}{2\pi} e^{-3\beta T/4} \tag{A.16}$$

Solving for β in terms of x_1/x_2 gives

$$\beta = \frac{2}{T} \ln \frac{x_1}{x_2} \tag{A.17}$$

and the initial velocity is then

$$\dot{x}_0 = \frac{2\pi}{T} x_1 e^{-\beta T/4} \tag{A.18}$$

The impulse I can then be calculated from

$$I = m \dot{x}_0 \tag{A.19}$$

APPENDIX E: DRAWINGS

This appendix includes the technical drawings of components of the testing equipment designed as part of this investigation.

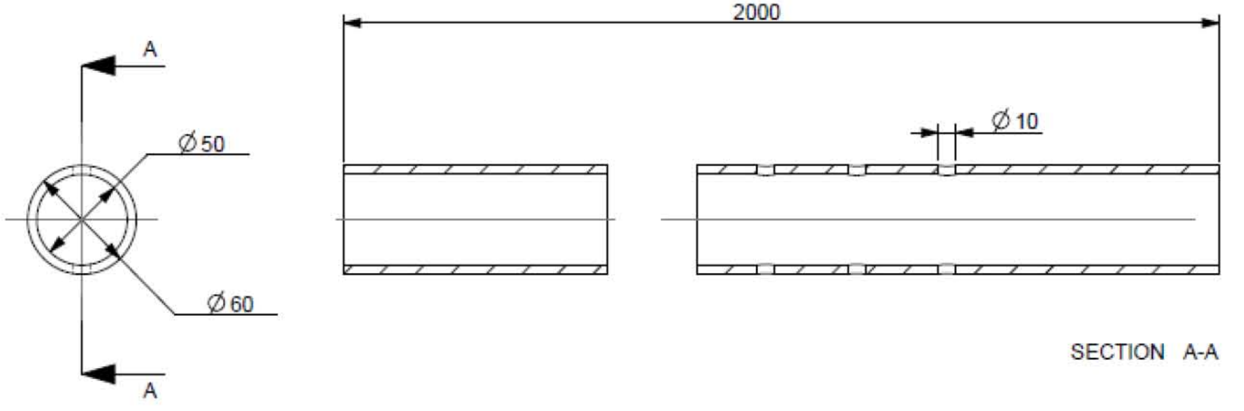

Item	Name		Qty	Material
	University of Cape Town Department of Mechanical Engineering			
	Title BARREL			
Dimensions in mm Tolerance U.O.S. 0.1	Scale 0,333	Date 29-07-2009	Sheet xx	of xx
	Drawn By R.P. MERRETT (MRRRIC009)		Drawing Number xx	

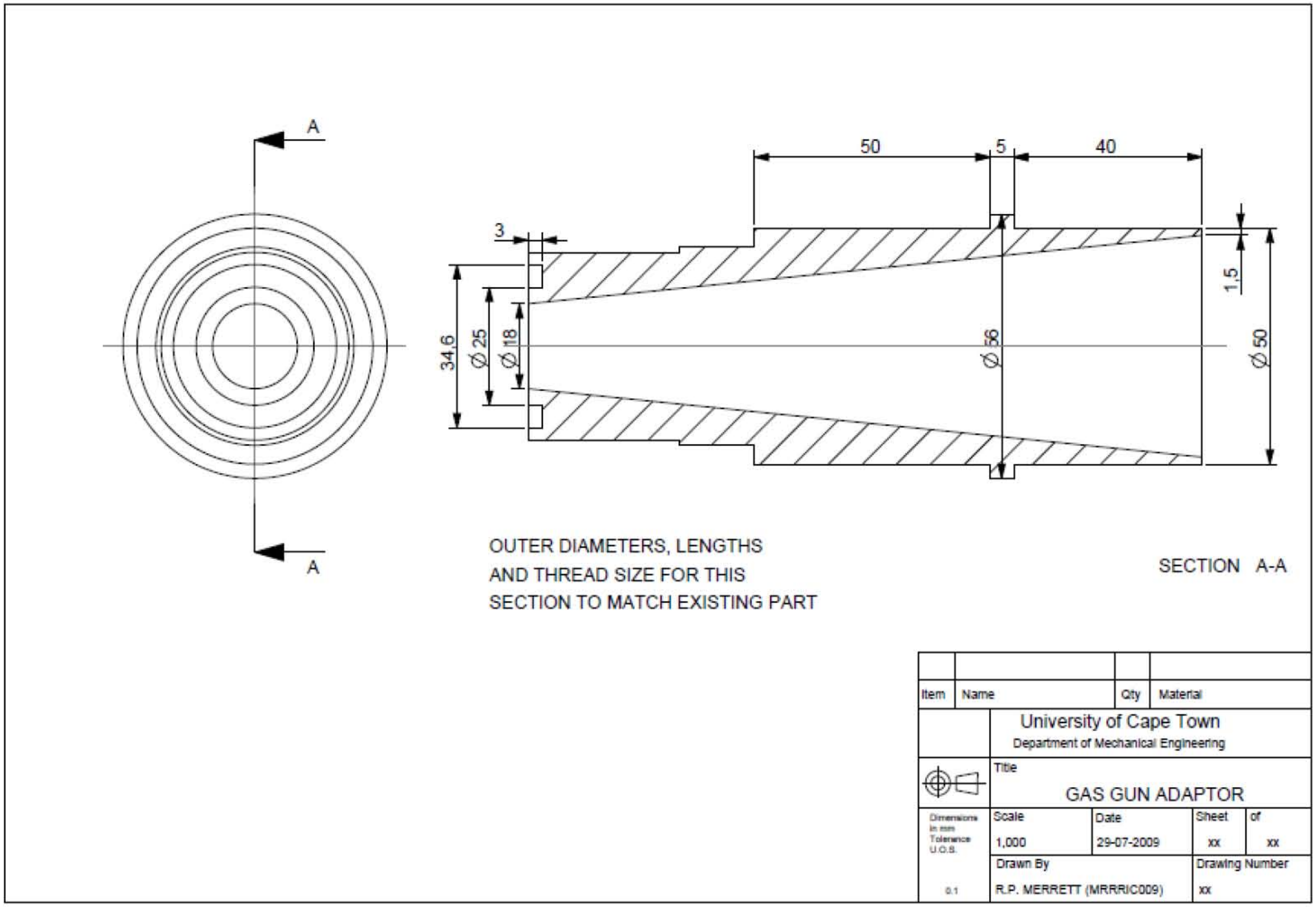

OUTER DIAMETERS, LENGTHS
AND THREAD SIZE FOR THIS
SECTION TO MATCH EXISTING PART

SECTION A-A

Item	Name	Qty	Material

University of Cape Town
Department of Mechanical Engineering

Title
GAS GUN ADAPTOR

Dimensions in mm
Tolerance U.O.S.
0.1

Scale	Date	Sheet	of
1,000	29-07-2009	xx	xx

Drawn By
R.P. MERRETT (MRRRIC009)

Drawing Number
xx

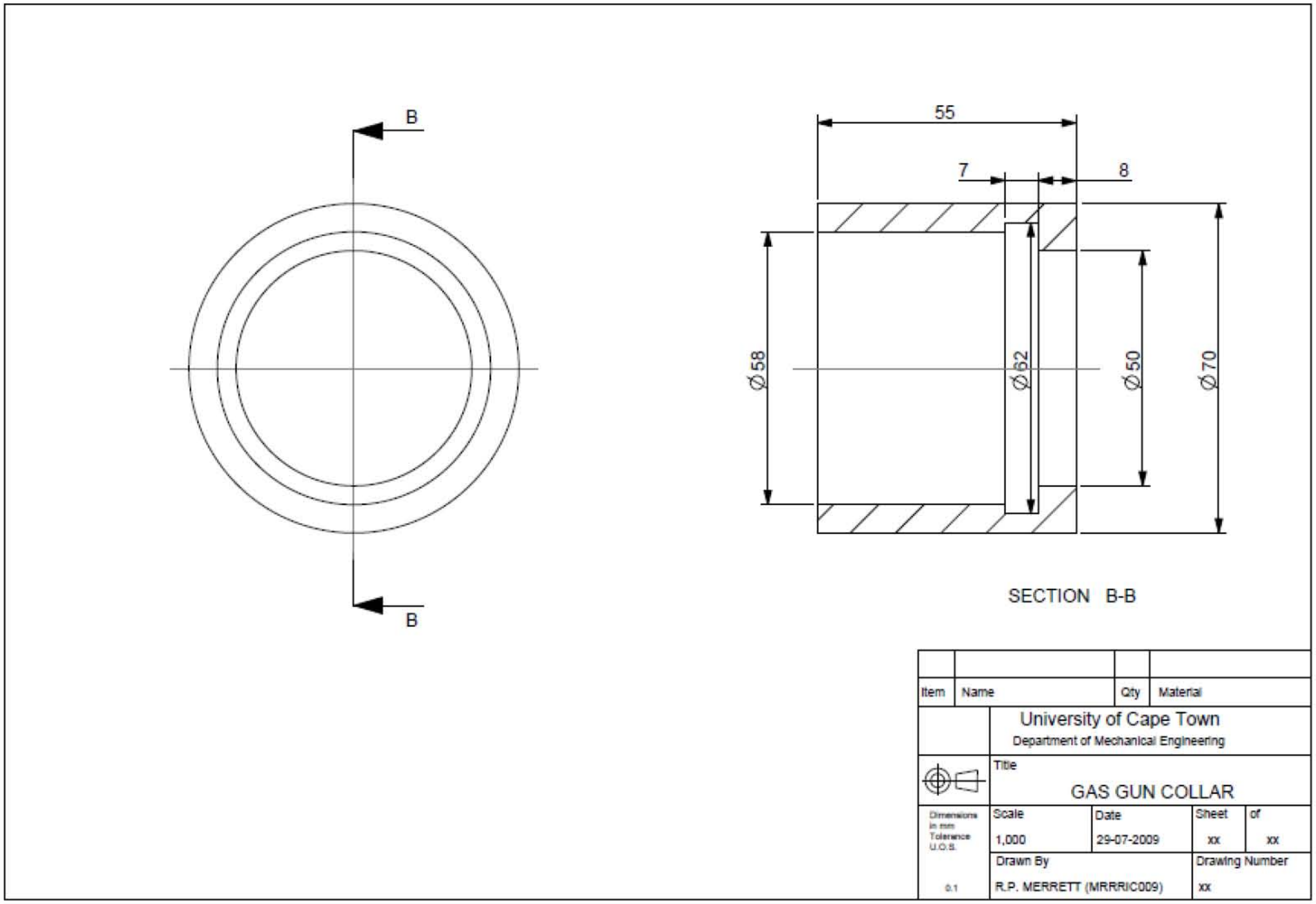
B
B
55
7
8
Ø58
Ø62
Ø50
Ø70
SECTION B-B
Item
Name
Qty
Material
University of Cape Town
Department of Mechanical Engineering
Title
GAS GUN COLLAR
Dimensions in mm Tolerance U.O.S.
0.1
Scale
1,000
Date
29-07-2009
Sheet
xx
of
xx
Drawn By
R.P. MERRETT (MRRRIC009)
Drawing Number
xx

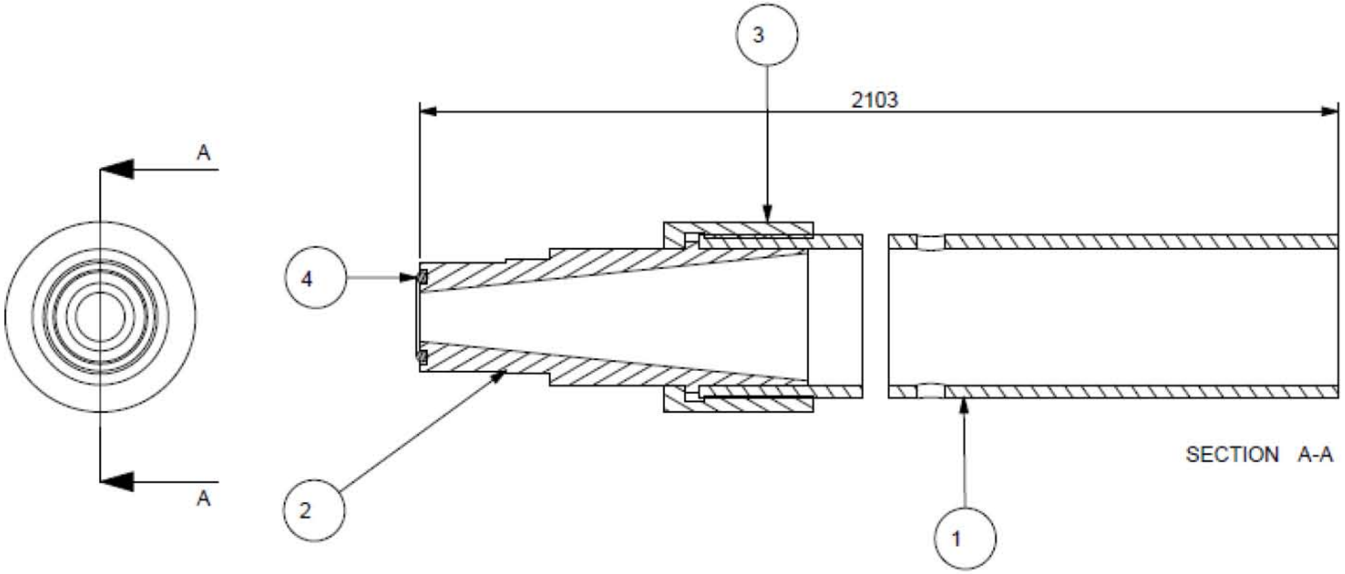

Item	Name	Qty	Material
4	O_RING	1	STEEL_LC
3	GAS_GUN_COLLAR	1	STEEL_LC
2	GAS_GUN_ADAPTOR	1	STEEL_LC
1	BARREL	1	STEEL_LC

University of Cape Town
Department of Mechanical Engineering

Title
GAS GUN ASSEMBLY

Dimensions in mm
Tolerance U.O.S.
0.1

Scale	Date	Sheet	of
0,500	29/07/2009	xx	xx

Drawn By
R.P. MERRETT (MRRRIC009)

Drawing Number
xx

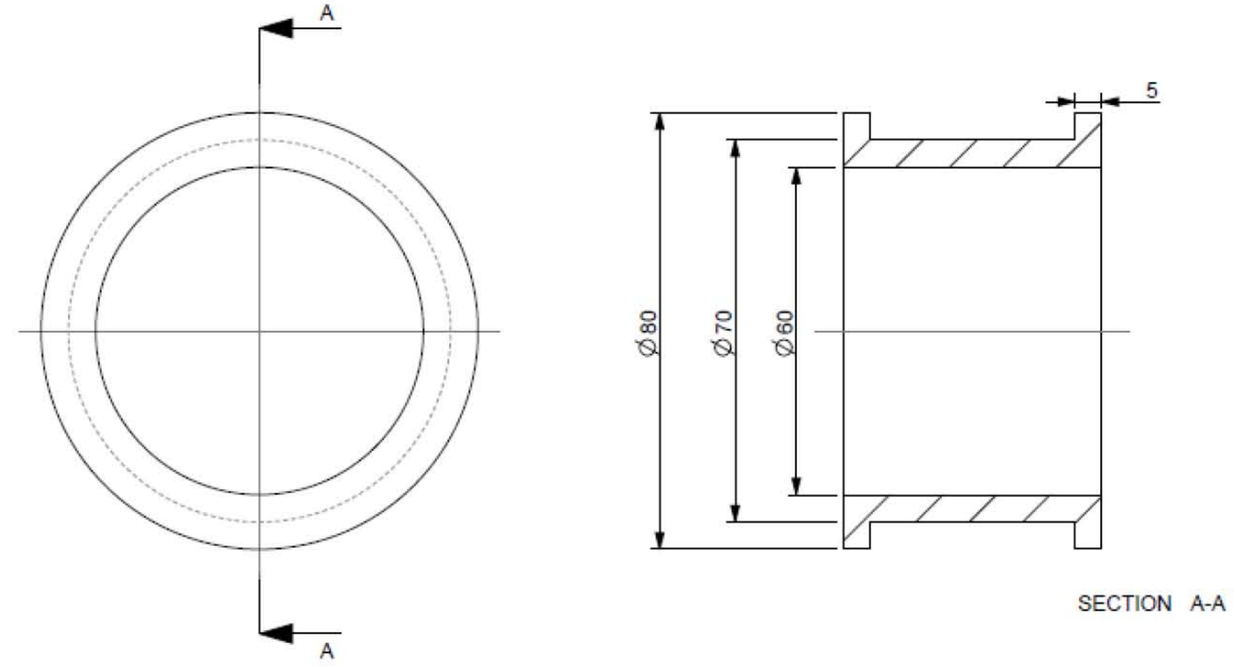

Item	Name	Qty	Material

University of Cape Town
Department of Mechanical Engineering

Title
BARREL SUPPORT

Dimensions in mm
Tolerance U.O.S.
0.1

Scale	Date	Sheet	of
1,000	29-07-2009	xx	xx

Drawn By
R.P. MERRETT (MRRRIC009)

Drawing Number
xx

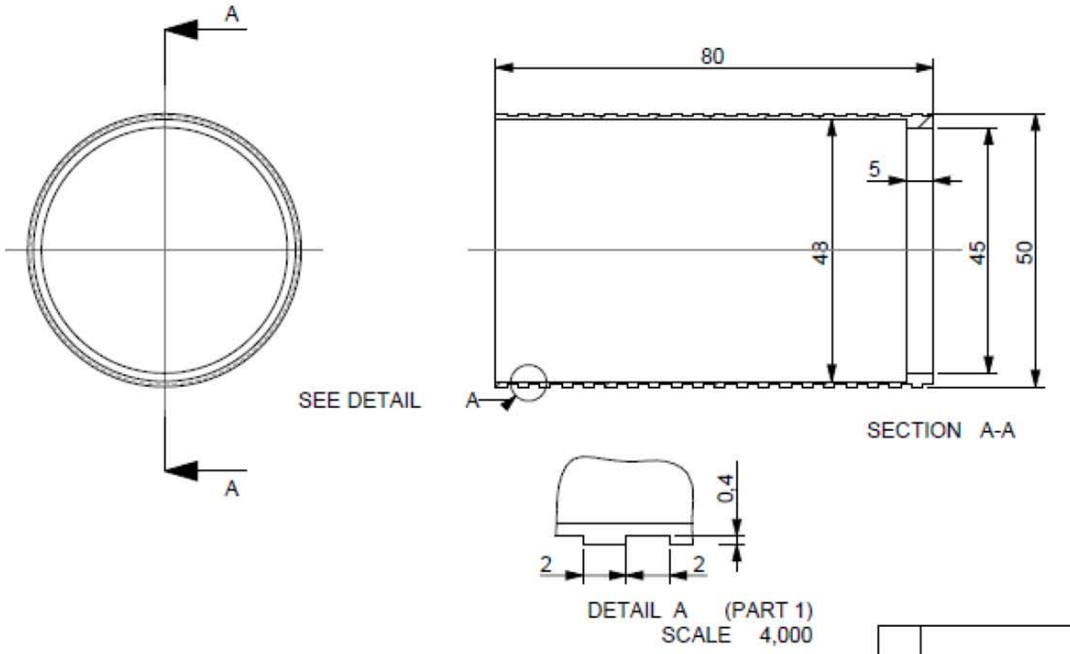

2 PARTS TO BE MACHINED, SAME DIMENSIONS EX. GROOVES
PART 1 - 2MM WIDE GROOVES, 2MM APART AND 0.4MM DEEP
PART 2 - GROOVES 1MM WIDE 1MM APART AND 0.4MM DEEP

Item	Name	Qty	Material

University of Cape Town
Department of Mechanical Engineering

Title
STRIKER ∅50 LONG

Dimensions in mm
Tolerance U.O.S.
0.1

Scale	Date	Sheet	of
1,000	18-02-2010	xx	xx

Drawn By
R.P. MERRETT (MRRRIC009)

Drawing Number
xx

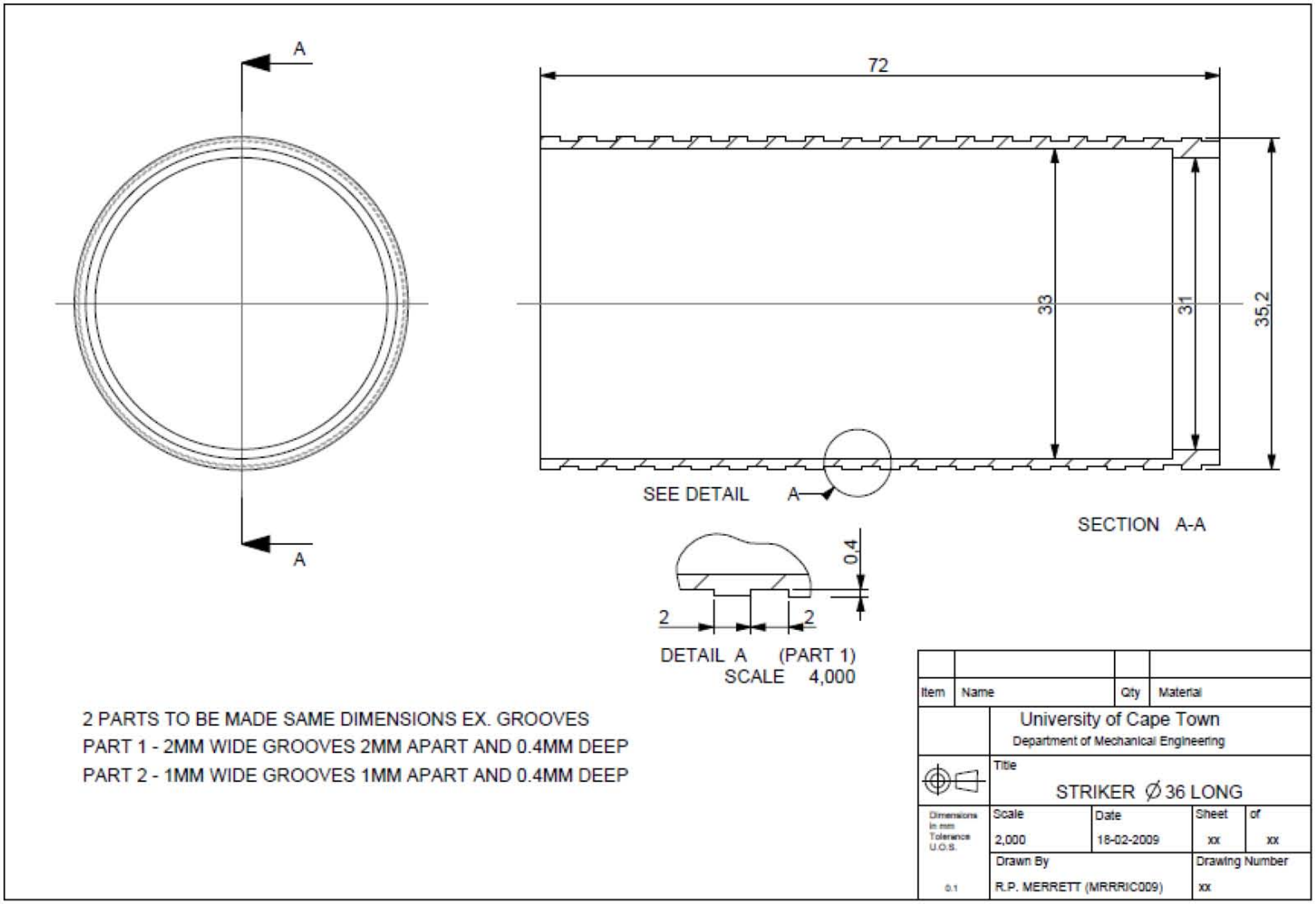

2 PARTS TO BE MADE SAME DIMENSIONS EX. GROOVES
PART 1 - 2MM WIDE GROOVES 2MM APART AND 0.4MM DEEP
PART 2 - 1MM WIDE GROOVES 1MM APART AND 0.4MM DEEP

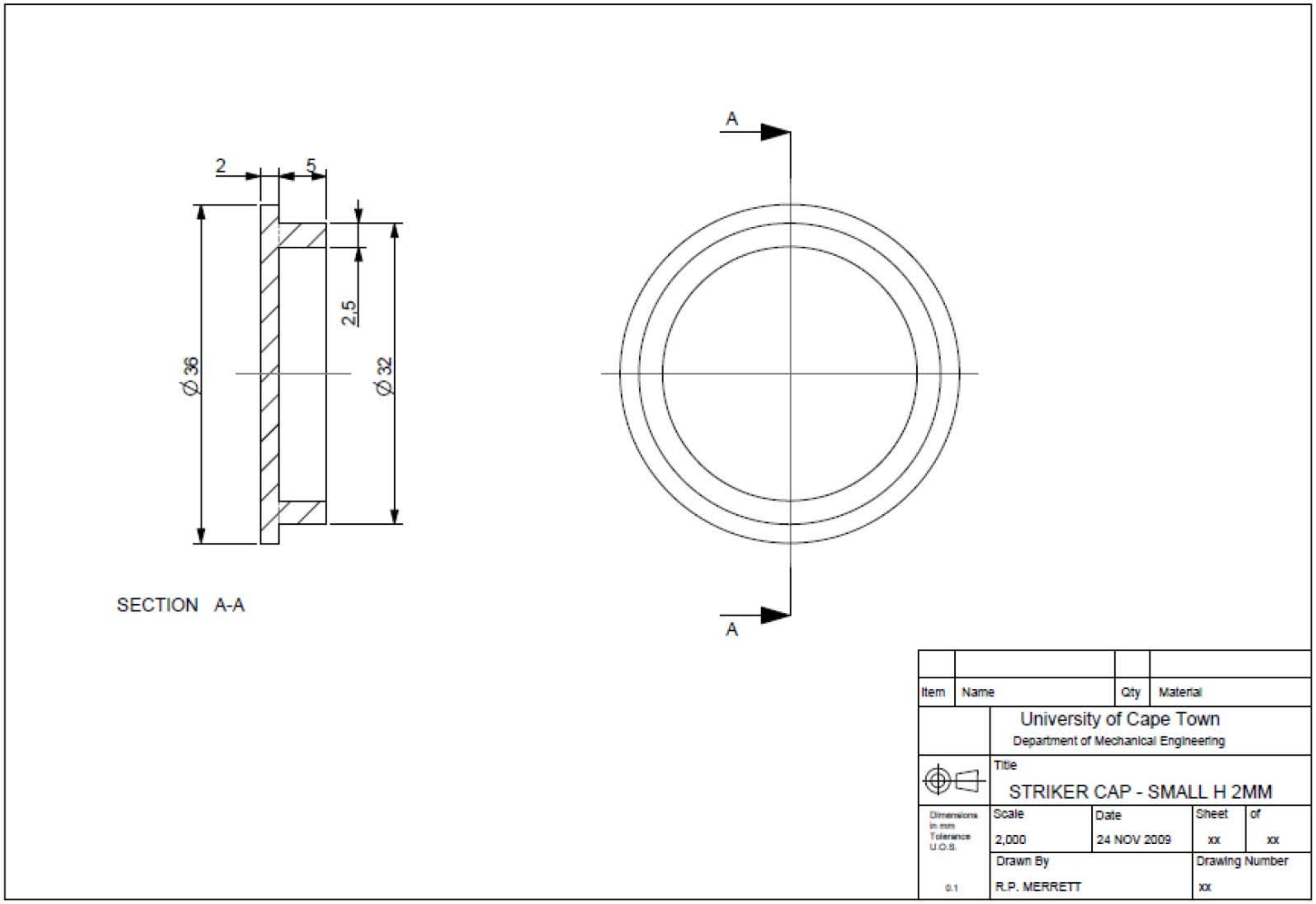

Item	Name	Qty	Material

University of Cape Town
Department of Mechanical Engineering

Title
STRIKER CAP - SMALL H 2MM

Dimensions in mm
Tolerance U.O.S.
0.1

Scale	Date	Sheet	of
2,000	24 NOV 2009	xx	xx

Drawn By	Drawing Number
R.P. MERRETT	xx

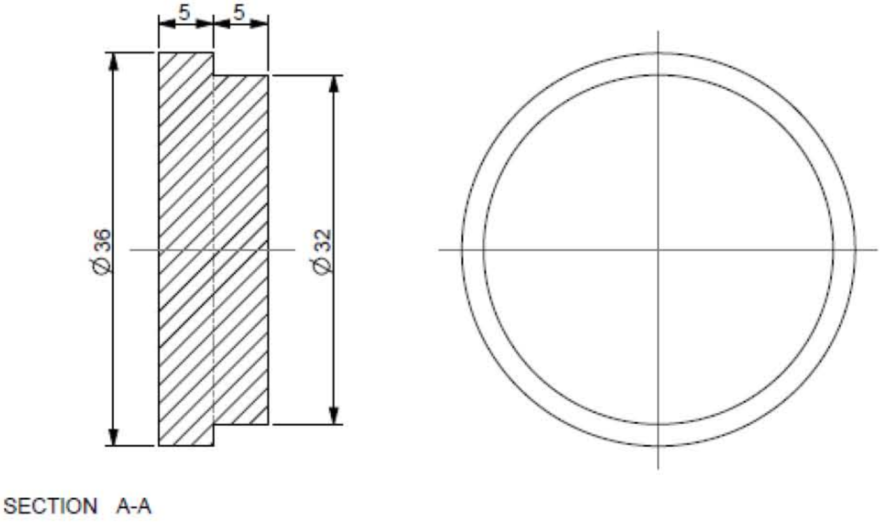

Item	Name	Qty	Material

University of Cape Town
Department of Mechanical Engineering

Title
STRIKER CAP - SMALL S 5MM

Dimensions in mm Tolerance U.O.S.	Scale	Date	Sheet	of
	2,000	24 NOV 2009	xx	xx
	Drawn By		Drawing Number	
0.1	R.P. MERRETT		xx	

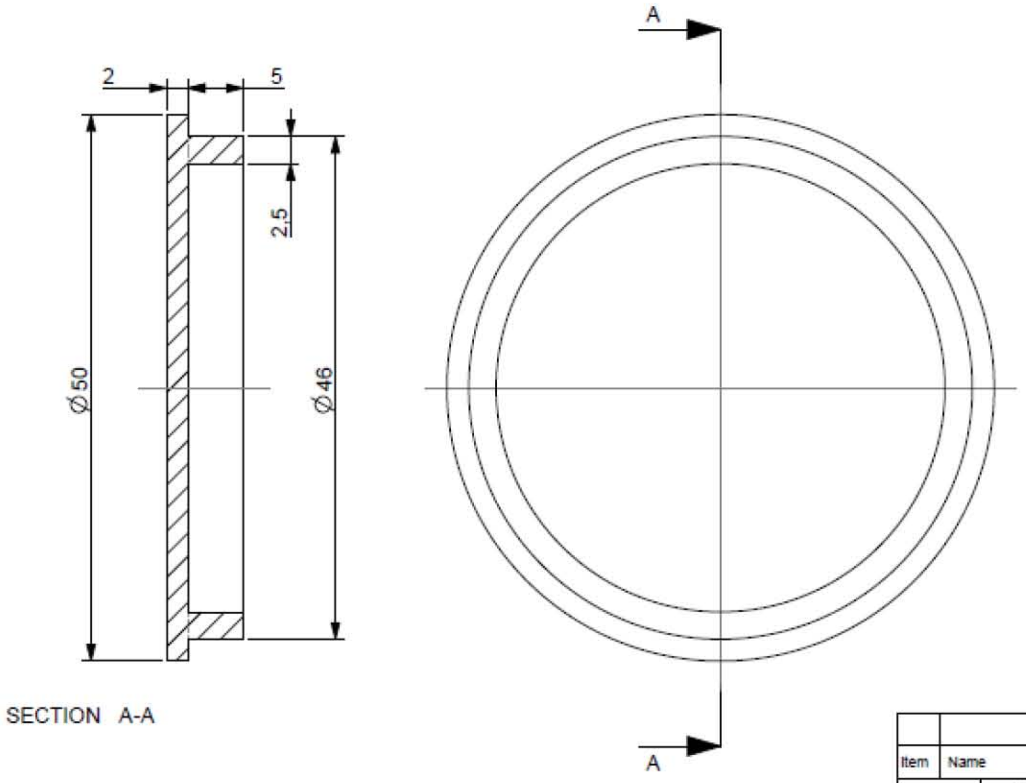

Item	Name	Qty	Material

University of Cape Town
Department of Mechanical Engineering

Title
STRIKER CAP - LARGE H 2MM

Dimensions in mm Tolerance U.O.S.	Scale	Date	Sheet	of
	2,000	24 NOV 2009	xx	xx
0.1	Drawn By R.P. MERRETT		Drawing Number xx	

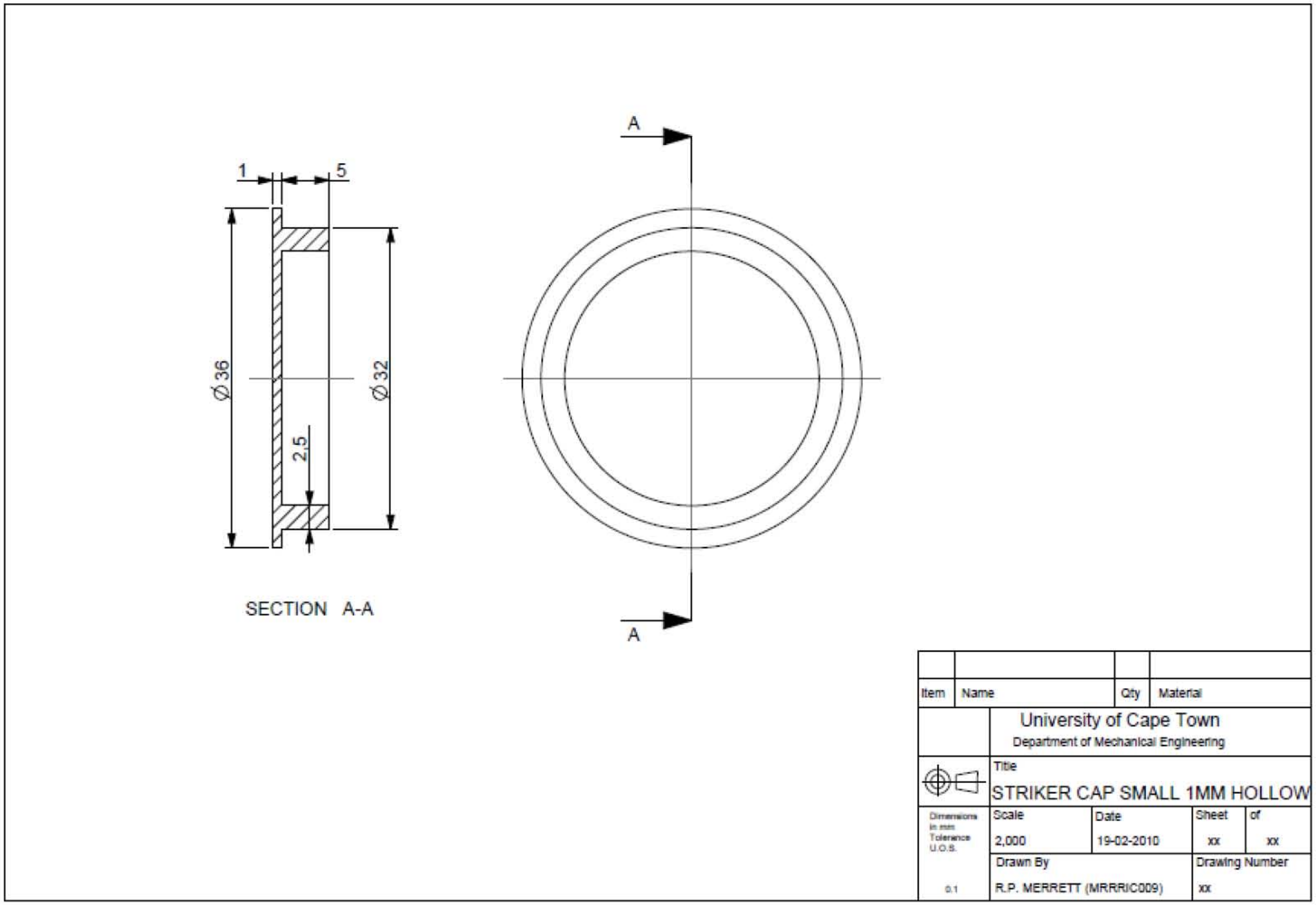

Item	Name	Qty	Material

University of Cape Town
Department of Mechanical Engineering

Title
STRIKER CAP SMALL 1MM HOLLOW

Dimensions in mm Tolerance U.O.S. 0.1

Scale	Date	Sheet	of
2,000	19-02-2010	xx	xx

Drawn By
R.P. MERRETT (MRRRIC009)

Drawing Number
xx

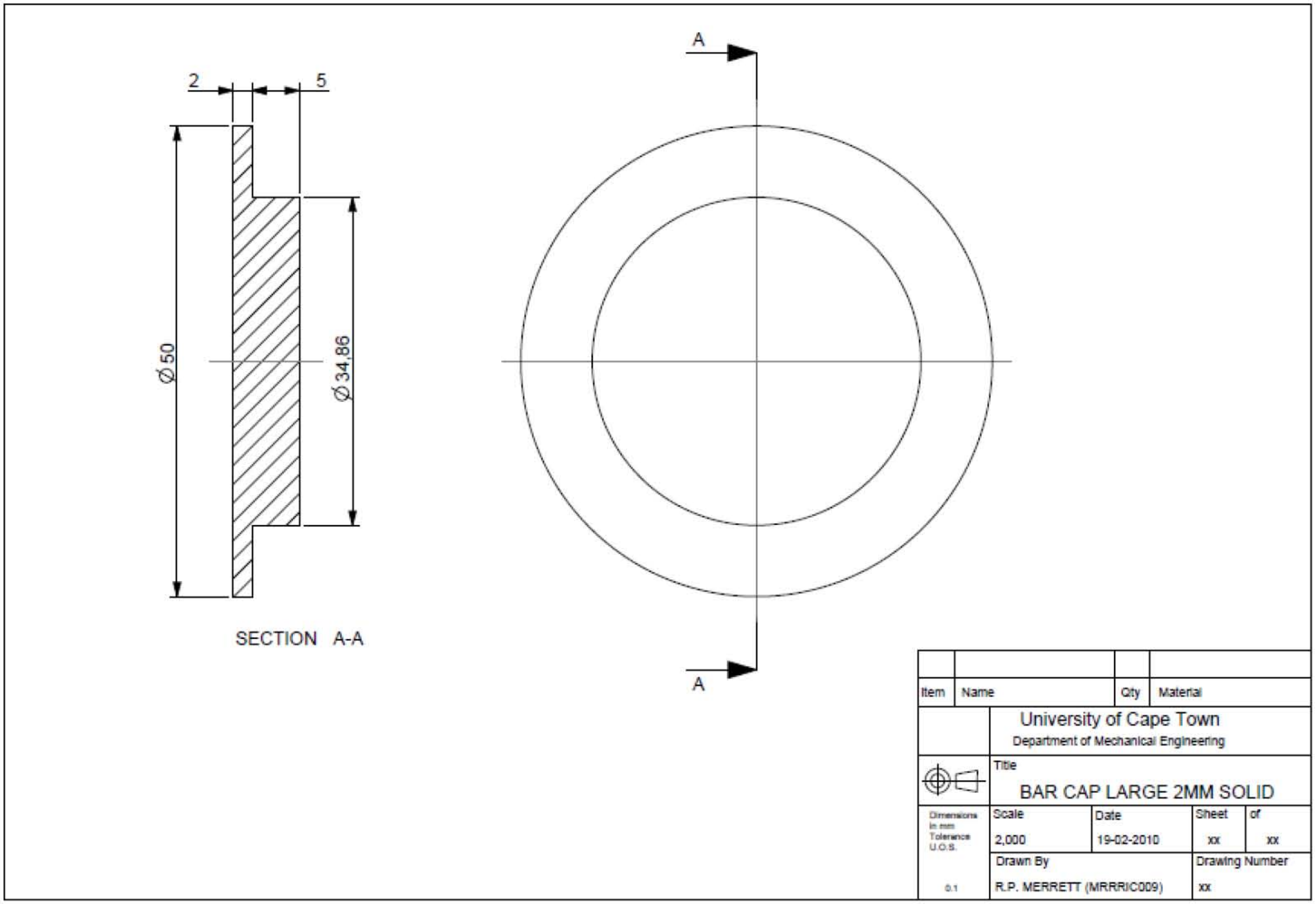

Item	Name	Qty	Material

University of Cape Town
Department of Mechanical Engineering

Title
BAR CAP LARGE 2MM SOLID

Dimensions in mm
Tolerance U.O.S.
0.1

Scale	Date	Sheet	of
2,000	19-02-2010	xx	xx

Drawn By
R.P. MERRETT (MRRRIC009)

Drawing Number
xx

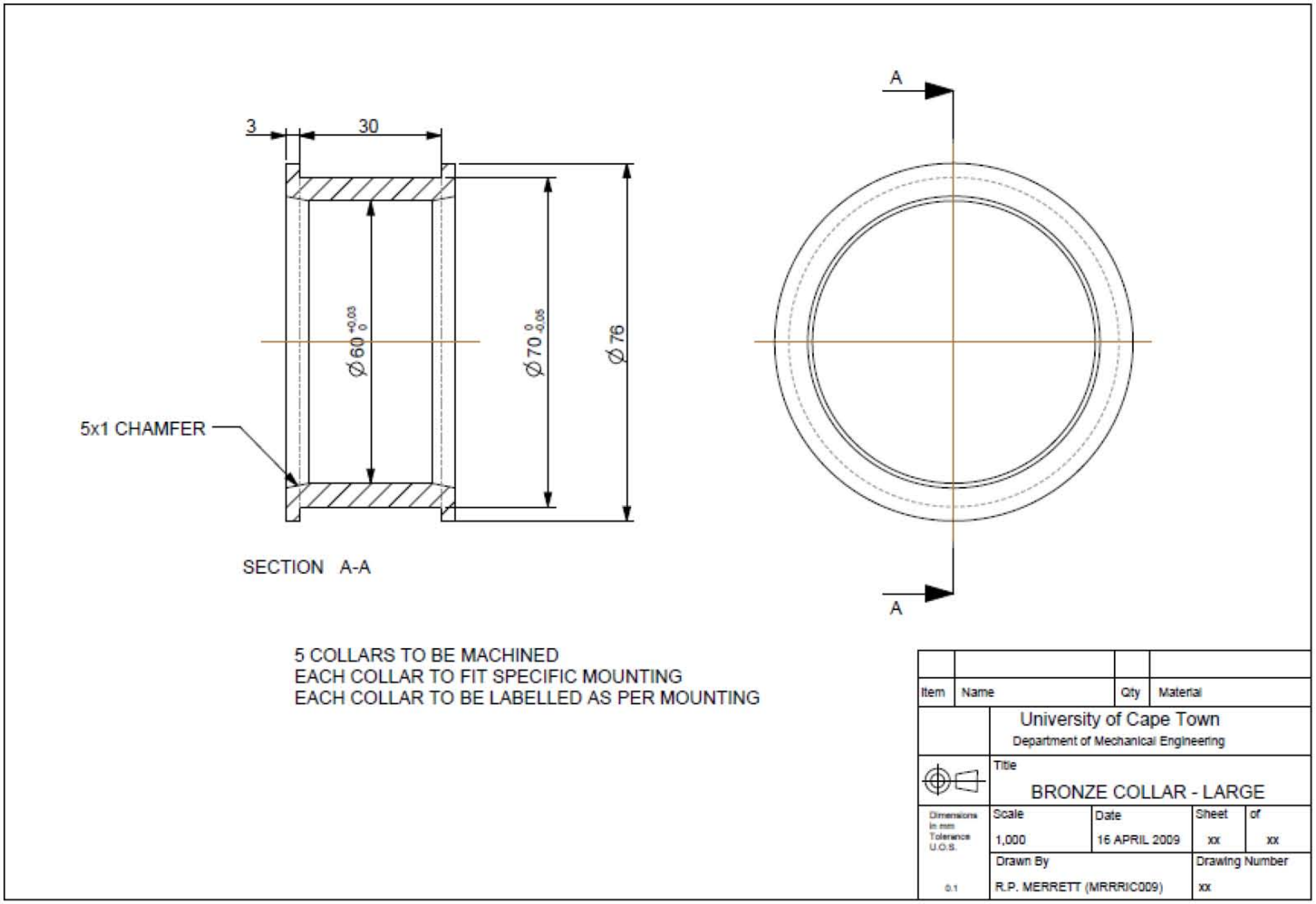

5 COLLARS TO BE MACHINED
EACH COLLAR TO FIT SPECIFIC MOUNTING
EACH COLLAR TO BE LABELLED AS PER MOUNTING

Item	Name	Qty	Material

University of Cape Town
Department of Mechanical Engineering

Title
BRONZE COLLAR - LARGE

Dimensions in mm
Tolerance U.O.S.
0.1

Scale	Date	Sheet	of
1,000	16 APRIL 2009	xx	xx

Drawn By	Drawing Number
R.P. MERRETT (MRRRIC009)	xx

1 SET OF 5 BUSHES TO BE MACHINED
BUSHES TO BE PRESS FITTED INTO BRONZE BUSH (LARGE)
CENTRE OF BUSHES TO BE BORED TO RUN SMOOTHLY ON ALUMINIUM TUBE

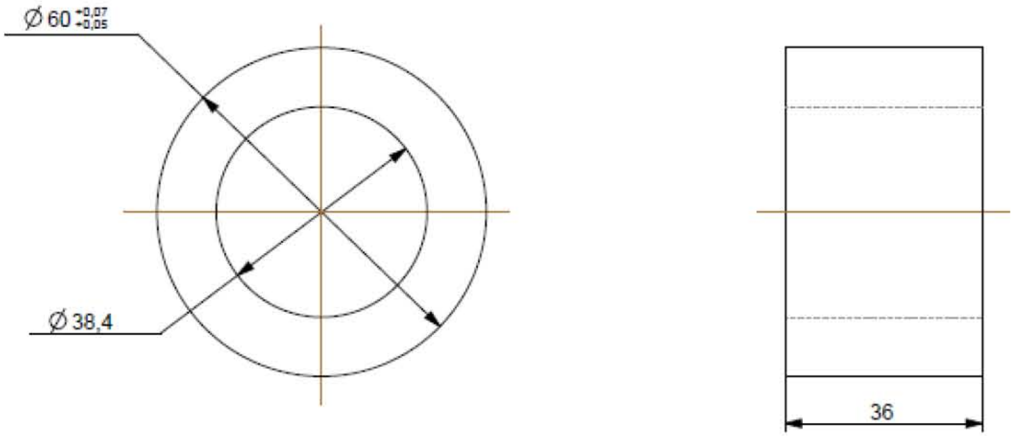

Item	Name	Qty	Material

University of Cape Town
Department of Mechanical Engineering

Title
TEFLON BUSH - LARGE

Dimensions in mm Tolerance U.O.S.	Scale	Date	Sheet	of
	1,000	16 APRIL 2009	xx	xx
	Drawn By		Drawing Number	
0.1	R.P. MERRETT (MRRRIC009)		xx	

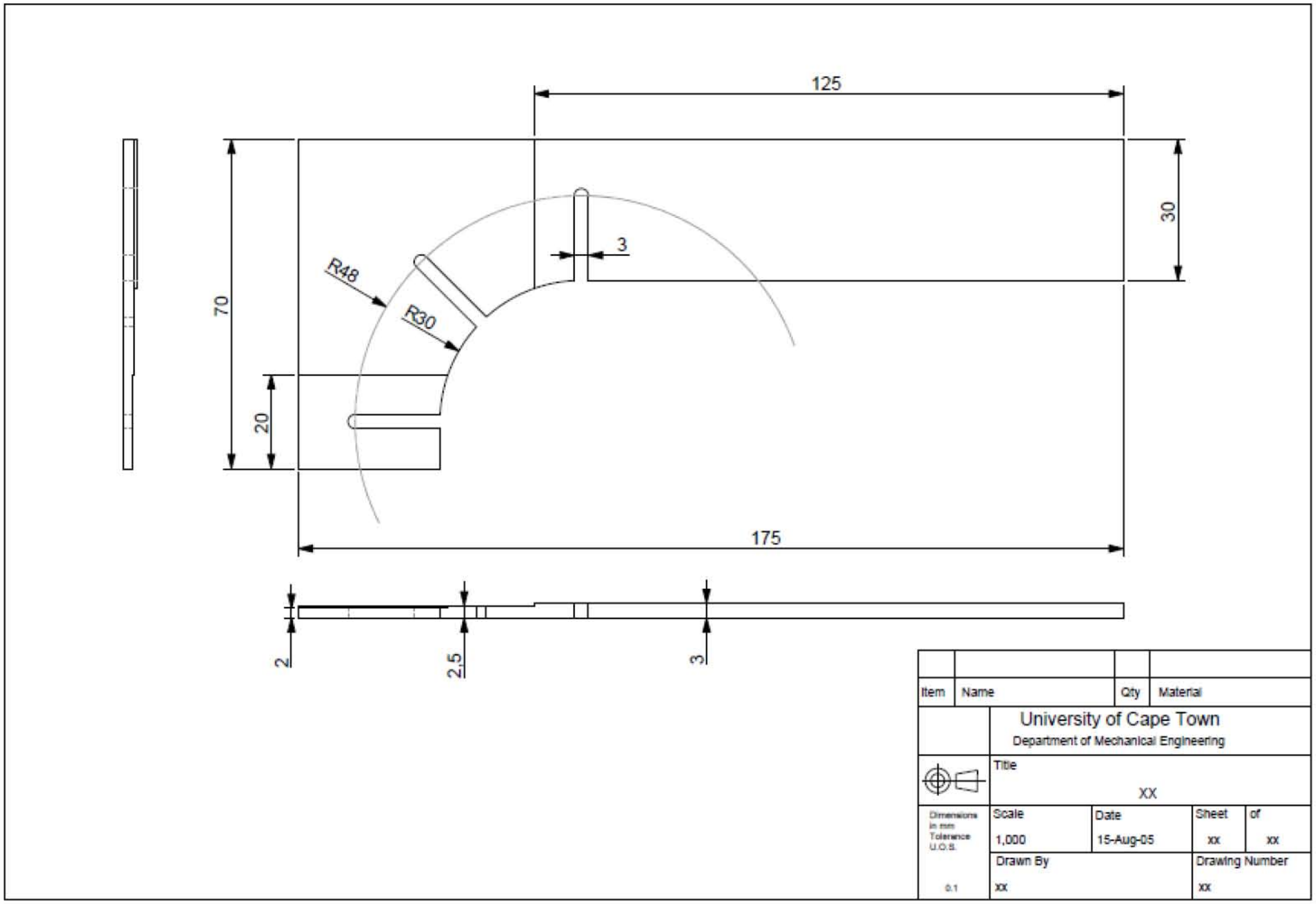
125
30
3
R48
R30
70
20
175
2
2,5
3
Item
Name
Qty
Material
University of Cape Town
Department of Mechanical Engineering
Title
XX
Dimensions in mm
Tolerance U.O.S.
0.1
Scale
1,000
Date
15-Aug-05
Sheet
xx
of
xx
Drawn By
xx
Drawing Number
xx

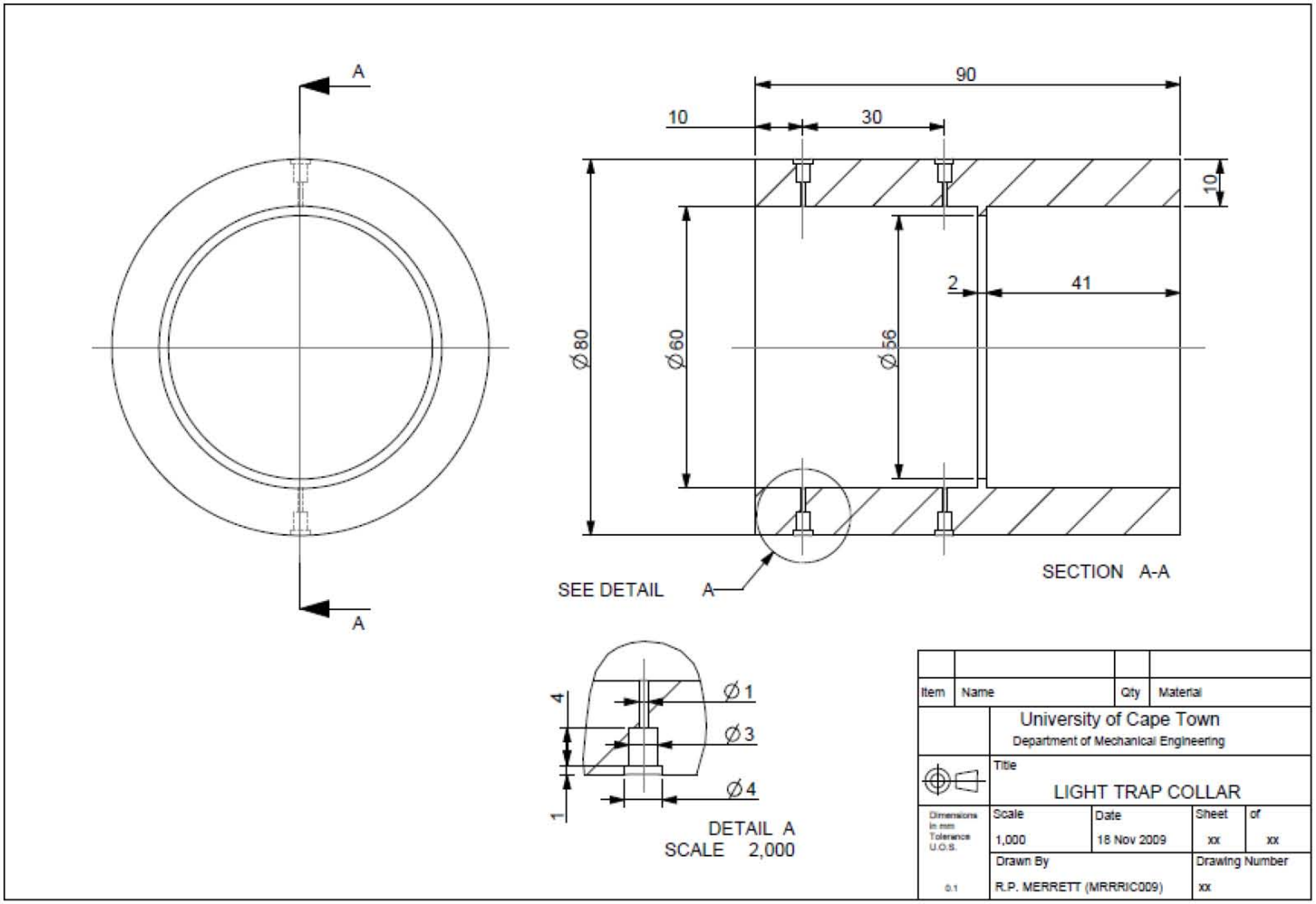
A
A
90
10
30
10
Ø80
Ø60
Ø56
2
41
SEE DETAIL A
SECTION A-A
Ø1
Ø3
Ø4
4
4
1
DETAIL A
SCALE 2,000
Item
Name
Qty
Material
University of Cape Town
Department of Mechanical Engineering
Title
LIGHT TRAP COLLAR
Dimensions in mm
Tolerance U.O.S.
0.1
Scale
1,000
Date
18 Nov 2009
Sheet
xx
of
xx
Drawn By
R.P. MERRETT (MRRRIC009)
Drawing Number
xx

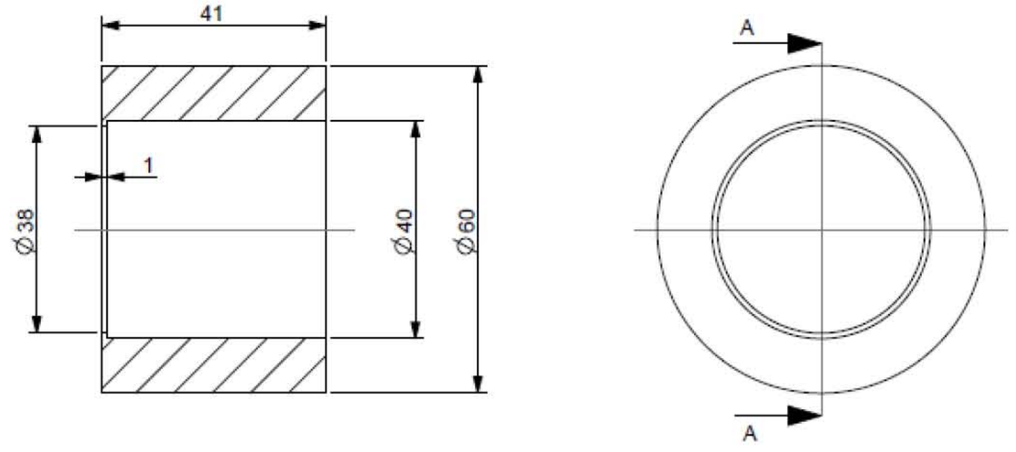

SECTION A-A

Item	Name	Qty	Material

University of Cape Town
Department of Mechanical Engineering

Title
LIGHT TRAP COLLAR

Dimensions in mm
Tolerance U.O.S.
0.1

Scale	Date	Sheet	of
1,000	18 Nov 2009	xx	xx

Drawn By	Drawing Number
R.P. MERRETT (MRRRIC009)	xx